

**Structures, activities, and mechanisms under the spectroscopes
the quest for unveiling the nature of active sites for highly selective CO₂ hydrogenation to methanol**

Phongprueksathat, N.

DOI

[10.4233/uuid:3939622b-ccb0-42b3-868f-bc0764a96b4f](https://doi.org/10.4233/uuid:3939622b-ccb0-42b3-868f-bc0764a96b4f)

Publication date

2023

Document Version

Final published version

Citation (APA)

Phongprueksathat, N. (2023). *Structures, activities, and mechanisms under the spectroscopes: the quest for unveiling the nature of active sites for highly selective CO₂ hydrogenation to methanol*. [Dissertation (TU Delft), Delft University of Technology]. <https://doi.org/10.4233/uuid:3939622b-ccb0-42b3-868f-bc0764a96b4f>

Important note

To cite this publication, please use the final published version (if applicable).
Please check the document version above.

Copyright

Other than for strictly personal use, it is not permitted to download, forward or distribute the text or part of it, without the consent of the author(s) and/or copyright holder(s), unless the work is under an open content license such as Creative Commons.

Takedown policy

Please contact us and provide details if you believe this document breaches copyrights.
We will remove access to the work immediately and investigate your claim.

Structures, activities, and mechanisms under the spectroscopes

— the quest for unveiling the nature of active sites for highly selective CO₂ hydrogenation to methanol



Structures, activities, and mechanisms under the spectroscopes

Nat Phongprueksathat

**Structures, activities, and mechanisms under
the spectroscopes — the quest for unveiling
the nature of active sites for highly selective
CO₂ hydrogenation to methanol**

Dissertation

for the purpose of obtaining the degree of doctor
at Delft University of Technology

by the authority of the Rector Magnificus, Prof.dr.ir. T.H.J.J. van der Hagen,

chair of the Board of Doctorates

to be defended publicly on

Tuesday 28 February 2023 at 15:00 o'clock

By

Nat PHONGPRUEKSATHAT

Master of Science in Petrochemical Technology,

Chulalongkorn University, Thailand

Born in Surat Thani, Thailand

This dissertation has been approved by the promotor.

Composition of the doctoral committee:

Rector Magnificus	Chairperson
Prof. dr. ir. A. Urakawa	Delft University of Technology, promotor
Prof. dr. E.A. Pidko	Delft University of Technology, promotor

Independent members:

Prof. dr. ir. E.J.M Hensen	Eindhoven University of Technology
Prof. dr. J.A. van Bokhoven	ETH Zürich
Prof. dr. ir. W. de Jong	Delft University of Technology
Dr. P.M. Abdala	ETH Zürich
Prof. dr. ir. J.J.C. Geerlings	Delft University of Technology, reserve member

*“Science works on the frontier between
knowledge and ignorance.
We’re not afraid to admit what we don’t know.
There’s no shame in that.
The only shame is to pretend that
we have all the answers.”*

— Neil deGrasse Tyson

from Cosmos: A Spacetime Odyssey

Nat Phongprueksathat

Structures, activities, and mechanisms under the spectroscopes

ISBN

978-94-6458-946-7 (paperback)

A catalog record is available at the Delft University of Technology library.

Copyright

© 2023 by Nat Phongprueksathat

About this work

The research described in this dissertation has been conducted in the laboratory of the Catalysis Engineering section, a part of the Chemical Engineering department of the Faculty of Applied Science at the Delft University of Technology, the Netherlands. The works described in Chapters 2 and 3 had been performed in the Urakawa Research Group at the Institute of Chemical Research of Catalonia (ICIQ), Tarragona, Spain.

The research described in this dissertation was funded by the Swiss National Science Foundation (Sinergia grant no. CRSII5-183495) and MINECO, Spain (CTQ2016-75499-R (FEDER-UE)).

Cover design, artwork & illustrations

Nat Phongprueksathat | Empowered by Midjourney

Printing

Ridderprint | www.ridderprint.nl | Alblasserdam, the Netherlands

Content

PREFACE

Summary	viii
Samenvatting	x
CHAPTER 1	
Introduction	1

PART I: Insights into Copper-based catalysts

CHAPTER 2	Greener and facile synthesis of Cu/ZnO catalysts for CO ₂ hydrogenation to methanol by urea hydrolysis of acetates	31
CHAPTER 3	From CO or CO ₂ ?: space-resolved insights into high-pressure CO ₂ hydrogenation to methanol over Cu/ZnO/Al ₂ O ₃	59
CHAPTER 4	Decisive roles of peripheral promoters in promoting methanol selectivity of CO ₂ hydrogenation over Cu-based catalysts	83

PART II: Insights into Rhenium-based catalysts

CHAPTER 5	Bifunctionality of Re supported on TiO ₂ in driving methanol formation in low-temperature CO ₂ hydrogenation	111
CHAPTER 6	A synergistic interplay between Ag and Re supported on TiO ₂ promotes methanol selectivity in low-temperature CO ₂ hydrogenation	159

OUTLOOK	193
----------------	-----

APPENDICES

APPENDIX A	Acknowledgments	199
APPENDIX B	List of publications	205
APPENDIX C	Curriculum Vitae	207

Preface



Summary

Since the industrial revolution in the 1760s, the CO₂ concentration in the atmosphere has been rising incessantly driving global warming closer to the point of no return. The world requires urgent actions to not only reduce CO₂ emissions but also capture the CO₂ for utilization to mitigate the future environmental crisis. CO₂ hydrogenation to CH₃OH offers an alternative to produce a feasible and economic substitute for oil. This technology also resembles the nearly 100 years old CH₃OH synthesis processes from syngas containing H₂, CO, and CO₂. The conventional Cu/ZnO/Al₂O₃ catalyst has also been applied for more than 50 years, and its high performance stems from synergies between Cu and ZnO. However, the true nature of the interfacial sites is still extensively debated. Moreover, lower temperature and higher pressure are thermodynamically favorable for maximum CO₂ conversion and CH₃OH selectivity according to Le Châtelier's principle and beneficial in terms of energy consumption and catalyst stability against sintering. The limitation in the catalytic performance of Cu/ZnO/Al₂O₃ in such conditions demands the exploration of novel catalysts.

Part I of this dissertation is dedicated to gaining a deeper understanding of Cu-ZnO synergistic structure as well as other Cu-based catalysts. In **Chapter 2**, we proposed a greener synthesis route for Cu/ZnO catalysts via urea hydrolysis of acetate precursors that can achieve comparable activity to commercial Cu/ZnO/Al₂O₃ catalysts without producing wastewater. Co-precipitated Cu-Zn hydroxycarbonate mineral-like precursors are crucial for a high inter-dispersion between CuO and ZnO after calcination and providing Cu-ZnO interfacial sites for the reaction.

In **Chapter 3**, the effects of key process conditions, namely temperature and pressure, on CO₂ hydrogenation over a commercial Cu/ZnO/Al₂O₃ catalyst were investigated using a space-resolved study. The gradients of reactants/products concentration and catalyst bed temperature within the catalytic reactor can reveal the significant effect of temperature on the dominant reaction pathways. CH₃OH is formed through direct CO₂ hydrogenation at low temperatures, while CH₃OH formation is mediated via CO which is formed by a reverse water-gas shift reaction at a high temperature. Although pressure did not influence the reaction pathway, higher pressure helped suppress CH₃OH decomposition to CO.

In **Chapter 4**, the decisive roles of peripheral promoters to Cu nanoparticles in promoting CH₃OH selectivity were elucidated. The model Cu-based catalysts (Cu-M/SiO₂, M = Zn, Ga, and In) were prepared via surface organometallic chemistry (SOMC). The M⁺ sites played important

roles in stabilizing formate species spillovered from Cu and determining the reactivity of formate hydrogenation. Improving the spillover and tuning the reactivity of formate help suppress formate decomposition to CO over Cu and ultimately boost CH₃OH selectivity.

Part II is dedicated to exploring the novel catalysts for low-temperature CO₂ hydrogenation, as well as, gaining a deeper understanding of the state-of-the-art Re/TiO₂ catalyst. In **Chapter 5**, the bifunctionality of Re supported on TiO₂ was deciphered, where metallic Re functions as the H₂ activator and cationic Re as the CO₂ activator. Re/TiO₂ suffers from additional CH₄ formation, and the active intermediates and reaction pathways for CH₃OH and CH₄ were identified. Understanding the nature of active sites and reaction mechanisms over Re/TiO₂ led to approaches for CH₄ selectivity mitigation in **Chapter 6**. Exploring various transition metals under low-temperature conditions provided insights into the formate stabilization of the coinage metals (Cu, Ag, and Au). Since the balance between metallic and cationic Re limited the CH₃OH selectivity of Re/TiO₂, the addition of Ag complemented the role of cationic Re. A synergistic interplay between Ag and Re did not only improve CH₃OH selectivity significantly by suppressing intermediates in the reaction pathways toward CH₄ but also exhibited superior stability.

Finally, the dissertation conveys a message that obtaining the definitive synthesis of well-defined active sites, expansive structure-activity relationships, and comprehensive reaction mechanisms are the major prerequisites for the rational design of novel catalysts.

Samenvatting

Sinds de industriële revolutie in de jaren 1760 is de CO₂-concentratie in de atmosfeer onophoudelijk gestegen, waardoor de opwarming van de aarde steeds dichterbij het kantelpunt komt. De wereld heeft dringend maatregelen nodig om niet alleen de CO₂-uitstoot te verminderen, maar ook om CO₂ op te vangen voor gebruik en om de toekomstige milieucrisis te beperken. CO₂-hydrogenering tot CH₃OH biedt een oplossing om een haalbaar en economisch alternatief voor olie te vinden. Deze technologie is erg vergelijkbaar met de bijna 100 jaar oude CH₃OH-syntheseprocessen uit syngas, wat H₂, CO en CO₂ bevat. De conventionele Cu/ZnO/Al₂O₃-katalysator wordt ook al meer dan 50 jaar toegepast, en zijn hoge prestaties komen voort uit de synergie tussen Cu en ZnO. Over de ware aard van de interfaciale sites wordt echter nog uitvoerig gedebatteerd. Bovendien zijn een lagere temperatuur en een hogere druk thermodynamisch gunstig voor een maximale CO₂-omzetting en CH₃OH-selectiviteit volgens het principe van Le Châtelier en gunstig voor het energieverbruik en de stabiliteit van de katalysator tegen sinteren. De beperking van de katalytische prestaties van Cu/ZnO/Al₂O₃ in dergelijke omstandigheden vereist de exploratie van nieuwe katalysatoren.

Deel I van dit proefschrift is gewijd aan het verkrijgen van een dieper inzicht in de synergetische structuur van Cu-ZnO en andere op Cu gebaseerde katalysatoren. In **Hoofdstuk 2** stelden we een groenere synthesroute voor Cu/ZnO katalysatoren voor via ureumhydrolyse van acetaatvoorlopers die een vergelijkbare activiteit kan bereiken als commerciële Cu/ZnO/Al₂O₃ katalysatoren zonder afvalwater te produceren. Co-geprecipiteerde Cu-Zn hydroxycarbonaat mineraalachtige precursoren zijn cruciaal voor een hoge interdispersie tussen CuO en ZnO na calcinatie en het leveren van Cu-ZnO interfaciale sites voor de reactie.

In **Hoofdstuk 3** werden de effecten van de belangrijkste procescondities, namelijk temperatuur en druk, op CO₂-hydrogenering over een commerciële Cu/ZnO/Al₂O₃-katalysator onderzocht met behulp van een ruimtelijke resolutie studie. De gradiënten van reactanten/productconcentratie en katalysatorbedtemperatuur binnen de katalytische reactor onthullen het significante effect van temperatuur op de dominante reactieroutes. CH₃OH wordt gevormd door directe CO₂-hydrogenering bij lage temperatuur, terwijl de vorming van CH₃OH wordt bemiddeld via CO₂ dat wordt gevormd door een omgekeerde water-gasverschuivingsreactie. Hoewel de druk geen invloed had op de

reactieroute, hielp een hogere druk de ontleding van CH_3OH tot CO te onderdrukken.

In **Hoofdstuk 4** werd de doorslaggevende rol van perifere promotors van Cu-nanopartikels bij het bevorderen van de CH_3OH -selectiviteit opgehelderd. De modelkatalysatoren op basis van Cu (Cu-M/SiO_2 , $\text{M} = \text{Zn}$, Ga en In) werden bereid via oppervlakteorganometaalchemie (SOMC). De M^+ sites speelden een belangrijke rol bij het stabiliseren van formiaatspecies die van Cu werden overgeheveld en bij het bepalen van de reactiviteit van formiaathydrogenering. Het verbeteren van de spillover en het afstemmen van de reactiviteit van formiaat helpen de ontbinding van formiaat tot CO over Cu te onderdrukken en verhogen uiteindelijk de selectiviteit van CH_3OH .

Deel II is gewijd aan de verkenning van nieuwe katalysatoren voor CO_2 -hydrogenering bij lage temperatuur en aan een beter begrip van de geavanceerde Re/TiO_2 -katalysator. In **Hoofdstuk 5** werd de bifunctionaliteit van Re ondersteund op TiO_2 ontrafeld, waarbij metallisch Re functioneert als H_2 -activator en kationisch Re als CO_2 -activator. Re/TiO_2 heeft last van extra CH_4 -vorming, en de actieve tussenproducten en reactieroutes voor CH_3OH en CH_4 werden geïdentificeerd. Inzicht in de aard van actieve sites en reactiemechanismen over Re/TiO_2 leidde tot benaderingen voor CH_4 -selectiviteitsvermindering in **Hoofdstuk 6**. Het onderzoeken van verschillende overgangsmetalen onder lage-temperatuurcondities gaf inzicht in de formaatstabilisatie van de metallische metalen (Cu , Ag en Au). Aangezien het evenwicht tussen metallisch en kationisch Re de CH_3OH -selectiviteit van Re/TiO_2 beperkte, vulde de toevoeging van Ag de rol van kationisch Re aan. Een synergetisch samenspel tussen Ag en Re verbeterde niet alleen de CH_3OH -selectiviteit aanzienlijk door het onderdrukken van tussenproducten in de reactieroutes naar CH_4 , maar vertoonde ook een superieure stabiliteit.

Het proefschrift brengt tenslotte de boodschap over dat de definitieve synthese van goed gedefinieerde actieve sites, uitgebreide structuur-activiteitsrelaties en uitgebreide reactiemechanismen de belangrijkste voorwaarden zijn voor het rationele ontwerp van nieuwe katalysatoren.

Introduction

Heterogeneously Catalyzed
 CO_2 Hydrogenation to methanol



Summary

To minimize the harmful environmental effects of CO₂ emissions, technologies for carbon capture and CO₂ recycling are needed to sustainably produce value-added chemicals and supplement the photosynthetic carbon cycle. In this chapter, the development of heterogeneous catalysts and processes for the direct CO₂ hydrogenation to methanol are summarized from past to present, with special emphasis on thermodynamics considerations, catalyst designs, mechanistic aspects, and recent advances. A more selective and technologically mature route for alcohol synthesis from CO₂ hydrogenation to methanol is introduced, a key chemical for an oil-independent economy (methanol economy). The major challenge, apart from the high energy cost for CO₂ capture and H₂ production, remains the true understanding of the active sites and reaction mechanism.



This chapter is based on the following publication:

Phongprueksathat, N., & Urakawa, A.

CO₂ Hydrogenation Catalysis (2021) 207–236. Weinheim, Germany: WILEY-VCH GmbH.

1.1 Introduction

Global warming, originating from anthropogenic CO₂ emission, had started to become a major concern by the end of the twentieth century since the environmental impacts became more significant. Consequently, CO₂ sequestration and utilization technologies have been developed as an approach to global warming mitigation. Among the various technologies being used for recycling CO₂, catalytic conversion of CO₂ into methanol, ethanol, and higher alcohols is a promising approach in terms of high CO₂ conversion rates and highly desired product selectivity. Moreover, these alcohols can be easily stored, transported, or continuously converted into high-octane gasoline and other feedstocks for a variety of chemical and energy industries.

In the following, we first discuss more selective and technologically matured routes for alcohol synthesis through CO₂ hydrogenation to methanol and then discuss a more challenging synthesis of higher alcohols. In each section, we highlight suitable catalysts, industrial process configurations, thermodynamic constraints, and recent development.

1.2 CO₂ Hydrogenation to Methanol – Past to Present

1.2.1 Syngas to Methanol

Methanol synthesis by CO₂ hydrogenation (**Eqn. 1.1**) is not a new concept. It was discovered almost in the same period (1925) as methanol synthesis from synthesis gas (**Eqn. 1.2**), a mixture primarily consisting of H₂ and CO.¹ At that time, the synthesis gas used for methanol synthesis had already contained a small amount of CO₂ – up to 10%. The CO₂ and H₂ obtained as a byproduct of fermentation processes were also used for methanol synthesis by some early plants operated in the United States.² However, hydrogenation of pure CO₂ appeared to be too costly because CO₂ requires more energy for C–O bond dissociation than CO to be converted into methanol or any other fuel.³



In an early process, CO₂ was even considered harmful for the methanol synthesis catalyst (e.g., ZnO/Cr₂O₃ and Cu/ZnO) due to its strong adsorption characteristic.^{4,5} Moreover, investigation of CO₂ hydrogenation is usually dismissed by the preconception that the carbon dioxide is converted to monoxide and subsequently follows the usual behavior of CO hydrogenation. It was not until decades later that the promotional effect of CO₂ on methanol synthesis was reported by Klier et al.⁵ During methanol synthesis from synthesis gas (**Eqn. 1.2**), the Cu/ZnO

catalysts experienced overreduction by the presence of CO that led to catalyst deactivation, even when the catalyst was pre-reduced with H₂ before reaction. It was found that a small concentration of CO₂ in synthesis gas can reoxidize the CO-reduced Cu catalyst and maintain the catalyst in an active state during the reaction. At higher concentrations, however, the reaction rate still suffered from strong adsorption of CO₂, and the selectivity of methanol was greatly reduced by the formation of methane, especially when the CO₂ concentration is above 10%. Therefore, the maximum reaction rate can be achieved by balancing those promoting and retarding effects. The synthesis rate, depending on carbon dioxide concentration, has a maximum of around 1% CO₂ for the commercial Cu/ZnO/Al₂O₃ catalyst (Imperial Chemical Industries [ICI] catalyst).⁶ After this finding, the role of CO₂ in methanol synthesis had been investigated widely on various kinds of Cu/ZnO catalysts.

1.2.2 CO₂ to Methanol

CO₂ hydrogenation has become a subject of considerable interest since CO₂ was identified as the main carbon source in methanol synthesis of syngas over the Cu/ZnO/Al₂O₃ catalyst.^{9, 10} The development of a catalytic system for pure CO₂ and feed is challenging since water produced during the reaction can adsorb on active site suppressing the catalytic activity and negatively affect the chemical equilibrium. Therefore, the early process was usually designed to eliminate water from the process consisting of two methanol synthesis reactors – a rectifier is simply introduced after the first reactor to remove water and methanol from the outlet stream before feeding into the second reactor. The CO produced from the first reactor is claimed to be beneficial for the catalyst since it acts as a water scavenger regenerating the Cu-active sites.¹¹ An increased methanol production by using such a design approach in a pilot plant was reported by Lurgi (a German engineering company) in 1994.¹² A similar approach was applied for two-step CO₂ conversion in the carbon dioxide hydrogenation to form methanol via a reverse-water-gas-shift reaction (CAMERE) pilot plant, in which the first reactor was designed to produce CO via reverse water-gas shift (RWGS) (**Eqn. 1.3**) before feeding to the second methanol synthesis reactor (**Figure 1.1a**).⁸ The traditional Cu/ZnO/Al₂O₃ catalyst is employed for both RWGS and methanol synthesis reactors. This process proves to have a higher methanol yield than a direct CO₂ hydrogenation process, achieving 100 kg of methanol production capacity per day on a pilot scale.

Generally, the economic feasibility of methanol plants depends on several factors such as the price of oil, electricity, CO₂, and byproducts. By the end of 2010, Carbon Recycling International (CRI) company established the first commercial direct CO₂ hydrogenation plant in Iceland. The plant was named in honor of Professor George A. Olah. The George Olah plant is capable of producing 3000 tons of methanol per year from recycled CO₂ and renewable hydrogen (i.e. hydrogen produced through renewable energy), as depicted in **Figure 1.2**. The CO₂ is recycled

from Svartsengi geothermal plant and an aluminum production plant, and hydrogen is generated from water electrolysis using geothermal power.^{13, 14}

Recently, the CAMERE process has been mathematically modeled in two dimensions and optimized numerically to employ a water perm-selective membrane in the methanol synthesis reactor for water removal (**Figure 1.1b**).¹⁵ The inlet temperature and pressure of the RWGS reactor are optimized at 700 °C and 30 bar over Ni/Al₂O₃ catalyst. The CAMERE process-assisted membrane can achieve a 20.8% higher methanol production rate than through the conventional route. In the CAMERE process without a membrane, water produced acts as a poison and deactivates the catalyst. Therefore, the CAMERE process-assisted membrane, in which water production is notably reduced, was proposed to increase the catalyst lifetime.

Although the CAMERE process has shown potential in prolonging catalyst lifetime, the commercially available Cu/ZnO/Al₂O₃ catalyst still suffers from low CO₂ conversion. Therefore, the concept of three-stage heat exchanger reactors (**Figure 1.1c**) is proposed by the same author.¹⁶ In the three-stage configuration, the product stream of each reactor is conveyed to a flash drum to remove methanol and water from unreacted H₂, CO, and CO₂. Then, the gaseous stream enters the top of the next reactor as the inlet feed. Using the same catalyst volume, the CO₂ conversion and methanol production rate from the three-stage reactor increased by ca. 50% and 103% compared to the one-stage reactor. These studies show that advanced reaction engineering concepts have the potential to exceed the performance of a more conventional process, although economic evaluations need to be carefully performed.

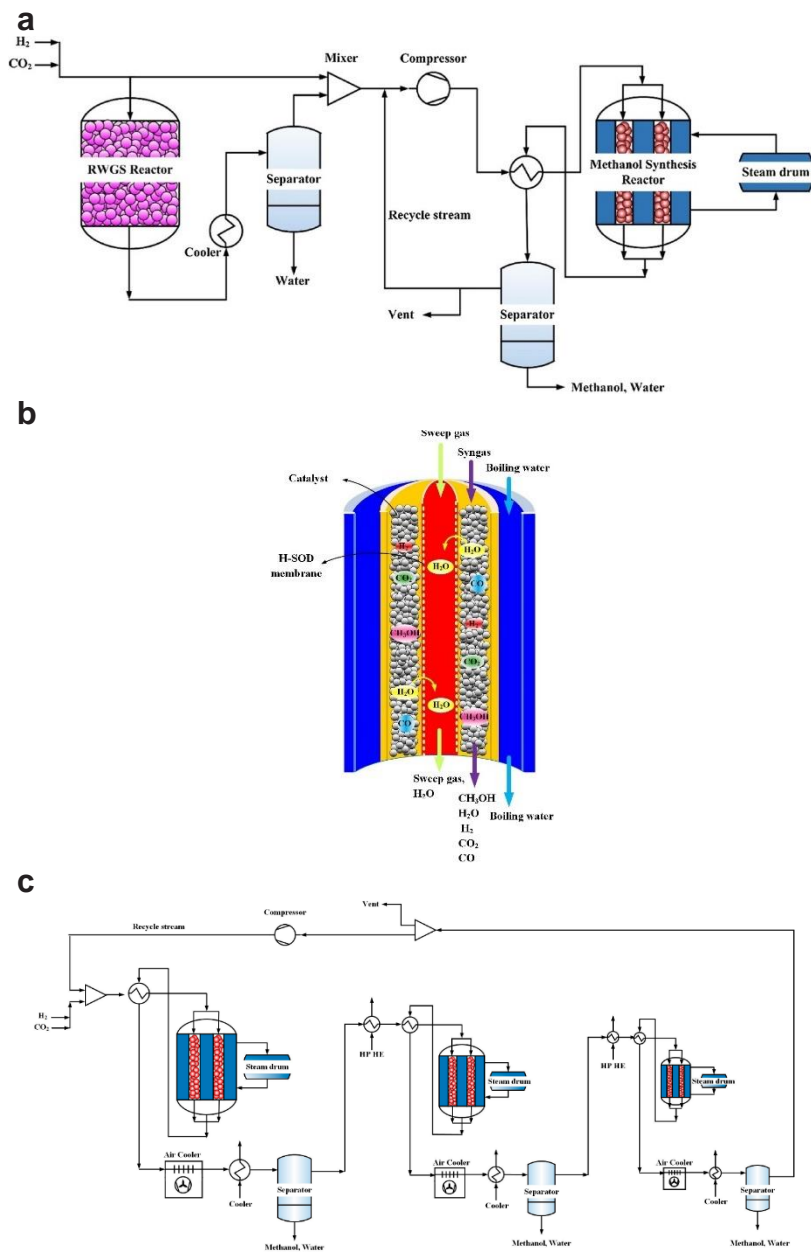


Figure 1.1 Schematic diagrams of the CAMERE process; **a** the original process, **b** with membrane reactors, and **c** with three-stage reactors. Source: **a**, **b** From Samimi et al.⁷ **c** Based on Joo et al.⁸



Figure 1.2 The “George Olah Carbon Dioxide to Renewable Methanol Plant” of Carbon Recycling International in Iceland based on local geothermal energy. The first commercial carbon dioxide recycling plant operating in the world.⁷

1.2.3 Thermodynamic Consideration – Chemical and Phase Equilibria

According to Le Châtelier’s principle, the thermodynamic equilibrium of methanol synthesis is mainly governed by the fugacity and enthalpy of the reaction. Therefore, the thermodynamically desirable conditions are low temperature due to its exothermicity, and high pressure due to the reduction in the number of molecules during the reaction. The reaction equilibrium calculation is based on the minimization of the Gibbs free energy. For decades, the reaction equilibrium of methanol synthesis from synthesis gas has been performed using the Soave-Redlich-Kwong (SRK) equation of state.¹⁷ This equation is one of the most accurate for a nonideal gas. In some cases, the theoretical calculation did not match with experiment results, especially at high pressure and low temperature. It was simply because methanol can condense to liquid at such conditions and the phase equilibrium was not considered in those calculations. Dew-point calculations are important for reactor and catalyst design. Precise predictive knowledge about when methanol condenses should facilitate taking advantage of *in situ* condensations for methanol synthesis beyond chemical equilibrium.

van Bennekom et al. proposed a model based on modified SRK to simultaneously calculate the phase and chemical equilibria of methanol synthesis from synthesis gas.¹⁹ The thermodynamic equilibria are consistent with experimental results performed in a packed bed reactor at 190-280 °C and 200 bar. The conversion values obtained in the experiments are higher than those of one-

phase chemical equilibrium, and this suggests that condensation is beneficial for methanol synthesis. Moreover, the visual inspection of phase separation during methanol synthesis of synthesis gas has been demonstrated for the first time by the authors.¹⁸ As shown in **Figure 1.3**, the liquid condensation was observed from a view cell at 200 °C and 200 bar.

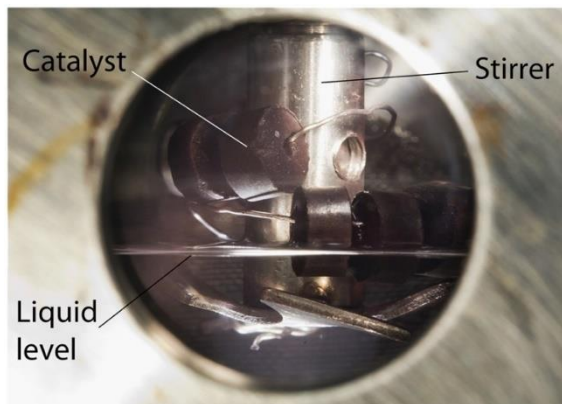


Figure 1.3 Liquid formation in a view cell during methanol synthesis of H₂, CO, and CO₂ (0.70/0.28/0.02) at 200 °C and 200 bar.¹⁸

To exploit *in situ* condensation in methanol synthesis, operating conditions may be selected to enhance the overall driving force in methanol synthesis, whereas the conversion at phase and chemical equilibria is considerably different from that at which condensation starts. The actual reaction rates result from a tradeoff between the reaction rate and the condensation rate. For example, the reaction rates increase with increasing temperature, while the saturation and condensation at the dew point decrease with increasing temperature. Therefore, a highly active catalyst is crucial for *in situ* condensation since it allows lower reaction temperature with sufficient conversion for saturating condensable products. Nowadays, conducting *in situ* condensation is possible not only in methanol synthesis from synthesis gas but also in chemically stable CO₂ thanks to the availability of active catalysts.

Thermodynamic equilibrium evaluation of methanol synthesis from only CO₂ and H₂ has been performed by Bansode and Urakawa²¹ and Gaikwad et al.²² The analysis considers both phases and chemical equilibria, and the calculation was based on the modified-SRK model reported by van Bennekom et al.^{18, 19} **Figure 1.4** shows the CO₂ conversion and methanol selectivity derived from such a model over a wide range of pressures and temperatures. The other possible product is CO and only the reactions of **Eqns. 1.1-1.3** were assumed to take place.

The indication of phase condensation and separation in CO₂ hydrogenation to methanol at a stoichiometric ratio (H₂/CO₂ = 3) is an abrupt change in CO₂ conversion within a narrow temperature range, especially at 100-300 bar (**Figure 1.4**). For example, the CO₂ conversion changes drastically within 230-240 °C at 200

bar, which is close to that reported by van Bennekom et al. On the other hand, the phase condensation does not seem to exist at all at $H_2/CO_2 = 10$, as thermodynamically expected, although CO_2 equilibrium conversion is greatly boosted. The change in CO_2 conversion becomes smoother at higher pressure (>400 bar) due to the formation of one dense phase.

The visual inspection of phase separation during CO_2 hydrogenation to methanol was demonstrated in a high-pressure view cell by Kommoß et al.²³ In this cell, a mixture of H_2 , CO_2 , CH_3OH , and H_2O was prepared to simulate a product stream outlet from a reactor at 50% CO_2 conversion and 67% CH_3OH selectivity. The results confirmed an *in situ* phase separation at 206 °C and 150 bar, which is close to the theoretical expectation (**Figure 1.4**). However, to take advantage of phase separation at that pressure, the reaction should be operated below 206 °C, which is not practical and kinetically favorable. The optimal temperature to maximize CO_2 conversion, CH_3OH selectivity, and thus methanol yield is reported to be around 260-280 °C. Therefore, to increase liquid condensation temperature to match the optimum temperature, increasing reaction pressure is suggested.

The advantage of high pressure in CO_2 hydrogenation to methanol has been exemplified by Gaikwad et al.²² About 90% CO_2 conversion and >95% methanol selectivity could be attained at 260-280 °C and 442 bar (partial pressure of the reactants) from the stoichiometric feed ($H_2/CO_2 = 3$). However, under such high-pressure conditions, a dense phase has formed and limited the internal mass transfer and ultimately decreasing the overall reaction rate. Mass transfer limitation inhibits the utilization of the whole catalyst pellet, which can be eliminated by reducing the catalyst pellet size. On the other hand, the mass transfer limitation is negligible at 331 bar and results show the almost-full (>95%) CO_2 conversion and >98% methanol selectivity at 260 °C. Therefore, when mass transfer limitations are minimized, it is possible to achieve ca. 90% methanol yield under continuous operation with unprecedentedly high weight time yield (gram of methanol produced per gram of catalyst per hour).

Another example of taking advantage of phase separation by a novel reactor design was reported by Bos and Brilman.²⁴ The reactor makes use of two temperature zones to shift the chemical equilibrium: a high-temperature zone for optimal catalyst activity and a low-temperature zone for full conversion by *in situ* condensations of a water/methanol mixture. Since the thermodynamic limitations are surpassed in this reactor, a full carbon conversion (>99.5%) and high methanol selectivity (>99.5% on a carbon basis) could be achieved at relatively low temperature and pressure (210 °C and 50 bar).

Recently, the concept of *in situ* water absorption has been proposed to overcome thermodynamic limitations similar to the *in situ* condensation concept.²⁵ The thermodynamic analysis has shown that the methanol yield can increase up to >130%, leading to a 15% higher methanol productivity. From the process simulation, *in situ* water sorption allows operation at much milder pressure conditions at 50 bar and 230 °C to produce ca. 70% methanol yield, whereas the conventional process

achieves only 25%. However, the methanol selectivity is slightly lower than the conventional process, as the RWGS equilibrium seems to be affected more than that of CO₂ hydrogenation to methanol.

Generally, high-pressure conditions are thermodynamically beneficial for methanol synthesis. At the same time, the reaction rates are enhanced by increased partial pressures of the reactants. The phase condensation allows full CO₂ conversion, and such a high conversion may offer a possibility to omit the necessity of a recycle stream. Particularly, high-pressure shows potential for the combination of methanol synthesis and reforming in supercritical water, where a high-pressure synthesis gas is produced by pressurizing a liquid.¹⁹

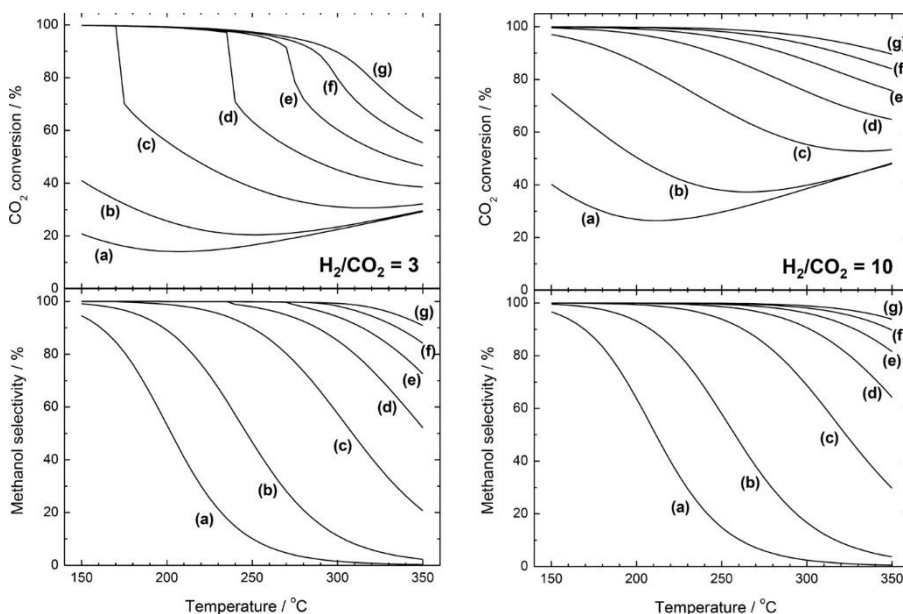


Figure 1.4 Equilibrium CO₂ conversion and methanol selectivity at different temperatures with initial H₂/CO₂ mixtures of 3 (left) and 10 (right), and at (a) 10 bar, (b) 30 bar, (c) 100 bar, (d) 200 bar, (e) 300 bar, (f) 400 bar, and (g) 500 bar.²⁰

1.2.4 Catalyst Developments

The first patented catalyst for the methanol synthesis process is Cu-based catalysts developed by Lormand in 1925.¹ Despite higher activity, abundance, and economic advantages compared to other transition metals at that time (e.g. Pt, Ni, Fe, and Co), these catalysts were still thermally unstable and susceptible to sulfur poisoning – these drawbacks hindered the commercial application of Cu-based catalysts for almost half a century.²⁶ It was not until 1966 that ICI could discover a new co-precipitation technique for the preparation of ternary Cu/ZnO/Al₂O₃ catalyst

and overcome the intrinsic drawbacks previously mentioned. Simultaneously, gas purification processes were improved to produce sulfur-free synthesis gas from natural gas, naphtha, and crude oil, such as the Rectisol process developed by Lurgi. Both cleaner feedstocks and better development ultimately resulted in a great enhancement of methanol synthesis in terms of activity and selectivity, and significantly milder reaction conditions toward lower temperature and pressure. This sparked the research trend toward Cu/ZnO based-catalysts ever since and eventually resulted in hundreds of publications. Even in the past 10 years, Cu/ZnO-based catalysts remained one of the most investigated for CO₂ hydrogenation, as shown in a statistical breakdown (**Figure 1.5**).

Technically, high Cu surface area, defects, and Cu-ZnO interfaces are well accepted to be required for the high catalytic activity of the Cu/ZnO-based catalysts. Those requirements are directly related to the method of preparation. Among various methods reported in the literature over the past 10 years, it is obvious that co-precipitation is by far the most successful and preferable method for the preparation of Cu/ZnO-based catalysts (**Figure 1.6**). The main advantage of the co-precipitation method is the ability to produce nanoparticles and porous microstructure of Cu-ZnO through a multistep synthesis route.

The prominent example is the original synthesis procedure for Cu/ZnO/Al₂O₃ catalyst developed by ICI shown in **Figure 1.7**. The initial step of co-precipitation is the formation of mineral-like hydroxycarbonate precursors by mixing between metal salt solution (e.g., aqueous nitrates, sulfates, or chlorides of Cu, Zn, and/or Al) and basic precipitating agent (e.g. carbonates, bicarbonates, or hydroxides). The hydroxycarbonate structure depends on Cu and Zn contents as well as precipitating conditions (temperature and pH), and varies from amorphous zincian georgeite to crystallite structure such as copper hydrozincite ((Cu_xZn_{1-x})₅(OH)₆(CO₃)₂, when $x < 0.1$), aurichalcite ((Cu_xZn_{1-x})₅(OH)₆(CO₃)₂, when $x < 0.5$), rosasite ((Cu_xZn_{1-x})₂(OH)₂(CO₃), when $0.5 < x < 0.7$), zincian malachite ((Cu_xZn_{1-x})₂(OH)₂(CO₃) when $x > 0.7$), and hydrotalcite (Cu_{1-x-y}Zn_yAl_x(OH)₂(CO₃)_{x/2}, when $0.3 < x < 0.4$, and $y = x/2$).^{20, 28-30} Typically, metastable amorphous precipitates are first obtained, then undergo several physicochemical processes (e.g. crystallization) upon remaining in the mother liquor under agitation – the so-called aging. Precise control of pH and temperature during co-precipitation and aging is very crucial; a tiny variation of pH by a fraction or temperature by a few degrees can cause a huge effect on metastable material that further restructures into hydroxycarbonates, and ultimately impacts the catalytic performance of resulting Cu/ZnO catalysts.

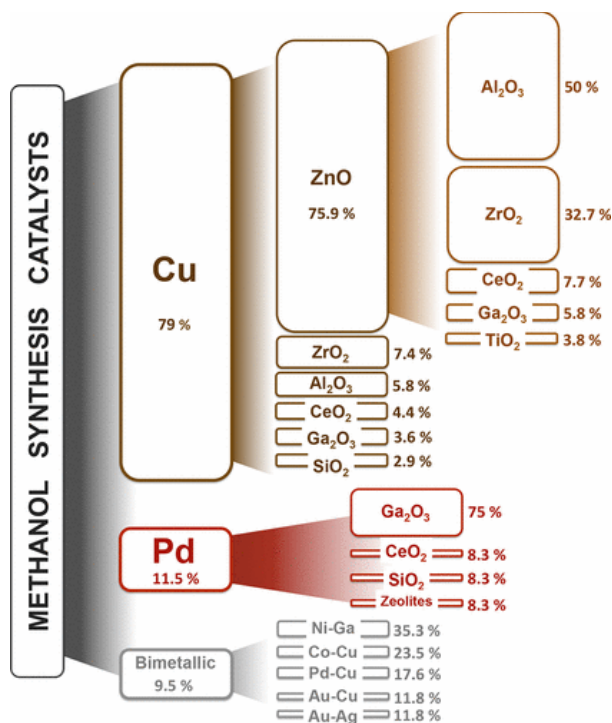


Figure 1.5 Types of catalyst material reported for CO₂ hydrogenation to methanol. The percentages have been calculated based on ca. 200 papers selected from a Scopus search from 2006 to 2016 on the principal catalyst materials.²⁰

The newly formed precipitates undergo a transformation in every stage of preparation as shown in **Figure 1.8**. The existence of hydroxycarbonate structures allows the formation of Cu/ZnO catalysts with high Cu dispersion, in spite of significantly high copper content. During calcination, the hydroxycarbonates undergo thermal decomposition producing interspersed CuO and ZnO mixture with intimate contacts. The properties of the final catalyst (e.g. morphology and defects) upon heat treatments (e.g. calcination and reduction) are dictated by precursor chemistry (e.g. synthesis kinetics) – the phenomenon is referred to as “chemical memory”.²⁷ For example, the porosity catalyst after thermal decomposition is predetermined by the geometry of the hydroxycarbonate precursors. Thin needle-like zincian malachite with large inner-particle pores is more desirable than large platelet-like aurichalcite for superior Cu dispersion and has been regarded as an ideal precursor for highly active catalysts.^{27, 29} The last step of preparation is to reduce the CuO component, typically in hydrogen, to produce Cu/ZnO nanoparticles.

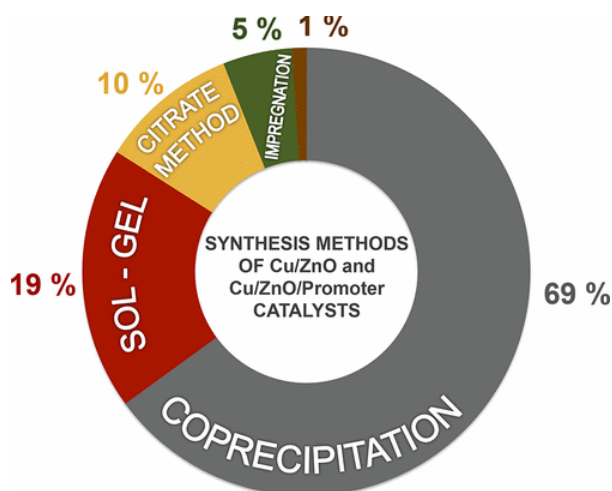


Figure 1.6 Synthesis methods of Cu/ZnO-based catalysts. The percentage was calculated based on the publications over the past 10 years.²⁰

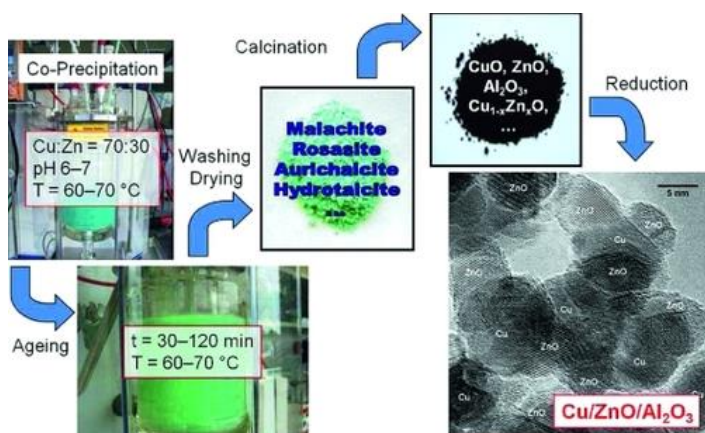


Figure 1.7 Schematic overview of the multistep synthesis route for Cu/ZnO catalysts developed by ICI in the 1960s.²⁷



Figure 1.8 Simplified preparation scheme of Cu/ZnO catalyst from zincian malachite precursor and electron microscopy images of the different stages of preparation.²⁷

1.2.5 Active Sites and Reaction Mechanisms: The Case of Cu/ZnO Catalysts

Nowadays, the mechanism for CO₂ hydrogenation over Cu-based catalysts is still controversial despite almost 100 years of technological availability. It is essential to understand the reaction pathway because mechanistic knowledge will allow the precise control of selectivity over side products and pave the way for the design of highly active catalysts. At a glance, the reaction pathway of CO₂ hydrogenation was perceived to be simple; CO₂ reduces to CO, then follows the reaction pathway of the common methanol synthesis (CO hydrogenation). The question regarding reaction pathways arose when high-pressure CO and CO₂ hydrogenation (400 bar) were compared in parallel in 1945.³¹ In this study, dimethyl ether (DME), the main byproduct from CO hydrogenation, was not formed during CO₂ hydrogenation. Therefore, it is possible that the CO₂ hydrogenation might not follow the usual CO hydrogenation pathway.

Various techniques have been used to differentiate the reaction pathways and intermediates of CO and CO₂ hydrogenation. An isotope-labeling study allows tracking of carbon transformation during methanol synthesis. The ¹⁴CO and ¹⁴CO₂ isotope-labeling experiment suggests that CO₂ is the primary source of methanol on Cu-based catalysts, instead of preconceived CO.³² The CO₂ hydrogenation rate is ~20 times faster than CO hydrogenation, especially at low conversion.³³ However, the C¹⁸O₂ isotope labeling over the Cu/ZnO indicated that methanol can be produced from both CO and CO₂ hydrogenation.¹¹ There are other reactions occurring in parallels such as CO–CO₂ exchange and water-gas shift. From the observation, CO₂

hydrogenation is the primary pathway at low conversions and low temperatures because of the faster reaction rate. The CO hydrogenation becomes faster than CO₂ hydrogenation at high conversion due to the significant formation of water. Water can preferentially suppress CO₂ hydrogenation promoting RWGS and allowing CO₂ hydrogenation to primarily produce methanol. Moreover, differences in the extent of product suppression by water during H/D isotope substitution indicate that CO₂ hydrogenation and RWGS proceed parallelly on different active sites over Cu/ZnO/Al₂O₃ catalyst.³⁴ In contrast, the CO hydrogenation is observed to be the primary reaction over the Pd-based catalysts, since the rate of methanol formation is directly proportional to the CO partial pressure but inversely proportional to CO₂ partial pressure.³³ The CO adsorption and dissociation are also confirmed by a ¹³CO/C¹⁸O isotope labeling experiment.³⁵ From these observations, it is obvious that the nature of the active site plays a crucial role in determining the reaction pathways.

The nature of the active site is controversial for the Cu-based catalyst under CO₂ hydrogenation reaction, especially the commercially available Cu/ZnO/Al₂O₃ catalyst. It has been suggested that metallic copper (Cu⁰) is an active site with uniform activity throughout the catalyst.³⁷ It was found that the Cu⁰ surface area is directly and linearly proportional to the catalytic activity and methanol formation from CO and CO₂.³⁸⁻⁴⁰ Experiments on single crystal Cu(100) and Cu(110) facets and polycrystalline Cu films (exposing mostly Cu(111) facet) demonstrate that methanol can be synthesized over Cu⁰ with the rate or turnover frequencies (TOFs) equal to the real Cu/ZnO catalysts.⁴¹⁻⁴⁴ These results suggest that the Cu⁰ is the active site on the real Cu/ZnO catalysts and the role of ZnO is only for enhancing Cu dispersion. In real Cu/ZnO/Al₂O₃ catalyst, ZnO particles act as spacers between Cu⁰ particles enhancing metal dispersion, stabilizing Cu⁰ particles, and forming a unique microstructure, while Al₂O₃ enhances thermal and chemical stability (**Figure 1.9**).³⁶

Despite concrete pieces of evidence supporting Cu⁰ as an active site, there is some evidence supporting ionic copper species (Cu^{δ+}). In industrial conditions, the catalytic activity is found to be independent of the Cu⁰ surface area in the presence of CO₂, where Cu⁰ is partially oxidized.³⁸ The Cu^{δ+} sites originated from the presence of impurity (promoter) incorporation of Cu into the lattice of support (e.g. ZnO) and.^{6, 45} In some cases, the presence of ZnO does not only stabilize the Cu^{δ+} that impacts catalytic activity but also exhibits structure sensitivity during the CO₂ hydrogenation.

The activity of a “structure-sensitive” catalyst can vary by orders of magnitude depending on catalyst preparation. How the catalyst is prepared can affect defects and lattice strain in the Cu nanoparticles and the intrinsic activity of the Cu surface. An obvious example of structure sensitive catalyst is the industrial Cu/ZnO/Al₂O₃ catalyst, whose activity depends on Cu particle sizes. When Cu particle size is smaller than 8 nm, the surface-specific activity decreases significantly.⁴⁶ The activity of Cu-based catalyst also depends on the presence of Zn or ZnO. The high activity can be generated by bulk defect structure and substitution of Zn into the Cu particles.⁴⁷ The sensitivity of the Cu-Zn structure is demonstrated

by depositing Zn on single-crystal Cu(111).⁴⁸ It was found that Zn with a surface coverage of 0.19 can increase TOF of CO₂ hydrogenation up to 13-fold compared with the bare Cu(111) surface. It is demonstrated that ZnO/Cu(100) is much more active than ZnO/ Cu(111), thus highlighting the structure-sensitivity effect of Cu catalysts.⁴⁹

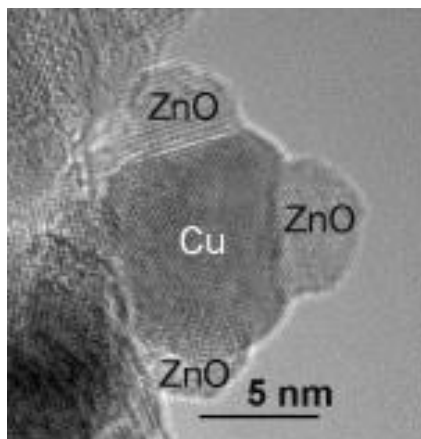


Figure 1.9 Microstructural features revealed with transmission electron microscopy (TEM) and high-resolution TEM.³⁶

A significant increase in activity with the presence of Zn suggests that the Cu⁰ site is not only the active site but there is also a Cu-Zn site that works cooperatively with Cu⁰.⁴⁸ There is evidence that surface Cu-Zn alloy formation occurs over industrial methanol synthesis catalysts even under a mild condition.⁴⁷ To identify the actual active sites, the activity between model ZnCu and ZnO/Cu(111) sites is directly compared.⁵⁰ From both experimental and theoretical results, the surface Zn over ZnCu catalyst undergoes surface oxidation into ZnO under the reaction conditions, allowing ZnCu to reach the activity of ZnO/Cu catalyst and the activity increased in the following sequence: Cu < ZnCu < ZnO-Cu. These results are in agreement with the previous experiment and pointed out that the ZnO-Cu interface is responsible for high catalytic activity.^{51, 52} It is undeniable that the Cu-ZnO interface plays an important role in the catalytic performance of Cu-based catalysts, apart from structure-sensitivity effect. This role is explained widely by “Cu-ZnO synergy.”

The “synergistic effect” concept is used to explain the phenomenon when the combination of two less active or inactive materials can produce a highly active catalyst. As previously discussed, Cu and ZnO are considered to be such a synergistic combination in respect of methanol synthesis. According to the hypothesis of Burch et al., the Cu-ZnO synergy can be summarized into six categories,⁵⁴ including that previously mentioned. First, the incorporation of Cu into the ZnO lattice-generating active Cu^{δ+} species.⁶ Second, electronic interactions

between Cu and ZnO lead to easier Cu reducibility or modulating the adsorption strength of reactants.⁵⁵ Third, Schottky Junction effects at the Cu/ZnO interface can increase the O vacancies, which are considered to be one kind of active site.^{56, 57} Fourth, the formation of CuZn alloy or Cu-Zn pair as active sites.⁶ Fifth, a specific reaction at the Cu/ZnO interface (e.g. CO formation by RWGS).⁴⁹ Sixth, stabilization of Cu in a morphologically active form by ZnO. The synergy listed above all requires intimate contact or strong metal-support interaction (SMSI) between Cu and ZnO, which originated from ZnO_x migration over the Cu surface during high-temperature reduction by H₂ or CO (Kirkendall effect).^{58, 59} There is clear evidence that activated Cu/ZnO catalysts carry an SMSI layer of metastable “graphitic-like” ZnO_x over Cu particles after reductive activation.⁶⁰ This migrated ZnO_x is reported to boost methanol synthesis activity for both CO and CO₂ hydrogenation.^{61, 62} With a mathematical model and rational design approach, a core-shell structure (Cu@ZnO_x) and a nano-core-shell structure (Cu@ZnO_x/ZnO) are developed to maximize the number of contacts between Cu and ZnO.^{62, 63} The contacts favor Zn migration and diffusion into Cu, thus creating an important Cu_xZn_(1-x)O_y active phase and increase methanol formation rate (**Figure 1.10**).⁵³ The authors proposed a spillover mechanism: hydrogen is dissociated on the Cu⁰ core, spills over the shell Cu_xZn_(1-x)O_y where CO₂ is adsorbed and then hydrogenates CO₂. The hydrogen spillover effect can be further enhanced by introducing Pd or graphene oxide (GO) to create more activated surface Cu sites with the assistance of ZnO as active sites.^{64, 65} The roles of Cu-ZnO synergy eventually extended to the stabilization of surface intermediates that are essential for CO₂ hydrogenation.

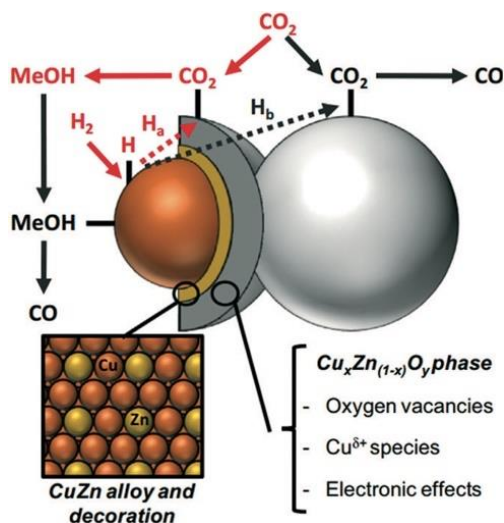


Figure 1.10 General scheme for methanol synthesis over Cu/ZnO-based catalysts.⁵³

The key intermediate species for methanol synthesis from CO₂ are widely debated. As previously described, CO₂ hydrogenation can occur directly from CO₂ or indirectly with CO formation through the RWGS reaction. From a mechanistic point of view, these two alternative pathways differ in the key reaction intermediates: formate (HCOO*) or hydrocarboxyl (COOH*) species, respectively. Although the isotopic effect from H/D substitution confirms that CO₂ hydrogenation and CO hydrogenation do not share common intermediates, the intermediates could not be actually observed by this technique.³⁴ Therefore, various spectroscopic techniques have been used to identify the possible intermediates together with density-functional theory (DFT) calculations to identify possible elementary reaction pathways.

An *in situ* IR spectroscopy over the Fischer-Tropsch catalyst (Fe/Al₂O₃) suggested three main species from both reactions: hydrocarbon, formate, and carboxylate.⁶⁶ Among those intermediates, formate (HCOO*) seems the most commonly found from reaction over various catalysts such as ZnO/Cr₂O₃, Cu/ZnO, ZnO, TiO₂, and ZrO₂.^{6, 67} The temperature-programmed reaction spectroscopy over Cu/ZnO/Al₂O₃ catalyst also suggested that hydrogenation/hydrogenolysis of formates is the rate-determining step in the methanol synthesis from CO₂.⁶⁸

In the case of the Zn/Cu(111) catalyst, the formate coverage increases linearly with Zn coverage (below 0.15), but it has no promotional effect on RWGS indispensable for the CO hydrogenation pathway.⁴⁸ The authors propose that a formate species is formed on Cu(111) surface and then migrates to the Cu-Zn site, where formate is hydrogenated to methanol through a methoxy species. Their conclusion is similar to the case of the ZnCu model catalysts that become ZnO/Cu after surface oxidation. Both experimental and theoretical studies prove that the ZnO-Cu interface favors the binding of formate intermediates and facilitates methanol synthesis.⁵⁰

The possible reaction mechanisms of CO₂ hydrogenation are summarized in **Figure 1.11**. Tabatabaei et al.⁶⁹ observed two types of formate species during the co-adsorption of CO₂/H₂ mixture over ZnO. Both methanol and CO formation (RWGS) are reported to proceed through formate intermediates, but in different binding geometries – bidentate formate for the RWGS reaction and monodentate formate methanol formation. On the other hand, Yang et al.⁷⁰ observed methanol formation on Cu surfaces via formate intermediate proceeding to formaldehyde via a dioxomethylene (H₂COO). The hydrogenation of both formate and dioxomethylene can limit the overall reaction rate of CO₂ hydrogenation. Grabow and Mavrikakis⁷¹ proposed methanol formation via formate (HCOO*) and methoxy (CH₃O*) species by fitting a microkinetic model with the experimental results over commercial Cu/ZnO/Al₂O₃ under realistic conditions. The DFT calculations also suggest that formate (HCOO*) favorably leads to the formation of formic acid (HCOOH*), which is further hydrogenated to CH₃O₂*, transforms to formaldehyde (CH₂O*), and, eventually forms methoxy (CH₃O*). Recently, the formate transformation via formic

acid, formaldehyde, and methoxy species over Cu/ZnO was also supported by Kattel et al.⁵⁰

Contrary to formate intermediate, Yang et al.⁷² suggest that methanol is not produced from the direct hydrogenation of bidentate formate (HCOO^*) on metallic Cu. On the other hand, a significant amount of methanol is produced when Cu is pretreated by N_2O or O_2 , which implies a critical role of surface oxygen or water-derived species in the reaction. In agreement with the previous finding, Zhao et al.⁷³ supported that CO_2 hydrogenation to hydrocarboxyl (COOH^*) is kinetically more favorable than formate species on Cu(111) when overall elementary steps are considered, especially with the presence of water due to a unique hydrogen transfer mechanism.

In reality, both CO and CO_2 hydrogenation pathways could be active under typical methanol synthesis conditions due to the formation of CO via RWGS over Cu-based catalysts. Based on DFT calculations, Yang et al.⁷⁰ reported that the CO produced from RWGS is not directly hydrogenated to methanol over Cu, but too unstable formyl (HCO^*) species that prefer dissociation back into CO and H. Eventually, Grabow and Mavrikakis confirmed that 2/3 of the methanol is produced from CO_2 hydrogenation under typical industrial reaction conditions.⁷¹

1.2.6 Beyond Industrial Cu/ZnO/ Al_2O_3 Catalysts

Nowadays, the global trend of CO_2 hydrogenation tends to shift toward milder conditions or even ambient conditions. This movement was partially triggered by the famous “12 principles of green chemistry.” Many works have focused on developing an innovative catalyst capable of working at lower temperatures and pressure. That poses a challenge to the well-established conventional Cu/ZnO/ Al_2O_3 catalyst for better CO_2 conversion and methanol selectivity. The catalytic performance of selected catalysts is shown in **Table 1.1**.

The conventional Cu/ZnO-based catalysts have been improved in several ways. Various supports have been studied, such as Al_2O_3 , SiO_2 , ZrO_2 , and ZSM-5. Although most supports produced carbon monoxide as a byproduct, Cu/ZnO-supported ZSM-5 produced methyl formate instead. Methyl formate is produced via catalytic dehydrogenation of methanol over acid sites, Brønsted acid from the ZSM-5 framework, and Lewis acid sites from incorporated Cu species. Not only is there a superior CO_2 conversion, but the Cu/ZnO/ZSM-5 catalyst also showed high selectivity toward methanol up to 77.70% and methyl formate up to 10%. With further exploration, the Cu/ZnO/ZSM-5 could improve CO_2 valorization into a variety of value-added chemicals.⁷⁴

The introduction of GO is reported to enhance the hydrogen spillover from Cu to adsorbed carbon species.⁶⁵ The GO-Cu/ZnO/ ZrO_2 catalyst could achieve selectivity up to ca. 76% at 200 °C and 20 bar and higher yield than Cu/ZnO/ ZrO_2 catalyst due to the increased active sites for CO_2 and H_2 adsorption and GO serves as a bridge between metal- metal oxides. In another experiment, the graphitic carbon

nitride ($g\text{-C}_3\text{N}_4$) is used to improve the electron-richness of ZnO by the formation of type-II heterojunction between ZnO and $g\text{-C}_3\text{N}_4$.⁷⁵ Replacing ZnO with $g\text{-C}_3\text{N}_4\text{-ZnO}$ hybrid in an industrial Cu/ZnO/Al₂O₃ catalysts (HiFUEL-R120) leads to enhanced selectivity up to ca. 57% at 250 °C and 12 bar. The catalyst also shows superior methanol yield to the original HiFUEL-R120 catalyst. This study has provided a feasible and economical method to modify the traditional catalyst.

Recently, various novel Pd-based catalysts have been extensively developed for CO₂ hydrogenation to complement some limited abilities of Cu/ZnO/Al₂O₃ catalysts such as moderate activity, low methanol selectivity, and stability.⁸³ The unsatisfied catalytic performance is explained by the activity toward RWGS, activity suppression by water, and catalyst sintering under the reaction conditions. The Pd-based catalysts, on the other hand, are better in H₂ dissociative adsorption ability and are used to improve the methanol TOF up to 4.7 times from Cu/ZnO catalyst via hydrogen spillover mechanism.⁶⁴ In the case of CeO₂ support, the interaction of highly dispersed Pd and Cu led to an increase in Cu dispersion and the surface concentration. The Pd donates electrons to Cu and CeO₂ generating more reduced Cu and CeO₂ sites and thus enhancing the activity of the PdCu/CeO₂ catalyst.⁸⁴ The Ca-doped PdZn/CeO₂ shows ca. 100% methanol selectivity at 220 °C, 30 bar, thanks to H₂ dissociation ability from PdZn and oxygen vacancy from reducible CeO₂.⁷⁶ Hydrogen dissociative adsorption ability is found to decrease with smaller Pd particle size. Highly dispersed Pd nanoparticles with a particle size of 3.6 nm can be prepared over In₂O₃ using thermal treatment of Pd/peptide composite.⁷⁷ The Pd-In₂O₃ interface and oxygen vacancy play in CO₂ activation and hydrogenation, and the theoretical study suggested that Pd-In₂O₃ interfaces are also active sites. Therefore, the activity of Pd/In₂O₃ catalysts is higher than Cu- and Pd- based catalysts reported largely in literature because of enhanced CO₂ and H₂ adsorption ability.

There is a synergistic effect among Cu, Pd, and Zn trimetallic catalysts prepared by impregnation.⁸⁵ Pd can interact with Zn and Cu to form PdZn and PdCu alloys selective toward the formation of methanol and CO, respectively, while the metal particle size is found to be smaller than bimetallic PdZn catalysts. A new preparation route with a well-controlled PdZn particle size can be derived from the Pd@zeolitic imidazolate framework (ZIF-8) precursor.⁷⁸ The pore framework of ZIF-8 confines the Pd particle growth at the sub-nano level and facilitates the formation of Pd-ZnO interfaces during direct pyrolysis. The small-sized PdZn alloy particles are believed to be the true active site and work together with a high content of oxygen defects on the ZnO surface to provide excellent activity. Moreover, strong Pd-ZnO interaction ensured the long-term stability of the catalyst. A strong Pd-Zn interaction is also found in Pd@Zn core-shell catalysts prepared via CdSe.⁷⁹ Enriched Zn decoration offers a superior H₂ adsorption and activation capacity to the Cu surface, thus providing superior activity at 20 bar comparable to the best reported under 50 bar. The catalyst also stabilizes surface HCOO* species over COOH* and then suppresses CO production from the RWGS reaction increasing selectivity. The

PdZn alloy particles (3-6 nm) on ZnO, TiO₂, and Al₂O₃ prepared by the chemical vapor impregnation (CVI) method are also reported to help stabilize HCOO* species, especially PdZn on TiO₂, which exhibits high metal dispersion and methanol productivity.⁸⁶ Despite an excellent promotional effect, the lack of Pd reserve is the main problem preventing the wide utilization of Pd in the industrial process. Therefore, enhancing the catalytic efficiency while minimizing the loading still remains a scientific challenge.

The efficiency per gram of Pd metal has been enhanced by nanoarchitecture concepts. The Ag@Pd-ZnO core@shell catalyst is successfully synthesized and could enhance both methanol selectivity and CO₂ conversion, achieving 3.32 times higher space-time yield (STY) than the Pd-ZnO catalyst of a similar size.⁸⁰ This core@shell structure is benefitted from the electron-rich Pd shell to interface and the formation of the PdZn phase that enhances the adsorption of the intermediate species. This novel strategy with sophisticated tailoring of the surface composition is proposed to reduce Pd loading by substitution with Ag while enhancing catalytic activity at the same time. Apart from using as a core for the Pd shell, Ag also showed a promotional effect on the methanol selectivity of Cu/ZrO₂ catalysts by the formation of special Ag⁺ and Zr^{q+} ($q < 4$) sites, which are not present in Cu/ZrO₂ and Ag/ZrO₂ catalysts.⁸¹ The new active species for CO₂ hydrogenation are created from Ag-Cu alloy formation. Moreover, it was found that H₂ can dissociatively adsorb on Cu/ZrO₂ and Ag/ZrO₂, while H₂ can adsorb non-dissociatively on Ag-Cu/ZrO₂. Since the TOF of methanol production is not changed by Ag addition, the increase in methanol selectivity must be due to a synergy between Ag and Cu.⁸⁷

Finally, the development of catalysts goes beyond relying on metal. A binary metal oxide, ZnO-ZrO₂ solid solution catalyst can achieve methanol selectivity of up to 91% and CO₂ conversion of more than 10% within a single-pass under the condition of 315 °C, 50 bar, H₂/CO₂ = 4, and gas hourly space velocity (GHSV) = 24000 NmL g⁻¹ h⁻¹. The catalyst is also stable for at least 500 h under reaction and even tolerates the presence of 50 ppm SO₂ or H₂S without deactivation. The excellent catalytic performance is attributed to the synergistic effect between Zn and Zr sites for H₂ activation.⁸²

Table 1.1 Catalytic performances of selected catalysts for gas-phase CO₂ hydrogenation to methanol in a continuous flow reactor.

Catalysts	Reaction conditions		H ₂ /CO	Catalytic performance				ref
	Temp (°C), Pressure [bar]	Space velocity		X _{CO2} [%]	S _{MeOH} (%)	Y _{MeOH} [g _{MeOH} g _{cat} ⁻¹ h ⁻¹]	SA _{metal} [m ² g ⁻¹]	
Cu/ZnO/Al ₂ O ₃	260, 331	(G) 20,000 h ⁻¹	10	95.7	98.2	1.58	17.5	20
Cu/ZnO/Al ₂ O ₃	280, 442	(G) 100,000 h ⁻¹	3	65.3	91.9	15.2	17.5	22
Cu/ZnO/ZSM-5	250, 22.5	(W) 10,800 NmL g _{cat} ⁻¹ h ⁻¹	3	20.3	74.9	0.06		74
GO- CuO/ZnO/ZrO ₂	200, 20	(W) 13,000 NmL g _{cat} ⁻¹ h ⁻¹	3	4.8	75.8	0.28		65
Cu/g-C ₃ N ₄ - ZnO/Al ₂ O ₃	250, 12	(W) 6,800 NmL g _{cat} ⁻¹ h ⁻¹	3	-	57.1	0.09		75
Pd-Cu/ZnO	270, 45	(G) 10,800 h ⁻¹	3	8.5	65	0.21	5	64
Ca-PdZn/CeO ₂	220, 30	(W) 2,400 NmL g _{cat} ⁻¹ h ⁻¹	3	7.7	100	0.07		76
Pd/In ₂ O ₃	300, 50	(W) 21,000 NmL g _{cat} ⁻¹ h ⁻¹	4	>20	>70	0.89		77
PdZn@ZIF-8	270, 45	(G) 21,600 h ⁻¹	3	15.1	51.9	0.65		78
Pd@Zn core-shell	270, 20	(W) 18,000 NmL g _{cat} ⁻¹ h ⁻¹	2.9	4.9	>70	0.31		79
Ag@Pd-ZnO	270, 45	(W) 9,600 NmL g _{cat} ⁻¹ h ⁻¹	3	18	47	0.28		80
Ag-CuO/ZrO ₂	230, 10	(W) 3,600 NmL g _{cat} ⁻¹ h ⁻¹	3	2.0	51.3	5.9		81
ZnO/ZrO ₂	320, 50	(W) 24,000 NmL g _{cat} ⁻¹ h ⁻¹	4	10	91	0.73	-	82

(G) = GHSV = volume flow rate/bed volume, (W) = WHSV = mass flow rate/catalyst mass

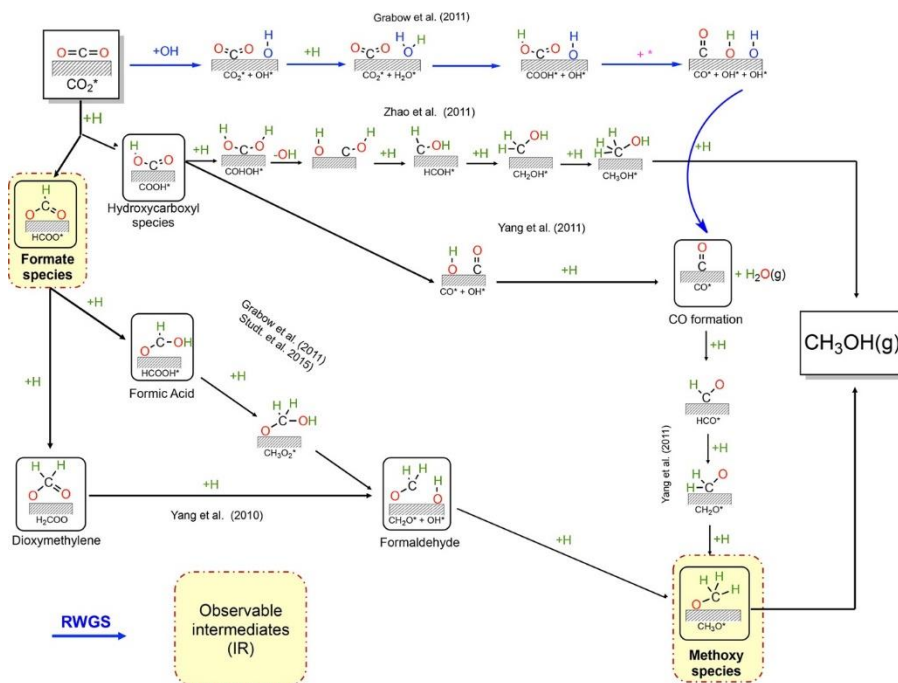


Figure 1.11 Proposed reaction mechanisms for the CO₂ hydrogenation toward methanol.²⁰

1.3 Summary

CO₂ hydrogenation to methanol can be a highly selective and technologically matured route for alcohol synthesis. The promotional effect of CO₂ in methanol synthesis from syn- gas has initiated a considerable interest in CO₂ hydrogenation. However, water formation in CO₂ hydrogenation limits catalytic performance, and thus forces the process design to remove water through a multistage or membrane reactor. On the other hand, water formation could induce *in situ* condensation under high pressure which is beneficial for shifting the thermodynamic equilibrium toward higher CO₂ conversion. In the past 10 years, Cu/ZnO- based catalysts prepared by co-precipitation are still the most preferable catalysts for CO₂ hydrogenation thanks to superior activities that originated from Cu-ZnO synergy and economic advantages from the abundance of the comprising elements. However, the nature of active sites (Cu⁰ or Cu^{δ+}) and reaction pathways (from CO₂ or CO) remain controversial. Various catalysts beyond industrial Cu/ZnO/Al₂O₃ catalysts have been developed to shift CO₂ hydrogenation conditions toward a milder one and simultaneously increase methanol selectivity.

1.4 Scope of this dissertation

This thesis aims to unveil the nature of active sites that lead to high-performance CO₂ hydrogenation to methanol, especially high methanol selectivity. Great attention was given to extracting insights from catalytic activities at various conditions, characterization of catalyst structures, and mechanistic studies using XAS, IR, or Raman spectroscopies. Eventually, the insights obtained from these studies will be valuable for the rational design of highly selective catalysts. The dissertation is divided into two parts; **Part I** focuses on gaining a further understanding of the Cu-based catalysts employed industrially in methanol synthesis and CO₂ hydrogenation processes, and **Part II** focuses on exploring the novel catalysts for low-temperature CO₂ hydrogenation and gaining a deeper understanding of such catalytic systems.

Chapter 2 describes a greener and simpler synthesis procedure of Cu/ZnO catalysts via urea hydrolysis of metal acetates, and the focus was given on optimizing the precipitation temperature, urea-to-metal salt ratio, and Cu-to-Zn ratio using acetate salts. Consequently, the quality of the methanol synthesis catalyst was improved resulting in (i) better control of the precipitation process, (ii) skipping the washing step of cations like Na⁺, and (iii) avoiding the use of nitrates in the precipitated precursor to prevent agglomeration of active Cu species upon calcination.

Chapter 3 describes the employment of a spatially resolved experiment at high pressure (184 and 331 bar) to clarify the reaction pathways and the sources of

carbon for methanol formation over a commercial Cu/ZnO/Al₂O₃ catalyst. The axial concentration profiles were obtained quantitatively using disruptive spatial sampling using gas chromatography (GC) as well as using non-disruptive Raman spectroscopy. The temperature profiles were obtained using infrared (IR) thermography. The spatial information of reactant/products and exo- and exothermicity revealed mechanistic insights of dominating reaction pathways; direct CO₂ hydrogenation to methanol or RWGS + CO hydrogenation, at various temperatures and pressures.

Chapter 4 describes the employment of *operando* DRIFTS in combination with an isotopic transient kinetic analysis (ITKA) to elucidate the nature of the active and selective sites for CO₂ hydrogenation to methanol, which is still actively under debate. Due to the sensitivity limitations of IR over Cu/ZnO/Al₂O₃ catalyst, the model catalysts were required to study the promotional effects of Zn. The model Cu-based catalysts with molecularly-defined single-site promoters (Zn, Ga, and In) were prepared using surface organometallic chemistry (SOMC). Transient experiments were used to distinguish between the active species participating in the reaction and spectators. It was revealed that the main surface intermediates and their stabilization over promoters at the periphery of Cu nanoparticles play a crucial role in determining the methanol selectivity. **Chapter 4** marks the end of **Part I** of this dissertation.

Chapter 5 describes the holistic approach to understanding the reaction mechanisms of low-temperature CO₂ hydrogenation over Re/TiO₂ catalysts. The unique structure-selectivity relationship of Re clusters play important role in determining selectivity toward methanol or methane. To visualize the whole picture of the catalytic process, the bulk properties of Re and TiO₂ under working conditions were studied using *operando* XAS and Raman, the surface properties of Re were studied by Ambient-Pressure X-ray Photoelectron Spectroscopy (AP-XPS), and the surface reaction intermediates were revealed by *operando* DRIFTS in combination with ITKA. Transient experiments were performed using various spectroscopic methods (similar to **Chapter 4**). Eventually, the origin of the structure-selectivity relationship associated with multiple active Re species and their unique interaction with active intermediates was revealed.

Chapter 6 is the last chapter of **Part II** and describes the exploration of various transition metals (e.g., Cu, Rh, Pd, Ag, Re, Pt, and Au) supported on TiO₂ as novel catalysts for low-temperature CO₂ hydrogenation and the exploitation of the insights from catalytic activity results as well as the knowledge from **Chapters 4 & 5** for the rational design of the new catalyst systems. The major disadvantage of Re/TiO₂, i.e. considerable methane selectivity, was found suppressed. The structure of Re-Ag/TiO₂ was characterized by XAS and Transmission electron microscopy (TEM), while the mechanistic insights were obtained using *operando* DRIFTS. It was revealed that the interplay between Re and Ag did not only suppress the intermediate for methane but also promote the intermediate for methanol, hence boosting methanol selectivity.

1.5 References

- 1 Lormand, C. (1925). *Ind. Eng. Chem.* 17: 430–432.
- 2 Cheng, W.H. (2013). *Choice Rev. Online* 32: 3898.
- 3 Fischer, F. (1925). *Ind. Eng. Chem.* 17: 574–576.
- 4 Taylor, H.S. and Kistiakowsky, G.B. (1927). *J. Am. Chem. Soc.* 49: 2468–2476.
- 5 Klier, K., Chatikavanij, V., Herman, R.G., and Simmons, G.W. (1982). *J. Catal.* 74: 343–360.
- 6 Klier, K. (1982). *Adv. Catal.* 31: 243–313.
- 7 Olah, G.A. (2013). *Angew. Chem. Int. Ed.* 52: 104–107.
- 8 Joo, O.-S., Jung, K.-D., Moon, I. et al. (1999). *Ind. Eng. Chem. Res.* 38: 1808–1812.
- 9 Waugh, K.C. (1992). *Catal. Today* 15: 51–75.
- 10 Sun, Q., Liu, C., Pan, W. et al. (1998). *Appl. Catal.* 171: 301–308.
- 11 Liu, G., Willcox, D., Garland, M., and Kung, H.H. (1985). *J. Catal.* 96: 251–260.
- 12 Goehna, H. and Koenig, P. (1994). *Chem. Tech. (Leipzig)* 24: 36–39.
- 13 <http://www.carbonrecycling.is/> (accessed 16 April 2019).
- 14 Shulenberg, A.M., Jonsson, F.R., Ingolfsson, O., and Tran, K.C. (2011). *United States Pat.* 2: 12–15. <https://patents.google.com/patent/US20070244208A1/en>.
- 15 Samimi, F., Karimipourfard, D., and Rahimpour, M.R. (2018). *Chem. Eng. Res. Des.* 140: 44–67.
- 16 Samimi, F., Rahimpour, M.R., and Shariati, A. (2017). *Catalysts* 7: 332.
- 17 Graaf, G.H., Sijtsma, P.J.J.M., Stamhuis, E.J., and Joosten, G.E.H. (1986). *Chem. Eng. Sci.* 41: 2883–2890.
- 18 van Bennekom, J.G., Venderbosch, R.H., Winkelman, J.G.M. et al. (2013). *Chem. Eng. Sci.* 87: 204–208.
- 19 van Bennekom, J.G., Winkelman, J.G.M., Venderbosch, R.H. et al. (2012). *Ind. Eng. Chem. Res.* 51: 12233–12243.
- 20 Álvarez, A., Bansode, A., Urakawa, A. et al. (2017). *Chem. Rev.* 117: 9804–9838.
- 21 Bansode, A. and Urakawa, A. (2014). *J. Catal.* 309: 66–70.
- 22 Gaikwad, R., Bansode, A., and Urakawa, A. (2016). *J. Catal.* 343: 127–132.
- 23 Kommoß, B., Klemenz, S., Schmitt, F. et al. (2017). *Chem. Eng. Technol.* 40: 1907–1915.
- 24 Bos, M.J. and Brilman, D.W.F. (2015). *Chem. Eng. J.* 278: 527–532.
- 25 Zachopoulos, A. and Heracleous, E. (2017). *J. CO₂ Util.* 21: 360–367.
- 26 Marsden, W.L., Wainwright, M.S., and Friedrich, J.B. (1980). *Ind. Eng. Chem. Prod. Res. Dev.* 19: 551–556.
- 27 Behrens, M. and Schlögl, R. (2013). *Z. Anorg. Allg. Chem.* 639: 2683–2695.
- 28 Behrens, M., Girgsdies, F., Trunschke, A., and Schlögl, R. (2009). *Eur. J. Inorg. Chem.* 2009: 1347–1357.
- 29 Behrens, M. and Girgsdies, F. (2010). *Z. Anorg. Allg. Chem.* 636: 919–927.
- 30 Behrens, M., Kasatkin, I., Kühl, S., and Weinberg, G. (2010). *Chem. Mater.* 22: 386–397.
- 31 Ipatieff, V.N. and Monroe, G.S. (1945). *J. Am. Chem. Soc.* 67: 2168–2171.
- 32 Chinchen, G.C., Denny, P.J., Parker, D.G. et al. (1987). *Appl. Catal.* 30: 333–338.
- 33 Borodko, Y. and Somorjai, G.A. (1999). *Appl. Catal., A* 186: 355–362.
- 34 Kunkes, E.L., Studt, F., Abild-Pedersen, F. et al. (2015). *J. Catal.* 328: 43–48.
- 35 Ihm, S.-K., Jeon, J.-K., and Lee, D.-K. (1997). *Stud. Surf. Sci. Catal.* 105: 901–907.
- 36 Kasatkin, I., Kurr, P., Kniep, B. et al. (2007). *Angew. Chem. Int. Ed.* 46: 7324–7327.
- 37 Bridgewater, A.J., Wainwright, M.S., and Young, D.J. (1986). *Appl. Catal.* 28: 241–253.
- 38 Chinchen, G.C., Waugh, K.C., and Whan, D.A. (1986). *Appl. Catal.* 25: 101–107.
- 39 Pan, W.X., Cao, R., Roberts, D.L., and Griffin, G.L. (1988). *J. Catal.* 114: 440–446.
- 40 Jingfa, D., Qi, S., Yulong, Z. et al. (1996). *Appl. Catal., A* 139: 75–85.
- 41 Rasmussen, P.B., Kazuta, M., and Chorkendorff, I. (1994). *Surf. Sci.* 318: 267–280.
- 42 Rasmussen, P.B., Holmblad, P.M., Askgaard, T. et al. (1994). *Catal. Lett.* 26: 373–381.
- 43 Yoshihara, J. and Campbell, C.T. (1996). *J. Catal.* 161: 776–782.

- 44 Yoshihara, J., Parker, S.C., Schafer, A., and Campbell, C.T. (1995). *Catal. Lett.* 31: 313–324.
- 45 Szanyi, J. and Goodman, D.W. (1991). *Catal. Lett.* 10: 383–390.
- 46 Van Den Berg, R., Prieto, G., Korpershoek, G. et al. (2016). *Nat. Commun.* 7: 13057.
- 47 Behrens, M., Studt, F., Kasatkin, I. et al. (2012). *Science* 759: 893–898.
- 48 Fujitani, T., Nakamura, I., Uchijima, T., and Nakamura, J. (1997). *Surf. Sci.* 383: 285–298.
- 49 Palomino, R.M., Ramírez, P.J., Liu, Z. et al. (2018). *J. Phys. Chem. B* 122: 794–800.
- 50 Kattel, S., Ramírez, P.J., Chen, J.G. et al. (2017). *Science* 355: 1296–1299.
- 51 Nakamura, J., Fujitani, T., Kuld, S. et al. (2017). *Science* 357: eaan8074.
- 52 Kattel, S., Ramírez, P.J., Chen, J.G. et al. (2017). *Science* 357: eaan8210.
- 53 Tisseraud, C., Comminges, C., Pronier, S. et al. (2016). *J. Catal.* 343: 106–114.
- 54 Burch, R., Golunski, S.E., Spencer, M.S. et al. (1990). *J. Chem. Soc., Faraday Trans.* 86: 2683–2691.
- 55 Bulko, J.B., Herman, R.G., Klier, K., and Simmons, G.W. (1979). *J. Phys. Chem.* 83: 3118–3122.
- 56 Frost, J.C. (1988). *Nature* 334: 577–580.
- 57 Liu, X.-M., Lu, G.Q., Yan, Z.-F. et al. (2003). *Ind. Eng. Chem. Res.* 42: 6518–6530.
- 58 Topsøe, N. and Topsøe, H. (1999). *Top. Catal.* 8: 267–270.
- 59 Naumann D’Alnoncourt, R., Xia, X., Strunk, J. et al. (2006). *Phys. Chem. Chem. Phys.* 8: 1525–1538.
- 60 Lunkenbein, T., Schumann, J., Behrens, M. et al. (2015). *Angew. Chem. Int. Ed.* 54: 4544–4548.
- 61 Kuld, S., Thorhauge, M., Falsig, H. et al. (2016). *Science* 352: 969–974.
- 62 Tisseraud, C., Comminges, C., Belin, T. et al. (2015). *J. Catal.* 330: 533–544.
- 63 Le Valant, A., Comminges, C., Tisseraud, C. et al. (2015). *J. Catal.* 324: 41–49.
- 64 Hu, B., Yin, Y., Liu, G. et al. (2018). *J. Catal.* 359: 17–26.
- 65 Witoon, T., Numpilai, T., Phongamwong, T. et al. (2018). *Chem. Eng. J.* 334: 1781–1791.
- 66 Perrichon, V., Pijolat, M., and Primet, M. (1984). *J. Mol. Catal.* 25: 207–217.
- 67 He, M.Y., White, J.M., and Ekerdt, J.G. (1985). *J. Mol. Catal.* 30: 415–430.
- 68 Bowker, M., Hadden, R.A., Houghton, H. et al. (1988). *J. Catal.* 109: 263–273.
- 69 Tabatabaei, J., Sakakini, B.H., and Waugh, K.C. (2006). *Catal. Lett.* 110: 77–84.
- 70 Yang, Y., Evans, J., Rodriguez, J.A. et al. (2010). *Phys. Chem. Chem. Phys.* 12: 9909–9917.
- 71 Grabow, L.C. and Mavrikakis, M. (2011). *ACS Catal.* 1: 365–384.
- 72 Yang, Y., Mims, C.A., Disselkamp, R.S. et al. (2010). *J. Phys. Chem. C* 114: 17205–17211.
- 73 Zhao, Y.-F., Yang, Y., Mims, C. et al. (2011). *J. Catal.* 281: 199–211.
- 74 Ayodele, O.B. (2017). *J. CO₂ Util.* 20: 368–377.
- 75 Deng, K., Hu, B., Lu, Q., and Hong, X. (2017). *Catal. Commun.* 100: 81–84.
- 76 Malik, A.S., Zaman, S.F., Al-Zahrani, A.A. et al. (2018). *Appl. Catal., A* 560: 42–53.
- 77 Rui, N., Wang, Z., Sun, K. et al. (2017). *Appl. Catal., B* 218: 488–497.
- 78 Yin, Y., Hu, B., Li, X. et al. (2018). *Appl. Catal., B* 234: 143–152.
- 79 Liao, F., Wu, X.P., Zheng, J. et al. (2017). *Green Chem.* 19: 270–280.
- 80 Li, X., Zeng, Z., Hu, B. et al. (2017). *ChemCatChem* 9: 924–928.
- 81 Tada, S., Watanabe, F., Kiyota, K. et al. (2017). *J. Catal.* 351: 107–118.
- 82 Wang, J., Li, G., Li, Z. et al. (2017). *Sci. Adv.* 3: e1701290.
- 83 García-Trenco, A., Regoutz, A., White, E.R. et al. (2018). *Appl. Catal., B* 220: 9–18.
- 84 Choi, E.J., Lee, Y.H., Lee, D.W. et al. (2017). *Mol. Catal.* 434: 146–153.
- 85 Díez-Ramírez, J., Díaz, J.A., Sánchez, P., and Dorado, F. (2017). *J. CO₂ Util.* 22: 71–80.
- 86 Bahruji, H., Bowker, M., Jones, W. et al. (2017). *Faraday Discuss.* 197: 309–324.
- 87 Tada, S. and Satokawa, S. (2018). *Catal. Commun.* 113: 41–45.
- 88 Forzatti, P., Tronconi, E., and Pasquon, I. (1991). *Catal. Rev.* 33: 109–168.

Part I

Insights into Copper-based catalysts



Greener and facile synthesis of Cu/ZnO catalysts

for CO₂ hydrogenation to methanol
by urea hydrolysis of acetates



Abstract

Cu/ZnO-based catalysts for methanol synthesis by CO_x hydrogenation are widely prepared via co-precipitation of sodium carbonates and nitrate salts, which eventually produces a large amount of wastewater from the washing step to remove sodium (Na⁺) and/or nitrate (NO₃⁻) residues. The step is inevitable since the remaining Na⁺ acts as a catalyst poison whereas leftover NO₃⁻ induces metal agglomeration during the calcination. In this study, sodium- and nitrate-free hydroxy-carbonate precursors were prepared via urea hydrolysis co-precipitation of acetate salt and compared with the case using nitrate salts. The Cu/ZnO catalysts derived from calcination of the washed and unwashed precursors show catalytic performance comparable to the commercial Cu/ZnO/Al₂O₃ catalyst in CO₂ hydrogenation at 240-280 °C and 331 bar. By the combination of urea hydrolysis and the nitrate-free precipitants, the catalyst preparation is simpler with fewer steps, even without the need for a washing step and pH control, rendering the synthesis more sustainable.



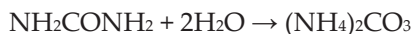
This chapter is based on the following publication:
Phongprueksathat, N., Bansode, A., Toyao, T., & Urakawa, A. (2021) *RSC Advances*, 11(24), 14323–14333.

2.1 Introduction

One of the strategies to reduce greenhouse gas emissions and alleviate the impacts of escalating global warming is carbon dioxide (CO₂) conversion with green H₂ (e.g., produced through water electrolysis sourced by renewable energies) into chemicals such as methane, formic acid, methanol, dimethyl ether, and methyl formate. Among those chemicals, methanol is positioned as the most versatile chemical feedstock and energy carrier towards a fossil-fuel-free economy, known as the “methanol economy”.¹ The green methanol production from CO₂ hydrogenation has been demonstrated successfully on a relatively large scale at the “George Olah Carbon Dioxide to Renewable Methanol Plant” in 2012 and it paves the way for sustainable recycling of CO₂.² On the other hand, the current synthesis processes for methanol synthesis catalysts are still far from eco-friendly. Most traditional synthesis processes inevitably produce contaminated wastewater, which requires extensive treatment before its release into the environment.³ This harmful effluent must be minimized and not released according to green chemistry principles as a key path for sustainable chemical synthesis in the 21st century.⁴

Conventionally, the majority of industrial methanol synthesis catalysts (e.g. Cu/ZnO/Al₂O₃) have been prepared by co-precipitation of metal nitrate salts and NaCO₃ precipitant,⁵ that contributes to a considerable amount of nitrate-containing wastewater from the washing process of the as-precipitated precursors (approximately 500 L kg⁻¹ of catalyst (Supporting information)). Washing off nitrate and sodium residues is crucial to prevent agglomeration of the active metal (Cu), its poisoning, and thus catalyst deactivation. Concerning residual nitrate anions, replacing Cu and Zn nitrates with other soluble inorganic salts such as respective chlorides and sulfates are detrimental to catalytic activity since Cl and S residues could act as poisons.^{6,7} An effective approach is the use of organic salts such as formates or acetates, avoiding the generation of nitrate-contaminated wastewater while forming active catalysts.^{7,8} Concerning the residual sodium cations, employing salts containing thermally decomposable cations, such as (NH₄)HCO₃ and (NH₄)₂CO₃, as a precipitant allows eliminating the washing step of sodium cations, although an effective removal of anion, typically nitrate, by calcination in the gas stream is still required to achieve the maximum activity.⁹ Supercritical antisolvent process is a recent approach to avoid the use of precipitant completely although special equipment for a high volume of supercritical CO₂ is required.^{10,11}

Typically, a precipitant is added together with the metal nitrate precursor(s) dropwise and in a controlled manner to precisely regulate the pH of the solution and control the growth of catalyst precursor crystals. In this regard, hydrolysis of urea (NH₂CONH₂) is interesting and potentially advantageous because the precipitant, (NH₄)₂CO₃, can be produced *in situ* in solution (Eqn. 2.1).¹²



Eqn. 2.1

Similar to the co-precipitation using $(\text{NH}_4)_2\text{CO}_3$ precipitant, the homogeneous alkalinization via urea hydrolysis of metal nitrate or chloride salts can yield sodium-free hydroxycarbonates, such as copper hydrozincite $((\text{Cu}_x\text{Zn}_{1-x})_5(\text{OH})_6(\text{CO}_3)_2$, when $x < 0.1$), aurichalcite $((\text{Cu}_x\text{Zn}_{1-x})_5(\text{OH})_6(\text{CO}_3)_2$, when $x < 0.5$), rosasite $((\text{Cu}_x\text{Zn}_{1-x})_2(\text{OH})_2(\text{CO}_3)$, when $0.5 < x < 0.7$), and zincian malachite $((\text{Cu}_x\text{Zn}_{1-x})_2(\text{OH})_2(\text{CO}_3)$ when $x > 0.7$),^{12–14} in which Cu and Zn are closely located in the same crystalline structure.^{15,16} These hydroxycarbonates are essential for the formation of **Eqn. 2.1** of CuO-ZnO inter-dispersion during calcination, improving Cu-ZnO contact after reduction and eventually producing more active catalysts than those obtained by the impregnation method.^{17,18} On the contrary, the catalysts prepared by urea hydrolysis usually possess higher crystallinity, smaller particle size, and more uniform size distribution than co-precipitation using conventional precipitants because of the gradient-free nature and less-fluctuating pH during the precipitation process thanks to the *in situ* precipitant $(\text{NH}_4)_2\text{CO}_3$ formation (**Eqn. 2.1**) whose concentration is regulated by the rate of hydrolysis influenced by the consumption of the precipitant in the solution. These features are beneficial to enhance the reproducibility of the complex and highly sensitive synthesis process, where precise semi-automatic synthesis equipment is generally required in the case of conventional co-precipitation.¹⁹ Moreover, its application can be readily transferred to an industrial-scale process employing a batch reactor.

In the past, Cu-based catalysts (e.g. Cu/ZnO and Cu/ZnO/Al₂O₃) prepared by urea hydrolysis of nitrate salts have been reported for steam reforming of methanol,^{20–28} water-gas shift reaction,^{28–32} selective hydrogenation,^{33–36} and liquid phase methanol synthesis from syngas.^{37–39} Most studies have shown higher copper surface area, stronger metal-support interaction, and better catalytic performance for CO₂-related reactions than conventional co-precipitated catalysts. These properties should be highly beneficial for methanol synthesis catalysts.^{40,41} The major parameters reported to influence the synthesis are temperature, aging time, urea content, and precursors (metal salts) type,¹² and they have been optimized in the case of urea hydrolysis of nitrate salts. Such parameters, however, cannot be applied directly for the urea hydrolysis of acetates due to the formation of different meta-stable/stable phases.⁸ Moreover, the washing remains crucial for nitrates-derived catalysts, and the influence of such a step has never been investigated in the urea hydrolysis of both nitrates and acetates.

In this study, we aim at simplifying the synthesis procedure of Cu/ZnO catalyst and improving the quality of resulting material as methanol synthesis catalyst by urea hydrolysis of metal acetates to (i) better control the precipitation process, (ii) skip the washing step of cation like Na⁺ and (iii) avoid the use of nitrates in the precipitated precursor to prevent agglomeration of active Cu species upon calcination. The focus of this work is given to optimize the precipitation temperature, urea-to-metal salt ratio, and Cu-to-Zn ratio using acetate salts.

2.2 Results and discussion

2.2.1 Influence of precipitation temperature

Temperature is one of the most critical parameters in solid synthesis by precipitation. Here, the optimum precipitation temperature was determined experimentally by correlating with the catalytic activity of the resulting catalyst. In literature, the optimum temperature for co-precipitation of the precursor yielding Cu/ZnO/Al₂O₃ catalyst for methanol synthesis is reported to be 60-70 °C.⁴² In the case of urea hydrolysis, however, the rate of urea hydrolysis (**Eqn. 2.1**) is associated with precipitation temperature, and eventually determines the rate of alkilation (the rate OH⁻ generation and consequently increasing pH) in the solution. The promoted nucleation rate from a rapid pH increase is beneficial for the formation of small particle sizes and high crystallinity of the as-precipitated precursor.¹⁴ The smaller Cu and ZnO particle sizes after calcination have been reported as increasing precipitating temperature and the optimal temperature is reported at 95 °C.^{14,23,43} The catalysts prepared at the same temperature using nitrate salts in this study possess comparable textural properties as reported in the aforementioned literature, as shown in **Table 2.2**. However, the temperature of 95 °C is not suitable with acetate salt since the catalytic activity obtained is inferior to that of 80 °C (**Table 2.1**). It should be noted that mostly methanol and carbon monoxide are detected under all conditions with only a trace amount (<1% selectivity) of other products (e.g., methane, methyl formate, and diethyl ether).

Table 2.1 Properties and catalytic activity of the Cu/ZnO catalysts (Cu:Zn = 1:1) prepared by urea hydrolysis of acetate at various U/M ratios at 70, 80, and 95 °C

Precipitation temperature (°C)	Average crystallite size (nm)		Composition ^a (wt%)		CO ₂ conversion (%)	CH ₃ OH selectivity (%)
	CuO	ZnO	CuO	ZnO		
70	8.1	4.7	80.1	19.9	62.3	96.0
80	4.1	6.7	45.8	55.2	67.7	97.8
95	4.9	6.4	37.6	62.4	64.6	96.5

^a Estimated by Rietveld refinement.

Clearly, incomplete precipitation of Zn²⁺ is observed at 70 °C after 24 h of synthesis since the rate constant of urea hydrolysis is 4 times lower than at 80 °C and results in insufficient alkalization of the solution.⁴⁴ As described in the phase diagrams of the Cu²⁺ + Zn²⁺ system, the Cu²⁺ would precipitate first due to the larger energy requirement for dehydration of aqueous Zn²⁺,¹⁴ which is directly related to the higher solubility of zinc acetate (0.43 g mL⁻¹) than copper acetate (0.072 g mL⁻¹).

Therefore, it is still challenging to carry out urea hydrolysis at even lower temperatures e.g., 40 °C to obtain a superior zincian georgeite phase reported recently.⁸

As shown in the X-ray diffraction (XRD) patterns of the as-precipitated precursors (**Figure 2.1**), the major component/phase obtained at 70, 80, and 95 °C is the aurichalcite phase. However, a large amount of CuO is precipitating at a temperature of 70 °C. The XRD patterns of calcined catalysts are analyzed using Rietveld refinement to estimate crystallite size and approximate phase composition (**Table 2.1**). The lower CuO content in the catalyst obtained at the synthesis temperature of 95 °C is likely associated with Cu leaching.³¹ On the other hand, higher CuO content in the catalyst obtained at 70 °C can be associated with the formation and decomposition of thermally unstable $\text{Cu}_2(\text{OH})_3(\text{CH}_3\text{COO})\cdot\text{H}_2\text{O}$ intermediate.⁴⁵ It is likely that the incomplete precipitation of Zn^{2+} could limit the formation of the aurichalcite phase and allows the firstly precipitated copper intermediate to decompose. Based on these observations and also catalytic activity (**Table 2.1**), the synthesis temperature of 80 °C is concluded to be optimal and is used throughout this work.

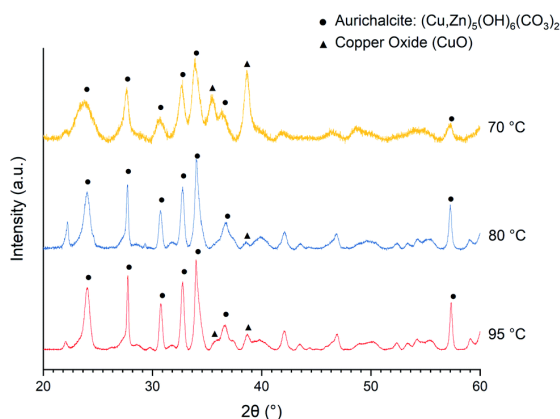


Figure 2.1 XRD patterns of the as-precipitated precursors for Cu/ZnO catalysts (Cu:Zn = 1:1) prepared by urea hydrolysis of acetate salts with urea to metal cations molar ratio (U/M) of 10 at 70, 80, and 95 °C.

2.2.2 Influence of urea to metal ratio

The amount of urea used in co-precipitation is one of the key factors determining the alkalinity of the solution in urea hydrolysis (**Eqn. 2.1**), thus impacting the precipitating time, the structure of as-precipitated precursors, and physical properties of the final catalyst. In early studies, an extremely excessive amount of urea had been used together with a diluted metal salts solution to obtain the aurichalcite structure.^{14,31,46} However, the excess of urea promotes the formation of copper ammonia complexes ($[\text{Cu}(\text{NH}_3)_4(\text{H}_2\text{O})_2]^{2+}$) that easily aggregate and in turn, produce larger Cu particle size.^{9,37} The optimal urea concentration should be

identified to yield a precursor containing both Cu and Zn at the optimal molar ratio with atomic dispersion and resulting in a highly active catalyst upon calcination.

To study the influences of urea concentration, the relationship between catalytic activity and the urea to metal cations molar ratio (U/M ratio) was studied using both nitrate and acetate salts (**Figure 2.2**). CO₂ conversion and CH₃OH selectivity at 260 °C and 331 bar increase significantly at a higher U/M ratio and reach a constant value for both nitrate- and acetate-derived catalysts. The catalysts synthesized at a higher U/M ratio exhibit comparable catalytic activity and higher intrinsic activity than the highly active and optimized commercial Cu/ZnO/Al₂O₃ catalyst (also containing MgO promoter).

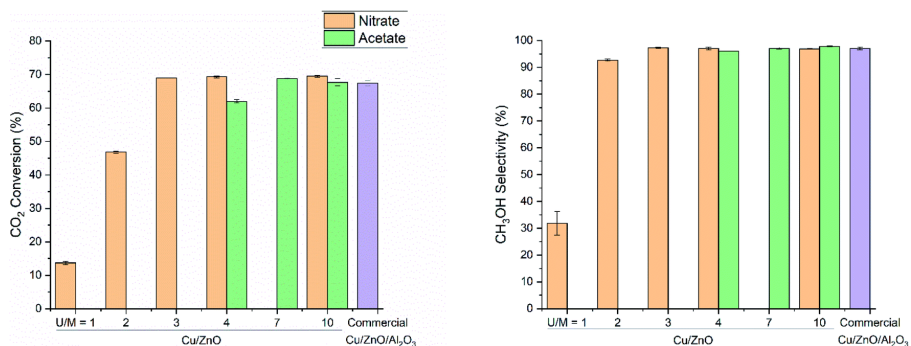


Figure 2.2 Influence of urea-to-metal molar ratio on the catalytic activity of Cu/ZnO catalyst (Cu:Zn = 1:1) derived from nitrate and acetate salts, and commercial Cu/ZnO/Al₂O₃ catalyst for CO₂ hydrogenation to methanol. H₂/CO₂ = 3, T = 260 °C, P = 331 bar, GHSV = 8500 h⁻¹, and TOS = 6 h.

Moreover, extraordinary catalytic performances are achieved by high pressure where the CO₂ conversion and CH₃OH selectivity are boosted by the enhanced reaction rate, thermodynamically favorable conditions, and surpassed chemical equilibrium due to *in situ* condensation of methanol and water.^{40,41,47,48} CO₂ conversion and CH₃OH selectivity obtained with Cu/ZnO catalysts under such conditions are by far the state-of-the-art.⁴⁹ Nevertheless, the values of the intrinsic activity are probably not representing a true intrinsic activity since the specific Cu surface area determined by N₂O titration may not be identical to the surface area during the reaction (severe deactivation).

The inferior activity of catalysts prepared at low U/M is attributed to poorer physical properties of calcined catalysts such as lower BET surface area and larger crystallite size of CuO and ZnO (**Table 2.2**). The XRD patterns of as-precipitated precursors using the nitrate salts (**Figure S2.1**) indicate the formation of the gerhardtite phase (Cu₂(OH)₃(NO₃)) at low U/M as the main phase. This phase was reported as an intermediate for aurichalcite and rosasite phases which were observed during precipitation at low pH.⁵⁰ The presence of such a crystal phase containing Cu as the only metal element should be avoided to obtain finely mixed CuO-ZnO after calcination. Too low alkalinity due to the little amount of urea likely

induced incomplete precipitation of Zn^{2+} since it requires a higher pH value (pH 10.1) than Cu^{2+} (pH 8.1) due to significantly higher solubility of zinc nitrate (184 g mL^{-1}) compare to copper nitrate (0.419 g mL^{-1}).⁴⁶

When acetate salts are used, the XRD patterns of as-precipitated precursors (Figure 2.3) show the mixture of aurichalcite and CuO phase at a low U/M ratio of 4. The surprising formation of CuO without calcination treatment is explained by the formation and decomposition of thermally unstable $\text{Cu}_2(\text{OH})_3(\text{CH}_3\text{COO})\cdot\text{H}_2\text{O}$ intermediate as reported by Jia et al.⁴⁵ On the other hand, the undesired copper ammonia complex ($[\text{Cu}(\text{NH}_3)_4(\text{H}_2\text{O})_2]^{2+}$) is not observed at a high U/M ratio of 7 and 10 (Figure 2.3). Therefore, the optimal U/M ratio for urea hydrolysis of acetate is found to be at least 7 up to 10.

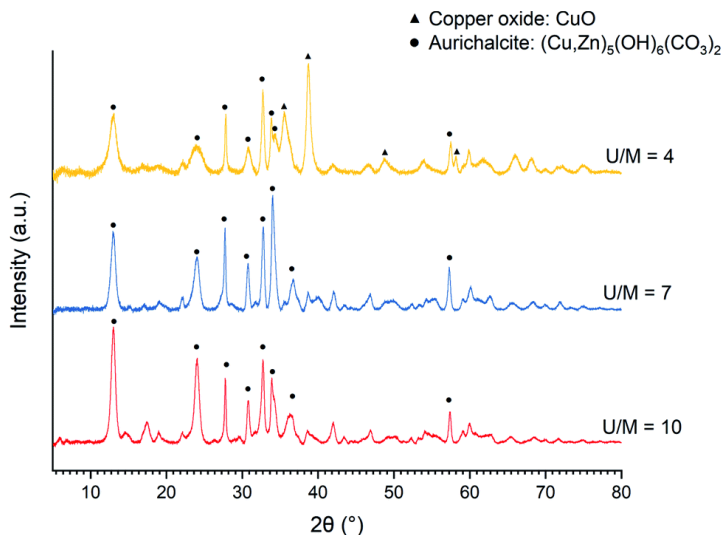


Figure 2.3 XRD patterns of the as-precipitated precursors of Cu/ZnO catalysts (Cu:Zn = 1:1) prepared by urea hydrolysis of acetate salts with various urea to metal molar ratios (U/M) of 4-7 at 80 °C.

Table 2.2 Textural properties of the Cu/ZnO catalyst (Cu:Zn = 1:1) prepared by urea hydrolysis of nitrate and acetate salts at various U/M ratios

Catalysts	Precipitation temperature (°C)	U/M ratio	BET surface area (m ² g ⁻¹)	Cu surface area ^a (m ² g ⁻¹)	Average crystallite size ^b (nm)		Intrinsic activity ^c (mmolCH OH m _{Cu} ⁻² h ⁻¹)
					CuO	ZnO	
Cu/ZnO (nitrate)	95	1	9	—	40.5	42.7	—
	95	2	28	—	27.5	18.7	—
	95	3	74	—	6.2	7.8	—
	95	4	57	—	6.9	6.9	—
	95	10	64	—	5.1	7.1	—
	80	10	53	7	6.9	8.5	5.0
Cu/ZnO (acetate)	80	4	56	11	8.5	5.1	2.8
	80	7	54	19	8.7	8.8	1.8
	80	10	70	13	4.1	6.7	2.6
Commercial Cu/ZnO/Al ₂ O ₃	—	—	102	19	6.3	4.2	1.8

^a Determined by N₂O chemisorption. ^b Estimated by Rietveld refinement. ^c Based on methanol productivity at H₂/CO₂ = 3, T = 260 °C, P = 331 bar, GHSV = 8500 h⁻¹, and TOS = 6 h.

2.2.3 Influence of metal salts and washing step

To compare the influence of metal salts on as-precipitated precursors, the urea hydrolysis of nitrate and acetate salts is carried out at the same temperature (80 °C) and U/M ratio of 10. The pH evolution of the suspension of nitrate and acetate salts is measured as shown in **Figure S2.2**. The nitrate and acetate solutions have different initial pH and progression suggesting the formation of different meta-stable phases. The overall pH of both nitrate and acetate suspension increases during urea hydrolysis and eventually reaches the same value of 6.5 after 24 h. It should be noted that the pH of 6.5-7 is commonly used for conventional co-precipitation where the alkaline solution is constantly added to maintain the pH value.^{8,9} A gradual increase in pH and simultaneous aging allows precipitation and active phase transformation to take place slowly, which improves crystallinity. However, there are sudden drops in pH during 2-8 h, which may indicate the crystallization of roasite ($((\text{Cu,Zn})_2(\text{OH})_2\text{CO}_3)$) and aurichalcite ($((\text{Cu,Zn})_5(\text{OH})_6(\text{CO}_3)_2)$).^{50,51} As shown by XRD patterns of as-precipitated precursors (**Figure S2.3**), only the aurichalcite phase is observed in the acetate-derived precursors, while the roasite phase is abundant in the nitrate-derived precursors. It should be noted that the precursor structure is sensitive to the precipitation temperature; only the aurichalcite phase is observed in the nitrate-derived precursors if prepared at 95 °C.

Moreover, the platelet shape of the aurichalcite phase and the needle-like shape of roasite are confirmed by a scanning electron microscope (SEM) (**Figure 2.4**). The needle-like structure of roasite has been proposed to give a superior catalyst after calcination than an unfavorably larger platelet structure of aurichalcite.¹⁶ However, it is noticeable that the crystallite sizes of the platelet aurichalcite derived from acetate salts (**Figure 2.4b**) are apparently much smaller than needle-like roasite derived from nitrate salts (**Figure 2.4a**). The smaller crystallite size of the aurichalcite phase is evident from the XRD patterns (**Figure S2.3**). The less thickness (smaller size) of the crystallite needle is reported to be one of the critical properties that affect Cu particle size since it makes Cu more accessible to reactant gas upon decomposition.^{7,52} Therefore, the smaller crystallite size of aurichalcite may explain the favorable textural properties of the acetate-derived catalysts after calcination in terms of metallic copper and total surface area than those of the nitrate-derived one (**Table 2.3**).

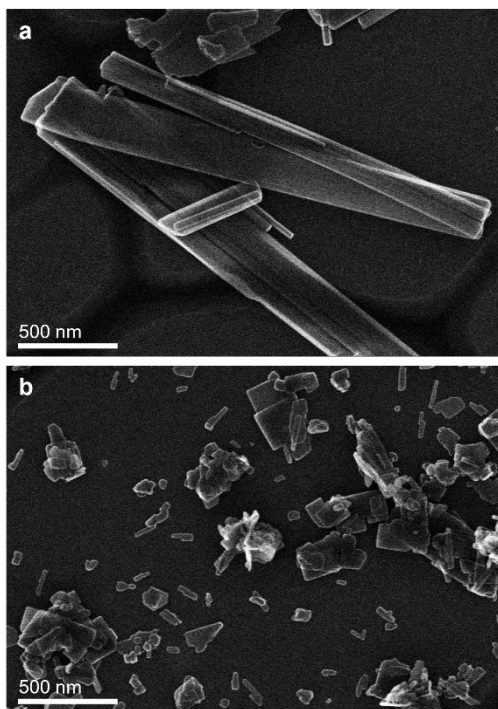


Figure 2.4 Representative SEM images of washed as-precipitated precursors for CuO/ZnO (Cu:Zn = 1:1) derived from urea hydrolysis of **a** nitrate and **b** acetate salts

Table 2.3 The textural properties of Cu/ZnO catalysts (Cu:Zn = 1:1) derived from urea hydrolysis of nitrate and acetate salts at 80 °C for 24 h with the urea-to-metal molar ratio of 10 and commercial Cu/ZnO/Al₂O₃ catalyst

Catalyst	BET surface area (m ² g ⁻¹)	Cu surface area ^a (m ² g ⁻¹)	Average crystallite size ^b (nm)		Intrinsic activity ^d (mmol _{CH₃OH} m _{Cu} ⁻² h ⁻¹)
			CuO	ZnO	
Nitrate-unwashed Cu/ZnO	25	4	19.2	47.9	3.9
Nitrate-washed Cu/ZnO	53	7	6.9	8.5	5.1
Acetate-unwashed Cu/ZnO	70	16	4.8	6.6	2.3
Acetate-washed Cu/ZnO	70	13	4.1	6.7	2.9
Commercial Cu/ZnO/Al ₂ O ₃ (64/25/ 10 wt%) ^c	102	19	6.3	4.2	1.9

^a Determined by N₂O chemisorption. ^b Estimated by Rietveld refinement. ^c Determined by ICP elemental analysis.^{40,d} ^d Based on methanol productivity at H₂/CO₂ = 3, T = 280 °C, P = 331 bar, GHSV = 8500 h⁻¹, and TOS = 6 h.

Scanning transmission electron microscopy (STEM) with high-angle annular dark field (HAADF) and X-ray energy dispersive spectroscopy (EDS) mapping images of the catalyst obtained after calcination of the washed

acetate-derived precursor are shown in **Figure 2.5**. The images confirm the inter-dispersion of ca. 8-10 nm size CuO and ZnO comparable to crystallite size as obtained from the Rietveld refinement (**Table 2.3**). Similar homogeneous inter-dispersion of CuO, ZnO and Al₂O₃ particles is observed in the EDS mapping from commercial Cu/ZnO/Al₂O₃ (**Figure 2.6**). On the other hand, the EDS mapping of the washed nitrate-derived catalyst (**Figure 2.7**) shows inter-dispersion Cu and Zn components but with larger CuO and ZnO particle sizes of 30-100 nm, which results in a relatively lower copper surface area than the acetate-derived catalyst (**Table 2.3**).

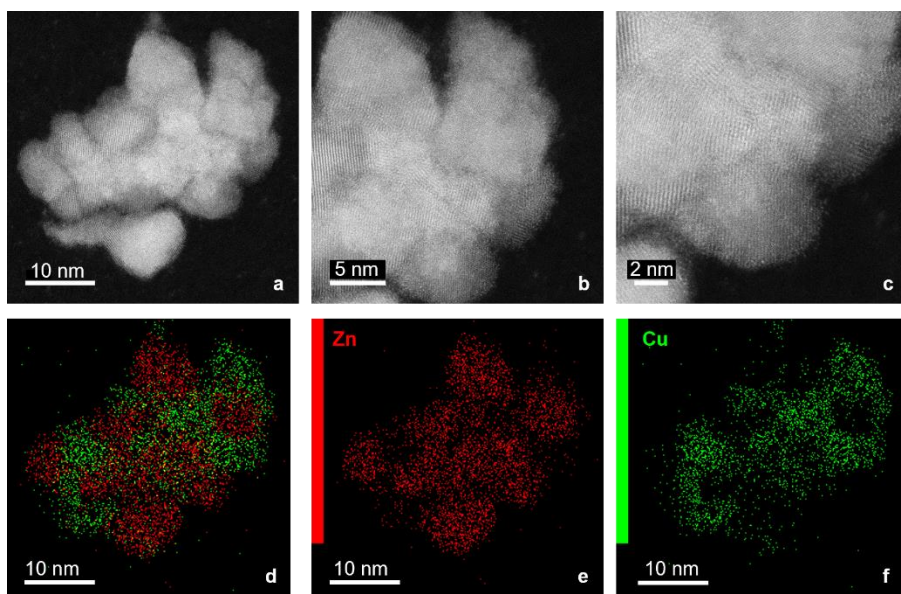


Figure 2.5 Representative HAADF-STEM images **a-c** and EDS analysis **d-f** of fresh CuO/ZnO (Cu:Zn = 1:1) catalyst derived from urea hydrolysis of acetate salts (washed).

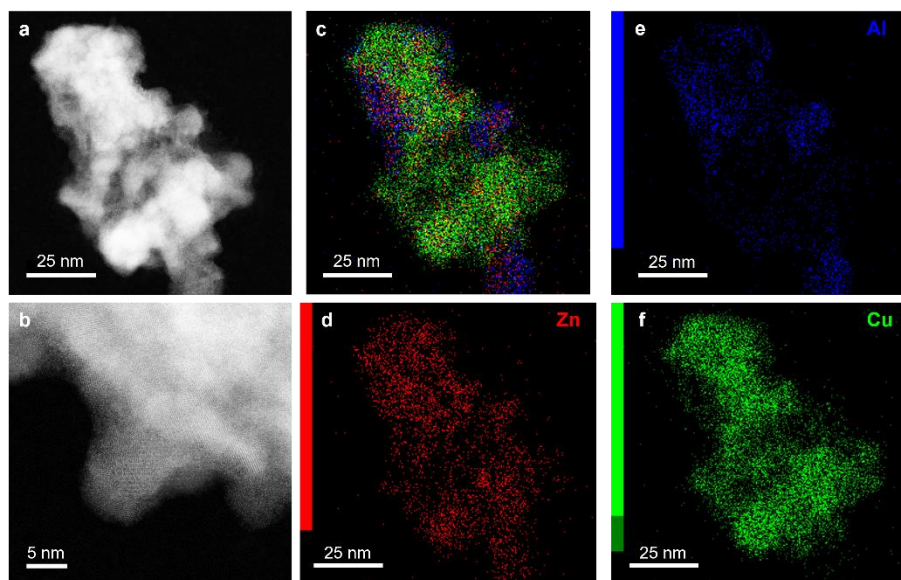


Figure 2.6 a-b Representative HAADF-STEM images and c-f EDS analysis of fresh commercial CuO/ZnO/Al₂O₃ catalyst.

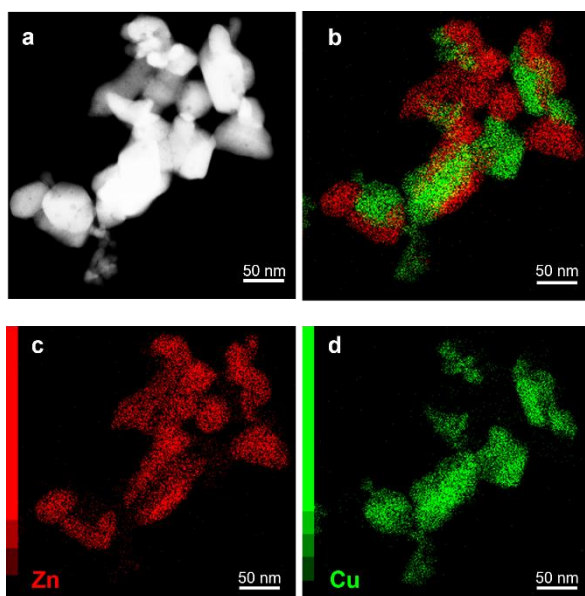


Figure 2.7 a Representative HAADF-STEM images and b-d EDS analysis of fresh CuO/ZnO (Cu:Zn = 1:1) catalyst derived from urea hydrolysis of nitrate salts (washed).

The washing procedure did not affect XRD patterns (**Figure S2.3**) and those of the washed and unwashed precursors are identical. On the other hand, the presence of unwashed residues is evident from the thermogravimetric analysis with derivative thermogravimetry (TGA/DTG) results (**Figure S2.4**). The total mass loss of as-precipitated precursors is 28-30% for the nitrate-derived catalysts and 26-28% for the acetate-derived catalysts. The unwashed residues account for ca. 2.5% of extra mass loss. The major mass losses at 350 and 400 °C are attributed to the decomposition of aurichalcite and rosasite, respectively,¹⁵ which correspond to the phases identified by XRD (**Figure S2.3**). From the TGA/DTG results (**Figure S2.4**), a high-temperature carbonate phase (HT-CO₃) is found only in the case of acetate-derived precursors at ca. 480 °C,¹⁵ similar to previously reported zincian georgeite precursor.⁸ The existence of HT-CO₃ after calcination provides a positive effect on Cu dispersion by suppressing sintering Cu during exothermic reduction pretreatment.^{53,54} However, low-temperature mass losses at 225 and 260 °C are detected only in the case of unwashed nitrate and acetate precursors, which are attributed to the decomposition of NH₄(NO₃) and CH₃COONH₄, respectively.^{8,55} The decomposition of such ammonium residues during calcination is exothermic and promotes not only the metal agglomeration but also the removal of the high-temperature carbonate phase.⁸ **Table 2.3** shows that the washing step is essential for nitrate-derived catalysts to exhibit more favorable textural properties as active catalysts. The activity loss during calcination of nitrate is due to the formation of NO_x that promotes metal agglomeration,⁵⁶ and can be avoided by decomposition under the gas flow (N₂, NO, or air), which was found to effectively remove remaining nitrate from the unwashed Na-free precursors.⁹ On the other hand, the textural properties of the catalyst derived from unwashed acetate precursors are not penalized, even upon calcination in the stagnant air of the muffle furnace, suggesting that the washing step could be skipped completely.

The catalytic performance of the materials listed in **Table 2.3** in comparison to the commercial Cu/ZnO/Al₂O₃ catalyst in high-pressure CO₂ hydrogenation to methanol at 240-280 °C and 331 bar is shown in **Figure 2.8**. The commercial Cu/ZnO/Al₂O₃ catalyst shows increasing CO₂ conversion and CH₃OH selectivity with increasing temperature from 240 to 280 °C. The improvement in the catalytic performance is small above 260 °C due to the shift from a kinetically controlled to a thermodynamically-controlled regime which can be achieved under very high-pressure conditions.⁴⁰ The optimal temperature is found to be 280 °C and higher temperatures will in turn decrease both CO₂ conversion and CH₃OH selectivity due to the thermodynamic equilibrium limitation.⁴¹ The catalysts derived from washed

acetate and nitrate precursors exhibit similar trends and achieve comparable CO₂ conversion and CH₃OH selectivity as commercial Cu/ZnO/Al₂O₃ catalysts, although the performance of the acetate-derived catalyst is superior. Importantly, the washing step did not affect the catalytic performance of the acetate-derived catalysts. In contrast, the unwashed nitrate-derived catalyst shows much lower activity than the washed one, as expected from the inferior textural properties (**Table 2.3**). The results clearly show that urea hydrolysis using acetate salts can produce a very active catalyst and render the catalyst preparation simpler with less amount of wastewater.

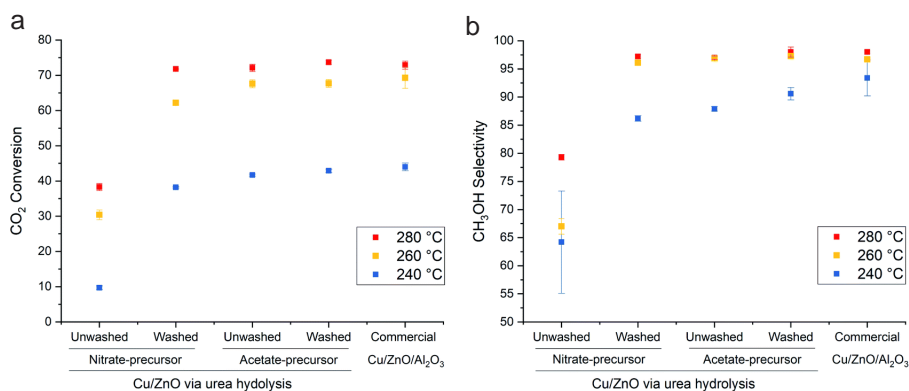


Figure 2.8 Influences of washing of as-precipitated precursors derived from nitrate and acetate salts on **a** CO₂ conversion **b** CH₃OH selectivity of Cu/ZnO catalyst (Cu:Zn = 1:1) for CO₂ hydrogenation to methanol. H₂/CO₂ = 3, T = 240, 260 and 280 °C, P = 331 bar, GHSV = 8500 h⁻¹, and TOS = 6 h.

It should be noted that Cu content in Cu/ZnO (1:1) catalysts (50 wt% CuO) is lower than the commercial Cu/ZnO/Al₂O₃ catalyst (64 wt% CuO) by 14 wt% so is the Cu surface area (**Table 2.3**). This indicates that the intrinsic activity is higher, which agrees with the study done by Behrens et al.; the intrinsic activity of Cu⁰ significantly decreases with increasing Al₂O₃ content and higher Cu surface area.⁵⁷ However, the Cu surface area alone cannot reflect the catalytic activity of the catalyst since Cu in the vicinity of ZnO has been reported to be particularly active for methanol production (e.g. Cu steps decorated with Zn atoms or strong metal-support interaction).^{58,59} The Cu content up to 80 wt% is employed for the preparation of Cu/ZnO or Cu/ZnO/Al₂O₃ catalysts via conventional co-precipitation since it is favorable for the formation of zincian malachite phase forming a highly active structure after calcination.^{15,42} With urea hydrolysis of acetate salts, an active catalyst can be prepared with lower active Cu metal usage and less water treatment,

which likely, in turn, reduces the cost of catalyst production. Therefore, the effect of Cu content (Cu:Zn ratio) will be further investigated in the following section.

2.2.4 Influence of Cu:Zn ratio

In addition to the studied parameters reported above, the ratio between Cu^{2+} and Zn^{2+} during co-precipitation plays also a decisive role in determining the structure of precipitated hydroxylcarbonate precursors that finally determine the Cu-ZnO inter-dispersion and the catalytic activity of final Cu/ZnO catalysts. The common reported structures are copper hydrozincite ($((\text{Cu}_x\text{Zn}_{1-x})_5(\text{OH})_6(\text{CO}_3)_2$, when $x < 0.1$), aurichalcite ($((\text{Cu}_x\text{Zn}_{1-x})_5(\text{OH})_6(\text{CO}_3)_2$, when $x < 0.5$), rosasite ($((\text{Cu}_x\text{Zn}_{1-x})_2(\text{OH})_2(\text{CO}_3)$, when $0.5 < x < 0.7$), and zincian malachite ($((\text{Cu}_x\text{Zn}_{1-x})_2(\text{OH})_2(\text{CO}_3)$ when $x > 0.7$).^{15,16} Industrially, Cu:Zn ratios in the range of 7:3 to 2:1 are chosen to yield a desired zincian malachite precursor.⁴² In this study, catalysts derived from acetate salts (washed) having Cu:Zn ratios of 1:3, 1:1, and 3:1 are tested. The XRD patterns of as-precipitated precursors confirm the formation of different phases upon changing from the Cu-rich to the Zn-rich solution. The aurichalcite phase is the main phase at the Cu:Zn ratio of 1:3 and 1:1, while the zincian malachite phase is the main one at 3:1 (**Figure S2.5**). Calcination of these precursors produce CuO/ZnO (or Cu/ZnO after reduction) with textural properties shown in **Table 2.4**. As expected, the increasing relative amount of Cu (i.e. higher Cu/Zn ratio) results in decreased Cu dispersion, while increasing the specific Cu surface area with a maximum at the Cu:Zn ratio of 1:1 (**Table 2.4**). In literature, the Cu:Zn ratio of 1:1 is hypothetically favorable for a highly active catalyst. The hydroxylcarbonate precursors with the Cu:Zn ratio of 1:1 should yield the smallest CuO and ZnO particles and the highest inter-dispersion upon decomposition (nano-structuring).^{42,52} The excess amount of Cu leads to lower specific Cu surface area and larger crystallite size mainly due to CuO agglomeration and insufficient ZnO stabilizer functioning as a spacer to prevent sintering (3:1, **Table 2.4**). As a reflection of the highest Cu surface area, the highest CO_2 conversion and CH_3OH selectivity are obtained with Cu/ZnO (1:1) catalyst (**Figure 2.9**).

Table 2.4 The textural properties of Cu/ZnO catalysts derived from urea hydrolysis of acetate salts at 80 °C for 24 h with the urea-to-metal molar ratio of 10 with washing step, and commercial Cu/ZnO/Al₂O₃ catalyst

Cu:Zn molar ratio of Cu/ZnO catalysts	BET surface area (m ² g ⁻¹)	Cu surface area ^a (m ² g ⁻¹)	Cu dispersion (%)	Average crystallite size ^b (nm)		Intrinsic activity ^d (mmol _{CH₃OH} m _{Cu} ⁻² h ⁻¹)
				CuO	ZnO	
1:3	65	9	18	2.8	7.1	3.8
1:1	70	13	13	4.1	6.7	2.9
3:1	71	12	8	4.8	3.8	3.0
Commercial Cu/ZnO/Al ₂ O ₃ (64/25/10 wt%) ^c	102	19	16	6.3	4.2	1.9

^a Determined by N₂O chemisorption. ^b Estimated by Rietveld refinement. ^c Determined by ICP elemental analysis. ^d Based on methanol productivity at H₂/CO₂ = 3, T = 280 °C, P = 331 bar, GHSV = 8500 h⁻¹, and TOS = 6 h.

Even though the catalytic activity of Cu/ZnO (1:3) is slightly lower than the commercial Cu/ZnO/Al₂O₃ and other Cu/ZnO catalysts reported in **Figure 2.9**, Cu utilization (weight basis) towards methanol formation is the highest thanks to the high copper dispersion. The weight-time-yields of methanol (WTY_{CH₃OH}) per amount of Cu at 280 °C and 331 bar are found to be Cu/ZnO (1:3) > Cu/ZnO (1:1) > Cu/ZnO/Al₂O₃ > Cu/ZnO (3:1) for 5177 > 2780 > 1887 > 1656 mg g_{Cu}⁻¹ h⁻¹, respectively. This suggests that the amount of Cu metal could be reduced with a slight compromise of catalytic activity.

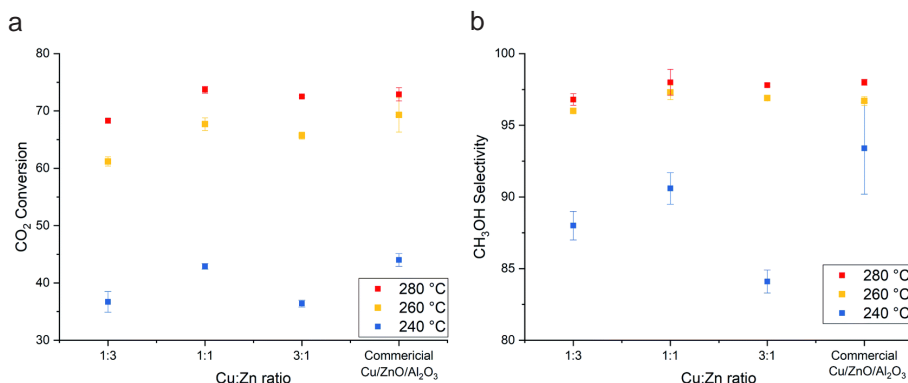


Figure 2.9 Influences of Cu:Zn molar ratio in Cu/ZnO catalyst derived from acetate salts (washed) on **a** CO₂ conversion and **b** CH₃OH selectivity from CO₂ hydrogenation to methanol. H₂/CO₂ = 3, T = 260 °C, P = 331 bar, GHSV = 8500 h⁻¹, and TOS = 6 h.

2.2.5 Stability test

The stability of the Cu/ZnO derived from the unwashed acetate precursors was compared with a commercial Cu/ZnO/Al₂O₃ catalyst at 280 °C and at a relatively high space velocity to induce faster deactivation (**Figure 2.10**). Both catalysts have shown similar trends of activity with time-on-stream (TOS) followed by a gradual decrease in CO₂ conversion. The Cu/ZnO/Al₂O₃ catalyst (**Figure 2.10a**) reached the maximum conversion of 76% and CH₃OH selectivity of 96% within 7 h, then these values started to decrease by 9% and 1.5% after 94 h, respectively. On the other hand, the Cu/ZnO catalyst (**Figure 2.10b**) has reached the same value of maximum conversion and selectivity within 5 h of TOS. However, the activity started to decline more rapidly, and the catalyst lost up to 24% lower CO₂ conversion and 3% lower methanol selectivity after 147 h. This comparably poor stability of the Cu/ZnO catalyst is expected since Al₂O₃ is known to function as a structural promoter that provides resistance against sintering.⁶⁰

Incorporation of such promoters using $\text{Al}(\text{CH}_3\text{COO})_2(\text{OH})$ via this synthesis route is possible without precursor washing; however, this is out of the scope of this work and the influences of Al amount on catalyst structures and activity need to be investigated.

Characterization of the spent catalysts by XRD (**Figure S2.6**) confirms that Cu sintering is the main cause of deactivation; the crystallite size of metallic Cu increases on average from 11.2 nm to 20.7 nm toward the end of stability testing. The increase in Cu size over time is related to a slight increase in CO selectivity, which reflects the structure-activity of the Cu/ZnO catalyst.⁶¹ The Cu crystallite growth over the Cu/ZnO/ Al_2O_3 catalyst due to the presence of the water partial pressure is reported.⁴⁸ Under a very high-pressure condition of 331 bar, CO_2 can react with ZnO into a more stable phase ZnCO_3 .⁶² The formation of rigid ZnCO_3 helps slower growth of Cu crystallite size.⁶³ Moreover, weaker interaction between water and ZnCO_3 than ZnO seems to improve the activity of the Cu-based catalyst under liquid phase methanol synthesis.⁶² The understanding of the involved mechanisms and electronic properties of both ZnO and ZnCO_3 is still limited, and the role of ZnCO_3 on catalytic activity and stability will be investigated in future work.

2.3 Conclusions

The sodium- and nitrate-free precursors of the Cu/ZnO catalysts were successfully prepared via the facile urea hydrolysis method using acetate and nitrate salts. At the optimal preparation conditions, the small aurichalcite structure is obtained leading to superior catalytic activity from the nitrate-derived catalyst. Moreover, the washing step was completely omitted from the acetate-derived catalyst while retaining high catalytic activity. This unwashed acetate-derived catalyst exhibited excellent time-on-stream stability even in an absence of Al_2O_3 which is normally present as a structural promoter in the commercial Cu/ZnO/ Al_2O_3 .

2.4 Experimental

2.4.1 Raw materials

The following raw materials were used for co-precipitation: copper (II) nitrate trihydrate (p.a. 99-104%, Sigma-Aldrich), zinc (II) nitrate hexahydrate (98%, Sigma-Aldrich), copper (II) acetate hydrate (98%, Sigma-Aldrich), zinc (II) acetate dihydrate ($\geq 97\%$, Alfa Aesar), urea (99%), deionized

water was used from a Millipore system. The commercial methanol synthesis catalyst (Cu/ZnO/Al₂O₃) was purchased from Alfa Aesar (Product ID: 45776).

2.4.2 Preparation of Cu/ZnO via urea hydrolysis method

The Cu/ZnO catalysts were prepared batchwise in a 500 mL round-bottom flask with reflux condensation and internal temperature control. An aqueous solution containing Cu(CH₃COO)₂, Zn(CH₃COO)₂, and urea were freshly prepared and mixed at room temperature. The total concentration of Cu²⁺ and Zn²⁺ in the solution was kept constant at 0.25 M. The Cu:Zn ratio in the solution was varied from 1:3 to 3:1 to adjust the Cu content of the CuO/ZnO catalyst, while the molar ratio of [urea]/[Cu²⁺ + Zn²⁺] was varied from 1-10. The mixed solution was added to the flask and heated to 70-95 °C with 10 °C min⁻¹ using a heating mantle and while stirring vigorously at 1000 rpm using a magnetic stirrer. After 24 h of the precipitation process, the as-precipitate precursor was filtrated, optionally washed with adequate deionized water, and dried in an oven at 80 °C overnight. The dried precursor was calcined at 300 °C in a muffle furnace for 1 h at a heating rate of 2 °C min⁻¹. The calcined catalyst powder was pelletized with a pressing die, crushed in a mortar, and sieved to the size of 100-300 µm. The palletization pressure was 370 kg cm⁻² or ca. 363 bar, similar to the reaction pressure, to ensure no deformation of the catalyst pellets during gas pressurization. The same synthesis procedure was used to prepare catalysts from aqueous Cu(NO₃)₂, and Zn(NO₃)₂ solution.

2.4.3 Catalyst characterizations

The fresh and spent catalysts were characterized by various methods. The thermal decomposition of catalyst precursors is measured by a Mettler Toledo DSC822 thermogravimetric analyzer (TGA). The BET surface area of the catalyst was analyzed using a Quantachrome Autosorb 1-MP surface area analyzer. The reducibility of the catalyst is studied by temperature-programmed reduction (H₂-TPR) on Thermo TPDRO 1100 equipped with a TCD detector. The copper surface areas were measured by N₂O pulse chemisorption at 90 °C, in which samples were reduced by 5% H₂ in the He stream at 300 °C before analysis.⁴⁰ A relatively harsh reduction condition is used to ensure the reduction of the catalysts as shown (**Figure S2.7**). Powder X-ray diffraction (XRD) patterns were attained using a Bruker AXS D8 Advance diffractometer equipped with a Cu tube. The Rietveld refinement were calculated using X'Pert HighScore Plus. Scanning electron microscope (SEM) images were obtained by Hitachi HD-2000. High-angle annular dark-

field imaging (HAADF) was performed using a JEM-ARM200F scanning transmission electron microscope (STEM) equipped with a JEOL JED-2300 X-ray energy dispersive spectrometer (EDS). Samples were prepared by dropping an ethanol solution containing the catalyst on carbon-supported Mo grids.

2.4.3 Catalyst testing

The catalytic tests were carried out in a high-pressure setup as reported elsewhere.⁴⁰ In a typical test, 200 mg catalyst was packed between quartz wool inside a 1/4 inch fixed-bed continuous flow reactor (ID 2.79 mm). The catalyst was reduced *in situ* at 260 °C with 90% H₂/Ar (25 NmL min⁻¹) for 2 h under atmospheric pressure. A relatively harsh reduction condition was used to ensure the reduction of the catalysts and to reach a stable state of the catalyst shortly. The reduction temperature had negligible effects on the catalytic activity (**Figure S2.8**). After cooling down to 30 °C, the H₂/CO₂/Ar mixture with vol% of 69%/23%/8% was fed into the reactor and pressurized to 360 bar (the reactant pressure is 331 bar). The total flow rate of the gas mixture is kept at 16.7 NmL min⁻¹ to achieve a gas-hourly space velocity of 8500 h⁻¹ equivalent to 5 NL g_{cat}⁻¹ h⁻¹. The products were analyzed by an online gas chromatograph (Bruker, GC-450) equipped with a flame ionization detector for methanol, methyl formate, diethyl ether, and other hydrocarbons, and a thermal conductivity detector for permanent gases e.g. CO₂, H₂, Ar, CO, CH₄.

2.5 References

- 1** G. A. Olah, A. Goeppert and G. K. S. Prakash, *Beyond Oil and Gas: The Methanol Economy*, Wiley, 2009, vol. 44.
- 2** G. A. Olah, *Angew. Chem., Int. Ed.*, 2013, 52, 104–107.
- 3** K. Klier, *Adv. Catal.*, 1982, 31, 243–313.
- 4** P. Anastas and N. Eghbali, *Chem. Soc. Rev.*, 2010, 39, 301–312.
- 5** S. Schimpf and M. Muhler, in *Synthesis of Solid Catalysts*, Wiley-VCH Verlag GmbH & Co. KGaA, Weinheim, Germany, 2009, pp. 329–351.
- 6** Y. Tang, Y. Liu, P. Zhu, Q. Xue, L. Chen and Y. Lu, *AIChE J.*, 2009, 55, 1217–1228.
- 7** M. Behrens, S. Kießner, F. Girsgdies, I. Kasatkin, F. Hermerschmidt, K. Mette, H. Ruland, M. Muhler and R. Schlögl, *Chem. Commun.*, 2011, 47, 1701.
- 8** P. J. Smith, S. A. Kondrat, P. A. Chater, B. R. Yeo, G. M. Shaw, L. Lu, J. K. Bartley, S. H. Taylor, M. S. Spencer, C. J. Kiely, G. J. Kelly, C. W. Park and G. J. Hutchings, *Chem. Sci.*, 2017, 8, 2436–2447.
- 9** G. Prieto, K. P. de Jong, and P. E. de Jongh, *Catal. Today*, 2013, 215, 142–151.
- 10** S. A. Kondrat, P. J. Smith, P. P. Wells, P. A. Chater, J. H. Carter, D. J. Morgan, E. M. Fiordaliso, J. B. Wagner, T. E. Davies, L. Lu, J. K. Bartley, S. H. Taylor, M. S. Spencer, C. J. Kiely, G. J. Kelly, C. W. Park, M. J. Rosseinsky and G. J. Hutchings, *Nature*, 2016, 531, 83–87.
- 11** S. A. Kondrat, P. J. Smith, J. H. Carter, J. S. Hayward, G. J. Pudge, G. Shaw, M. S. Spencer, J. K. Bartley, S. H. Taylor and G. J. Hutchings, *Faraday Discuss.*, 2017, 197, 287–307.
- 12** U. Costantino, F. Marmottini, M. Nocchetti and R. Vivani, *Eur. J. Inorg. Chem.*, 1998, 1998, 1439–1446.
- 13** R. J. Candal, A. E. Regazzoni and M. A. Blesa, *J. Mater. Chem.*, 1992, 2, 657–661.
- 14** G. J. d. A. A. Soler-Illia, R. J. Candal, A. E. Regazzoni and M. A. Blesa, *Chem. Mater.*, 1997, 9, 184–191.

Supporting information

Chapter 2

Estimation of wastewater production

According to the study of Prieto et al. (Catal. Today, 2013, 215, 142–151.), the influence of washing on physical properties and catalytic performance has been thoroughly studied. The as-precipitated precursors were submitted to up to 7 washing steps by resuspending the solid in deionized water, vigorously stirring the suspension for 5 min, and following by filtration of the solid. Each washing step required 50 mL g⁻¹ dried solid and 7 steps are required to remove nitrate and sodium from the precipitate and achieve the highest catalytic performance. From that information, the amount of wastewater produced per amount of catalyst can be calculated as follows (assuming 70% weight loss from calcination).

The volume of wastewater =

$$7 \text{ steps} \times \frac{50 \text{ L}}{\text{kg}_{\text{precipitate}} \cdot \text{step}} \times \frac{100 \text{ kg}_{\text{precipitate}}}{70 \text{ kg}_{\text{catalyst}}} = 500 \text{ L/kg}_{\text{catalyst}}$$

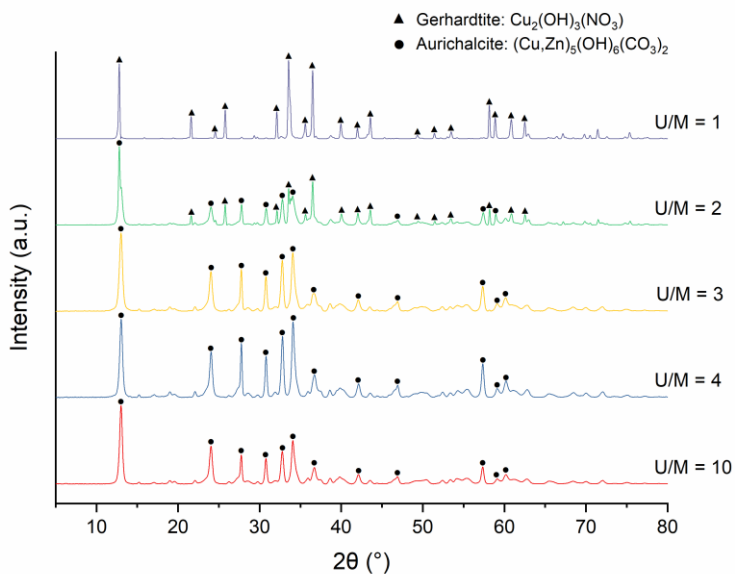


Figure S2.1 XRD patterns of the as-precipitated precursors and calcined Cu/ZnO catalysts (Cu:Zn = 1:1) prepared by urea hydrolysis of nitrate salts with various urea to metal molar ratios (U/M) of 1-10 and washing step at 95 °C

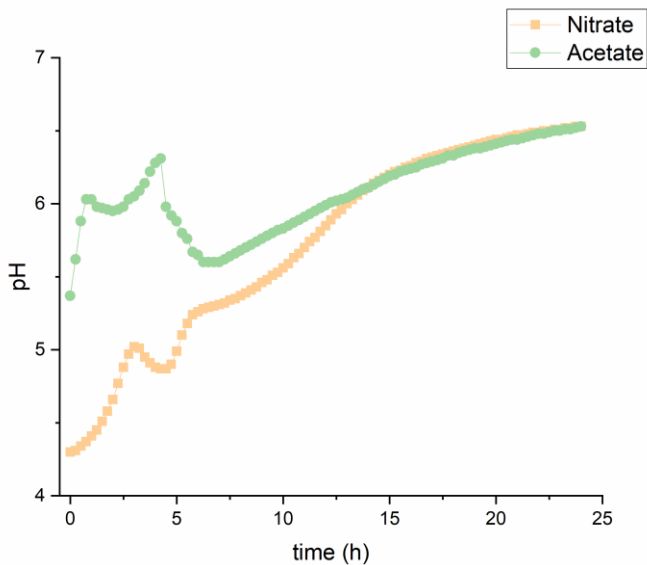


Figure S2.2 Evolution of the pH of the solution during synthesis of Cu/ZnO catalysts (Cu:Zn = 1:1) through urea hydrolysis of nitrate or acetate salts with urea to the metal molar ratio (U/M) of 10 at 80 °C.

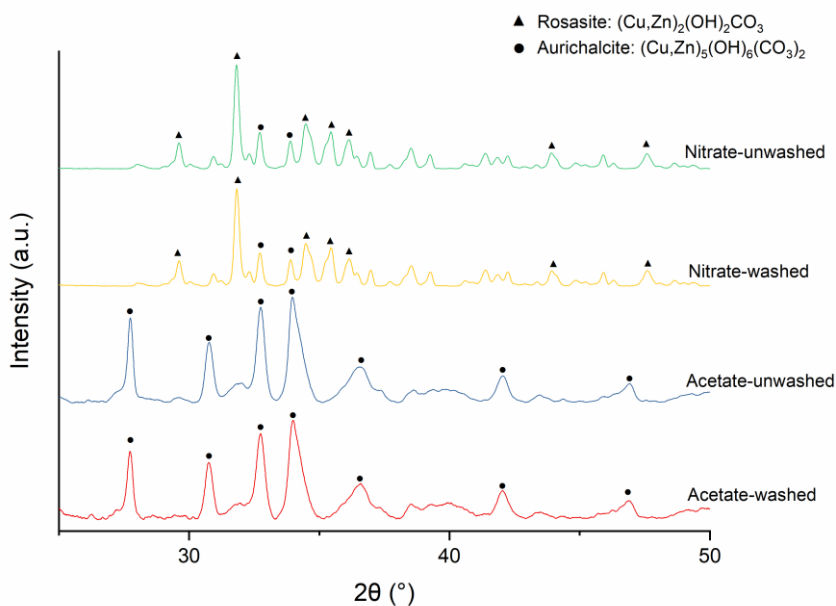


Figure S2.3 XRD patterns of as-precipitated precursors for Cu/ZnO (Cu:Zn = 1:1) prepared by urea hydrolysis of nitrate and acetate salts with urea to the metal molar ratio (U/M) of 10 at 80 °C.

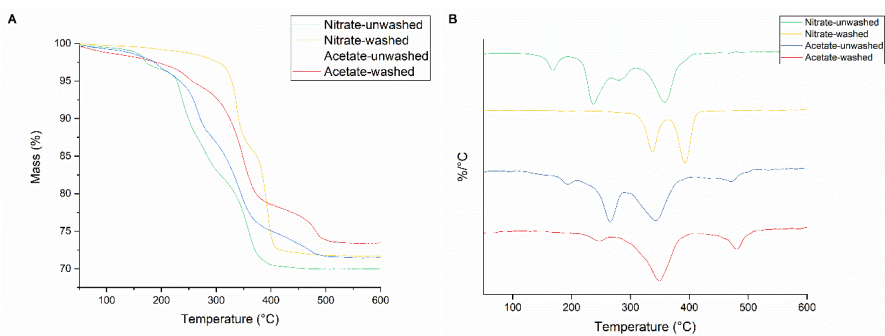


Figure S2.4 Thermogravimetric analysis (TGA) and differential thermal gravimetric (DTG) of washed and unwashed as-precipitated precursors derived from urea hydrolysis of nitrate and acetate metal salts with urea to the metal molar ratio (U/M) of 10 at 80 °C. T = 30-600 °C, ramp rate 10 °C min⁻¹ under air.

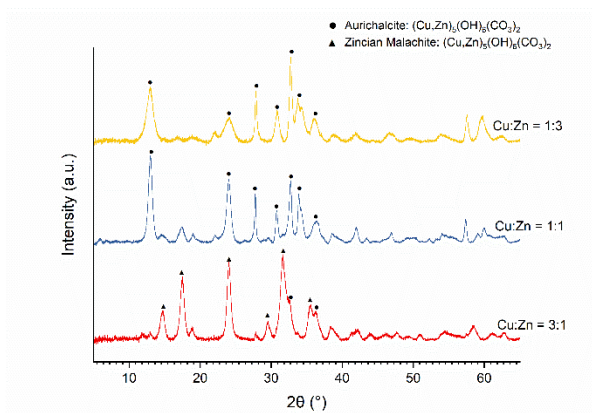


Figure S2.5 XRD patterns of as-precipitated precursors for Cu/ZnO with Cu:Zn of 1:3, 1:1, and 3:1 prepared by urea hydrolysis of acetate salts.

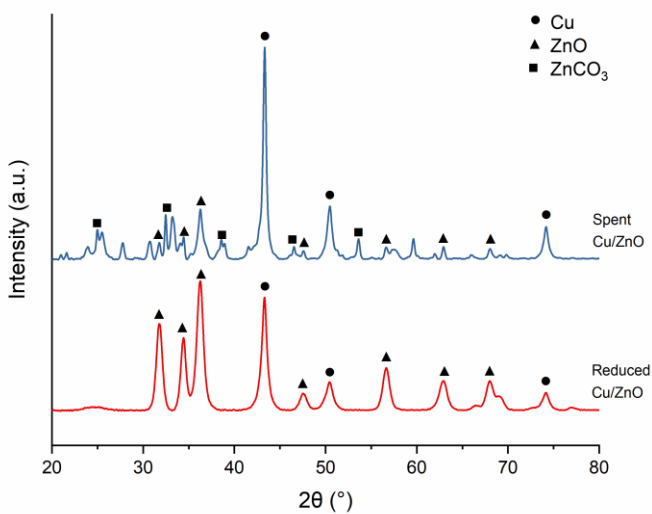


Figure S2.6 XRD patterns of Cu/ZnO (1:1) catalyst prepared by urea hydrolysis of acetate salts without washing step after reduction and stability test. $\text{H}_2/\text{CO}_2 = 3$, $T = 280^\circ\text{C}$, $P = 331\text{ bar}$, and GHSV $17,000\text{ h}^{-1}$.

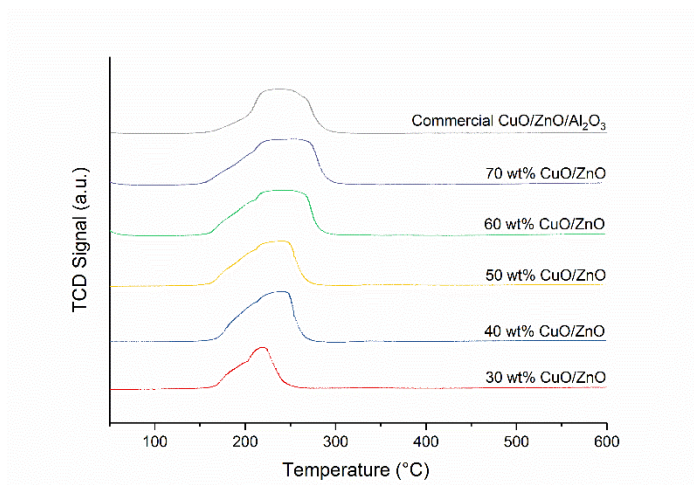


Figure S2.7 H₂-TPR profiles of the CuO/ZnO catalysts with various Cu contents.
Reduction conditions: 5% H₂/N₂, F = 20 NmL min⁻¹, T = 50-600 °C and ramp rate = 2 °C min⁻¹.

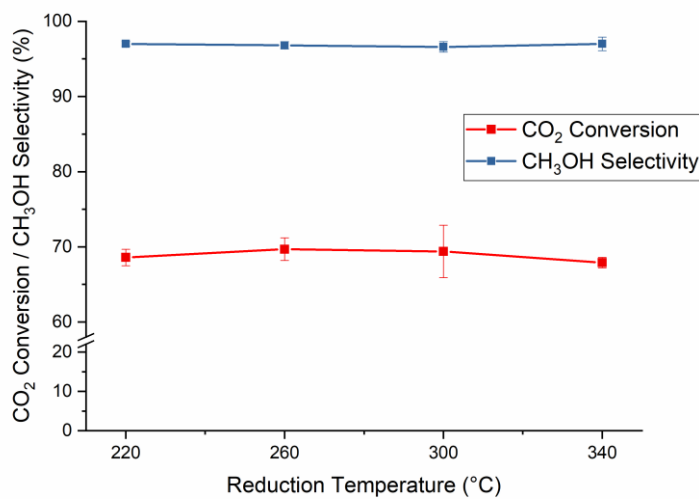


Figure S2.8 Effect of reduction temperature on the catalytic activity of the Cu/ZnO (1:1) catalyst.
Reduction conditions: 90% H₂/Ar, F = 20 NmL min⁻¹, and T = 220-340 °C. Reaction conditions: H₂/CO₂ = 3, T = 260 °C, P = 331 bar, GHSV = 8500 h⁻¹, and TOS = 6 h.

From CO or CO₂?: space-resolved insights

into high-pressure CO₂ hydrogenation
to methanol over Cu/ZnO/Al₂O₃



Abstract

The reaction pathway of high-pressure CO₂ hydrogenation over a Cu/ZnO/Al₂O₃ catalyst is investigated through the gradients of reactants/products concentration and catalyst temperature within the catalytic reactor. This study reveals that methanol is formed through direct CO₂ hydrogenation at low temperature, while above 260 °C methanol formation is mediated via CO which is formed by reverse water-gas shift reaction.



This chapter is based on the following publication:

Gaikwad, R., Reymond, H., **Phongprueksathat, N.**, Rudolf von Rohr, P., & Urakawa, A. (2020) *Catalysis Science & Technology*, 10(9), 2763–2768.

**The three first authors contributed equally to this work.*

3.1 Introduction

The increasing atmospheric CO₂ concentration demands urgent actions to reduce CO₂ emissions by converting CO₂ into useful chemicals and fuels. Among various chemicals derived from CO₂, methanol has considerable potential as a liquid fuel, hydrogen carrier, and C₁ feedstock.^{1,2} Methanol can now be synthesized on commercially relevant scales via CO₂ hydrogenation over Cu/ZnO/Al₂O₃-based catalysts at 200-300 °C and 10-100 bar,^{3,4} which is by far the most mature technology for efficient CO₂ conversion.¹ From a mechanistic point of view, methanol synthesis from CO₂ over Cu/ZnO/Al₂O₃ catalysts may occur through direct CO₂ hydrogenation (Eqn. 3.1) or through reverse water-gas shift (RWGS) (Eqn. 3.2) followed by CO hydrogenation (Eqn. 3.3).²

Since methanol synthesis from CO₂ accompanies CO formation, early studies concluded that CO hydrogenation is the main reaction pathway over Cu/ZnO catalysts.⁵⁻⁷ However, the C¹⁸O₂ isotopic labeling indicated that methanol can be produced from both CO and CO₂, by which CO₂ hydrogenation is the primary pathway at 220 °C.⁸ The ¹⁴CO and ¹⁴CO₂ isotopic labeling also supported that CO₂ is the primary source of methanol instead of CO at 250 °C.⁹ The intrinsic CO₂ hydrogenation rate is ~20 times faster than CO hydrogenation, especially at low conversion,¹⁰ although the CO₂ hydrogenation is suppressed at high conversion due to water formation.¹¹ In contrast, DFT calculations showed the rate of the RWGS to form CO becomes ~100 times higher than CO₂ hydrogenation to methanol at a higher temperature (300 °C), in agreement with the experiment.¹² However, such CO rather accumulates as a product since CO hydrogenation is slower than CO₂ hydrogenation. Another set of DFT calculations fitted to published experimental rate data under realistic conditions suggested that CO₂ hydrogenation is responsible for ~2/3 of methanol production.¹³ It was later confirmed by isotope tracing experiments in ¹³CO/¹²CO₂/H₂ that CO₂ is the dominant carbon source in methanol product at 240 °C. However, the source of carbon gradually shifts from CO₂ to CO as the temperature is lowered (toward 160 °C).¹⁴ It was proposed that CO hydrogenation could also be inhibited by the formation of formate intermediates at higher CO₂ concentrations (230 °C).^{15,16} The isotopic labeling using H/D substitution suggested that methanol formation from CO₂ does not occur via consecutive RWGS and CO hydrogenation (at 250 °C),¹⁷ and rather RWGS and CO₂ hydrogenation occur independently (220-260 °C).^{17,18} Although some debates exist, methanol formation from CO₂ as the carbon source is currently the most widely accepted mechanism for

Cu/ZnO-based catalysts, supported by both experimental findings and theoretical calculations mentioned above.

Thermodynamically, both CO and CO₂ hydrogenation reactions produce methanol, but the predominant reactions depend on the operating conditions.¹⁹ The favorable conditions for CO₂ hydrogenation to methanol are high pressure and low temperature according to Le Châtelier's principle, as obvious from **Eqn. 3.1**,² and the advantages of high-pressure reaction conditions above 200 bar in terms of CO₂ conversion (>90%), methanol selectivity (>95%), and methanol yield have been recently demonstrated.^{20,21} In practice, however, there is an optimum reaction temperature where reaction kinetics are favorable, and simultaneously, endothermic RWGS does not rule the product selectivity. For example, in the previous studies (200 and 360 bar), the CO selectivity is surprisingly high at 170-200 °C, while it starts to decrease to the minimum as the temperature increases to 260 °C, indicating the CO hydrogenation towards the formation of methanol.²¹ Similarly, CO selectivity increases at high space velocities, implying that CO-mediated path may be active under high-pressure conditions, which is indeed in accordance with early studies at high pressure (415 bar).⁵ Most mechanistic studies aiming at elucidation of the reaction pathway are performed at low to moderate pressure (<30 bar) and there are no convincing mechanistic clues reported to date for high-pressure methanol synthesis above such pressure.

This study aims at clarifying dominating reaction pathways and the source of carbon, CO or CO₂, resulting in methanol from the concentration profiles of the reactants/products as well as that of the catalyst temperature along the axial direction of the reactor packed with a commercial Cu/ZnO/Al₂O₃ catalyst at 200 and 360 bar (reactant pressure of 184 and 331 bar).^{20,21} Changing space velocity by varying the reactant flow rate and/or catalyst amount is one way to gain the information;²² however, this approach may influence mass transfer characteristics and also temperature gradient (higher mass flow rate can result in more prominent temperature gradient due to endo-/exo-thermicity of the reactions). In this study, we developed a method to study quantitatively the concentration of reactant/product fluids based on gas chromatography (GC) and Raman spectroscopy looking at different locations of the catalyst bed. Furthermore, infrared (IR) thermography was used to monitor the catalyst temperature under *operando* high-pressure reaction conditions to gain support on the reaction mechanisms through exo- and endo-thermicity.

3.2 Experimental

The high-pressure reactor setup and used materials are explained in detail in supporting information. Briefly, the commercial Cu/ZnO/Al₂O₃ catalyst²⁰ was packed in a stainless steel (SS) or sapphire capillary reactor where three split catalyst beds were separated by empty spaces (P1-P4) for gas sampling and quantification. In the case of the SS reactor (**Figure 3.1a**), the gas sampling for GC analysis was performed by needle valves connected to the void sections. The amount of the sampled gas was sufficiently small (confirmed by GC) so that it did not affect the overall catalytic activity. For Raman spectroscopic determination of fluid concentration, a Raman laser (532 nm) was focused onto the void sections filled with quartz wool in the sapphire reactor (**Figure 3.1b**, **S3.1** and **S3.2**, holding reactant pressure up to 200 bar, 350 °C). The major advantage of the GC analysis is the accuracy in the quantification and that of the Raman analysis is the non-perturbing nature of the sampling on the flow behavior.

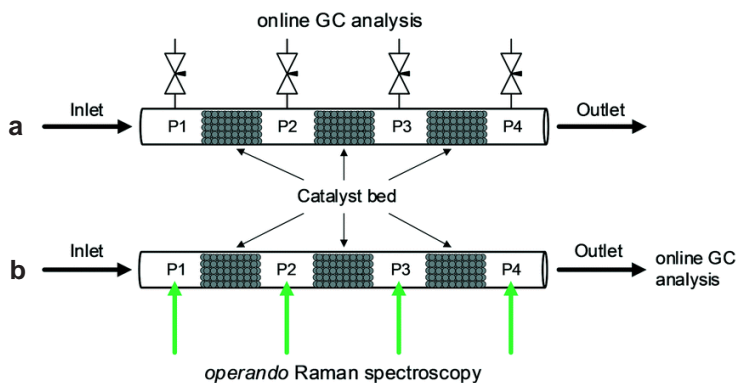


Figure 3.1 Schematic of catalyst beds configuration for **a** a stainless-steel reactor with gas sampling valves at P1-P4, and **b** a sapphire reactor with Raman spectroscopic gas analysis at P1-P4 and gas chromatographic analysis at the outlet.

3.3 Result and discussions

First, concentration profiling at P1-P4 was performed during CO₂ hydrogenation at the stoichiometric ratio ($H_2/CO_2 = 3$) in the SS reactor at three temperatures (180, 260 and 340 °C) and two pressure conditions (184 and 331 bar). CO₂ conversion and carbon-based mole fractions F (both in %), which are defined as CO₂ conversion scaled by respective product selectivity (that is in 0-1 scale, leading to $F_{CH_3OH} + F_{CO} = X_{CO_2}$). These quantities were used

to understand in a facile fashion how much CO₂ is converted and into which product.

Figure 3.2a and **3.2b** show the catalytic performance in terms of X_{CO_2} , $F_{\text{CH}_3\text{OH}}$ and F_{CO} at 180 °C at 184 bar and 331 bar, respectively. At this low reaction temperature, we observe low CO₂ conversion but high methanol selectivity, thus a high fraction of methanol. What is prominent are the X and F profiles and their differences. At this low conversion, virtually the partial pressure of the reactants (CO₂ and H₂) is unaltered throughout the catalyst bed and generally one expects little change in the reaction rate and product selectivity due to full kinetic control at different positions of the catalyst bed. However, this is not the case and lower CO₂ conversion is more prominent at the lower investigated pressure (184 bar, **Figure 3.2a**) where CO₂ conversion does not linearly increase between P2-P3, and even drops between P3-P4. When the rate of CO₂ conversion is decreased, the fraction of methanol also decreases. Assuming that the intrinsic reaction selectivity at this temperature is almost 100% towards methanol (judging from the values at P2), the only explanation for the CO₂ conversion drop is methanol decomposition ($\text{CH}_3\text{OH} \rightarrow \text{CO} + 2\text{H}_2$),²³ especially between P2-P3. However, since the water partial pressure is expected to rise along with along the catalyst bed and the CO₂ conversion between P3-P4, steam reforming ($\text{CH}_3\text{OH} + \text{H}_2\text{O} \rightarrow \text{CO}_2 + 3\text{H}_2$) is supposed to take place. Although the reports on gas-phase methanol decomposition and steam reforming at such high pressure are expectedly limited, there is evidence suggesting that such reactions occur even at 250-450 bar under supercritical water,²⁴ and its kinetics can be enhanced as the number of collisions increases with pressure. Moreover, the slight decrease in CO fraction also indicates the forward water gas shift reaction. This explanation is also in accordance with high CO selectivity at low temperatures, as found in the previous work.²¹ Based on the profiles of CO₂ conversion and product fractions, at 331 bar (**Figure 3.2b**) this methanol decomposition and steam reforming to CO and CO₂ (generalized as “methanol decompositions”) also takes place but to a significantly lesser extent. This is likely due to the pressure effects affecting to shift the equilibrium towards the product (methanol) side, showing one of the unique advantages of high-pressure reaction conditions.^{20,21}

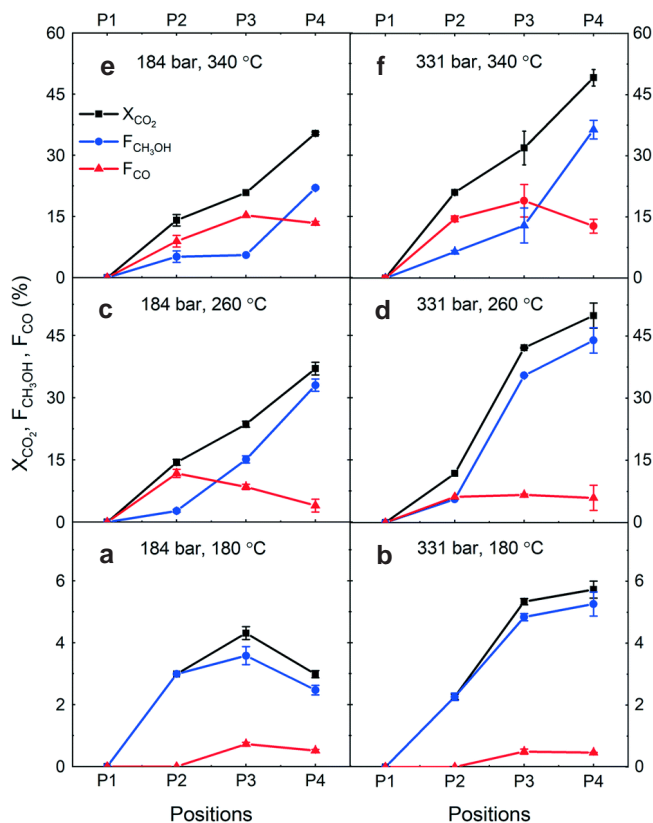


Figure 3.2 CO_2 conversion (X_{CO_2}), the mole fraction of methanol (F_{CH_3OH}) and CO (F_{CO}) at different axial positions (P1-P4) during CO_2 hydrogenation to methanol over the commercial Cu/ZnO/ Al_2O_3 catalyst. $H_2/CO_2 = 3$, $T = 180, 260$, and $340\text{ }^\circ\text{C}$, $P = 184$ and 331 bar, and GHSV = 10000 h^{-1} .

The same experiment was performed at two higher temperatures (260 and $340\text{ }^\circ\text{C}$) and the results obtained at $260\text{ }^\circ\text{C}$ are summarized in **Figure 3.2c** and **3.2d**. First, the CO_2 conversion values are about one order of magnitude higher than those at $180\text{ }^\circ\text{C}$. Also, at both examined pressures, relatively high CO selectivity was observed. At 184 bar (**Figure 3.2c**), CO was the major product, but then the fraction of CO decreased towards the outlet position. This is indicative of CO conversion to methanol, although there is a possibility of water-gas shift reaction forming CO_2 and H_2 from CO and H_2O (reverse reaction of **Eqn. 3.2**). However, the methanol fraction drastically increases as CO fraction dropped towards the outlet direction. This indicates the former reaction (i.e. CO hydrogenation to methanol, **Eqn. 3.3** is likely the major active path under the studied reaction condition. At 331 bar (**Figure 3.2d**) CO fraction remained relatively constant, whereas the methanol

fraction increased drastically along with CO₂ conversion between P2 and P3. At 184 bar (**Figure 3.2c**) CO₂ conversion linearly increased and did not drop as observed at 180 °C. These results indicate three important insights into high-pressure CO₂ hydrogenation at 260 °C: (i) methanol formation is faster than its decompositions, (ii) CO₂ is constantly converted to methanol or CO as the intermediate at 184 bar and (iii) there is another factor promoting/enhancing CO₂ conversion at 331 bar. Regarding the point (ii), at 184 bar at P2, very high CO selectivity was observed and its continuous decrease and drastic increase in methanol production towards the reactor outlet implies that CO₂ is converted to CO at an almost constant rate and then CO is further converted to methanol. In this case, the latter reaction rate would mainly determine the final fraction of methanol and CO in the reactor. The point (iii) indicates the important effects of reaction pressure. According to **Figure S3.4**, at 260 °C, we expect phase condensation at 331 bar but not at 184 bar. This may explain the sudden surge in CO₂ conversion between P2-P3; the CO₂ conversion was sufficiently high to reach the dew point of the condensable products (methanol and water) at this position in the reactor, positively impacting on the reaction rate or shifting the equilibrium towards methanol.

The presence of water in the fluid phase can promote Cu crystallite growth²⁵ and induce transformation of ZnO into ZnCO₃, as shown in the XRD patterns of spent catalysts (**Figure S3.3** and **Table S3.1**). However, it is still difficult to establish the relationship between mechanism and catalyst structure from the existing results, especially using the bulk sensitive techniques.

Furthermore, the results obtained at the highest examined temperature (340 °C) are presented in **Figure 3.2e** and **3.2f**. Similar to the case of 260 °C, a large amount of CO was observed with a decrease in its fraction with respect to methanol towards the reactor outlet. On the other hand, CO₂ conversion increased almost linearly. These two observations indicate that RWGS is the first main step of CO₂ hydrogenation and produced CO reacts further with H₂ to produce methanol. It is also interesting to note the boosted methanol formation between P3-P4. A similar observation at 260 °C was interpreted to be caused by phase condensation. At this temperature, however, we do not expect such phase condensation to occur (**Figure S3.4**). One possibility may be a dense phase formation, like surface wetting, in the pore of the catalyst which is virtually identical to phase condensation. Besides, it is worth highlighting the maximum CO fraction observed in the reactor at 260 and 340 °C. According to the thermodynamic calculation (**Figure S3.5**), the equilibrium CO₂ conversions for RWGS at H₂/CO₂ = 3 are ca. 14% and 21% at 260 and 340 °C, respectively. A careful look at **Figures**

3.2e and 3.2f shows that the CO fraction is close to the equilibrium CO₂ conversion in the middle of the reactor (since the fraction is the percentage of CO₂ converted to methanol; therefore, these numbers can be directly compared). Still, the CO fraction decreases accompanying the increase in methanol fraction close to the outlet of the reactor, implying that the methanol synthesis rate is accelerated at the position. It is speculated that the dense phase formation over the catalyst accelerates CO hydrogenation to methanol. In addition, methanol decompositions may take place, but it is not possible to gain information about this point from the data obtained. Nevertheless, it is certain that the consumption rate of CO and CO₂ to form methanol is much greater than the methanol decompositions rate under these high-pressure conditions.

Based on the above studies, we conclude that the pressure effects on the reaction paths are relatively minor compared to the temperature effects, although increasing pressure is indeed advantageous for methanol synthesis because of favorable kinetics (more collisions), phase separation, and chemical equilibrium.²⁶ Interestingly, at 260 °C where we find optimum catalytic performance and liquid-phase condensation seems indeed to boost the reactivity of CO₂ to methanol by a concerted kinetic and thermodynamic interplay.

Furthermore, similar concentration profiling experiments were performed using Raman spectroscopy instead of GC. The major advantage of this spectroscopic approach is that the reaction and flow patterns are not disturbed in contrast to the case of GC analyses. **Figure S3.6** shows a typical Raman spectrum of the reaction stream obtained at 260 °C at the outlet (P4). The rotational transitions of H₂ (355, 587, 812, 1033, 1246, 1447 cm⁻¹), as well as the Fermi dyad of CO₂ and satellite bands (1265, 1286, 1387, 1408 cm⁻¹), were clearly identified. Because of the small Raman scattering cross-section of CO, its characteristic feature at 2140 cm⁻¹ was not sufficiently strong for quantitative analysis and only its formation could be confirmed at high CO concentration. The features at 2840 and 2945 cm⁻¹ are attributed to methanol, showing a too weak signal for quantitative analysis. For these reasons, the intense bands of H₂ and CO₂ at 587 and 1387 cm⁻¹, respectively, were considered here to gain mechanistic insights.

Figure 3.3 shows the evolution of the H₂/CO₂ ratio determined from the band areas at different void positions (**Figure 3.1**) at 180 °C and 260 °C at 184 bar. The initial area ratio at P1 was scaled to 2.5 to represent the molar ratio of unreacted feed confirmed by GC measurements. The reaction at 180 °C showed a slight decrease in the ratio moving from P1 to P2, before increasing towards P3, and no major change was observed moving from P3 to P4.

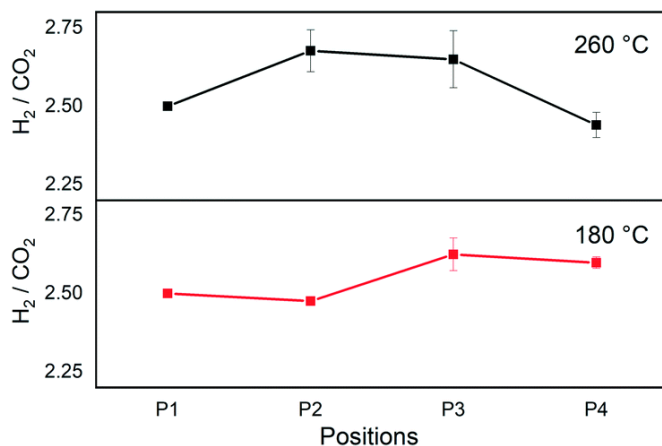


Figure 3.3 H₂/CO₂ ratio at different positions during CO₂ hydrogenation to methanol over the commercial Cu/ZnO/Al₂O₃ catalyst. H₂/CO₂ = 2.5, T = 180 and 260 °C, P = 184 bar, and GHSV = 80000 h⁻¹.

In the case of direct methanol synthesis from CO₂ (Eqn. 3.1), 3 moles of H₂ would be consumed per mole of CO₂ for the production of methanol, rendering H₂ the limiting reactant in our experimental condition (feed H₂/CO₂ = 2.5). On the other hand, if CO₂ is consumed to form CO via RWGS (Eqn. 3.2), CO₂ would become a limiting reactant. Therefore, a decrease in the H₂/CO₂ ratio would signify an excessive H₂ consumption as in the former case of direct methanol synthesis, whereas an increase in the ratio would be a sign of a gradual CO₂ shortage by RWGS. In case methanol is a secondary product obtained from the subsequent hydrogenation of CO, as a net, the ratio is expected to decrease as an equivalent amount of H₂ is required whichever the CO_x ($x = 1$ or 2) is the carbon source in the methanol. The initial slight decrease in the ratio at P1-P2 at 180 °C implies a direct methanol synthesis reaction. Then at P2-P3, the ratio increases, which is indicative of RWGS. However, as discussed above, this is most likely due to the decompositions of methanol since such drastic selectivity change is unlikely at the low CO₂ conversion level. The increase in the ratio is therefore attributed to methanol decompositions, which is fully consistent with the observation and the previous results at 180 °C (Figure 3.2). In this Raman study, however, the ratio did not increase further as expected from the results in Figure 3.2. This may be due to the higher space velocity of this Raman study compared to the study by GC and the consequent less pronounced change in the ratio from less prominent methanol decompositions.

At 260 °C there was a clear initial increase of the ratio and then a decrease towards the outlet (Figure 3.3). The increasing ratio indicates the increase in the amount of CO by RWGS in the reactor and then the

subsequent decrease indicates the increase in the amount of methanol, no matter which reaction paths (**Eqn. 3.1** vs. **Eqn. 3.3**) are active. This profile is in full accordance with the results presented in **Figure 3.2** obtained in a comparable reaction condition where initially CO was produced and then CO was hydrogenated to methanol.

The sharp drop in the ratio at 260 °C coincided with the observation of condensation as liquid droplets at the rear end of the packed bed at P4 (**Figure S3.8**). As discussed above, the condensation is attributed to enhanced methanol synthesis via CO or CO₂, by *in situ* separation of the less volatile components, namely water, and methanol. Indeed, upon focusing the Raman laser spot on the condensed phase, a more intense methanol peak was observed, and the H₂/CO₂ ratio dropped to further lower values, suggesting the higher miscibility of CO₂ than H₂ in the condensed phase. According to the thermodynamic expectations at H₂/CO₂ = 3 (**Figure S3.4**), liquid phase condensation is not expected at 184 bar, 260 °C.

Lastly, IR thermography was used to measure the temperature of the catalyst bed under the reaction in order to validate the sequential nature of the methanol formation (RWGS and CO hydrogenation to methanol) from the endo-/exo-thermicity of the reactions (**Eqn. 3.1-3.3**). The reaction was performed at the stoichiometric ratio at 184 bar in a sapphire reactor similar to the Raman study without separating the catalyst bed, as shown in **Figure 3.4a**. At 180 °C, the IR signal, as well as CO₂ conversion, were too low to detect changes in the temperature of the catalyst bed. Thus, the experiments were performed at 260 and 340 °C. To detect subtle differences in the temperature of the catalyst bed, the thermogram showing a temperature distribution is obtained by the subtraction of thermograms during reaction and calibration, as shown in **Figure S3.9**.

The differential IR thermogram (**Figure 3.4b**) displays an exothermic region of the catalyst bed during the reaction. The differential temperature profiles (**Figure 3.4c**) are calculated from the radial temperature average along the catalyst bed. Evidently, the temperature profile at 340 °C is spatially varying. A relatively colder region located close to the front of the catalyst bed at 340 °C and subsequent temperature increase (then decrease) along the flow direction indicate endothermicity of RWGS near the fluid inlet and then methanol is formed. Such a temperature variation along the catalyst bed is barely observable at 260 °C (**Figure S3.10**), indicating that RWGS and CO hydrogenation likely occur in close proximity and cause overlapping of the two regions. The results at two different temperatures are in line with the methanol and CO selectivity profiles and the reaction mechanisms suggested above.

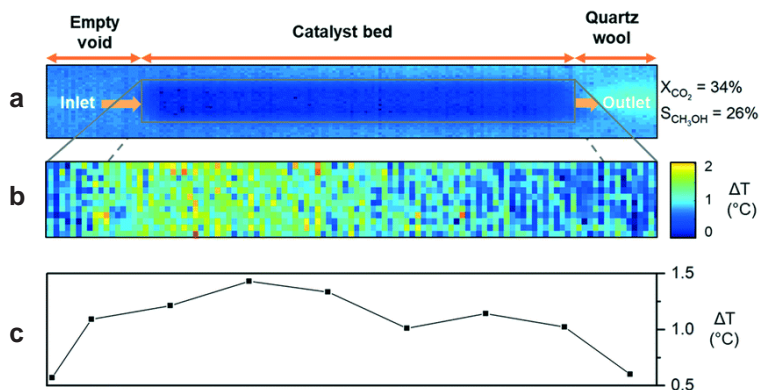


Figure 3.4 **a** IR thermogram of catalyst bed at room temperature, **b** subtracted IR thermogram at the reaction temperature and **c** temperature deviation (ΔT) profile along the catalyst bed during CO_2 hydrogenation to methanol over the commercial $\text{Cu/ZnO/Al}_2\text{O}_3$ catalyst. $\text{H}_2/\text{CO}_2 = 3$, $T = 340^\circ\text{C}$, $P = 184\text{ bar}$, and $\text{GHSV} = 80000\text{ h}^{-1}$.

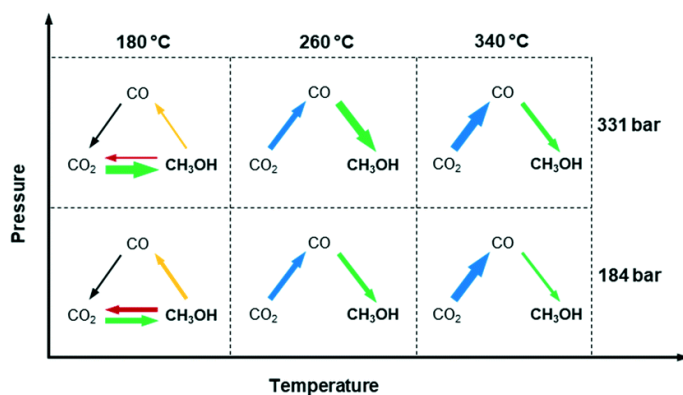


Figure 3.5 Major reaction pathways in high-pressure CO_2 hydrogenation over $\text{Cu/ZnO/Al}_2\text{O}_3$ catalyst at 180°C , 260°C , and 340°C at 184 and 331 bar . The width of the arrow shows the amount of one species' transformation to others.

3.4 Conclusion

In conclusion, the effects of temperature and pressure on reaction pathways were clarified by the space-resolved methodologies under *operando* conditions. The temperature has a significant influence on the dominant reaction pathways of methanol synthesis, as summarized in **Figure 3.5**. It is confirmed that methanol is produced via direct CO₂ hydrogenation at 180 °C, and via RWGS and CO hydrogenation at 260-340 °C. This could be explained by the limited RWGS activity at 180 °C, and more dominant RWGS activity as temperature increases. Moreover, there is a sign that methanol could possibly decompose or be steam reformed after formation, which is effectively suppressed by increasing pressure. Although pressure seems to have no influence on the reaction pathways, it greatly enhances methanol selectivity by inducing *in situ* condensation. This work demonstrates how spatially resolved *operando* study can be performed at high-pressure conditions to gain insights into the reaction mechanisms that have practical implications of potential advantages of multicomponent catalysts (i.e., selective in CO or CO₂ to methanol) in a reactor.

3.5 References

- 1 A. Goeppert, M. Czaun, J.-P. Jones, G. K. Surya Prakash and G. A. Olah, *Chem. Soc. Rev.*, 2014, 43, 7995–8048.
- 2 A. Álvarez, A. Bansode, A. Urakawa, A. V. Bavykina, T. A. Wezendonk, M. Makkee, J. Gascon and F. Kapteijn, *Chem. Rev.*, 2017, 117, 9804–9838.
- 3 G. A. Olah, *Angew. Chem., Int. Ed.*, 2013, 52, 104–107.
- 4 G. A. Olah, A. Goeppert and G. K. S. Prakash, *Beyond Oil and Gas: The Methanol Economy*, Wiley, 2009, vol. 44.
- 5 V. N. Ipatieff and G. S. Monroe, *J. Am. Chem. Soc.*, 1945, 67, 2168–2171.
- 6 K. Klier, *Adv. Catal.*, 1982, 31, 243–313.
- 7 K. Klier, V. Chatikavanij, R. G. Herman and G. W. Simmons, *J. Catal.*, 1982, 74, 343–360.
- 8 G. Liu, D. Willcox, M. Garland, and H. H. Kung, *J. Catal.*, 1985, 96, 251–260.
- 9 G. C. Chinchin, P. J. Denny, D. G. Parker, M. S. Spencer, and D. A. Whan, *Appl. Catal.*, 1987, 30, 333–338.
- 10 M. Sahibzada, I. S. Metcalfe and D. Chadwick, *J. Catal.*, 1998, 174, 111–118.
- 11 C. V. Ovesen, B. S. Clausen, J. Schiøtz, P. Stoltze, H. Topsøe and J. K. Nørskov, *J. Catal.*, 1997, 168, 133–142.
- 12 Y. Yang, J. Evans, J. A. Rodriguez, M. G. White and P. Liu, *Phys. Chem. Chem. Phys.*, 2010, 12, 9909.
- 13 L. C. Grabow and M. Mavrikakis, *ACS Catal.*, 2011, 1, 365–384.
- 14 Y. Yang, C. A. Mims, D. H. Mei, C. H. F. Peden, and C. T. Campbell, *J. Catal.*, 2013, 298, 10–17.
- 15 F. Studt, M. Behrens, E. L. Kunkes, N. Thomas, S. Zander, A. Tarasov, J. Schumann, E. Frei, J. B. Varley, F. Abild-Pedersen, J. K. Nørskov and R. Schlögl, *ChemCatChem*, 2015, 7, 1105–1111.
- 16 W. J. Van Rensburg, M. A. Petersen, M. S. Datt, J. A. Van Den Berg and P. Van Helden, *Catal. Lett.*, 2015, 145, 559–568.
- 17 E. L. Kunkes, F. Studt, F. Abild-Pedersen, R. Schlögl and M. Behrens, *J. Catal.*, 2015, 328, 43–48.
- 18 A. Karelovic, G. Galdames, J. C. Medina, C. Yévenes, Y. Barra and R. Jiménez, *J. Catal.*, 2019, 369, 415–426.
- 19 X.-M. Liu, G. Q. Lu, Z.-F. Yan and J. Beltramini, *Ind. Eng. Chem. Res.*, 2003, 42, 6518–6530.
- 20 R. Gaikwad, A. Bansode and A. Urakawa, *J. Catal.*, 2016, 343, 127–132.
- 21 A. Bansode and A. Urakawa, *J. Catal.*, 2014, 309, 66–70.
- 22 S. K. Wilkinson, L. G. A. Van De Water, B. Miller, M. J. H. Simmons, E. H. Stitt, and M. J. Watson, *J. Catal.*, 2016, 337, 208–220.
- 23 Y. Choi and H. G. Stenger, *Appl. Catal., B*, 2002, 38, 259–269.
- 24 N. Boukis, V. Diem, W. Habicht and E. Dinjus, *Ind. Eng. Chem. Res.*, 2003, 42, 728–735.
- 25 J. T. Sun, I. S. Metcalfe and M. Sahibzada, *Ind. Eng. Chem. Res.*, 1999, 38, 3868–3872.
- 26 J. G. van Bennekom, R. H. Venderbosch, J. G. M. Winkelman, E. Wilbers, D. Assink, K. P. J. Lemmens and H. J. Heeres, *Chem. Eng. Sci.*, 2013, 87, 204–208.

Supporting information

Chapter 3

Experimental

Chemicals

A commercial methanol synthesis catalyst (Cu/ZnO/Al₂O₃, Product No.: 45776) was purchased from Alfa Aesar. A CO₂/H₂/Ar (23/69/8%) gas mixture cylinder was purchased from Abelló Linde (Spain). A sapphire capillary reactor with outer diameter = 1.5 mm, inner diameter = 1 mm, and length = 100 mm was purchased from Saint-Gobain Crystals, USA.

High-pressure reactor setup

The details of a high-pressure reactor setup are explained elsewhere.¹ High-pressure CO₂ was dispensed from a syringe pump and H₂ was pressurized and controlled by a gas booster and a mass flow controller, respectively. The total pressure of the reactor was controlled by a back-pressure regulator. The commercial Cu/ZnO/Al₂O₃ catalyst was packed in a specific type of reactor explained later. Two pressure indicators were used to measure the pressure drop over the catalyst bed, which was negligible in all experiments (<2 bar). Prior to running the reaction, the catalyst was reduced with 90% H₂/He at 330 °C for 30 min then cooled down to room temperature. The reactor was pressurized by the feed gas to the desired pressure before started heating to the reaction temperature.

Experimental setup for space-resolved gas analysis using SS reactor

The space-resolved gas analysis was performed in a high-pressure setup explained elsewhere.² The commercial Cu/ZnO/Al₂O₃ catalyst with a particle size of 100-300 μm was packed in a 1/8" SS tube reactor. As shown in

Figure 3.1b, the catalyst was separated into three catalyst beds, B1, B2, and B3, with 60 mg each. Each catalyst bed was supported on a 10 μm frit to avoid moving due to high-pressure flow. The space before/between each catalyst bed (P1, P2, P3, and P4) was created for gas sampling purposes and a sampling rate of 2 mL min^{-1} was controlled by a needle valve. The impact of gas sampling on catalytic performance was minimized by meticulous valve opening to maintain overall pressure and flow pattern. The gas composition from four different positions was analyzed by online GC and MS.

Experimental setup for *operando* Raman spectroscopy

The sapphire capillary reactor setup for *operando* Raman spectroscopy is shown in **Figure S3.1**. The most crucial part for operating at a pressure of up to 200 bar is a leak-tight sealing between the sapphire capillary and SS VICI fitting. For this purpose, the polyimide film was coated at the end of the capillary to provide adhesion between graphite-reinforced polyimide ferrule and the sapphire surface. The commercial $\text{Cu}/\text{ZnO}/\text{Al}_2\text{O}_3$ catalyst with a particle size of 63-80 μm was packed in the same manner as the previous setup. As shown in **Figure S3.2**, three catalyst beds (5 mg and 5 mm each) were supported on quartz wool and SS rods (OD 0.6 mm), and separated with 10-12 mm void sections for gas analysis purposes. The gas products and intermediates in the void sections were analyzed by a Raman microscope (Renishaw, InVia, $\lambda = 532 \text{ nm}$) in backscattering mode, as reported elsewhere.³ A fiber-coupled Raman probe was mounted and motorized remotely along the axial direction of the reactor by a linear actuator. The probe was focused on the P1-P4 positions shown in **Figure S3.2** to analyze the unreacted feed and the product after each catalyst bed. The phase condensation in void sections was inspected simultaneously by a white-light camera. Eventually, the outlet composition was analyzed by an online GC.

The H_2/CO_2 feed ratio was decreased from the usual stoichiometric ratio of 3 to 2.5 in order to improve the signal-to-baseline ratio and the quality of the Raman spectra as a result of increasing density. An increase in density lessened the light transmittance through the transparent reactor and improved the light-collection efficiency. However, the decrease in signal intensity due to complicated light-matter interactions (e.g., refraction and reflection) still existed.

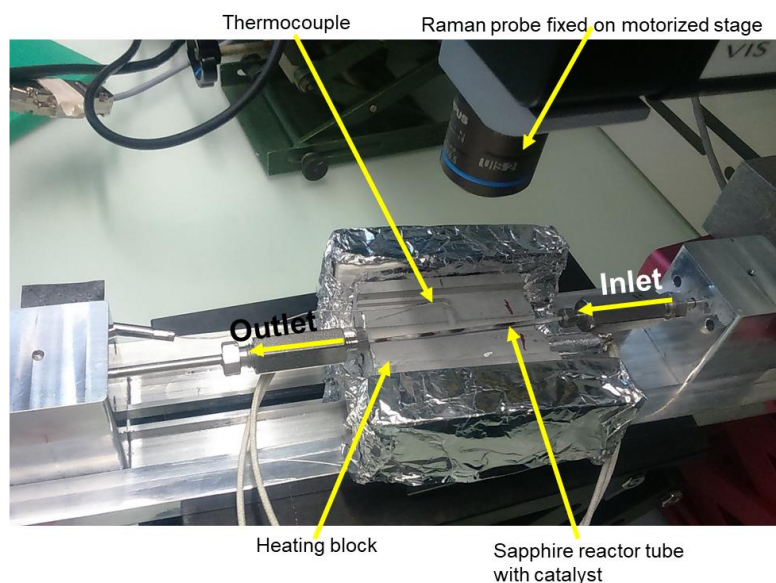


Figure S3.1 High-pressure reactor setup for operando Raman spectroscopy.

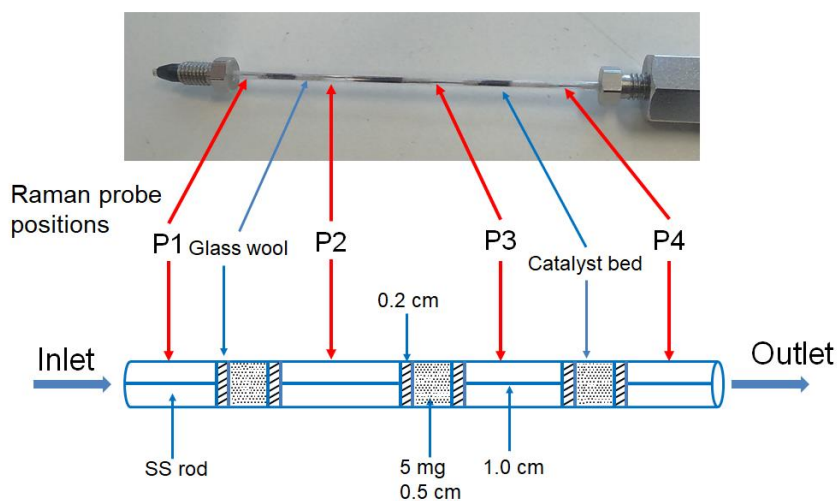


Figure S3.2 **a** The picture of the sapphire capillary reactor packed with the catalyst, **b** Schematic of the catalyst bed configuration with multiple catalyst beds and void sections. P1-P4 denote the positions analyzed by Raman microscopy.

Characterization of the spent catalysts by XRD

XRD patterns were recorded on Bruker AXS D8 advance diffractometer equipped with a Cu tube, a Ge (111) incident beam monochromator (1.54184 Å), and Vantec-1 PSD operated in transmission mode. Signal was recorded in 20-80° 2θ with a step size of 0.02° and a counting time of 4 seconds per step. Crystal phases were confirmed using Bruker X'Pert Pro software and the JCPDS database. The spent catalyst beds extracted from P1-P4 were analyzed by XRD, as shown in **Figure S3.3**. The bulk copper oxidation state was found to remain in metallic copper (Cu⁰). However, the crystallite size of Cu (111) has increased since the presence of water in the fluid phase can promote Cu crystallite growth.⁴ The ZnO phase has also been transformed to ZnCO₃ at the bed positions towards the outlet due to the production of water that likely induces the formation of carbonic acid (H₂CO₃) by contacting high-pressure CO₂. However, the presence of ZnCO₃ in the catalyst does not seem to pose any negative influence on the activity of the Cu-based catalyst, and in turn, either ZnO or ZnCO₃ has probably the coordinating assistance to the catalytic activity of the Cu-based catalyst.⁵

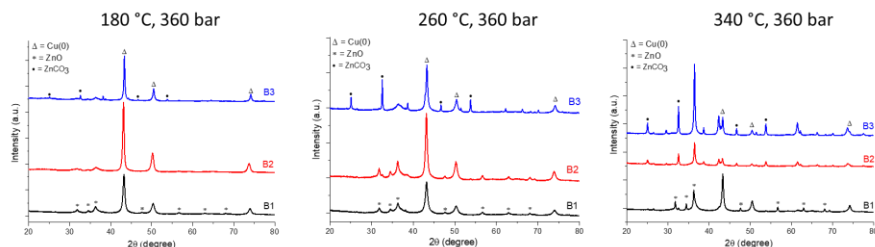


Figure S3.3 PXR analysis of the catalyst beds B1, B2, and B3 placed between P1-P2, P2-P3, and P3-P4 respectively. The reaction was performed at 180, 260, and 340 °C at 360 bar.

Table S3.1 The average crystallite size of Cu (111) was calculated from the Scherer equation of the spent catalyst under CO₂ hydrogenation at various temperatures and 360 bar.

Catalyst bed	Average crystallite size of Cu (111) (nm)		
	180 °C	260 °C	340 °C
B1	14	12	18
B2	18	15	21
B3	25	19	27

Thermodynamic calculations

In order to facilitate the interpretation and discussion of the results, the thermodynamic equilibrium of CO₂ hydrogenation was calculated by Aspen HYSYS V8.6 simulation software using the Soave Redlich Kwong (SRK) equation of state (EOS). The binary interaction parameters for CO, CO₂, H₂, methanol, and water were modified according to van Bennekom et al.^{6,7} The equilibrium CO₂ conversion and product selectivity from CO₂ hydrogenation and RWGS at the temperature range of 150-400 °C, and pressure of 184 and 331 bar were shown in **Figure S3.3** and **S3.4**, respectively.

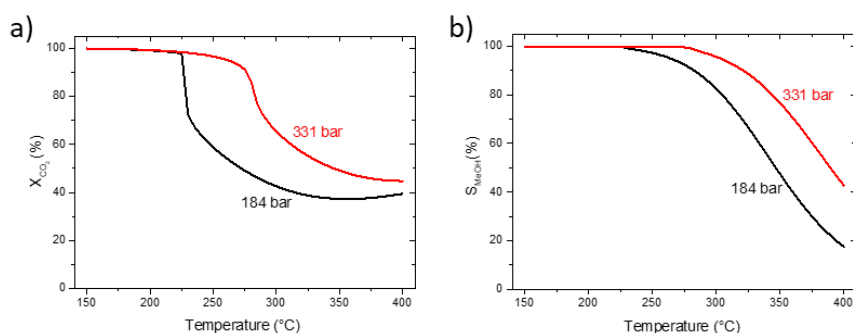


Figure S3.4 Thermodynamic equilibrium of CO₂ conversion and methanol selectivity (the rest is CO) at H₂/CO₂ = 3 at P = 184 and 331 bar. The steep increase in CO₂ conversion shows the phase transition due to liquid phase condensation at lower temperatures.

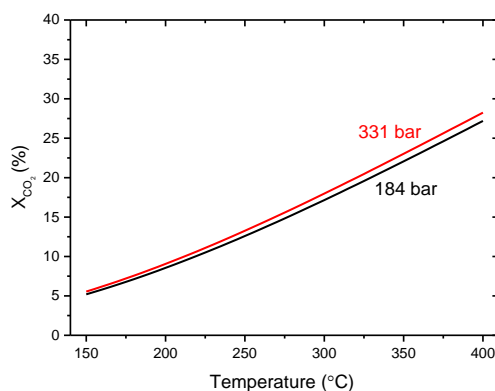


Figure S3.5 Thermodynamic equilibrium of CO₂ conversion from RWGS reaction at H₂/CO₂ = 3, T = 150-400 °C, and P = 184 and 331 bar.

Raman spectroscopy for quantitative analysis

A typical Raman spectrum of the reaction stream obtained at 260 °C at the reactor outlet (P4) is shown in **Figure S3.5**. The rotational transitions of H_2 (355, 587, 812, 1033, 1246, 1447 cm^{-1}) and the Fermi dyad of CO_2 and satellite bands (1265, 1286, 1387, 1408 cm^{-1}) are clearly identified.⁸ Due to a small Raman scattering cross-section, the characteristic feature of CO at 2140 cm^{-1} and the features of methanol at 2840 and 2945 cm^{-1} are too weak for quantitative analysis. Therefore, the most intense bands of H_2 at 587 cm^{-1} , and CO_2 , at 1387 cm^{-1} are considered for quantitative composition analysis. All band areas were normalized with respect to the most intense band of all (H_2 at 587 cm^{-1}) to correct for the difference in focal depth. The initial area ratio at P1 is scaled to 2.5 to match the molar ratio of unreacted feed confirmed by online GC analysis at room temperature.

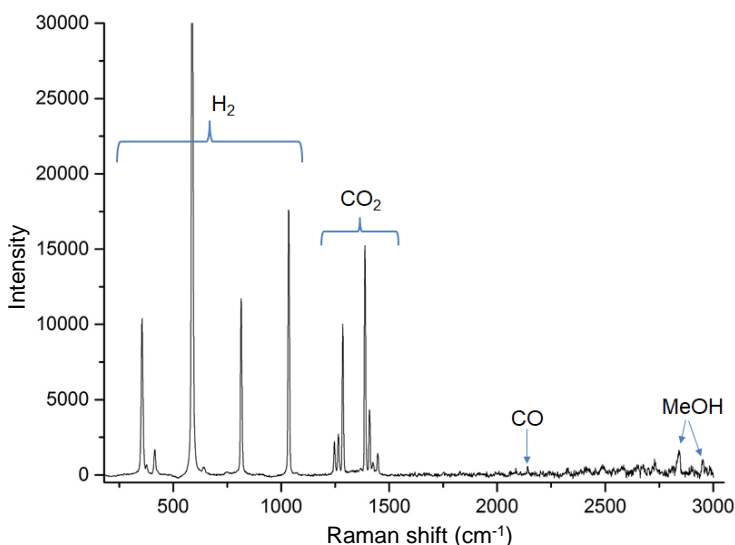


Figure S3.6 Representative Raman spectrum at $T = 260\text{ }^{\circ}\text{C}$, 184 bar at P4.

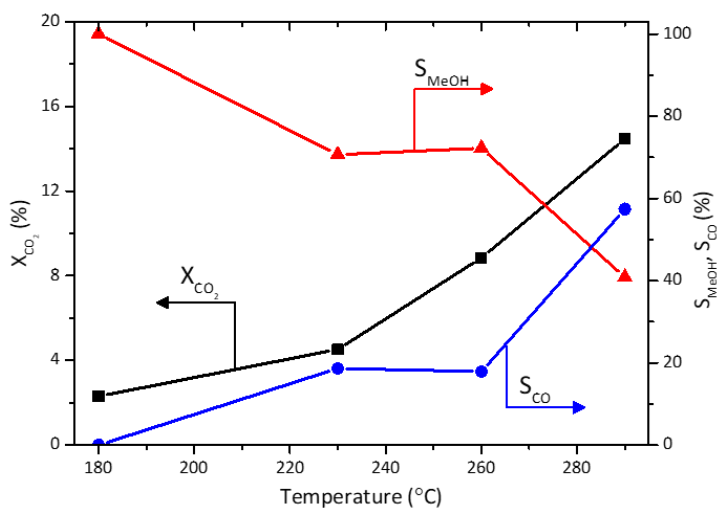


Figure S3.7 CO_2 conversion (X_{CO_2}), selectivity of methanol and CO (S_{MeOH} , S_{CO} respectively) observed in CO_2 hydrogenation over the commercial Cu/ZnO/ Al_2O_3 catalyst using sapphire reactor tube at $T = 180, 230, 260$, and $290\text{ }^\circ\text{C}$, $P = 184\text{ bar}$, $H_2/CO_2 = 3$, and at P1-P4 at 80000 h^{-1} .

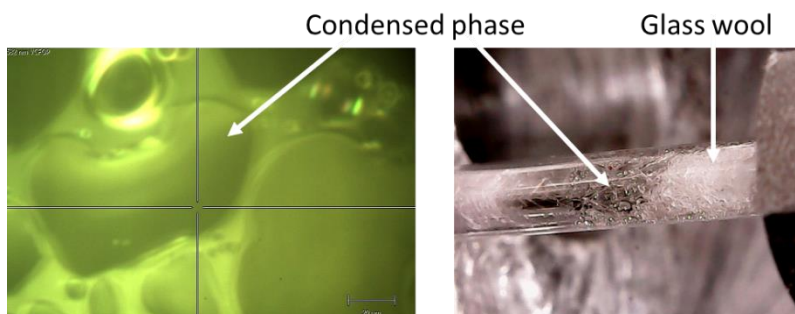


Figure S3.8 Phase condensation at the P4 position during CO_2 hydrogenation to methanol over Cu/ZnO/ Al_2O_3 catalysts. $H_2/CO_2 = 3$, $T = 260\text{ }^\circ\text{C}$, $P = 184\text{ bar}$, and GHSV = 80000 h^{-1} .

Reactor setup for thermal imaging using IR camera

The CO₂ hydrogenation at stoichiometric ratio ($H_2/CO_2 = 3$) was carried in a sapphire capillary reactor as previously mentioned in the *operando* Raman spectroscopy. In this setup, however, a heat gun (Bosch, GHG 660) was used to control the reaction temperature to minimize infrared interference. The reactor was covered with firebricks to minimize heat loss and light disturbance. The thermal images during the reaction were taken from the top of the reactor by an IR camera (Sensors Unlimited, Micro-SWIR 320CSX). The IR camera took 1000 images at 60 frames per second before averaging into a single image shown in **Figure S3.9**. After the reaction, the thermal image under H₂ flow at 1 atm was used for temperature calibration. Finally, the thermal image taken during the reaction was subtracted with calibration to investigate the temperature change contributed by exothermic and endothermic reactions.

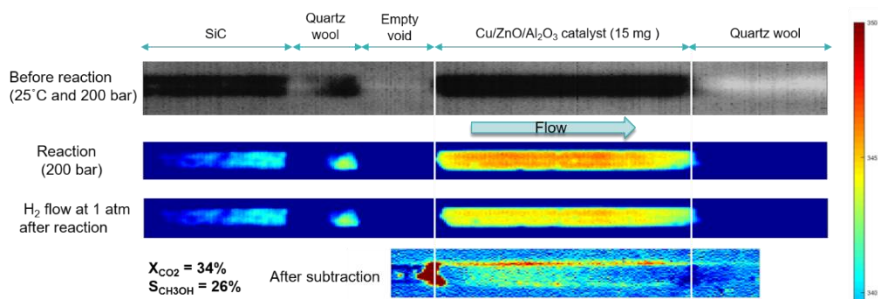


Figure S3.9 Thermal images during CO₂ hydrogenation to methanol reaction over the commercial Cu/ZnO/Al₂O₃ catalyst. $H_2/CO_2 = 3$, $T = 340\text{ }^{\circ}\text{C}$, $P = 184\text{ bar}$, and GHSV = 80000 h⁻¹.

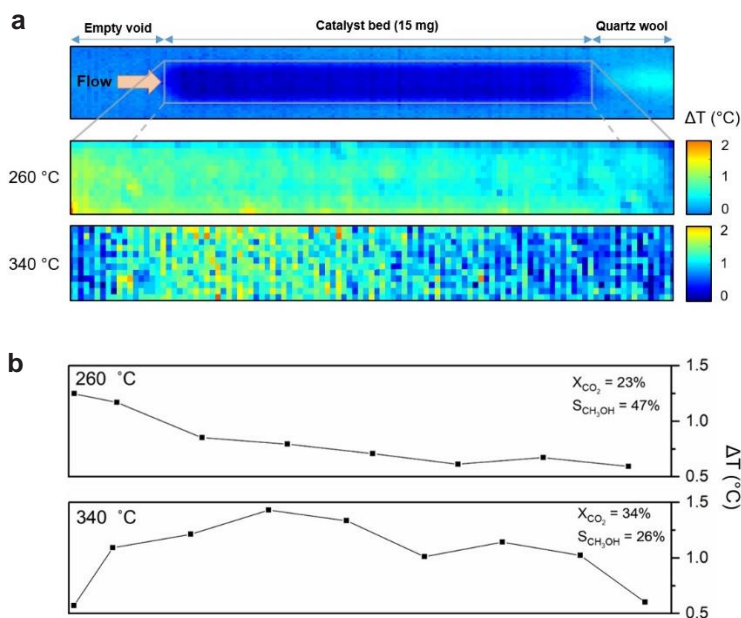


Figure S3.10 **a** IR thermogram along the catalyst bed and **b** temperature deviation (ΔT) profile and during CO_2 hydrogenation to methanol over the commercial $Cu/ZnO/Al_2O_3$ catalyst. $H_2/CO_2 = 3$, $T = 260$ and 340 °C, $P = 184$ bar, and $GHSV = 80000$ h^{-1} .

References

- 1 A. Bansode and A. Urakawa, *J. Catal.*, 2014, 309, 66–70.
- 2 R. Gaikwad, A. Bansode and A. Urakawa, *J. Catal.*, 2016, 343, 127–132.
- 3 H. Reymond and P. Rudolf von Rohr, *Rev. Sci. Instrum.*, 2017, 88, 114103.
- 4 J. T. Sun, I. S. Metcalfe and M. Sahibzada, *Ind. Eng. Chem. Res.*, 1999, 38, 3868–3872.
- 5 S. Lee, B. G. Lee and C. J. Kulik, *Fuel Sci. Technol. Int.*, 1991, 9, 977–998.
- 6 J. G. van Bennekom, J. G. M. Winkelman, R. H. Venderbosch, S. D. G. B. Nieland and H. J. Heeres, *Ind. Eng. Chem. Res.*, 2012, 51, 12233–12243.
- 7 J. G. van Bennekom, R. H. Venderbosch, J. G. M. Winkelman, E. Wilbers, D. Assink, K. P. J. Lemmens and H. J. Heeres, *Chem. Eng. Sci.*, 2013, 87, 204–208.
- 8 H. Reymond, V. Amado-Blanco, A. Lauper, P. Rudolf von Rohr and P. Rudolf von Rohr, *ChemSusChem*, 2017, 10, 1166–1174.

Decisive roles of peripheral promoters

in promoting methanol selectivity of CO_2 hydrogenation over Cu-based catalysts



Abstract

The nature of the active site of the industrial Cu/ZnO/Al₂O₃ catalysts is still under debate despite 50 years after the discovery. The structures of active Cu-ZnO synergy were prevalently reported; however, their roles in the mechanistic aspects are still ambiguous. Moreover, interfacial metal sites such as Ga and In at the periphery of Cu nanoparticles can also play a similar role in boosting methanol selectivity over Cu-based catalysts. In this study, *operando* transient DRIFTS-SSITKA was employed to elucidate the roles of cationic M sites (Zn, Ga, and In) on Cu-M/SiO₂ catalyst prepared via surface organometallic chemistry (SOMC). The M⁺ sites at the periphery of Cu particles can stabilize formate species spillovered from Cu for faster hydrogenation. Formate over Zn is more reactive, while the formate spillover toward Ga is more facile. Rapid formate spillover can improve methanol selectivity by suppressing formate decomposition to CO over Cu. This highlights the essence of interfacial sites of Cu-M in determining selectivity and provides important insight towards rational design of nano-structured catalysts for selective CO₂-to-methanol.



This chapter is based on the following publication:
Phongprueksathat, N., Docherty, S.R., Noh, G., Copéret, C. & Urakawa, A.
In preparation

4.1 Introduction

One of the strategies to reduce greenhouse gas emissions and alleviate the impacts of global warming is CO₂ conversion with green H₂ (e.g. produced through water electrolysis sourced by renewable energies) into methanol, which is positioned as the most versatile chemical feedstock and energy carrier toward a fossil-fuel-free economy, known as the “methanol economy”.¹

CO₂ hydrogenation in the major presence of CO to CH₃OH is a well-established technology and commercially employed Cu/ZnO/Al₂O₃ catalyst.² However, the origin of the high performance of the industrial Cu/ZnO/Al₂O₃ catalyst for methanol synthesis is still ambiguous since the nature of the active sites and the mechanism are being highly debated. Moreover, Cu/ZnO/Al₂O₃ catalyst is dynamic and continuously changes structure.³ During reductive catalyst activation, Cu-Zn alloy could be formed via migration of ZnO_x onto Cu⁰.⁴ Under CO₂ hydrogenation, CO₂ oxidizes Zn⁰ into Zn^{δ+} species at the defective Cu⁰ surface leading to Cu⁰ particles partially covered with ZnO_x.⁵ This also increases the activity of the catalyst due to the creation of adsorption sites for oxygen-bound intermediates. Further migration of Zn forms a graphitic-like ZnO_x layer,⁶ and subsequently forms a more crystalline and stable thick ZnO layer on Cu⁰, which is reported to facilitate methanol formation via formate intermediates.⁷ The reduction of CuO and the ripening/re-oxidation of ZnO upon CO₂ hydrogenation are the drastic events that determine Cu-ZnO synergy.⁸

The pressure gap toward industrial conditions has recently been bridged in terms of catalyst structures.⁹ However, the material gap remains an impediment for mechanistic studies over industrial Cu/ZnO/Al₂O₃ catalysts due to the heterogeneity of active site structures, requiring model but relevant catalysts.¹⁰ Such model Cu-based catalysts with molecularly-define single site promoters can be prepared using surface organometallic chemistry (SOMC).¹¹ The interface between copper particles and ZrO₂ support (e.g. Zr⁴⁺ sites) plays roles in adsorbing and converting formate intermediate to methoxy and methanol, which is absent over Cu/SiO₂.¹² The structural and bulk properties of ZrO₂, e.g. oxygen vacancies, apart from Zr⁴⁺ at the periphery of Cu particles are not responsible for CH₃OH selectivity.¹³ Moreover, the Lewis acid nature of isolated Ti⁴⁺ sites over Cu-Ti/SiO₂ plays an identical promotional role to Zr⁴⁺ sites with higher methanol formation rates.¹⁴ Interestingly, the presence of isolated Lewis acidic Zr⁴⁺ and Ti⁴⁺ sites is sufficient to promote CH₃OH activity/selectivity by forming the same formate/methoxy intermediate species. In the case of Cu-Zn/SiO₂, the Cu-Zn_x alloy is also partially converted into Cu⁰ and Zn²⁺ under reaction conditions.¹⁵

The similar alloying/dealloying behavior of CuGa and PdGa over Cu-Ga/SiO₂ and Pd-Ga/SiO₂, respectively, is consistent with the higher methanol selectivity.^{16,17} This is contrast to Cu-Ti/SiO₂ and Cu-Zr/SiO₂ that remained as isolated Ti⁴⁺ and Zr⁴⁺ sites during activation of Cu. Notably, the Cu-Ga/SiO₂ and Cu-Zn/SiO₂ displayed CH₃OH selectivity up to 90% and 86%,^{15,16} respectively, higher than the Cu-Ti/SiO₂ (85%),¹⁴ benchmark Cu/ZnO/Al₂O₃ (79%),¹⁵ Pd-Ga/SiO₂ (78%),¹⁷ Cu-Zr/SiO₂ (77%),¹⁸ and Cu/SiO₂ (48%).¹²

The formate intermediates were unobservable *ex situ* with IR or solid-state NMR over Cu-Zn/SiO₂, Cu-Ga/SiO₂, and Pd-Ga/SiO₂ in contrast to Cu-Ti/SiO₂, and Cu-Zr/SiO₂. However, *operando* IR over Pd-Ga/SiO₂ confirms the presence of formate intermediate under reaction conditions in contrast to *ex situ* experiments. Therefore, in this study, we aim to employ *operando* IR to elucidate the nature of the active and selective sites for CO₂ hydrogenation to methanol over the copper-based catalysts with single-site promoters (Cu-M/SiO₂, M = Zn, Ga, and In) prepared precisely via SOMC.^{15,19} The example of Cu-Zn/SiO₂ prepared by such a technique is illustrated in **Figure 4.1**. The common intermediates during the reaction were identified by *operando* DRIFTS, while the roles of the promoter were shed light by isotopic transient experiment (SSITKA).

4.2 Results and discussion

4.2.1 Temporal evolution of surface species during CO₂ hydrogenation

The surface intermediate species formed during the CO₂ hydrogenation over Cu/SiO₂, Cu-In/SiO₂, Cu-Ga/SiO₂, and Cu-Zn/SiO₂ catalysts were investigated by *operando* DRIFTS at the relevant catalytic conditions (230 °C, 10-20 bar, **Figure 4.1b**) after the pretreatment in H₂ (300 °C, 2 h) followed by purging with He. The evolution of surface species was monitored after switching to the H₂/CO₂ = 3 gas flow. The identification and assignment of each IR band. **Table S4.1**. During the transient state, bidentate formate on Cu ($\kappa^2\text{-HCOO}^*(\text{Cu})$) at 2856 and 2931 cm⁻¹ was the first and common surface species detected over all catalysts, which appeared simultaneously with bidentate formate on ZnO ($\kappa^2\text{-HCOO}^*(\text{Zn}^{2+})$) over Cu-Zn/SiO₂ (**Figure 4.1a**). However, $\kappa^2\text{-HCOO}^*(\text{on Ga}^{3+} \text{ or In}^{3+})$ was not observed during CO₂ hydrogenation. The time-resolved *operando* DRIFT spectra of Cu/SiO₂, Cu-In/SiO₂, and Cu-Ga/SiO₂ catalysts are similar (**Figure S4.4**). After reaching 90 mins, methoxy on SiO₂ CH₃O*(SiO₂) at 2858 cm⁻¹ and surface-bound methanol (CH₃OH*) at 2981 cm⁻¹ built up slowly on the catalysts (**Figure 4.2**). This resulted from the adsorption of CH₃OH product over Si-OH as indicated by the delay in mass spectrometry response of CH₃OH from

H₂O (**Figure 4.1b**). It should be noted that carbonyl species (CO*) were not detected over all catalysts.

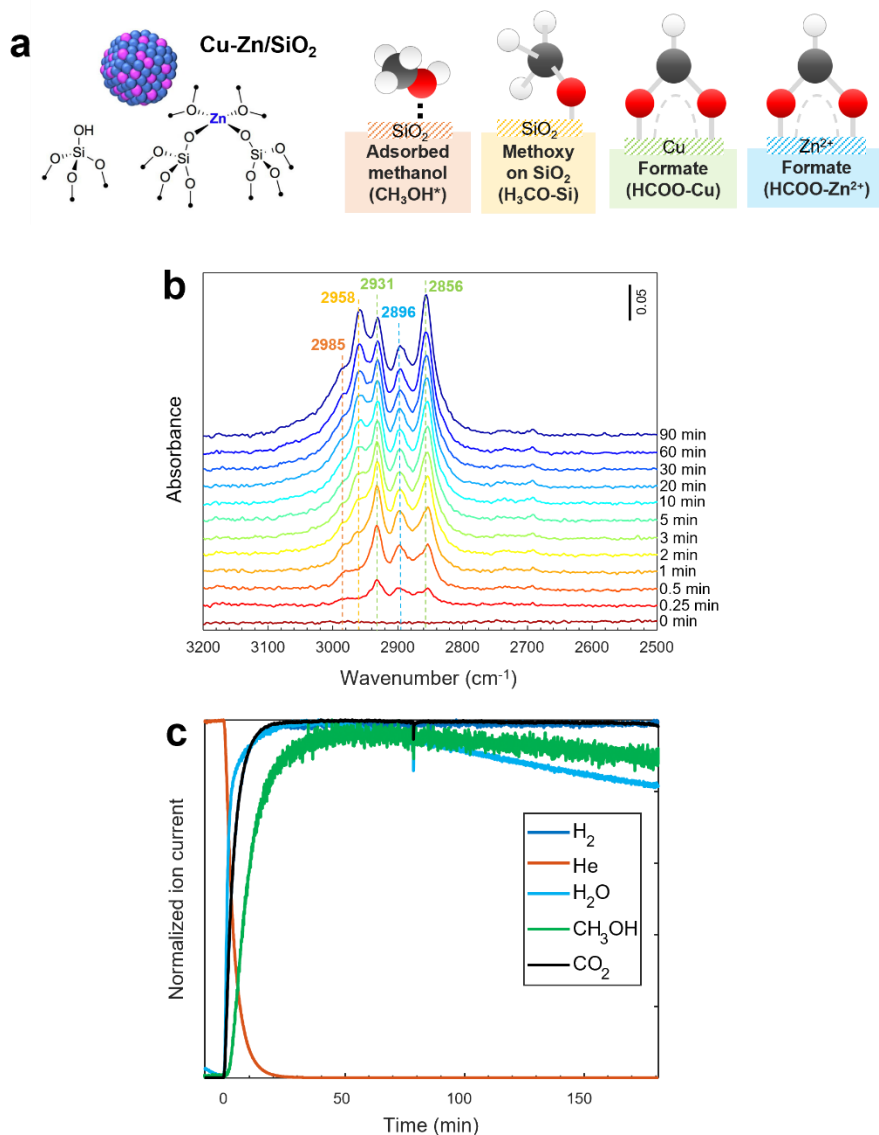


Figure 4.1 **a** Structure of Cu-Zn/SiO₂ prepared via SOMC reported elsewhere,¹⁵ and structures of relevant surface species. **b** Time-resolved *operando* DRIFT spectra of the surface species formed during the CO₂ hydrogenation reaction over pre-reduced Cu-Zn/SiO₂ catalysts. **c** Corresponding normalized ion current signal obtained from mass spectrometry. Pretreatment was performed at 300 °C under 10 NmL min⁻¹ of H₂ for 2 h. Reaction conditions: ca. 10 mg catalyst, H₂/CO₂ = 3, T = 230 °C, P = 10 bar, and F_{total} = 10 NmL min⁻¹.

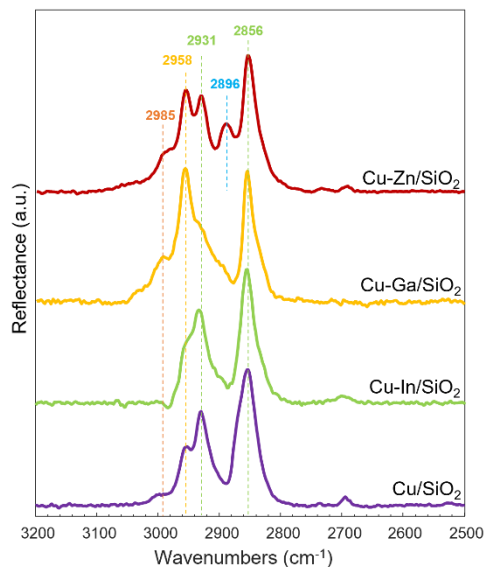


Figure 4.2 Operando DRIFT spectra of the surface species formed during the CO₂ hydrogenation reaction over Cu/SiO₂, Cu-In/SiO₂, Cu-Ga/SiO₂, and Cu-Zn/SiO₂ catalysts. Pretreatment was performed at 300 °C under 20 NmL min⁻¹ of H₂ for 2 h. Reaction conditions: ca. 10 mg catalyst, H₂/CO₂ = 3, T = 230 °C, P = 10 bar, F_{total} = 10 NmL min⁻¹, and TOS = 180 min.

4.2.2 Mechanistic insights from isotopic transient experiments

The isotopic transient switching can provide insights into active species without disturbing feed conditions (e.g., partial pressure of CO₂ and H₂). As shown in **Figure 4.3** after switching from H₂+CO₂ to D₂+CO₂ and vice versa, κ^2 -HCOO*(Cu) at 2931 and 2850 cm⁻¹ and κ^2 -HCOO*(Zn²⁺) at 2896 cm⁻¹ exchanged instantaneously to κ^2 -DCOO*(Cu) at 2167 cm⁻¹ and κ^2 -DCOO*(Zn²⁺) at 2181 cm⁻¹, while CH₃O*(SiO₂, 2958 and 2858 cm⁻¹) and CD₃O*(SiO₂, 2080 cm⁻¹) exchanged slowly. The separation of kinetically unique spectral features of the surface species during the SSITKA experiment can be obtained from the multivariate spectral analysis enabling blind-source separation (i.e., without references). Here, multivariate curve resolution (MCR) was used.^{20,21} As shown in **Figure 4.4**, MCR analysis of the time-resolved spectra shown in **Figure 4.3** yielded deconvoluted spectra of kinetically similar but distinct species. The kinetics of formation and hydrogenation of the κ^2 -HCOO* (Zn²⁺) were indistinguishable from κ^2 -HCOO* (Cu) with the time resolution of this study (10 sec). The fast decay

responses of surface $\kappa^2\text{-HCOO}^*$ (Cu and Zn^{2+}) and the inversely symmetrical response of $\kappa^2\text{-DCOO}^*$ indicate that they were easily hydrogenated to CH_3OH and not a spectator in CO_2 hydrogenation. The isotopic exchange of $\kappa^2\text{-HCOO}^*/\kappa^2\text{-DCOO}^*$ species is almost instantaneous (**Figure 4.4b**), suggesting that H_2/D_2 dissociative adsorption and formates formation were not affected by kinetic isotope effects (KIE) and not the rate-limiting step. On the other hand, prominent KIE was observed for $\text{CH}_3\text{OH}/\text{CD}_3\text{OD}$ formation after switching from H_2+CO_2 to D_2+CO_2 and vice versa (**Figure 4.4c**), which suggests the presence of KIE for both formate hydrogenation to CH_3OH and/or also for CH_3O^* activation for H addition/activation towards formation/desorption of CH_3OH . A closer look indicates that the latter seems to be affected more significantly by the CH_3OH formation/desorption rate, while there was a slight KIE for formate hydrogenation (**Figure S4.5**). Since the exchange of the surface CH_3O^* (and CH_3OH , **Figure 4.4b**) is linked to the formation rate more directly (**Figure 4.4c**), the desorption of CH_3OH seemed to be rate limiting during CO_2 hydrogenation.

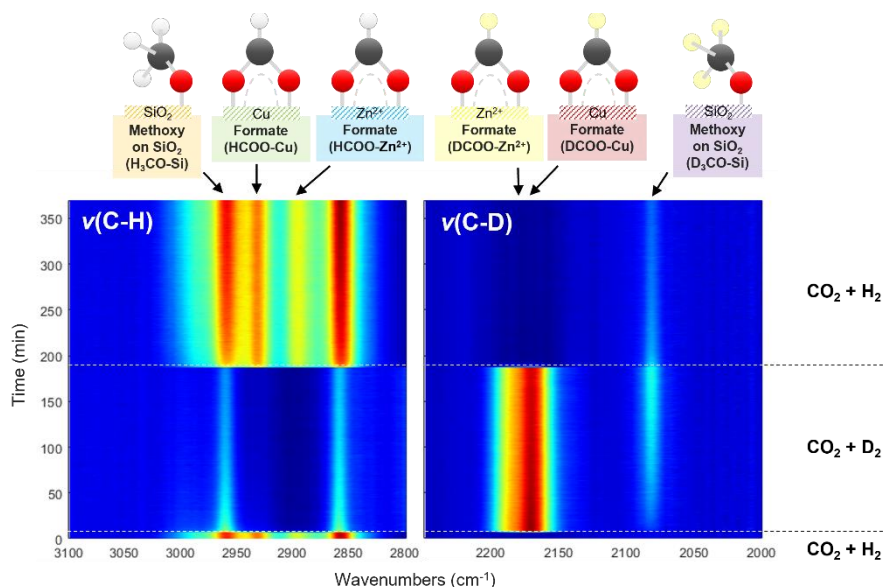


Figure 4.3 Transient responses of surface species and gas products during transient isotopic switching from CO_2+D_2 to CO_2+H_2 over Cu-Zn/ SiO_2 catalysts. Time-resolved DRIFT spectra of **a** $\nu(\text{C-H})$ region and **b** $\nu(\text{C-D})$ region. Reaction conditions: 10 mg catalyst, $\text{H}_2(\text{or } \text{D}_2)/\text{CO}_2 = 3$, $T = 230^\circ\text{C}$, $P = 10$ bar, $F_{\text{total}} = 10$ NmL min^{-1} .

The vibrational frequencies of the surface formates provide hints to understand the effects of the single site promoters in the vicinity of Cu nanoparticles. Introduction of the single site, namely Zn^{2+} , Ga^{3+} , or In^{3+} , to

Cu/SiO₂ weakens the C–O bond and strengthened the C–H bond of κ^2 -HCOO*, as summarized in **Figure 4.5a**. Lewis acid sites over transition metal oxides (M = YO_x, ScO_x, ZrO_x, TaO_x) on Cu-M/ γ -Al₂O₃ can similarly weaken the C–O bond while strengthening the C–H bond of κ^2 -HCOO* due to increasing electron-withdrawing character.²² Stronger Lewis acidity stabilizes HCOO* and may reduce apparent activation energy for CH₃OH formation. Similarly, the enhanced CH₃OH formation rate by Lewis acid sites on Cu-M/SiO₂ (M = TiO_x, ZrO_x, HfO_x, NbO_x, TaO_x) prepared by SOMC is likely originating from the stabilization of HCOO* and CH₃O* at the periphery of Cu nanoparticles.²³ The increased stability of HCOO* can suppress CO selectivity produced via HCOO* decomposition and promote CH₃OH selectivity.²⁴ However, over-stabilization of HCOO* due to strong Lewis acidic Al₂O₃ can promote further reaction with CH₃OH to HCOOCH₃ and subsequent decomposition to CO (and CH₃OH), thus promoting CO selectivity.²⁵

Figure 4.4 Transient responses of surface species and gas products during the steady-state isotopic switching from CO₂+D₂ to CO₂+H₂ over Cu-Zn/SiO₂ catalysts. **a** Components spectra obtained by MCR applied on the time-resolved DRIFT spectra. **b** Concentration profiles of the spectra of the corresponding components obtained by MCR. **c** Corresponding normalized ion current signal of isotope-labeled products. Reaction conditions: 10 mg catalyst, H₂(or D₂)/CO₂ = 3, T = 230 °C, P = 10 bar, F_{total} = 10 NmL min⁻¹.

bond by introducing promoters could in principle suppress $\kappa^2\text{-HCOO}^*$ decomposition while facilitating CH_3OH formation. Therefore, the major role of M^+ promoters is to destabilize C–O bond for faster hydrogenation.

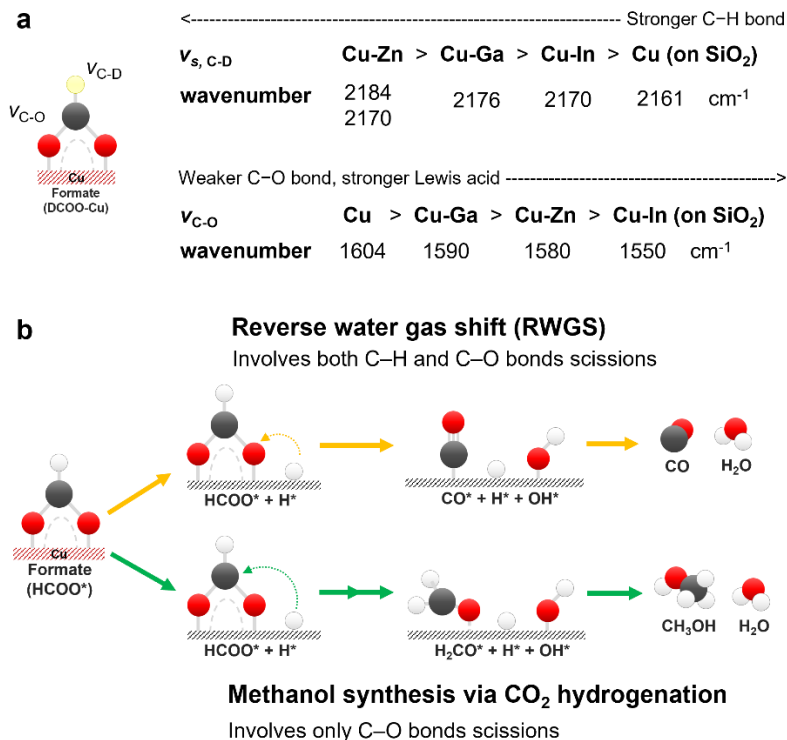


Figure 4.5 Mechanistic insight obtained from isotopic transient experiment. **a** wavenumber of $\nu(\text{C-D})$ and $\nu(\text{C-O})$ of DCOO^* species located on Cu/SiO_2 , Cu-Zn/SiO_2 , Cu-Ga/SiO_2 , and Cu-In/SiO_2 catalyst. **b** Proposed pathways for reverse water gas shift,²⁶ and CO_2 hydrogenation to CH_3OH over Cu .²⁷

Notably, Cu/SiO_2 , Cu-In/SiO_2 , and Cu-Ga/SiO_2 during the isotopic transient experiment showed a similar response of surface species and isotopic methanol products, suggesting the common reaction mechanism via formate hydrogenation (**Figure S4.6-S4.8**). However, the intriguing details lay in the resolved spectra after MCR analysis. Similar to Cu-Zn/SiO_2 , the kinetics of $\kappa^2\text{-HCOO}^*(\text{Ga}^{3+})$ are indistinguishable from $\kappa^2\text{-HCOO}^*(\text{Cu})$ (i.e. they appear in the same MCR-resolved spectrum, **Figure S4.7**) and suggest the similar role of Ga^{3+} to Zn^{2+} . On the other hand, $\kappa^2\text{-HCOO}^*(\text{In}^{3+})$ was not observed after MCR analysis (**Figure S4.8**). Furthermore, the relative intensity of $\kappa^2\text{-DCOO}^*$ to CD_3O^* during the D_2+CO_2 phase can be related to the hydrogenation rate of $\kappa^2\text{-DCOO}^*$ to CD_3O^* . Only over Cu-Ga/SiO_2 was the $\kappa^2\text{-DCOO}^*$ intensity lower than CD_3O^* , suggesting faster $\kappa^2\text{-DCOO}^*$

hydrogenation to methanol/methoxy than any other catalysts. This led to less abundant and unobservable surface $\kappa^2\text{-HCOO}^*$ (Ga^{3+}) during the H_2+CO_2 phase and consequently less $\kappa^2\text{-HCOO}^*$ decomposition to CO.

The nature of the active site of Cu/ZnO-based catalyst remains highly debated and it was proposed that CO_2 hydrogenation of CH_3OH occurs via $\text{Zn}(\text{HCOO})_2$ intermediates originated from hydrogen dissociation over Cu, H-spillover to ZnO, and subsequent CO_2 activation over ZnO.²⁸ Even using a well-defined Cu-Zn/SiO₂ prepared via SOMC, it was also challenging to pinpoint the origin of the high CH_3OH selectivity due to the presence of Lewis acidic zinc sites and/or reduced zinc sites (alloy).¹⁵ However, Lewis acidic sites can play an important role as an active perimeter site and a reservoir for $\kappa^2\text{-HCOO}^*$, which can spillover from the metal particle and be stabilized.^{29,30} The selectivity to CH_3OH over CO should be both related to the spillover rate toward M^+ sites (Zn^{2+} , Ga^{3+} , and In^{3+}) as well as the stability of HCOO^* over M^+ sites, which can be elucidated by transient experiments (*vide infra*).

4.2.3 Insights into species spillover using transient experiment

Separating the CO_2 and H_2 activation steps in a transient experiment by alternately passing CO_2 or H_2 can provide further insights into CO_2 activation and subsequent hydrogenation. The limited supply of reactants (especially H_2) allows the capturing of the fast-forming species (e.g. CO^* or $\kappa^2\text{-HCOO}^*$ over Zn^{2+} or Ga^{3+}) which were readily hydrogenated during steady-state CO_2 hydrogenation.

The evolution of the surface species during the CO_2 and H_2 phases over the Cu-Zn/SiO₂ are presented in **Figure 4.6** (the MCR-resolved spectra are shown in **Figure S4.9**). Unlike the previous experiment, the responses of $\kappa^2\text{-HCOO}$ (Cu) and $\kappa^2\text{-HCOO}$ (Zn^{2+}) (e.g., formation and consumption) became kinetically distinguishable. At the beginning of the H_2 phase (after CO_2 saturated the surface), it was obvious that the $\kappa^2\text{-HCOO}$ (Cu) formed earlier than $\kappa^2\text{-HCOO}$ (Zn^{2+}) and was rapidly consumed. After delayed formation, $\kappa^2\text{-HCOO}$ (Zn^{2+}) also started to decay at a much slower rate than $\kappa^2\text{-HCOO}$ (Cu) and the decay profiles correlate with the CH_3OH formation profile detected by MS. This evidence of $\kappa^2\text{-HCOO}$ (Cu) spillover to Zn^{2+} sites and its hydrogenation to methanol. The Zn^{2+} sites play a role as a $\kappa^2\text{-HCOO}$ stabilizer as well as for selective hydrogenation by strengthening the C-H bond while weakening the C-O bond of $\kappa^2\text{-HCOO}$ (Zn^{2+}), as previously discussed.

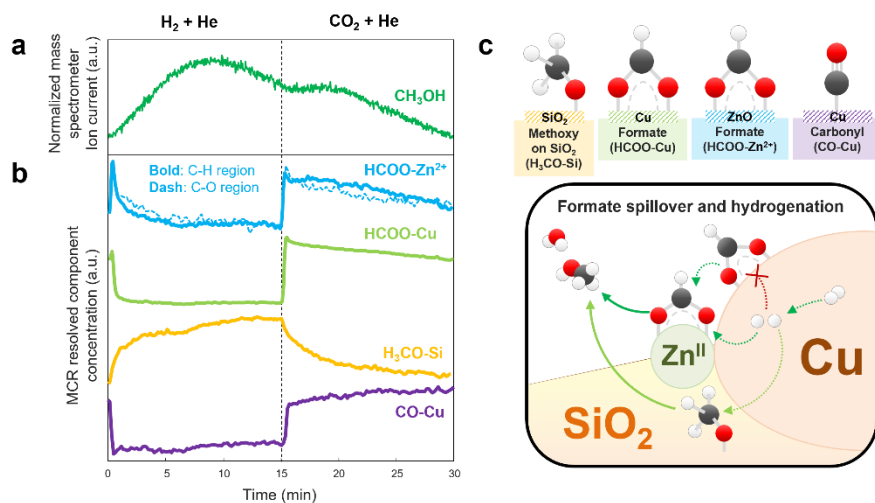


Figure 4.6 Transient responses of surface species and gas products during switching from He+CO₂ to H₂+He over Cu-Zn/SiO₂ catalysts. **a** Corresponding normalized ion current signal of CH₃OH products. **b** Concentration profiles of the spectra of the corresponding components obtained by MCR. **c** the proposed reaction pathway for formate hydrogenation via spillover to Zn²⁺ sites. Reaction conditions: 10 mg catalyst, He/CO₂ = H₂/He = 3, T = 230 °C, P = 20 bar, F_{total} = 10 NmL min⁻¹.

During the transient experiment, Cu/SiO₂, Cu-Zn/SiO₂ and Cu-In/SiO₂ produced CO* (on Cu⁰) under the CO₂ phase apart from κ^2 -HCOO (Cu and Zn²⁺) (Figure S4.9-S4.11). Both κ^2 -HCOO and CO* are converted rapidly under the H₂ phase and formed reproducibly under the CO₂ phase. However, CO* remains undetectable over Cu-Ga/SiO₂ (Figure S4.12), which likely resulted from faster formate hydrogenation making it less susceptible to decomposition to CO (more selective toward CH₃OH). This suggested that κ^2 -HCOO plays a role as an intermediate for CO* formation. The interplay between κ^2 -HCOO* (Cu) and CO* can be observed during the CO₂ phase; the decrease of HCOO* (Cu) species after formation in the opposite trend to the increase of CO* species over Cu/SiO₂, Cu-Zn/SiO₂ and Cu-In/SiO₂ catalyst. In contrast, Cu-Ga/SiO₂ has shown rapid κ^2 -HCOO hydrogenation to CH₃OH as shown by indistinguishable MCR-resolved spectra among κ^2 -HCOO (Cu), κ^2 -HCOO (Ga³⁺), and CH₃OH (Figure S4.12). Unobservable κ^2 -HCOO (In³⁺) might be the indication that In³⁺ cannot stabilize κ^2 -HCOO for further hydrogenation.

Based on the weaker C–O bonds and stronger C–H bonds of κ^2 -DCOO shown in Figure 4.5b, κ^2 -HCOO (Zn²⁺) is more reactive for hydrogenation to CH₃OH than κ^2 -HCOO (Ga³⁺), which explains the origin of the higher intrinsic CH₃OH formation rate of Cu-Zn/SiO₂ (1.6 g h⁻¹ g_{Cu}⁻¹) than Cu-Ga/SiO₂ (1.3 g h⁻¹ g_{Cu}⁻¹) in our previous work.^{15,16} Notably, the intrinsic CO

formation rate of Cu-Zn/SiO₂ is similar to Cu/SiO₂ (0.3 g h⁻¹ g_{Cu}⁻¹) while the CH₃OH formation rate was boosted by 5 times. This indicated that Zn²⁺ introduction to Cu/SiO₂ did not play role in suppressing CO formation. On the other hand, the Ga³⁺ introduction did not only suppress CO formation over Cu-Ga/SiO₂ (0.1 g h⁻¹ g_{Cu}⁻¹) by 3 times lower than Cu/SiO₂ but also boosted the CH₃OH formation rate was boosted by 4 times. The lower intrinsic CO formation rate over Cu-Ga/SiO₂ is hypothetically due to much faster κ^2 -HCOO (Cu) spillover to Ga³⁺ sites than to Zn²⁺, which made κ^2 -HCOO (Cu) less susceptible to decomposition into CO and ultimately improved CH₃OH selectivity.

4.3 Conclusion

The Cu-M/SiO₂ catalysts (M = Zn, Ga, and In) were prepared by surface organometallic chemistry. Formate on Cu is the common intermediate over Cu-M/SiO₂ catalyst. The role of M⁺ sites is the stabilization of formate species resulting in weakened C–O bond and strengthen C–H bond. Stabilized formate is more reactive toward hydrogenation to methanol. Moreover, the transfer of formate from Cu to M⁺ sites via spillover can suppress formate decomposition to CO over Cu. Despite more reactive formate over Zn²⁺, the formate spillover toward Ga³⁺ is faster, leading to higher CH₃OH selectivity due to suppressed formate decomposition to CO.

All the Cu-M/SiO₂ catalysts proceeded through the same reaction mechanism via formate hydrogenation. The H₂ dissociative adsorption and formates formation were not affected by kinetic isotope effects (KIE). There was slight KIE for formate hydrogenation and significant KIE for methanol activation towards formation/desorption to methanol. The latter was identified as the rate-limiting step for CO₂ hydrogenation. The mechanistic insights from the model Cu-Zn/SiO₂ catalyst help explain the nature of highly debated Cu-ZnO synergy that plays a crucial role in defining the catalytic activity of the industrial Cu/ZnO/Al₂O₃ catalysts. Moreover, understanding the roles of interfacial metal sites at the periphery of Cu nanoparticles can facilitate the rational design of highly selective catalysts and the nano-structures/acidity around the metal site where formates can be formed.

4.4 References

- 1 G. A. Olah, A. Goepfert and G. K. S. Prakash, *Beyond Oil and Gas: The Methanol Economy*, Wiley, 2009, vol. 44.
- 2 G. A. Olah, *Angew. Chem., Int. Ed.*, 2013, 52, 104–107.
- 3 D. Laudenschleger, H. Ruland and M. Muhler, *Nat. Commun.*, 2020, 11, 1–10.
- 4 J. Nakamura, Y. Choi, and T. Fujitani, *Top Catal.*, 2003, 22, 277–285.

- 5 M. Behrens, F. Studt, I. Kasatkin, S. Köhl, M. Hävecker, F. Abild-Pedersen, S. Zander, F. Girgsdies, P. Kurr, B. L. Kniep, M. Tovar, R. W. Fischer, J. K. Nørskov and R. Schlögl, *Science*, 2012, 336, 893–897.
- 6 T. Lunkenbein, J. Schumann, M. Behrens, R. Schlögl, M. G. Willinger, M. G. Willinger, M. Behrens and R. S. Schlögl, *Angew. Chem.*, 2015, 127, 4627–4631.
- 7 S. Kattel, P. J. Ramírez, J. G. Chen, J. A. Rodriguez and P. Liu, *Science*, 2017, 355, 1296–1299.
- 8 A. Beck, M. A. Newton, M. Zabilskiy, P. Rzepka, M. G. Willinger and J. A. van Bokhoven, *Angew. Chem., Int. Ed.*, 2022, 61, e202200301.
- 9 A. Beck, M. Zabilskiy, M. A. Newton, O. Safonova, M. G. Willinger and J. A. van Bokhoven, *Nat. Catal.*, 2021, 4, 488–497.
- 10 A. Urakawa, *Nat. Catal.*, 2021, 4, 447–448.
- 11 S. R. Docherty and C. Copéret, *J. Am. Chem. Soc.*, 2021, 143, 6767–6780.
- 12 K. Larmier, W. C. Liao, S. Tada, E. Lam, R. Verel, A. Bansode, A. Urakawa, A. Comas-Vives and C. Copéret, *Angew. Chem., Int. Ed.*, 2017, 56, 2318–2323.
- 13 E. Lam, K. Larmier, P. Wolf, S. Tada, O. v. Safonova and C. Copéret, *J. Am. Chem. Soc.*, 2018, 140, 10530–10535.
- 14 G. Noh, E. Lam, J. L. Alfke, K. Larmier, K. Searles, P. Wolf and C. Copéret, *ChemSusChem*, 2019, 12, 968–972.
- 15 E. Lam, G. Noh, K. Larmier, O. V. Safonova and C. Copéret, *J. Catal.*, 2021, 394, 266–272.
- 16 E. Lam, G. Noh, K. W. Chan, K. Larmier, D. Lebedev, K. Searles, P. Wolf, O. V. Safonova and C. Copéret, *Chem. Sci.*, 2020, 11, 7593–7598.
- 17 S. R. Docherty, N. Phongprueksathat, E. Lam, G. Noh, O. v. Safonova, A. Urakawa and C. Copéret, *JACS Au*, 2021, 1, 450–458.
- 18 E. Lam, K. Larmier, P. Wolf, S. Tada, O. V. Safonova and C. Copéret, *J. Am. Chem. Soc.*, 2018, 140, 10530–10535.
- 19 E. Lam, G. Noh, K. W. Chan, K. Larmier, D. Lebedev, K. Searles, P. Wolf, O. v. Safonova and C. Copéret, *Chem. Sci.*, 2020, 11, 7593–7598.
- 20 A. de Juan, J. Jaumot and R. Tauler, *Anal. Methods*, 2014, 6, 4964–4976.
- 21 J. Jaumot, A. de Juan and R. Tauler, *Chemom. Intell. Lab. Syst.*, 2015, 140, 1–12.
- 22 J. Kim, B. B. Sarma, E. Andrés, N. Pfänder, P. Concepción and G. Prieto, *ACS Catal.*, 2019, 9, 10409–10417.
- 23 G. Noh, E. Lam, D. T. Bregante, J. Meyet, P. Šot, D. W. Flaherty and C. Copéret, *Angew. Chem., Int. Ed.*, 2021, 60, 9650–9659.
- 24 C. Tang, S. Tang, F. Sha, Z. Han, Z. Feng, J. Wang and C. Li, *J. Phys. Chem. C*, 2022, 10399–10407.
- 25 E. Lam, J. J. Corral-Pérez, K. Larmier, G. Noh, P. Wolf, A. Comas-Vives, A. Urakawa and C. Copéret, *Angew. Chem., Int. Ed.*, 2019, 58, 13989–13996.
- 26 S. Choi, B. I. Sang, J. Hong, K. J. Yoon, J. W. Son, J. H. Lee, B. K. Kim and H. Kim, *Sci. Rep.*, 2017, 7, 1–10.
- 27 L. C. Grabow and M. Mavrikakis, *ACS Catal.*, 2011, 1, 365–384.
- 28 M. Zabilskiy, V. L. Sushkevich, D. Palagin, M. A. Newton, F. Krumeich and J. A. van Bokhoven, *Nat. Commun.*, 2020, 11, 2409.
- 29 J. J. Corral-Pérez, A. Bansode, C. S. Praveen, A. Kokalj, H. Reymond, A. Comas-Vives, J. VandeVondele, C. Copéret, P. R. von Rohr and A. Urakawa, *J. Am. Chem. Soc.*, 2018, 140, 13884–13891.
- 30 J. J. Corral-Pérez, C. Copéret and A. Urakawa, *J. Catal.*, 2019, 380, 153–160.

Supporting information

Chapter 4

1. Transient experimental setup and procedures of *operando* DRIFTS

The flow of gases (H_2 , CO_2 , and He) is controlled by 6 mass flow controllers (Bronkhorst). Switching between two reactant gas streams is done by a 4-way valve. The pressure of the two gas streams (to the cell and vent) is controlled by back pressure regulators (Bronkhorst). The outlet gas stream is analyzed by a Pfeiffer OmniStar GSD 300C mass spectrometer.

Before the measurements, the sample is reduced *in situ* at 300 °C in the H_2 stream (20 NmL min⁻¹ H_2) for 1 h and subsequently cooled to a reaction temperature of 150 °C in the He stream. The cell is pressurized to 10-20 bar and immediately exposed to the reactant mixture ($\text{H}_2/\text{CO}_2 = 3/1$ molar ratio, total flow 20 NmL min⁻¹) at the same pressure by the switching valve. The transient experiment utilizes a periodic perturbation of a system by external parameters (stimulation) to influence the concentration of active species.¹ This experiment is performed in the above-mentioned setup by using a switching valve to change the stream of reactant gases to introduce the periodic concentration perturbation.

***Operando* DRIFTS experiment**

The catalyst powder (10-15 mg) is located in a cylindrical cavity (3 mm in diameter and 3 mm vertical length) of a custom-made high-pressure reaction cell (tested up to 40 bar). The cell is mounted in a Harrick Praying Mantis diffuse reflection (DRIFTS) accessory. The spectra were collected using a Thermo Scientific Nicolet 6700 FT-IR spectrometer equipped with a liquid-nitrogen-cooled MCT detector at 4 cm⁻¹ resolution. The spectra were acquired continuously every 10 seconds in a time-resolved manner to monitor the reaction, stabilization process of the catalysts as well as evolution of surface species. No baseline correction was applied to the time-resolved spectra due to the baseline movement.

Temporal evolution of surface species after introducing $\text{H}_2 + \text{CO}_2$

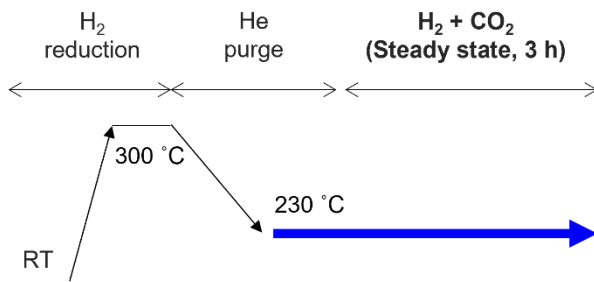


Figure S4.1 Experimental procedure for the temporal evolution of surface species Reduction condition: $300\text{ }^\circ\text{C}$ under 10 NmL min^{-1} of H_2 for 1 h. Reaction conditions: ca. 10 mg catalyst, $\text{H}_2/\text{CO}_2 = 3$, $T = 230\text{ }^\circ\text{C}$, $P = 10\text{ bar}$, $F_{\text{total}} = 10\text{ NmL min}^{-1}$.

Steady-state isotopic transient kinetic analysis (SSITKA) using $\text{D}_2 + \text{CO}_2$

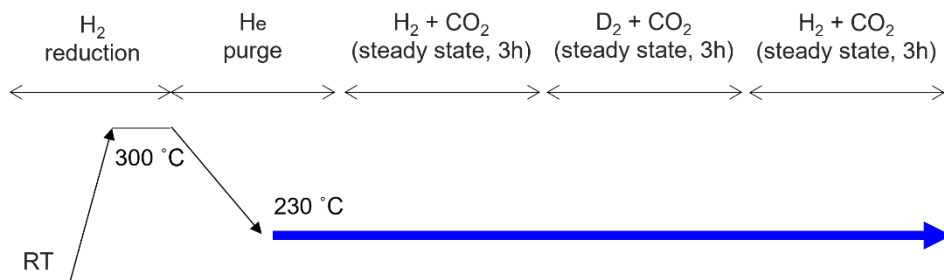


Figure S4.2 Experimental procedure for SSITKA. Reduction condition: $300\text{ }^\circ\text{C}$ under 10 NmL min^{-1} of H_2 for 1 h. Reaction conditions: ca. 10 mg catalyst, H_2/CO_2 or $\text{D}_2/\text{CO}_2 = 3$, $T = 230\text{ }^\circ\text{C}$, $P = 10\text{ bar}$, $F_{\text{total}} = 10\text{ NmL min}^{-1}$.

Transient experiment using He+CO₂ vs H₂+He

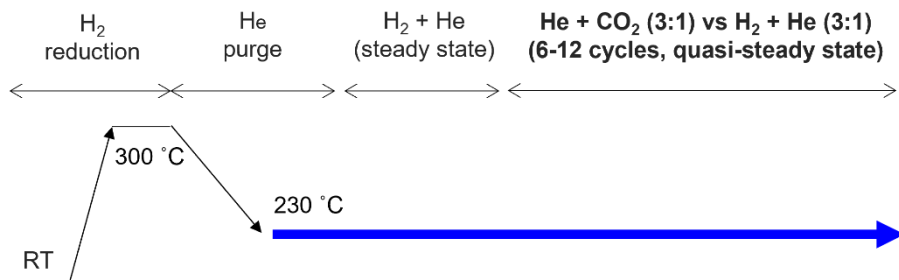


Figure S4.3 Experimental procedures for the transient experiment. Reduction condition: 300 °C under 10 NmL min⁻¹ of H₂ for 1 h. Reaction conditions: ca. 10 mg catalyst, He/CO₂ or H₂/He = 3, T = 230 °C, P = 10 bar, F_{total} = 10 NmL min⁻¹.

Multivariate spectral analysis

Multivariate spectral analysis is performed by the Multivariate Curve Resolution-Alternating Least Squares (MCR-ALS) algorithm, as described elsewhere.² MCR is a chemometric method used for better data processing and deconvolution of complex spectra down to individual components based on kinetic resolution. It can deliver the pure response profiles (e.g. spectra, pH profiles, time profiles, elution profiles) of the chemical species of an unresolved mixture when no previous information is available about the nature and composition of these mixtures.

Temporal evolution of surface species during CO₂ hydrogenation

Tables S4.1 Assignment of surface species

Wavenumber (cm ⁻¹)	Vibrational mode	Band assignment	Ref.
2996	$\nu_{as}(C-H)$	Adsorbed methanol (CH ₃ OH*)	3,4
2958	$\nu_{as}(C-H)$	Methoxy (CH ₃ O*) on SiO ₂	3,4
2936	$\nu(C-H)$	Bidentate formate (κ^2 -HCOO*) on Cu	5-7
2926	$\nu_{as}(C-H)$	Methoxy (CH ₃ O*) on Cu	3
2921	$\nu_s(C-H)$	Adsorbed methanol (CH ₃ OH*)	3,4
2893	$\nu(C-H)$	Bidentate Formate (κ^2 -HCOO*) on ZnO	4
2858	$\nu_s(C-H)$	Methoxy (CH ₃ O*) on SiO ₂	3
2853	$\nu(C-O) + \delta(C-H)$	Bidentate formate (κ^2 -HCOO*) on Cu	5-7
2852	$\nu_s(C-H)$	Adsorbed methanol (CH ₃ OH*)	3,4
2842	$\nu_{as}(C-H)$	Methoxy (CH ₃ O*) on ZnO	4
2830	$\nu_s(C-H)$	Methoxy (CH ₃ O*) on ZnO	4
2815	$\nu_s(C-H)$	Methoxy (CH ₃ O*) on Cu	3
1604	$\nu(C-O)$	Bidentate formate (κ^2 -HCOO*) on Cu	8
1590	$\nu(C-O)$	Bidentate formate (κ^2 -HCOO*) on ZnO	8

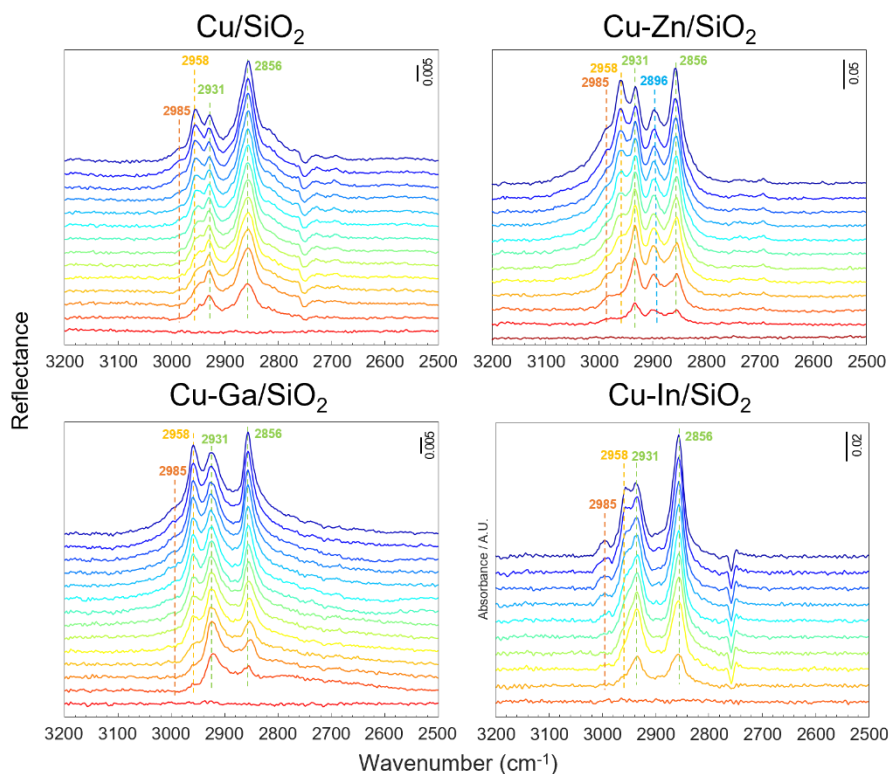


Figure S4.4 Time-resolved *operando* DRIFT spectra of the surface species formed during the CO₂ hydrogenation reaction over Cu/SiO₂, Cu-Zn/SiO₂, Cu-Ga/SiO₂, Cu-In/SiO₂ catalysts. Reduction condition: 300 °C under 10 NmL min⁻¹ of H₂ for 1 h. Reaction conditions: ca. 10 mg catalyst, H₂/CO₂ = 3, T = 230 °C, P = 10 bar, F_{total} = 10 NmL min⁻¹.

Mechanistic insights from the isotopic transient experiment

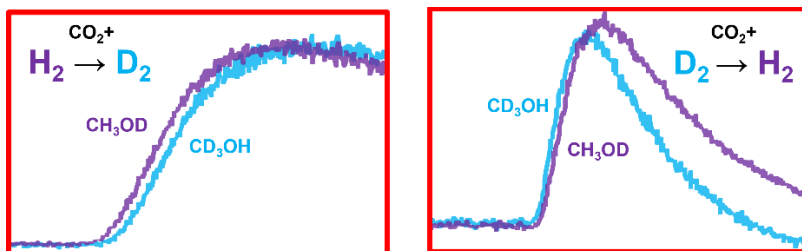


Figure S4.5 Transient responses of surface species and gas products during the steady-state isotopic switching from CO₂+D₂ to CO₂+H₂: Corresponding normalized ion current signal of isotope-labeled products. Reaction conditions: 10 mg catalyst, H₂(or D₂)/CO₂ = 3, T = 230 °C, P = 10 bar, F_{total} = 10 NmL min⁻¹.

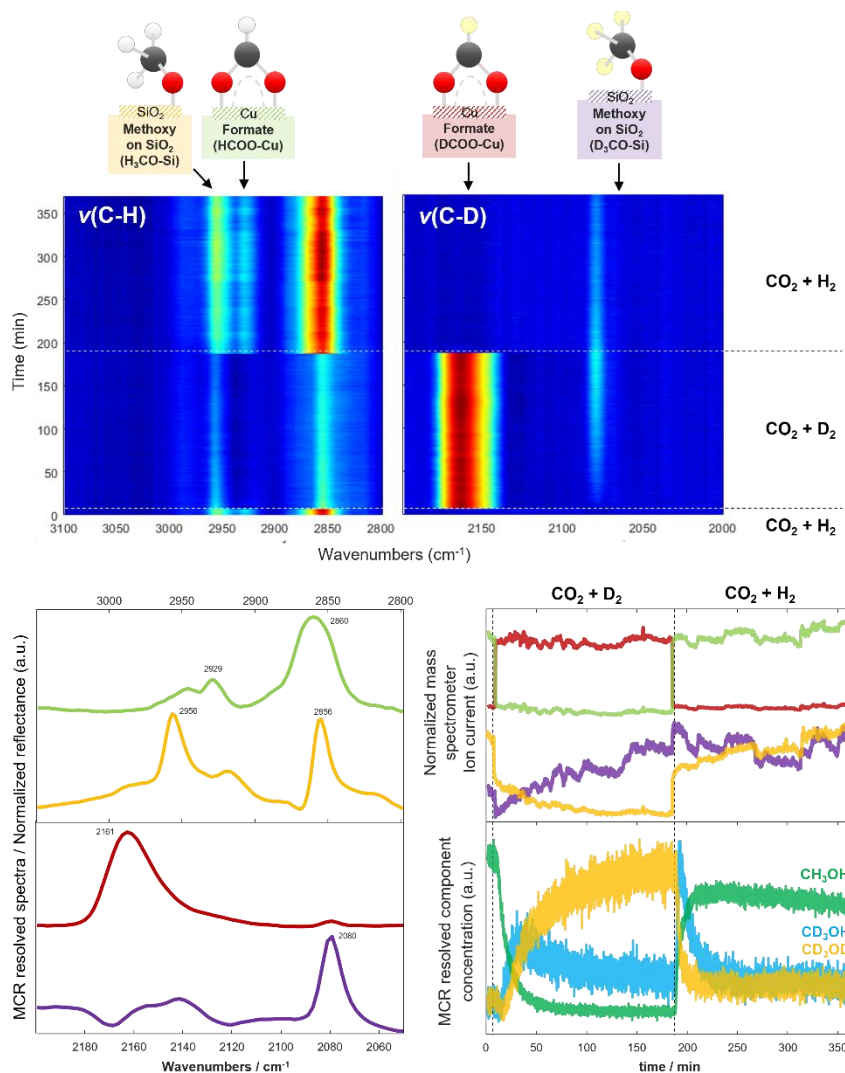


Figure S4.6 Transient responses of surface species and gas products during transient isotopic switching from $\text{CO}_2 + \text{D}_2$ to $\text{CO}_2 + \text{H}_2$ over Cu/SiO_2 . Time-resolved DRIFT spectra of $\nu(\text{C-H})$ region and $\nu(\text{C-D})$ region. Component spectra obtained by MCR were applied to the time-resolved DRIFT spectra. Concentration profiles of the spectra of the corresponding components obtained by MCR. Corresponding normalized ion current signal of isotope-labeled products. Reaction conditions: 10 mg catalyst, $\text{H}_2(\text{or D}_2)/\text{CO}_2 = 3$, $T = 230^\circ\text{C}$, $P = 10\text{ bar}$, $F_{\text{total}} = 10\text{ NmL min}^{-1}$.

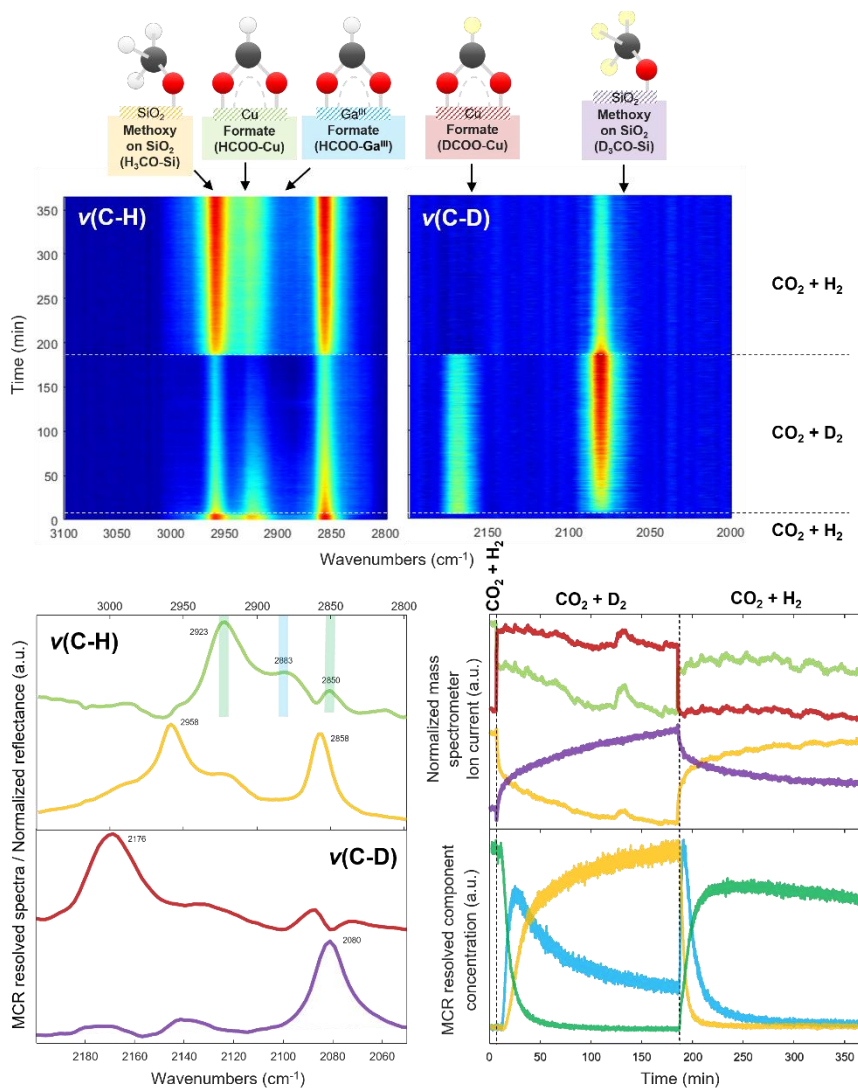


Figure S4.7 Transient responses of surface species and gas products during transient isotopic switching from $\text{CO}_2 + \text{D}_2$ to $\text{CO}_2 + \text{H}_2$ over Cu-Ga/SiO₂. Time-resolved DRIFT spectra of $\nu(\text{C-H})$ region and $\nu(\text{C-D})$ region. Component spectra obtained by MCR were applied to the time-resolved DRIFT spectra. Concentration profiles of the spectra of the corresponding components obtained by MCR. Corresponding normalized ion current signal of isotope-labeled products. Reaction conditions: 10 mg catalyst, H_2 (or D_2)/ $\text{CO}_2 = 3$, $T = 230^\circ\text{C}$, $P = 10\text{ bar}$, $F_{\text{total}} = 10\text{ NmL min}^{-1}$.

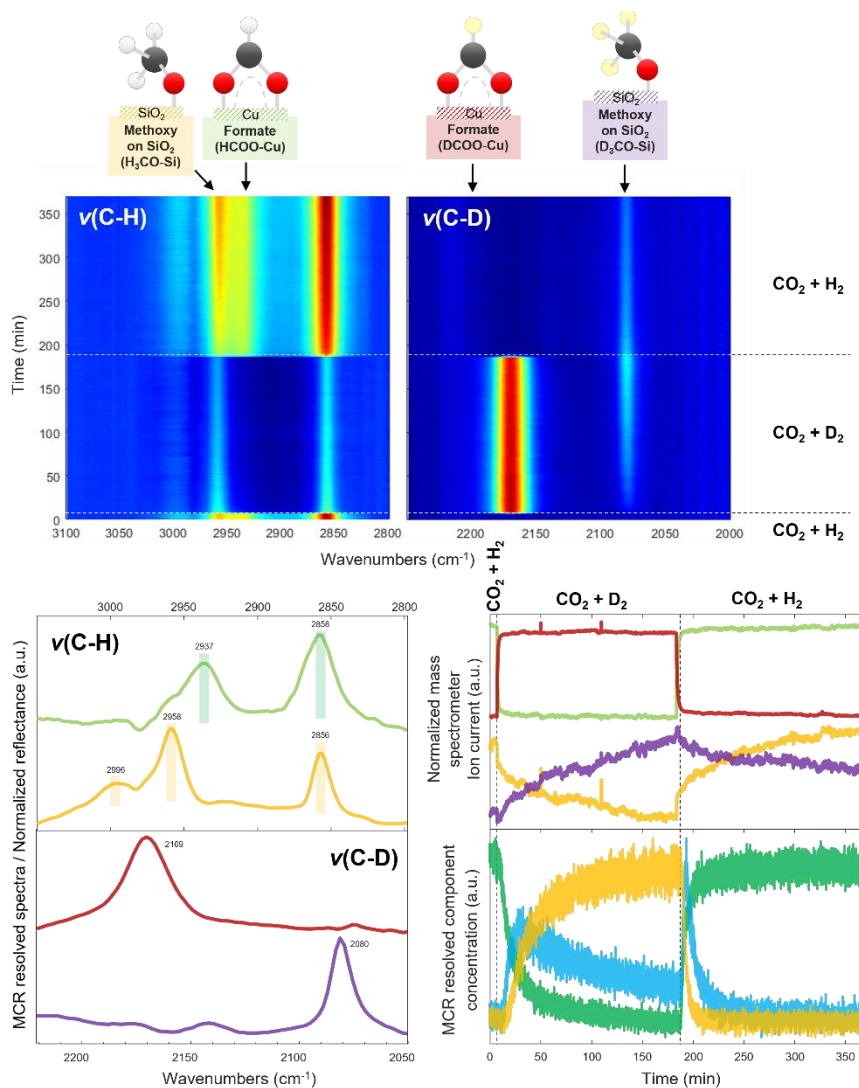


Figure S4.8 Transient responses of surface species and gas products during transient isotopic switching from $\text{CO}_2 + \text{D}_2$ to $\text{CO}_2 + \text{H}_2$ over Cu-In/SiO₂. Time-resolved DRIFT spectra of $\nu(\text{C-H})$ region and $\nu(\text{C-D})$ region. Component spectra obtained by MCR were applied to the time-resolved DRIFT spectra. Concentration profiles of the spectra of the corresponding components obtained by MCR. Corresponding normalized ion current signal of isotope-labeled products. Reaction conditions: 10 mg catalyst, $\text{H}_2(\text{or D}_2)/\text{CO}_2 = 3$, $T = 230^\circ\text{C}$, $P = 10\text{ bar}$, $F_{\text{total}} = 10\text{ NmL min}^{-1}$

Insights into species spillover using transient experiment

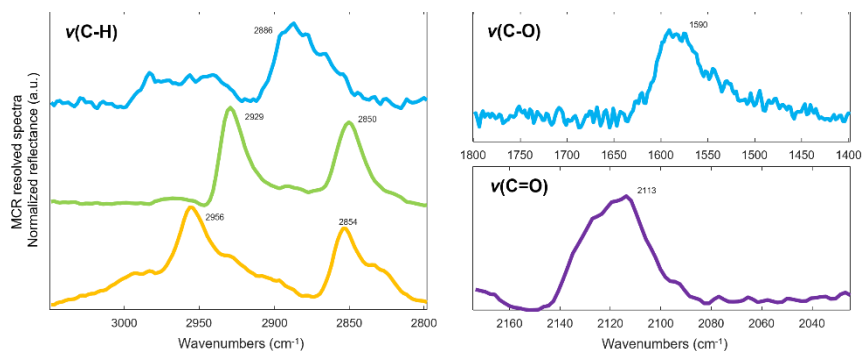


Figure S4.9 Transient responses of surface species and gas products during switching from He+CO₂ to H₂+He over Cu-Zn/SiO₂ catalysts: Components spectra obtained by MCR applied on the time-resolved DRIFT spectra. Reaction conditions: 10 mg catalyst, H₂/CO₂ = 3, T = 230 °C, P = 20 bar, F_{total} = 10 NmL min⁻¹.

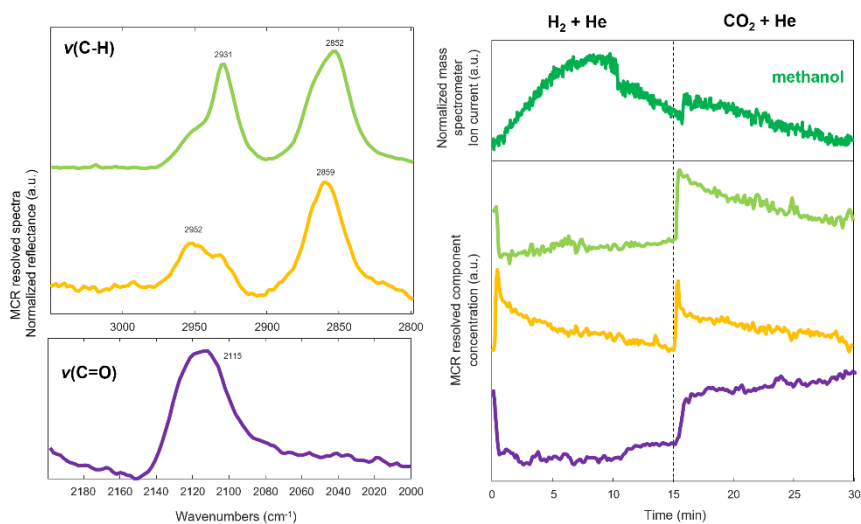


Figure S4.10 Transient responses of surface species and gas products during switching from $\text{He}+\text{CO}_2$ to H_2+He over Cu/SiO_2 catalysts: Components spectra obtained by MCR applied on the time-resolved DRIFT spectra. Concentration profiles of the spectra of the corresponding components obtained by MCR. Corresponding normalized ion current signal of products. Reaction conditions: 10 mg catalyst, $\text{H}_2/\text{CO}_2 = 3$, $T = 230\text{ }^\circ\text{C}$, $P = 20\text{ bar}$, $F_{\text{total}} = 10\text{ NmL min}^{-1}$.

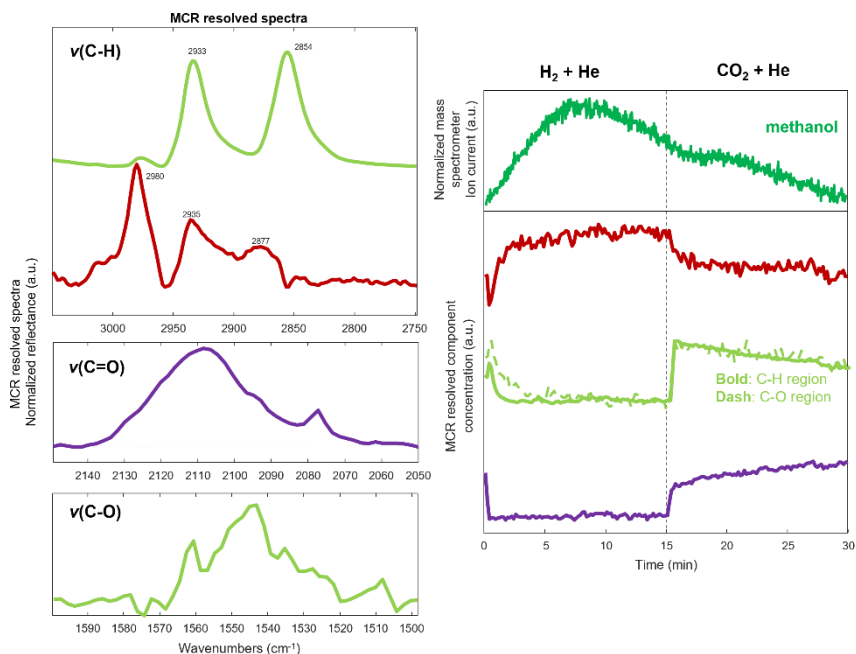


Figure S4.11 Transient responses of surface species and gas products during switching from $\text{He}+\text{CO}_2$ to H_2+He over Cu-In/SiO_2 catalysts: Components spectra obtained by MCR applied on the time-resolved DRIFT spectra. Concentration profiles of the spectra of the corresponding components obtained by MCR. Corresponding normalized ion current signal of products. Reaction conditions: 10 mg catalyst, $\text{H}_2/\text{CO}_2 = 3$, $T = 230^\circ\text{C}$, $P = 20\text{ bar}$, $F_{\text{total}} = 10\text{ NmL min}^{-1}$.

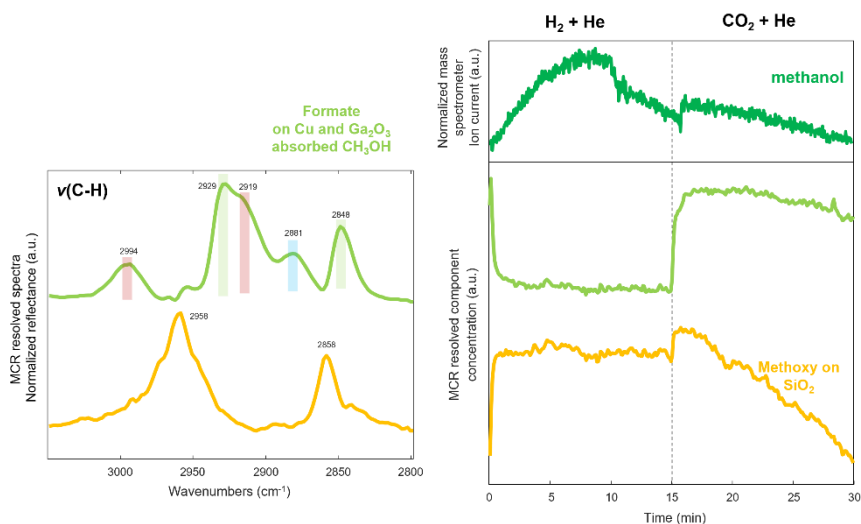


Figure S4.12 Transient responses of surface species and gas products during switching from He+CO₂ to H₂+He over Cu-Ga/SiO₂ catalysts: Components spectra obtained by MCR applied on the time-resolved DRIFT spectra. Concentration profiles of the spectra of the corresponding components obtained by MCR. Corresponding normalized ion current signal of products. Reaction conditions: 10 mg catalyst, H₂/CO₂ = 3, T = 230 °C, P = 20 bar, F_{total} = 10 NmL min⁻¹.

References

- 1 A. Urakawa, T. Bürgi and A. Baiker, *Chem. Eng. Sci.*, 2008, 63, 4902–4909.
- 2 J. Jaumot, A. de Juan and R. Tauler, *Chemom. Intell. Lab. Syst.*, 2015, 140, 1–12.
- 3 G. J. Millar, C. H. Rochester and K. C. Waugh, *J. Chem. Soc. Faraday. Trans.*, 1991, 87, 2795.
- 4 G. J. Millar, C. H. Rochester and K. C. Waugh, *J. Chem. Soc. Faraday. Trans.*, 1992, 88, 2257–2261.
- 5 G. J. Millar, C. H. Rochester and K. C. Waugh, *J. Catal.*, 1995, 155, 52–58.
- 6 G. J. Millar, C. H. Rochester and K. C. Waugh, *J. Chem. Soc. Faraday. Trans.*, 1991, 87, 2785.
- 7 G. J. Millar, D. Newton, G. A. Bowmaker and R. P. Cooney, *Appl. Spectrosc.*, 1994, 48, 827–832.
- 8 S. G. Neophytides, A. J. Marchi and G. F. Froment, *Appl. Catal. A. Gen.*, 1992, 86, 45–64.

Part II

Insights into Rhenium-based catalysts



Bifunctionality of Re supported on TiO₂ in driving methanol formation in low-temperature CO₂ hydrogenation



Abstract

Lower-temperature and higher-pressure are thermodynamically more favorable conditions to achieve high conversion and high methanol selectivity in CO₂ hydrogenation. However, low temperature activity is generally very poor due to the sluggish kinetics, and thus designing highly selective catalysts active below 200 °C is a great challenge in CO₂-to-methanol. Recently, Re/TiO₂ was reported as a promising catalyst. We show that Re/TiO₂ is indeed more active in continuous and high-pressure (331 bar) operations at 150 °C compared to an industrial Cu/ZnO/Al₂O₃ catalyst which suffers from the formation of methyl formate which is decomposed to carbon monoxide. At lower temperatures, precise understanding and control over the active surface intermediates are crucial to boost the conversion kinetics. This work aims at elucidating the nature of active sites and active species by means of *in situ/operando* XAS, Raman, AP-XPS, and DRIFTS. Transient *operando* DRIFTS studies uncover the activation of CO₂ to form active formate intermediates leading to methanol formation and also active rhenium carbonyl intermediates leading to methane over cationic Re single atoms characterized by rhenium tricarbonyl complexes. The transient techniques afford to differentiate the active species from the spectator one on TiO₂ support, such as less reactive formate originating from spillover and methoxy from methanol adsorption. The AP-XPS supports that metallic Re species act as H₂ activators, leading to H-spillover and importantly to hydrogenation of active formate intermediate present over cationic Re species. The origin of the unique reactivity of Re/TiO₂ was suggested as the coexistence of cationic highly-dispersed Re including single atoms, driving the formation of monodentate formate, and metallic Re clusters in the vicinity, activating the hydrogenation of the formate to methanol.



This chapter is based on the following publication:

Phongprueksathat, N., Ting K.W., Mine, S., Jing, Y., Toyoshima, R., Kondoh, H., Shimizu, K., Toyao, T., & Urakawa, A

In preparation

5.1 Introduction

Recycling fossil fuel-derived carbon dioxide (CO₂) by converting it into chemicals or fuels such as methanol, ethanol, and dimethyl ether is a promising approach toward alleviating the impact of global warming.¹ Among those chemicals, methanol is one of the most versatile chemicals as an energy carrier and an alternative petrochemical feedstock towards a less fossil-fuel-dependent and/or circular economy, known as the “methanol economy”.²

Methanol can be synthesized on industrially relevant scales via CO₂ hydrogenation over the most known Cu/ZnO/Al₂O₃ catalysts at 220-250 °C and 10-30 bar.³ According to Le Chatelier’s principle, however, lower temperature and higher pressure than the aforementioned conditions are more thermodynamically favorable. Taking both chemical and vapor-liquid equilibria into the thermodynamic calculation, conditions below 200 °C and above 150 bar are required to achieve nearly full CO₂ conversion and CH₃OH selectivity.⁴ This is thanks to the *in situ* separation of condensable products (e.g., methanol and water) from reactant gases, thereby driving forward the reaction equilibrium.^{5,6} Furthermore, operating the reaction below 200 °C is expected to be not only beneficial by reducing energy consumption but also alleviating deactivation due to sintering.

In practice, low-temperature high-pressure CO₂ hydrogenation over a Cu/ZnO/Al₂O₃ catalyst yields high CO selectivity below 260 °C despite the thermodynamically favorable conditions towards methanol formation ($P = 331$ bar and $H_2/CO_2 = 10$).⁷ At and above 260 °C, the reaction mechanisms of methanol formation appears as reverse water-gas shift and subsequent CO hydrogenation according to the residence time and space-resolved *operando* studies.⁸ CO hydrogenation was kinetically limited at a lower temperature, whereas the direct CO₂ hydrogenation to methanol is the major path at a low temperature (180 °C). The reaction path may be condition (e.g. pressure and catalyst) dependent; one study reports contrary results where the source of carbon can gradually shift from CO₂ to CO as the temperature decreases toward 160 °C.⁹ In literature, it is widely accepted that using Cu-based catalysts CO₂ is the main source of carbon in CH₃OH and that CO is formed independently via different intermediates and converted to methanol via CO hydrogenation, by an order of magnitude slower than CO₂ hydrogenation.^{10,11} Moreover, CH₃OH formed via direct CO₂ hydrogenation can decompose to CO.⁸ Lewis-acidic sites over Al₂O₃ play a key role in CH₃OH decomposition to CO via methyl formate-mediated pathway.¹² Thus, the development of novel catalysts with well-defined active sites with a clear understanding of

the reaction mechanisms is crucial for suppressing CO formation, while achieving high CO₂ conversion and CH₃OH selectivity.

Supported Re catalysts show remarkable potential in heterogeneous catalysis, especially for CO₂ hydrogenation.^{13–15} Recently, Re/TiO₂ was found to exhibit the highest turnover frequency (TOF) and CH₃OH selectivity among various metal catalysts (Co, Ni, Cu, Ru, Rh, Pd, Ag, Re, Ir, and Pt) supported on TiO₂, bulk Re catalysts (Re⁰, NH₄ReO₄, ReO₂, ReO₃, Re₂O₇), and Re supported on various supports (ZrO₂, Al₂O₃, SiO₂, C, CeO₂, MgO, SiO₂-Al₂O₃, SnO₂, H-ZSM-5, HY) under a batch reaction condition at 150 °C and 60 bar (H₂/CO₂ = 5, 24 h).¹⁶ Despite the uniquely high activity, the major challenge of the catalyst is the formation of CH₄ as a byproduct. CH₄ selectivity over Re/TiO₂ is promoted not only by the reaction conditions (higher reaction temperature and longer contact time^{14,15}),^{17,18} but also by the catalyst structures such as larger Re cluster size and Re oxidation state.¹⁶ Structural chemistry of Re on metal oxide support materials is complex. The reduction of Re⁷⁺ (Re₂O₇) supported on γ -Al₂O₃ can disperse Re particles into majorly single Re atoms, Re nanoclusters, and unreduced Re (due to oxophilic nature).¹⁹ After a similar reduction treatment to Re₂O₇/TiO₂, subnanometer Re clusters are formed with oxidation numbers between Re⁰ and Re⁴⁺ that were suggested to be favorable for high CH₃OH selectivity.¹⁶ The fluxional oxidation states of both Re and Ti can influence the nature of the acid site on Re/TiO₂; the hydroxyl group attracted by Re⁶⁺ or Re⁶⁺ generates Brønsted acid sites, while the incorporation of Re⁴⁺ into TiO₂ forming Reⁿ⁺-O-Ti⁴⁺(Ti³⁺) bonds creates Lewis acid sites.²⁰ For Cu-based catalysts, the Lewis acid strength of Ti sites next to Cu can stabilize surface intermediates such as formate and methoxy in proximity to metal nanoparticles leading to boosting the CH₃OH formation rate.^{21,22} For Re/TiO₂, *in situ* IR, showed that formate and methoxy are possible intermediates for CH₃OH formation, while carbonyls are a possible intermediate for CH₄ formation.^{16,17} However, the observable surface species under the steady-state DRIFTS experiment could be both active or spectator species. Elucidation of the precise reaction mechanisms and involved active species requires more advanced approaches such as transient techniques with periodic external stimulus for species discrimination.^{23–25} Transient techniques are applicable for pinpointing the state and structure of active sites from multi-oxidation states Re particles and understanding the interrelationship between the nature of active sites and surface intermediates.

In this study, the catalytic activity of Re/TiO₂ was investigated at low temperature and high pressure of 150 °C and 331 bar. The results from various *in situ/operando* spectroscopy techniques such as diffuse reflectance infrared Fourier transform spectroscopy (DRIFT), X-ray absorption

spectroscopy (XAS), Raman spectroscopy, and ambient-pressure X-ray photoelectron spectroscopy (AP-XPS) provide insights into surface species, the oxidation state of Re, and the structural change of TiO₂. DRIFTS combined with steady-state isotopic transient kinetic analysis (SSITKA) using D₂ and ¹³CO₂ elucidate distinct surface intermediates and pathways toward CH₃OH and CH₄ formation. Correlating the surface species, catalyst structures, and outlet gas product, we provide molecular-level insights into the reaction mechanisms and the nature of active sites, which could further assist the development of superior catalysts.

5.2 Results and Discussion

5.2.1 Selectivity progression during low-temperature CO₂ hydrogenation at high pressure.

The catalytic performance of 3 wt% Re/TiO₂ and commercial Cu/ZnO/Al₂O₃ (64/25/10 wt%) were studied at the stoichiometric H₂/CO₂ ratio of 3 at 150 °C and 331 bar (reactant pressure, the reaction pressure is 360 bar including an inert gas for calibration) for 24 h (**Figure 5.1**). Initially, both catalysts showed higher CO₂ conversion that declined with time-on-stream, more prominently for Cu/ZnO/Al₂O₃. Re/TiO₂ showed a comparable and higher CO₂ conversion to Cu/ZnO/Al₂O₃ over time despite significantly lower metal loading. CH₃OH selectivity displayed three distinguished stages within the 24 h experiment: activation (0-10 h), stable performance (10-20 h), and stabilization and deactivation (>20 h). During the activation period, methyl formate (HCOOCH₃) is the main product over Cu/ZnO/Al₂O₃. After initial >60% selectivity followed by a decrease, methyl formate selectivity reaches ca. 47% at ca. 8 h before a rapid decline to less than 5%. Along with the decrease of methyl formate selectivity, CH₃OH and CO selectivities gradually increase and become stable. On the other hand, Re/TiO₂ shows a high initial CH₄ selectivity (>40%) that rapidly declines within 5 h. HCOOCH₃ selectivity over Re/TiO₂ is lower than that of Cu/ZnO/Al₂O₃ during the first 10 h, but it becomes higher over time. Generally, the drops in HCOOCH₃ selectivity accompany counteracting increase of methanol selectivity, implying their close correlation and balance of the surface intermediates leading to the two products.

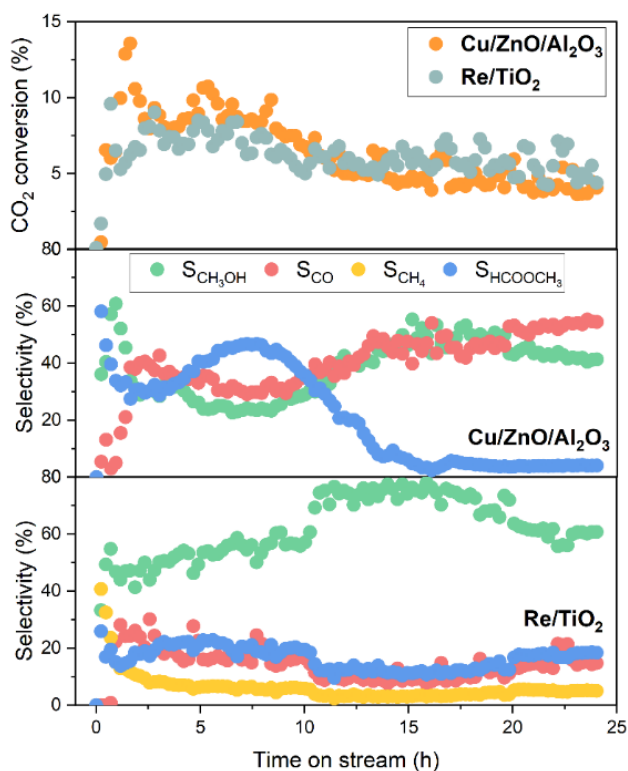
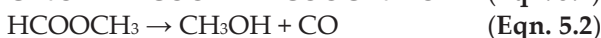


Figure 5.1 Catalytic activity of Cu/ZnO/Al₂O₃ and 3 wt% Re/TiO₂ in CO₂ hydrogenation. H₂/CO₂ = 3, T = 150 °C, P = 331 bar, and GHSV = 2,000 h⁻¹ (2 NL g_{cat}⁻¹ h⁻¹).

The selectivity toward HCOOCH₃ has become increasingly noticeable at low temperatures and high-pressure operations, especially over Cu/ZnO/Al₂O₃. The Lewis acid sites on Al₂O₃ can strongly adsorb formate (HCOO*) intermediates that react further with CH₃OH to HCOOCH₃ (Eqn. 5.1),²⁶ or transiently produced formic acid through protonation of the formate may undergo esterification reaction with adsorbed CH₃OH to produce HCOOCH₃. The sudden drop in HCOOCH₃ selectivity contrarily to the increased CH₃OH and CO selectivity suggested that the HCOOCH₃ decomposition path over Al₂O₃ into CH₃OH and CO (Eqn. 5.2) is likely active.¹²



Considerable amounts of H_2O formed during the reaction can activate hydrophilic Al_2O_3 and create Brønsted acid sites that promote HCOOCH_3 decomposition. On the other hand, weaker Lewis acidic sites and less hydrophilicity of TiO_2 compared to Al_2O_3 ,²² result in generally lower HCOOCH_3 selectivity over Re/TiO_2 . A closer look into the CO formation profile of Re/TiO_2 shows that it behaves similarly or rather identically to that of HCOOCH_3 , indicating a different mechanism for HCOOCH_3 formation/decomposition or the CO formation pathway for the two catalysts. The initial high selectivity to HCOOCH_3 and its unstable formation profile are interesting by themselves. Based on the observations and also the previous studies aiming at HCOOCH_3 synthesis where methanol adsorption is found rate-limiting and the support, especially its perimeter with an active metal, plays decisive roles, the amount of surface methanol and thus the coverage of methanol on the catalyst surface is important for the formation of HCOOCH_3 .^{26,27} During the initial phase of the reaction, the concentration of adsorbed methanol is expected to vary drastically where formed methanol reacts immediately with reactive formates/formic acid on the catalyst surface, but at a certain point this will reach a steady value and this may decrease the amount of reactive formates/formic acid, explaining the formation profile of methyl formate. Overall and importantly, Re/TiO_2 exhibits a superior activity for CH_3OH production to $\text{Cu/ZnO/Al}_2\text{O}_3$ at the low temperature and different activation mechanisms are indicated from the product selectivity and their temporal profiles.

5.5.2 Effect of Re loading

In the previous study on Re/TiO_2 , a sub-nanometer size of Re was found important for high CH_3OH selectivity, whereas larger Re clusters favored CH_4 formation by the Re loading study.¹⁶ **Figure 5.2** confirms the finding and shows that higher Re loading does not have a positive impact on the catalytic performance, decreasing both CO_2 conversion and CH_3OH selectivity. This trend is uncommon and shows the strikingly high structure sensitivity or the presence of a highly reactive active site to form methanol when Re is highly dispersed.

Larger Re cluster size due to increased Re loading promotes not only CH_4 but also HCOOCH_3 selectivity instead of CH_3OH selectivity. CH_4 selectivity reaches a plateau above 10 wt% and further increase of Re loading only resulted in the promotion of HCOOCH_3 selectivity. Interestingly, CO selectivity appears to be independent of Re loading. This independence of HCOOCH_3 and CO formation amount may indicate that the latter, as reported for $\text{Cu/Al}_2\text{O}_3$,²⁸ is not formed by the decomposition of the former on

Re/TiO₂ or that the formation of CO takes place at a specific site which is not Re-loading dependent.

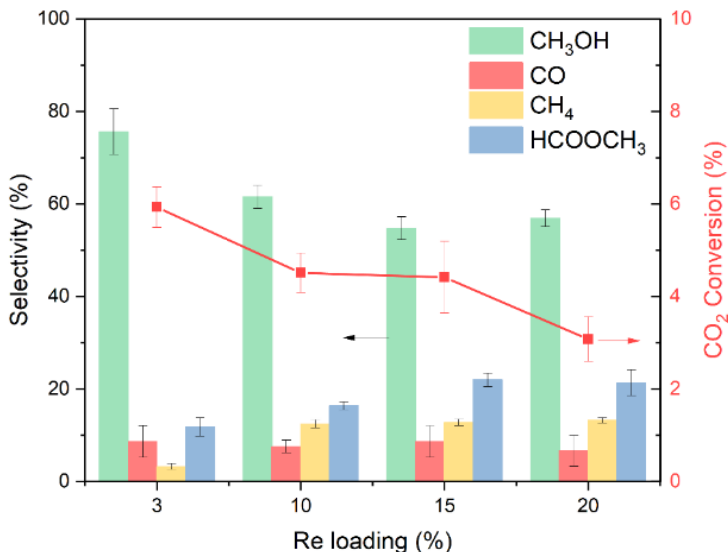


Figure 5.2 Effect of the Re loading (wt%) of Re/TiO₂ in CO₂ hydrogenation. H₂/CO₂ = 3, T = 150 °C, P = 331 bar, GHSV = 2,000 h⁻¹ (2 NL g_{cat}⁻¹ h⁻¹), and TOS = 15 h.

The previous study indicated that highly dispersed Re particles having oxidation states higher than Re⁰ and below Re⁴⁺ (ReO₂) are beneficial in achieving high CH₃OH selectivity.¹⁶ The results of this study once again show that higher Re loading has negative effects and larger Re particles accelerate both CH₄ and HCOOCH₃ formation. Most importantly, the Re loading affects the active sites and reaction pathways, which needs to be elucidated under *operando* conditions.

5.5.3 *In situ* characterization of fresh and reduced Re/TiO₂ catalysts

Re is well-known to alter its oxidation state in a wide range and TiO₂ is also known for its redox properties.^{29–31} The combination of Re and TiO₂ yields the uniquely active catalyst and the reducible/oxidizable nature of these may be important for the creation of the active sites or inducing specific reaction pathways. To gain deeper insights, the structure of fresh and reduced Re/TiO₂ was characterized *in situ* using XAS and Raman spectroscopy to follow the oxidation states of Re and structural changes/disorder of the TiO₂ lattices, respectively.

The Re L₃-edge XANES spectra of Re/TiO₂ before and after reduction are shown in **Figure 5.3a**. The white line intensity and position of calcined (fresh) catalyst at 10542.0 eV have decreased and shifted toward lower energy of 10540.1 eV after reduction with H₂ at 500 °C for 0.5 h indicating the reduction of Re₂O₇ species. Determining the precise oxidation states of reduced Re is challenging since the white line intensity is also influenced by the cluster size of Re.¹⁹ The relatively low loading of Re (3 wt%) and high XAS measurement temperature would render an EXAFS analysis difficult. In addition, as can be seen in the HAADF-STEM images, the Re species are highly dispersed and heterogeneous. These features should render an EXAFS analysis particularly difficult. Note that we found that Re/TiO₂ with 5 wt% Re loading contains features associated with both Re–O and Re–Re bonds.³² The coordination numbers of the Re–O and Re–Re bonds were determined to be 2.7 and 3.4, respectively.

On the other hand, the Raman spectra of fresh Re/TiO₂ catalyst (**Figure 5.3b**) have shown a peak at ca. 970 cm⁻¹, which is attributed to ν_s (Re=O) of highly oxidized Re species (isolated hydrated Re₂O₇ species).³³ There are no other peaks of Re=O bonds from the reduced catalysts suggesting that most Re₂O₇ particles were transformed into more reduced ReO_x. The peaks position at 163 (E_g), 193 (E_g), 390 (B_{1g}), 510 (A_{1g} or B_{1g}), and 632 (E_g) cm⁻¹ are assigned to the vibrational modes of the lattice and O–Ti–O bonds of the anatase structure. The peak position of TiO₂ remains the same after reduction suggesting no change in the anatase phase after reduction at 500 °C. The emergence of a new broad peak at 810 cm⁻¹ after H₂ exposure can either indicate the surface structural changes due to the formation of oxygen vacancies^{34,35} or the formation of ν_s (Re–O) of Ti–O–Re or Re–O–Re bridging oxygen within the Re_xO_y clusters.³⁶ Although the origin of the broad peak cannot be understood by this study, the increase in Ti–O–Re coordination was expected because Re/TiO₂ showed the tendency to form single atoms Re and sub-nanoclusters after reduction.³⁷ The same observation was made in this study, in which Re disperse into single atoms after reaction (*vide infra*) and the broad peak may indicate the atomic dispersion of Re into the TiO₂ surface.

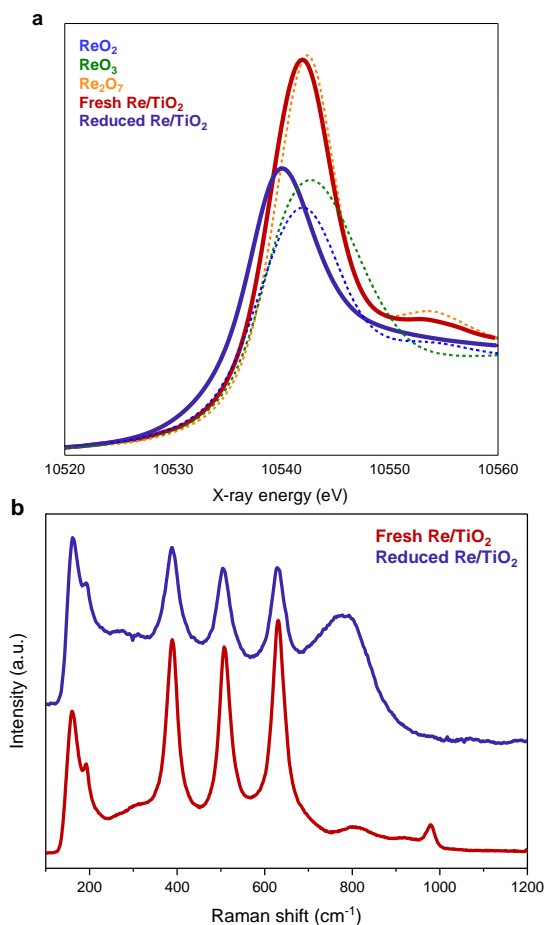


Figure 5.3 *In situ* characterization of 3 wt% Re/TiO₂ catalyst before and after reduction with H₂ at 500 °C, atmospheric pressure: **a** *in situ* Re L₃-edge XANES spectra and **b** *in situ* Raman spectra.

5.2.4 Structural changes and temporal evolution of surface species during CO₂ hydrogenation over Re/TiO₂

CO₂ hydrogenation over Re/TiO₂ under working conditions of 150 °C and 10 bar was investigated using *operando* XAS, Raman, and DRIFTS. The Re L₃-edge XANES before and during steady-state reaction showed a slight increase in the white line intensity with a minor shift by ca 0.2 eV (**Figure S5.1a**). These changes indicate reoxidations of Re by CO₂ and/or redispersion of the Re cluster. More detailed results and discussion are given later. The Raman spectroscopy (**Figure S5.1b**) showed no shift in peak positions but a

decreased baseline, which is only related to the reduced and oxidized state of the TiO₂ surface.

Time-resolved DRIFTS provides insights into the temporal evolution of surface species during CO₂ hydrogenation over the freshly reduced catalyst (**Figure 5.4**). Identified surface species are kinetically distinguishable, which facilitates the identification and assignment of each IR band. **Table S5.1** summarizes the peak assignments from literature for each surface species and IR vibrational modes. CO₂ hydrogenation using D₂ (²H₂) helps identify surface species containing H atoms, e.g., through C–H and O–H bonds due to the shift in the vibrational frequencies (**Figure S5.2**). Moreover, kinetic isotope effects (KIE) can alter the intermediate/product formation rates and one can learn about rate-limiting steps.^{9,10} On the other hand, ¹³CO₂ hydrogenation helps identify the species containing the C=O bond (**Figure S5.3**). For example, in this study both D₂ and ¹³CO₂ played a crucial role in the identification of rhenium hydride (Re–H), which are obscured by carbonyls (CO*).

The $\nu(\text{C–H})$ bands in the 2500–3200 cm^{–1} region are presented in **Figure 5.4a**, while $\nu(\text{C–O})$ bands in 1000–1800 and 1800–2300 cm^{–1} regions are shown in **Figures 5.4b** and **5.4c**. The structures of relevant surface species are illustrated in **Figure 5.4d**. The characteristic IR bands of rhenium hydride (Re–H, 1965 cm^{–1}) and bridging or chelating bidentate formate on TiO₂ ($\kappa^2\text{-HCOO}^*$, 2950, 2869, 1560, and 1357 cm^{–1}) appear immediately after the reaction was initiated. Linear carbonyl species ($\mu_1\text{-CO}^*$, 2030 cm^{–1}) appear after 0.5 min. Bridge carbonyls ($\mu_2\text{-CO}^*$, 1936 and 1880 cm^{–1}) appear after 2 min. However, we later confirm that the bands assigned $\mu_1\text{-CO}^*$ and $\mu_2\text{-CO}^*$ are the parts of the rhenium tricarbonyls complex (Re(CO)₃) (*vide infra*). The bands that appeared simultaneously at 2883, 2848, 2732, 1640, and 1405 cm^{–1} can be assigned to adsorbed methyl formate (HCOOCH₃*)^{38,39} or adsorbed formic acid (HCOOH*)^{40,41}. However, those adsorbed molecules were not usually observed under *operando* DRIFTS since they are prone to chemically adsorbed in form of $\kappa^2\text{-HCOO}^*$.^{26,27,42} These bands were later assigned as monodentate formate on Re ($\kappa^1\text{-HCOO}^*$) or bridging formate ($\mu_2\text{-HCOO}^*$) over Re or Re–O–Ti interface.⁴³ Methoxy species (CH₃O*, 2829, and 2927 cm^{–1}) appear in the latest order after 10 min of reaction.

In summary, the surface species temporally evolved in the following orders: $\kappa^2\text{-HCOO}^* = \text{Re–H}$ (0.25 min) $\rightarrow \mu_1\text{-CO}^*$ (0.5 min) $\rightarrow \mu_2\text{-CO}^*$ (Re(CO)₃ formation) = $\mu_2\text{-HCOO}^*$ (2 min) $\rightarrow \text{CH}_3\text{O}^*$ (10 min). It should be highlighted that a faster spectral acquisition than 10 s is required to distinguish the formation rate between $\kappa^2\text{-HCOO}^*$ and Re–H.

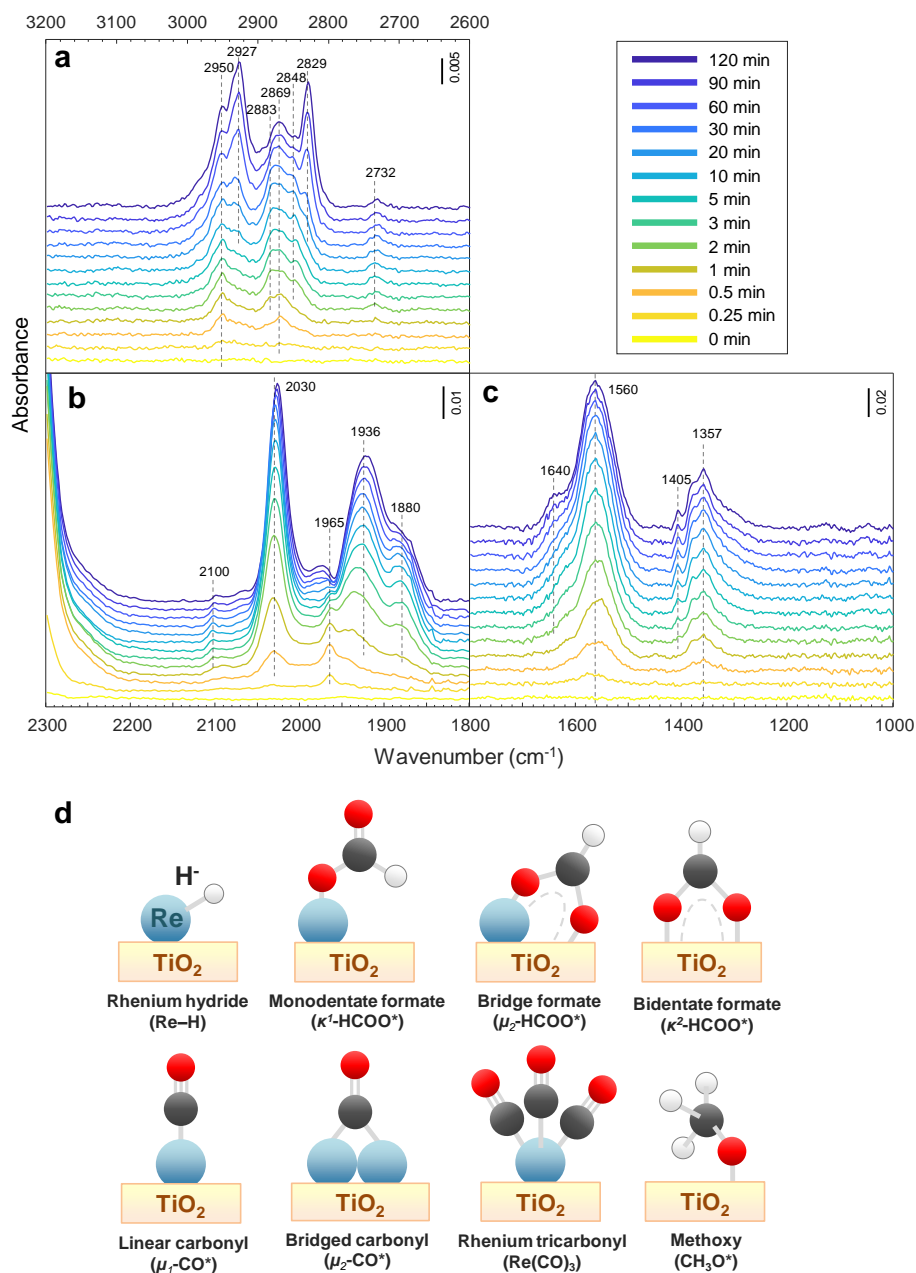


Figure 5.4 Temporal evolution of surface species obtained by *operando* DRIFTS during the initial phase of the reaction with H_2/CO_2 over pre-reduced 3 wt% Re/TiO_2 . **a** $\nu(\text{C-H})$ region, **b**, **c** $\nu(\text{C-O})$ region, and **d** structures of relevant surface species. Reaction conditions: 10 mg catalyst, $\text{H}_2/\text{CO}_2 = 3$, $T = 150\text{ }^\circ\text{C}$, $P = 10\text{ bar}$, $F_{\text{total}} = 10\text{ NmL min}^{-1}$.

An identical experiment was performed over bare TiO₂ to understand the role of TiO₂ support (**Figure S5.4**). In absence of Re metal, only monodentate carbonate (κ^1 -CO₃*, 1369 and 1583 cm⁻¹), monodentate bicarbonate (κ^1 -HCO₃*, 1429, and 1656 cm⁻¹), bidentate bicarbonate (κ^2 -HCO₃*, 1223, 1503 and 1618 cm⁻¹), and weakly adsorbed carbon dioxide (CO₂*, 1334 cm⁻¹) form over TiO₂. There is no signal of C–H bonds in the 2500–3200 cm⁻¹ region, confirming that formate cannot be formed without Re. CO₃* and HCO₃* could form with CO₂ via lattice oxygen and surface hydroxy group (Ti–OH), respectively. Additionally, no traces of CO* were detected since coordination to Re atoms is required for CO* species.

The formation of carbonyl species over Re/TiO₂ during the reaction (**Figure 5.4b**) indicates the reduction of the Re=O bond, which is generally required to form a coordination complex with CO. The tentatively-assigned μ_1 -CO* and μ_2 -CO* form with distinct kinetics. However, the formation of bridge carbonyls is less favored or not possible on atomically-dispersed Re due to the lack of adjacent Re atoms. At the reaction temperature, the adsorption of CO can lead to disruption and dispersion of Re crystallites, which indeed takes place during the reaction as described later, and eventually, lead to the formation of rhenium carbonyls complexes like Re(CO)₃.⁴⁴ Here, based on the spectral features, the carbonyl species are assigned to Re(CO)₃, although the number of carbonyls can fluctuate depending on the coordinating groups and environment around Re.

The involvement of Re–H (1965 cm⁻¹) in the HCOO* formation is confirmed by both ¹³CO₂ hydrogenation (**Figure S5.3**) and CO₂ hydrogenation using D₂ (²H₂) (**Figure S5.2**). Since Re–H band is usually overlapping with that of CO*, the red-shift of all CO* species bands using ¹³CO₂ can reveal an unaffected Re–H vibrational band. On the other hand, the consumption of Re–H (formed during reduction) was revealed by the D₂ exchange, causing the red-shift of Re–D to 1355 cm⁻¹ (overlapping with κ^2 -HCOO*). However, the role of Re–H in HCOO* formation remains ambiguous: through hydrogenation of CO₃* and/or HCO₃* on TiO₂,⁴⁵ or direct activation of CO₂ via hydride transfer over the Re atom.

The normalized IR bands of surface species and mass spectrometry (MS) signals of gaseous products are compared in **Figure 5.5**. During the CO₂ hydrogenation, CH₃OH formation (**Figure 5.5d**) reaches a steady state within 20 min and its profile is similar to that of κ^2 -HCOO* formation (**Figure 5.5a**). In contrast, CH₃O* formation has shown a significant delay in its increase on the catalyst surface. This suggests that the observed CH₃O* is not required as the intermediate for CH₃OH formation. ¹³CO₂ hydrogenation yielded similar temporal evolution of surface and gaseous species to the case of ¹²CO₂ (**Figures 5.5c and 5.5f**).

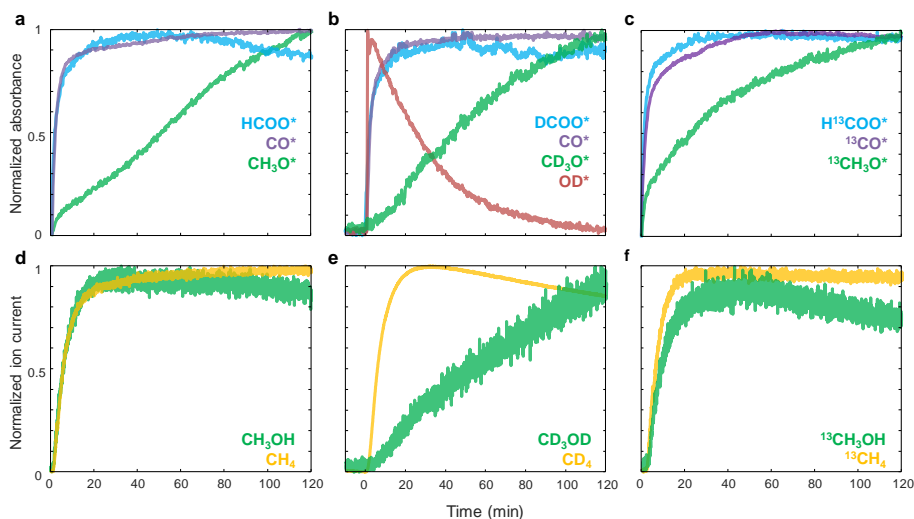


Figure 5.5 Temporal evolution of normalized absorbance of the main surface species obtained from *operando* DRIFTS during reaction with **a** H_2+CO_2 , **b** D_2+CO_2 , and **c** $\text{H}_2+^{13}\text{CO}_2$ over pre-reduced 3 wt% Re/TiO₂. Corresponding normalized ion current signal of methanol and methane obtained from mass spectrometer during reaction with **d** H_2+CO_2 , **e** D_2+CO_2 , and **f** $\text{H}_2+^{13}\text{CO}_2$ over 3 wt% Re/TiO₂. Wavenumber (cm^{-1}): $\kappa^2\text{-HCOO}^*$ (1565), $\mu_1\text{-CO}^*$ (2026), CH_3O^* (2830), $\kappa^2\text{-DCOO}^*$ (2181), $\mu_1\text{-CO}^*$ (2026), CD_3O^* (2063), OD^* (2074), $\kappa^2\text{-H}^{13}\text{COO}^*$ (1527), $\mu_1\text{-}^{13}\text{CO}^*$ (1976), $^{13}\text{CH}_3\text{O}^*$ (2827). The MS of CD_4 at $m/z = 18$ is shown instead of $m/z = 20$ because of overlapping with D_2O and H_2O contribution was assumed to be negligible (**Table S5.2**).

Furthermore, an identical isotopic labeling experiment was performed using D_2 instead of H_2 . During the CO_2 hydrogenation with D_2 , a similar $\kappa^2\text{-DCOO}^*$ (2180 cm^{-1}) formation profile to that of HCOO^* is observed, suggesting that CO_2 activation to $\kappa^2\text{-HCOO}^*$ is not affected by the KIE (**Figure 5.5b**). However, the CD_3OD formation (**Figure 5.5e**) is much slower compared to CH_3OH formation (**Figure 5.5d**) while CD_4 is virtually unaffected (**Figure 5.5e**). This indicates completely different formation mechanisms and involved intermediates to form methanol and methane. The CD_3OD signal shows a similar profile to that of CD_3O^* (2061 cm^{-1}), which behaves oppositely to the terminal deuteroyl group (OD^* , 2704 cm^{-1}). To understand the location and roles of this CD_3O^* as well as the correlation between CD_3O^* and OD^* , a CH_3OH adsorption experiment was performed, followed by titration using D_2 (**Figure S5.5**). After CH_3OH was adsorbed as CH_3O^* , titration of CH_3O^* by D_2 produced CH_3OD and regenerated OD^* similar to the inverted relationship between CD_3O^* and OD^* . This suggested that the observed CH_3O^* species are located on TiO_2 support and originated from CH_3OH adsorption over the Ti-OH sites. A similar experiment is performed over TiO_2 support (**Figure S5.6**). However, the Ti-OD at 2704 cm^{-1}

¹ was not observed, which indicates that the formation of the Ti-OH group via heterolytic dissociation of H₂ is not possible over TiO₂, at least at this temperature. This confirms the role of Re for H₂ dissociation and hydride transfer over TiO₂ via H-spillover.⁴⁶ Moreover, the CD₃O* is unreactive to D₂ without Re. From the results above, it is clear that CD₃OD produced during CO₂ hydrogenation (with D₂) reacted with OD* to form CD₃O*. Therefore, the slower product formation rate due to CD₃OD adsorption led to delayed detection of CD₃OD compared to CD₄.

The instantaneous formation of OD* during CO₂ hydrogenation with D₂ suggests that D-spillover from Re is rapid within the time-scale of the experiment compared to the consumption of Re-H (produced during catalyst activation via reduction with H₂) to form DCOO*. The gradual decline of the OD* concentration discarded the Ti-OH role in κ^2 -HCOO* formation via CO₂ activation into HCO₃* and its subsequent hydrogenation at low temperatures, since κ^2 -HCOO* saturation on the surface was significantly faster than OD* consumption. Notably, the quickly formed OD* on TiO₂ is gradually replaced by CD₃O*. This gradual surface species evolution might be linked to the initial selectivity changes and consequent methyl formate formation during the catalytic tests (**Figure 5.1**).

In addition, CO hydrogenation was also carried out to understand the mechanistic differences to CO₂ hydrogenation, as shown in **Figure S5.7**. Compared with CO₂ hydrogenation, similar Re(CO)₃ (2029, 1915, and 1873 cm⁻¹) are observed. The gaseous CO (2169 cm⁻¹) and, additional peaks of Re₂(CO)₁₀ (2104 and 1995 cm⁻¹) also appear. Only a trace amount of adsorbed H₂O, κ^2 -HCOO*, and CH₃O* is observed, which indicated the lack of CH₃OH formation.¹⁶ There is no indication of formyl (HCO*) and formaldehyde (H₂CO*) produced via stepwise hydrogenation of carbonyls as the main intermediate for CO hydrogenation.⁴⁷ The formate specie which is a more natural intermediate in CO₂ hydrogenation via hydride transfer to CO₂ seems indeed the key intermediate in producing methanol over Re/TiO₂. The roles of both HCOO*, CH₃O*, and CO* were further investigated using D₂ and ¹³CO₂ SSITKA.

5.2.4 Steady-state isotopic transient kinetic analysis (SSITKA)

The SSITKA-DRIFTS is a powerful technique that combines transient isotopic exchanges and *operando* surface species responses while maintaining the characteristics of the steady-state operation keeping the constant partial pressure of reactants. The time-resolved DRIFT spectra containing the kinetically separable and isotopically labeled surface species were analyzed using multivariate spectral analysis, more precisely multivariate curve

resolution (MCR),^{48,49} to obtain their kinetically pure spectra and corresponding concentration profiles. Furthermore, the surface species concentration will be correlated with the concentration of gaseous products detected by MS to extract mechanistic information. To avoid misinterpretation, it should be noted that we show the MS signals of the isotopic products that the m/z are not overlapping. For example, the abundant signals of CD_4 at m/z 20 and 18 overlap with D_2O and H_2O , respectively (Table S5.2).

The roles of formate and carbonyls can be investigated by switching from the $^{13}CO_2+H_2$ to the $^{12}CO_2+H_2$ stream. As shown in Figures 5.6a and 5.6b, $^{13}CO^*$ (1936, 1872, and 1836 cm^{-1}) and $\kappa^2-H^{13}COO^*$ (1527 and 1334 cm^{-1}), formed during the steady-state $^{13}CO_2$ hydrogenation, disappeared after isotopic switching, leading to the formation of $^{12}CO^*$ (2030, 1936 and 1880 cm^{-1}) and $\kappa^2-H^{12}COO^*$ (1560 and 1357 cm^{-1}), respectively. The overlapping bands could be deconvoluted by MCR. Especially, if the concentrations of surface species are kinetically distinguishable, MCR affords to obtain a chemically pure spectrum of each surface species. The MCR-resolved spectra of κ^2-HCOO^* (Figure 5.6d) show two distinguishable characteristics of $\kappa^2-H^{12}COO^*$ and $\kappa^2-H^{13}COO^*$. On the other hand, the MCR-resolved spectra of CO^* show three bands with the same kinetic response, confirming the formation of $Re(CO)_3$ complexes (Figure 5.6c) with kinetically indistinguishable carbonyls on this time-scale.⁵⁰

The MCR-resolved concentration profiles of CO^* and $HCOO^*$ are shown in Figure 5.6e. The symmetrical responses between ^{13}C - and ^{12}C -containing species after isotopic switching are observed. The consumption/formation of κ^2-HCOO^* is noticeably faster than that of $Re(CO)_3$, indicating higher reactivity of κ^2-HCOO^* toward hydrogenation. Moreover, the $Re(^{12}CO)_3$ formation had shown a significant delay compared to $\kappa^2-H^{12}COO^*$ after isotopic switching. This indicates that κ^2-HCOO^* could be the intermediate for CO^* via κ^2-HCOO^* decomposition,⁵¹ and eventually transforms into $Re(CO)_3$ complexes. This finding is consistent with the result from the temporal evolution experiment, in which $Re-H$ and $HCOO^*$ were the first species to form (*vide supra*).

In the gas phase, the $^{13}CH_3OH$ response decays faster than $^{13}CH_4$ (Figure 5.6f), which is congruent to the faster consumption rate of $\kappa^2-H^{13}COO^*$ compared to $^{13}CO^*$ (Figure 5.6e). This suggested the different pathways of CH_3OH and CH_4 formation: CH_3OH via direct hydrogenation of κ^2-HCOO^* , and CH_4 via CO^* formation and subsequent hydrogenation. It should be noted that there was no noticeable change in the CH_3O^* profile detected from $\nu(C-H)$ upon switching from the $^{13}CO_2+H_2$ to the $^{12}CO_2+H_2$ stream, which suggested no correlation between CH_3O^* and CH_4 .

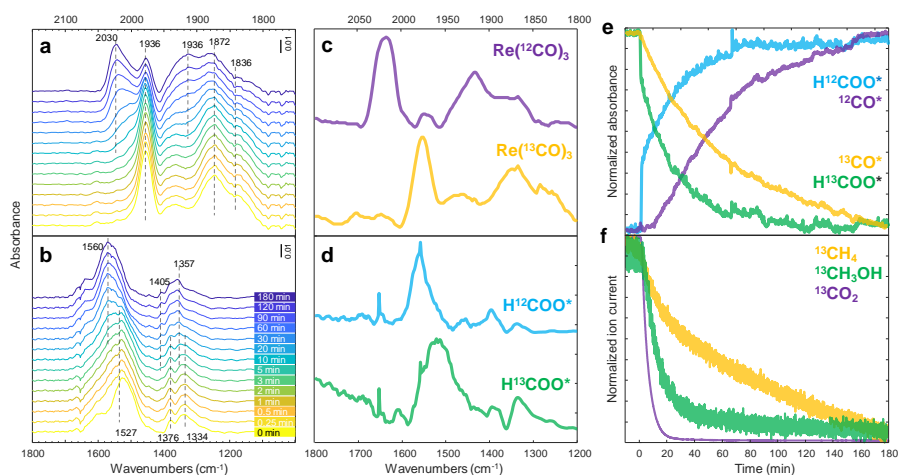


Figure 5.6 Transient responses of surface species and gas products during the steady-state isotopic switching from $^{13}\text{CO}_2+\text{H}_2$ to $^{12}\text{CO}_2+\text{H}_2$. Time-resolved DRIFT spectra of **a** $^{12}\text{CO}^*$ and $^{13}\text{CO}^*$, and **b** $\text{H}^{12}\text{COO}^*$ and $\text{H}^{13}\text{COO}^*$. **c** and **d** Components spectra obtained by MCR applied on the time-resolved DRIFT spectra. **e** Concentration profiles of the spectra of the corresponding components obtained by MCR. **f** Corresponding normalized ion current signal of isotope-labeled products. *The formation of $^{12}\text{CH}_4$ and $^{12}\text{CH}_3\text{OH}$ are not shown due to the contribution from $^{13}\text{CH}_4$ and $^{13}\text{CH}_3\text{OH}$. Reaction conditions: 10 mg catalyst, $\text{H}_2/\text{CO}_2 = 3$, $T = 150^\circ\text{C}$, $P = 10\text{ bar}$, $F_{\text{total}} = 10\text{ Nml min}^{-1}$.

Transient isotopic switching from steady-state CO_2+D_2 to CO_2+H_2 feed can shed light on the roles of $\kappa^2\text{-HCOO}^*$ and CH_3O^* . As shown in **Figure 5.7a**, $\kappa^2\text{-DCOO}^*$ and CD_3O^* formed during the previous steady-state started to disappear after isotopic switching, leading to the formation of $\kappa^2\text{-HCOO}^*$ and CH_3O^* , as shown in **Figure 5.7b**. However, the consumption/formation of $\kappa^2\text{-DCOO}^*/\kappa^2\text{-HCOO}^*$ was noticeably faster than those of $\text{CD}_3\text{O}^*/\text{CH}_3\text{O}^*$. Similar profiles were observed in transient isotopic switching from steady-state CO_2+H_2 to CO_2+D_2 (**Figures S5.8 and S5.9**). The MCR provides two kinetically distinguishable spectra of $\kappa^2\text{-HCOO}^*$ and CH_3O^* in the C–H stretching region, and the other two spectra of $\kappa^2\text{-DCOO}^*$ and CD_3O^* in the C–D stretching region (**Figures 5.7c and 5.7d**), as well as their concentration profiles (**Figure 5.7e**). The concentration profiles obtained by MCR show a symmetrical relationship between deuterated species and hydrogenated species, indicating the isotopic exchange. CD_3OH spiked rapidly after isotopic switching followed by a long decay (**Figure 5.7f**), indicating that the reaction between CD_3O^* and spilled-over H takes place and takes time due to the high stability of the former on TiO_2 .

Importantly, CH_3OH is produced right after switching and reaches the steady state after 20 min regardless of the remaining $\kappa^2\text{-DCOO}^*$ that disappears after 60 min and of CD_3O^* that reacts slowly and remains on the surface even after 120 min. This piece of evidence confirms that observable

CH_3O^* on TiO_2 is a spectator and not the intermediate for CH_3OH formation. Similarly, the slowly reacted $\kappa^2\text{-HCOO}^*$ on TiO_2 could be proven as a spectator as well. However, there is the possibility that only $\kappa^2\text{-HCOO}^*$ located adjacently to the Re is the active species, while those not in proximity are unreactive. Transient techniques are required to capture the short-lived surface species responsible for CH_3OH .

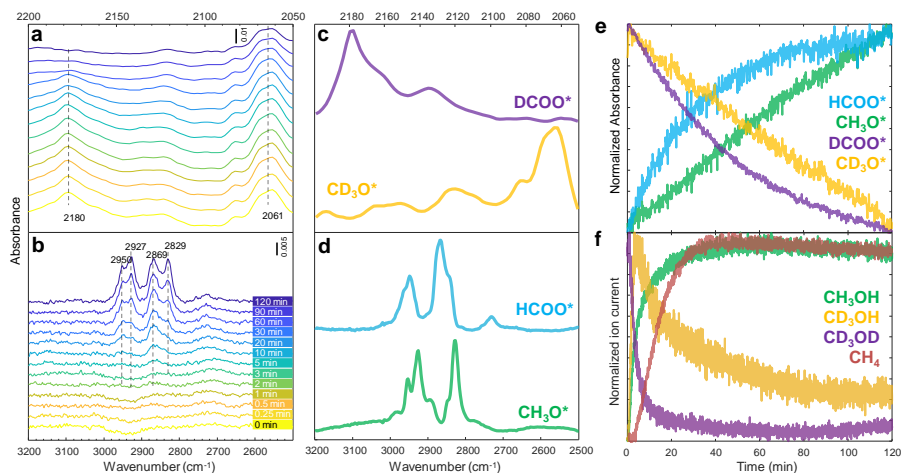


Figure 5.7 Transient responses of surface species and gas products during the steady-state isotopic switching from CO_2+D_2 to CO_2+H_2 . Time-resolved DRIFT spectra of **a** DCOO^* and CD_3O^* , and **b** HCOO^* and CH_3O^* . **c** and **d** Components spectra obtained by MCR applied on the time-resolved DRIFT spectra. **e** Concentration profiles of the spectra of the corresponding components obtained by MCR. **f** Corresponding normalized ion current signal of isotope-labeled products. Reaction conditions: 10 mg catalyst, $\text{H}_2(\text{or } \text{D}_2)/\text{CO}_2 = 3$, $T = 150^\circ\text{C}$, $P = 10\text{ bar}$, $F_{\text{total}} = 10\text{ Nml min}^{-1}$.

5.2.5 Transient experiment: concentration modulation

The transient experiment can utilize not only isotopes but also the drastic changes in the reactant concentration, e.g., passing only one of the reactants momentarily, allowing the detection of surface species responding to periodic perturbation. This technique can improve sensitivity and unveils spectral features that are not accessible by steady-state experiments. The transient experiment requires multiple modulation cycles for the system to reach a quasi-steady state. Such states include the oxidation state of active metal, local structure, surface species coverage, etc. The responses of those states after the quasi-steady state are similar in the following cycles, allowing cycle averaging to improve the signal-to-noise ratio.^{23,24}

The example of a quasi-steady state over Re/TiO₂ is clearly shown in the transient experiment of the modulated flow of H₂+CO₂ vs. CO₂. As shown in **Figure 5.8a**, the reaction under H₂+CO₂ had reached a steady state (①) before the transient experiment. Modulation with CO₂ induced structural change of Re/TiO₂, leading to an increase in the CH₃OH signal in the gas phase. The structural change reached a quasi-steady state after 3 cycles (②) and remained irreversible after the transient experiment (③). The Re L₃-edge XANES showed a notable increase in the white line intensity compared to the previous steady-state (**Figure 5.8b**). During the quasi-steady state (②) the change in response to the periodic concentration change was infinitesimal, but the subtle change was confirmed by the phase-resolved spectra obtained by phase-sensitive detection (**Figure 5.8c**).⁵² The in-phase and out-of-phase positions are at 10537 eV and 10543.5 eV, but they are assumed to be artificially created peaks to describe the shift of absorption peaks. Rather this study shows that the Re redox state does change, although the extent is small, around the peak around 10540 eV, which can be in the range of Re⁰-Re⁴⁺.

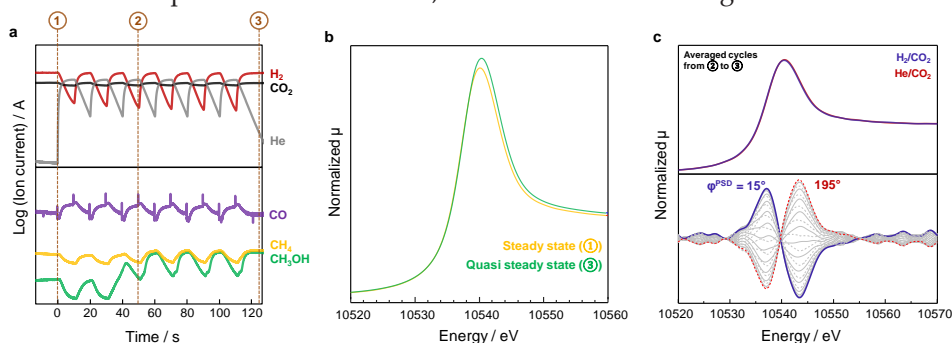


Figure 5.8 Transient H₂+CO₂ and He+CO₂ experiment. **a** Corresponding normalized ion current signal from a mass spectrometer. **b** *operando* Re L₃-edge XANES spectra. **c** Phase-resolved amplitude spectra from Re L₃-edge XANES: Spectra is within $\phi^{\text{PSD}} = 0\text{--}360^\circ$ at steps of $\phi^{\text{PSD}} = 15^\circ$. He balances are used in the CO₂ phase to maintain partial pressure. Reaction conditions: H₂/CO₂ = 3, T = 150 °C, P = 10 bar, F_{total} = 10 Nml min⁻¹.

Representative HAADF-STEM images of reduced and spent Re/TiO₂ (**Figures 5.9a and 5.9b**) show that increased dispersion of Re clusters is responsible for the irreversible change until reaching the quasi-steady state (①). As shown in **Figures 5.9c and 5.9d**, the particle size distribution of Re clusters becomes narrower toward single Re atoms and clusters containing a few Re atoms after the transient reaction. The decomposition and (re)dispersion of metal nanoparticles are often related to the concentration of defect sites that enthalpically stabilize adatoms.^{53,54} The Raman spectra during the transient experiment show no shifts in two E_g modes (163 and 193 cm⁻¹) toward higher frequency as an indication of oxygen vacancy over

TiO₂.^{55,56} However, the lower signal intensity during H₂+CO₂ than He+CO₂ due to the baseline shift implies the relatively oxygen-deficient TiO₂ that may facilitate the decomposition and (re)dispersion of Re particles (**Figure S5.10**).

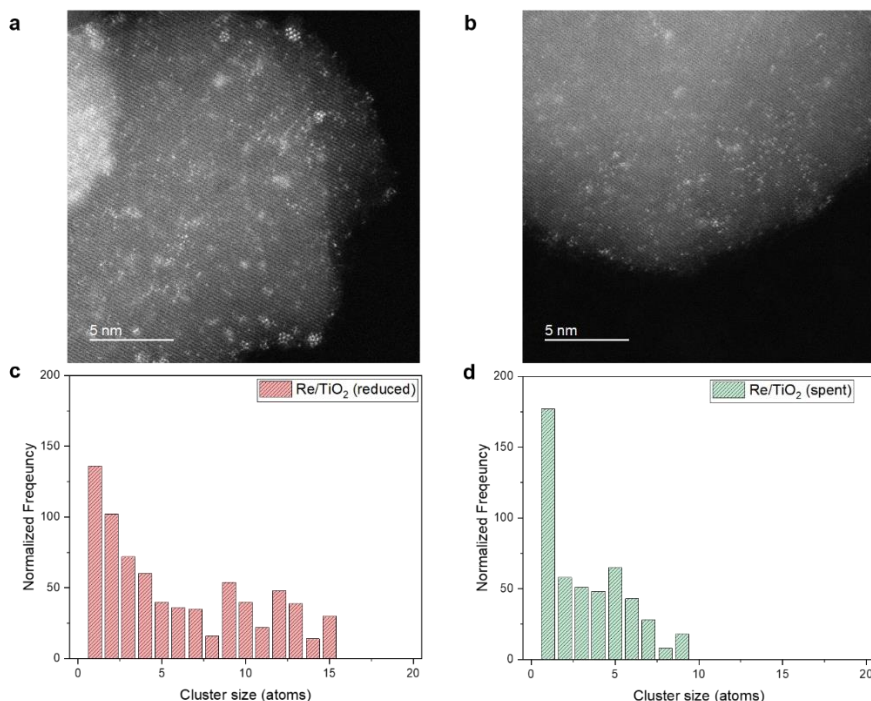


Figure 5.9 Representative HAADF-STEM images of Re/TiO₂: **a** after reduction (500 °C in H₂) and **b** after the transient experiment (150 °C and 10 bar). **c** Re cluster size distribution of Re/TiO₂ was determined from HAADF-STEM: **c** after reduction (500 °C in H₂) and **d** after the transient experiment (150 °C and 10 bar). Normalized frequency = Number of atoms in a specific cluster size × Frequency.

To gain more precise insights into the redox state of Re, an AP-XPS study was performed (**Figure 5.10**). Re/TiO₂ was reduced at 450 °C, which is lower than the standard reduction temperature for the pretreatment, due to a limitation of our experimental setup (For more detailed experimental and analysis procedures, see the Supporting Information). Re/TiO₂ after reduction at 450 °C was found to contain multi-oxidation states of Re such as Re⁰, Re²⁺, and Re⁴⁺. Although Re²⁺ is not known to exist as a stable bulk oxide, it can exist as surface species.²⁹ Note that other species including Re³⁺ and Re¹⁺, which have been reported as surface species and/or in metal complexes,²⁹ can also be present although the fitting with Re⁰, Re²⁺, and Re⁴⁺ gave a sufficient fit in the present study. The amount of surface cationic Re^{δ+} species increased under the CO₂ atmosphere at 150 °C, suggesting the Re⁰ oxidation by CO₂

(Table 5.1). The subsequent introduction of H₂ reduced the formed cationic Re^{δ+} species, followed by reoxidation by CO₂. These results indicate that CO₂ oxidizes the supported Re and the oxidized Re is reduced by H₂ reversibly, suggesting the participation of surface cationic Re^{δ+} species such as Re⁴⁺ and Re²⁺ in CO₂ hydrogenation, while the remaining Re⁰ plays role in H₂ activation. We are aware that measurements at low pressures (millibar scale) may lead to different conclusions to identify catalytic species.⁵⁷ However, direct observations of the surface Re species under repeated reduction (H₂) – oxidation (CO₂) cycles with XPS techniques can give qualitative insights into the redox behavior of the Re species.

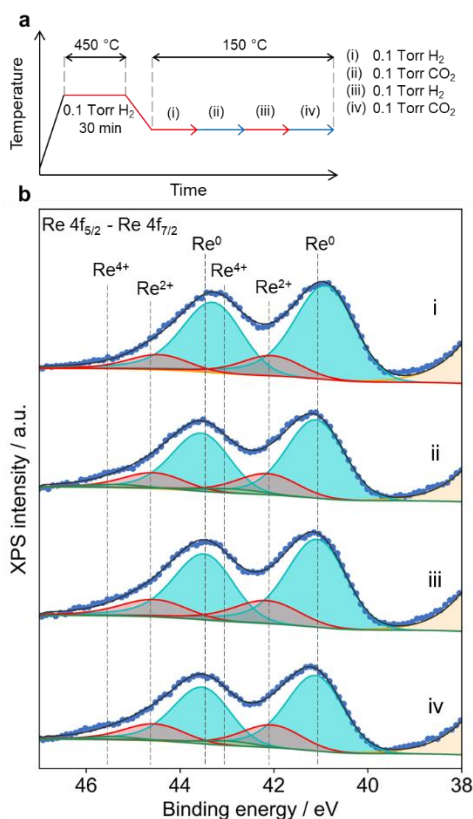


Figure 5.10 (a) Experimental conditions during the AP-XPS study. (b) Re 4f AP-XPS spectra of Re/TiO₂ under exposure to (i) H₂, (ii) CO₂, (iii) H₂, and (iv) CO₂ at 150 °C. Blue dots: raw spectrum; black line: sum; green: Re⁴⁺; red: Re²⁺; light blue: Re⁰; yellow: Ti 3p.

Table 5.1 Peak concentrations in the Re 4f AP-XPS spectra of Re/TiO₂ at 150 °C under various gas conditions (**Figure 5.10**).

Gas condition	Peak concentration / %		
	Re ⁰	Re ²⁺	Re ⁴⁺
(i) 0.1 Torr H ₂ ^a	83.2	14.5	0
(ii) 0.1 Torr CO ₂	73.9	20.4	4.4
(iii) 0.1 Torr H ₂ (2 nd)	76.8	22.8	0.4
(iv) 0.1 Torr CO ₂ (2 nd)	74.5	21.6	3.9

^a Measured at 150 °C right after the H₂ reduction pretreatment at 450 °C.

The transient DRIFT spectra obtained by alternatingly passing H₂+CO₂ and (He+CO₂) are shown in **Figure 5.11a**. After CO₂ hydrogenation at a steady state, the surface of the catalyst, especially the TiO₂, is expected to be saturated with CH₃O* and HCOO*, and switching to CO₂ allows capturing the activation process of CO₂ by Re–H with less formate spillover. The MCR-resolved spectra obtained after a quasi-steady state reveal additional surface species at 1643, 1583, 1405 1359 1307 cm⁻¹ (**Figure 5.11b**, green)^{50,5131,32} apart from κ^2 -HCOO* (**Figure 5.11b**, blue). Regarding κ^2 -HCOO*, H spillover from Re over TiO₂ may create OH*, but the reaction D₂+CO₂ (**Figure 5.5b**) suggested that CO₂ was not activated over OH* into HCO₃* which could be further hydrogenated to HCOO*. These observations pointed out that the origin of HCOO* on TiO₂ is via formate spillover from the Re sites. The Ti⁴⁺ Lewis acidic sites at the interface could promote formate spillover similar to the surface chemistry observed over Ag on Al₂O₃ or ZrO₂.^{26,27}

On the other hand, the more complex spectra (**Figure 5.11b**, green) could be interpreted as H₂O*, CO₃*, HCO₃*^{58,59} or even HCOOCH₃*.^{38,39} However, MCR-resolved spectra of CO₃* and HCO₃* identified under the CO₂ hydrogenation condition over TiO₂ did not match with the spectral features of the observed surface species excluding the possibility of (bi)carbonates.^{23,24} The bands at 1583, 1405, and 1359 cm⁻¹ can be assigned to bridging formate (μ_2 -HCOO*) located over Re or Re-O-Ti interface.⁴³ The unassigned bands at 1643 and 1307 cm⁻¹ could be carboxylate on rhenium (Re–COOH), 1647 cm⁻¹,^{52,53} but this is unlikely with CO₂ directly interacting with Re. On the other hand, CO₂ can be hydrogenated molecularly over Re(CO)₃ complexes (i.e. its hydride form).⁶⁰ Thus-formed monodentate formate (κ^1 -HCOO*) binding on the rhenium center of Re(CO)₃ complexes was reported around 1630 and 1280 cm^{-1,55–57} which is in close agreement with the observed bands. All assignments seem congruent with the results obtained during CO₂ hydrogenation (**Figure 5.4**), in which these bands appeared after the formation of the Re(CO)₃ complex. The complexity of the

MCR-resolved spectrum suggested that CO₂ activation over Re-center and subsequent hydrogenation of CO₂ over Re-H into μ_2 -HCOO*, located on Re or Re-O-Ti, and κ^1 -HCOO* are kinetically indistinguishable at the current time resolution as they appear in the same spectrum (**Figure 5.11b**, green).

The concentration profiles of the two kinetically distinguishable spectra obtained by MCR are shown in **Figure 5.11c**. During the CO₂ phase, the amount of Re-H and κ^1 -HCOO* decreases rapidly and gradually, respectively, while κ^2 -HCOO* increases via spillover of formate from Re to TiO₂. This indicates that CO₂ is immediately activated by Re-H and the formed formate spills over onto TiO₂ very quickly. The gradual decrease of κ^1 -HCOO* indicates that the formate on Re is unstable under CO₂ without hydrogen as expected, but the slow decay may imply that the formates on TiO₂ may be reversibly transformed to κ^1 -HCOO* to some extent and thus delaying its decomposition. After switching to the H₂+CO₂ phase, Re-H is rapidly regenerated and subsequently produces κ^1 -HCOO* (fast formate) as a source of CH₃OH (**Figure 5.11d**). Interestingly, κ^2 -HCOO concentration decrease, indicating that the κ^2 -HCOO* close to the perimeter spills over back towards Re instantaneously. The proposed mechanisms of formate formation and spillover are summarized in **Figure 5.11e**.

The MCR-resolved spectra obtained in C-H stretching region (**Figure S5.11**) have shown a multi-band spectrum of HCOO* with a similar concentration profile of κ^1 -HCOO* in the C-O stretching region, while that of CH₃O* on TiO₂ is kinetically non-overlapping and behaves similarly to κ^2 -HCOO* during CO₂ phase but decays much slower in H₂+CO₂ phase. This CH₃O* is produced via κ^1 -HCOO* hydrogenation to CH₃OH that instantly adsorbed TiO₂ to form relatively stable CH₃O*.

Furthermore, aiming to decouple the influences of two reactive components on surface species evolution, another type of transient experiment was performed by alternately passing (He+)-CO₂ and H₂-(+He) over Re/TiO₂. From the pristine reduced catalyst under H₂, surface species from CO₂ started to evolve every cycle after switching to CO₂ until a quasi-steady state is reached, indicating the reaction between CO₂ and adsorbed Re-H. Due to its transient nature, a short-lived species that cannot be detected under steady-state CO₂ hydrogenation can be revealed (**Figure 5.12a**). The MCR resolved spectra show a characteristic band at 1690 cm⁻¹ apart from κ^2 -HCOO* (**Figure 5.12b**), which can be assigned as formyl group (HCO*)⁶¹⁻⁶³ or formic acid (HCOOH*).^{41,64} The missing corresponding C-H bonds suggested that such species could also be carboxylate (COOH*) on Re,⁶⁵⁻⁶⁷ or κ^1 - or κ^2 -HCO₃* on TiO₂.⁵⁹ However, the formation of HCO₃* was more congruent with the role of TiO₂ support in CO₂ activation to CO₃* and HCO₃* during CO₂ hydrogenation in absence of Re (**Figure S5.4**).

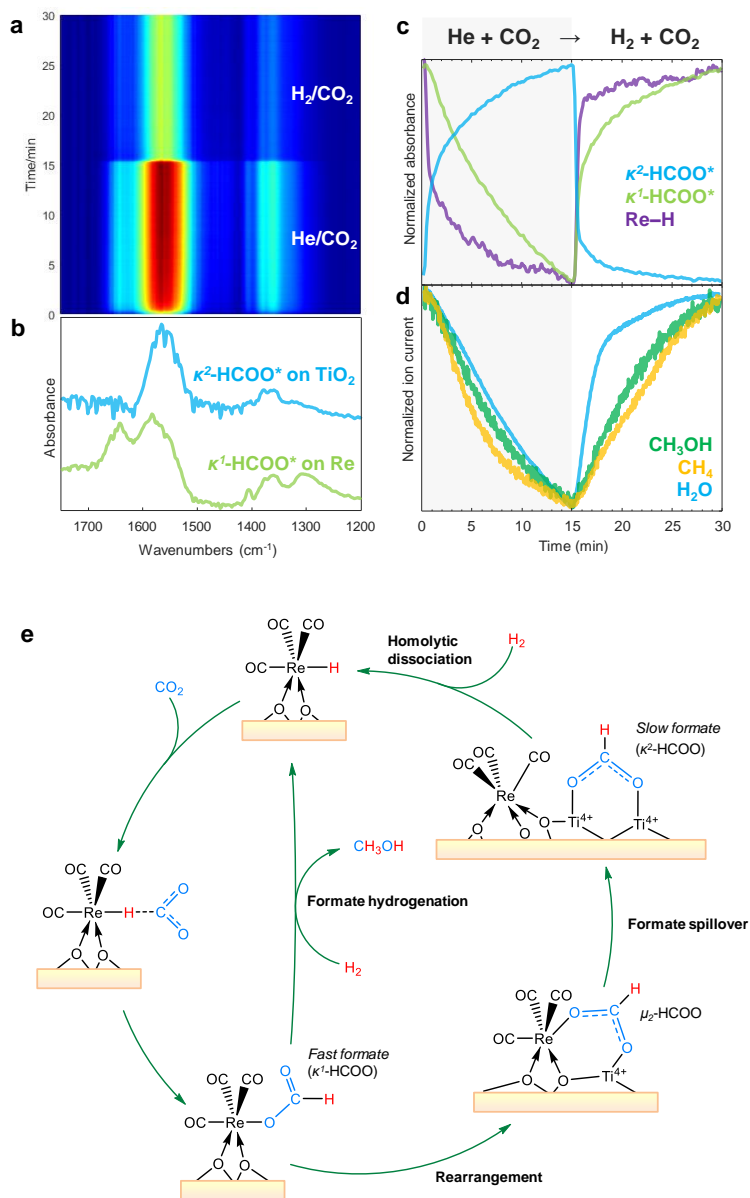


Figure 5.11 Transient DRIFTS study on CO_2 hydrogenation over 3 wt % Re/TiO_2 catalyst. **a** Time-resolved DRIFT spectra upon transient concentration perturbation using $\text{H}_2 + \text{CO}_2$ and $\text{He} + \text{CO}_2$ at 150 °C and 10 bar. **b** Components spectra obtained by multivariate spectral analysis applied on the time-resolved DRIFT spectra. **c** Concentration profiles of the corresponding components spectra obtained by the multivariate spectral analysis. **d** Corresponding normalized ion current signal obtained from MS. **e** Proposed mechanism for CO_2 activation to monodentate formate. Possible dihydride species are shown as monohydride. Reaction conditions: 10 mg catalyst, $\text{H}_2/\text{CO}_2 = 3$, $T = 150$ °C, $P = 10$ bar, $F_{\text{total}} = 10 \text{ N mL min}^{-1}$.

The concentration profile (**Figure 5.12c**) showed that $\kappa^2\text{-HCOO}^*$ forms during the CO_2 phase faster than HCO_3^* while both are rapidly converted off during the H_2 phase. However, not all $\kappa^2\text{-HCOO}^*$ was completely removed during the H_2 phase (**Figure 5.12a**), confirming the existence of unreactive or slow formates as spectators. On the other hand, the vanishing of HCO_3^* suggested the short-lived nature that makes it unobservable during steady-state CO_2 hydrogenation (**Figure 5.4**). HCO_3^* appeared only during the CO_2 phase due to the limited hydrogenation (by Re-H or H^*). Since the CH_4 is produced in combination with HCO_3^* formation during the CO_2 phase (**Figure 5.12d**), hydrogenation of HCO_3^* into Re-CO could be the pathway for CH_4 formation. This was supported by the observation of methyl (CH_3^*) on ReO_x at 2975 cm^{-1} , which forms simultaneously during the CO_2 phase (**Figure S5.12**).⁶⁸ The SSITKA: D_2+CO_2 to H_2+CO_2 experiment (**Figure S5.9**) also confirms the hydrogenation of CD_3^* intermediate into CHD_3 , which occurs before CH_4 formation. A long decay in the CHD_3 profile and delayed CH_4 formation suggest that CD_3^* is less reactive than HCOO^* intermediates forming CH_3OH . Moreover, HCO_3^* hydrogenation to Re-CO is less favorable under common CO_2 hydrogenation conditions due to the tendencies for HCOO^* formation assisted by Re-H , as well as the occupation of Re sites in the form of $\text{Re}(\text{CO})_3$. This is confirmed by the slower exchange between $\text{Re}(\text{CO})_3$ isotopes than HCOO^* during the SSITKA: $^{13}\text{CO}_2+\text{H}_2$ to $^{12}\text{CO}_2+\text{H}_2$ experiment (**Figure 5.6**). All mechanistic insights from transient experiments affirm the main intermediates for both CH_3OH and CH_4 formation over sub-nano cluster Re/TiO_2 . Unfortunately, the insight into intermediates of HCOOCH_3 remains missing in this study due to the pressure limitation. However, the mechanism can be extrapolated from our previous works in which CH_3OH reacts with HCOOH retaining by HCOO^* spillover^{26,27} and surface-coverage dependent productivity (**Figure 5.1**). HCOOH formation from HCOO^* was proposed over cluster-sized Cd_4/TiO_2 via hydride-coordinated metal center and proton-bonded O site of TiO_2 ,⁶⁹ which could be similar in the case of Re/TiO_2 .

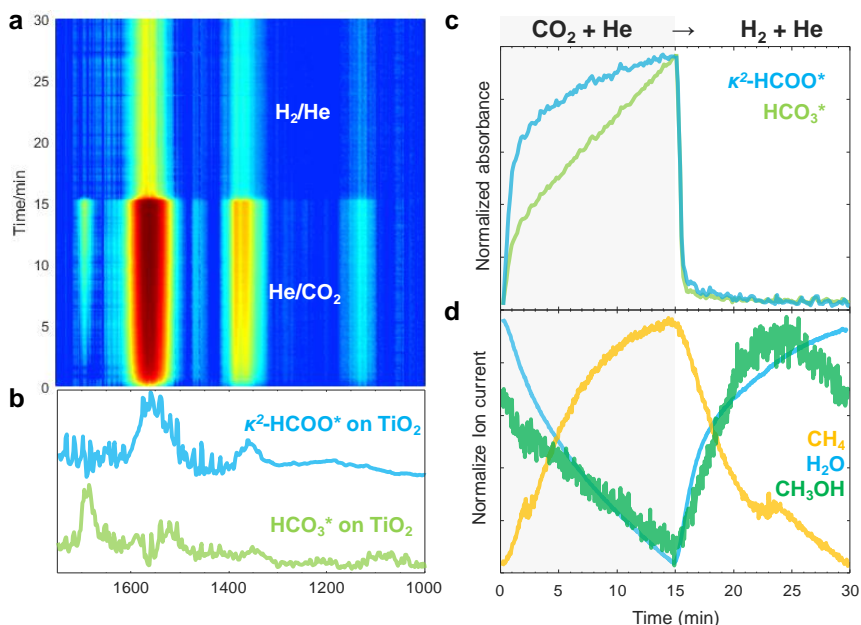


Figure 5.12 Transient DRIFTS study on CO₂ hydrogenation over 3 wt % Re/TiO₂ catalyst. **a** Time-resolved DRIFT spectra upon transient concentration perturbation using H₂+He and He+CO₂. **b** Components spectra obtained by multivariate spectral analysis applied on the time-resolved DRIFT spectra. **c** Concentration profiles of the corresponding components spectra obtained by the multivariate spectral analysis. **d** Corresponding normalized ion current signal obtained from MS. Reaction conditions: 10 mg catalyst, H₂/He = He/CO₂ = 3, T = 150 °C, P = 10 bar, F_{total} = 10 Nml min⁻¹.

5.2.6 Proposed reaction mechanisms

The mechanistic insights uncover the origin of high performance observed for the Re/TiO₂ catalyst at low temperatures. For 3 wt% Re/TiO₂, redispersion of Re clusters into smaller clusters and single-atom Re improved the CH₃OH formation performance. The redispersion of Re clusters resulted in an increase in the number of highly-dispersed Re^{δ+} species while maintaining a large number of Re⁰ species in the (sub)nano-clusters. The Re⁰ sites play a role as an H₂ activator and transfer H to the Re^{δ+} species present near the perimeter or rather single-atom Re^{δ+}. The latter forms Re(CO₃) complex and its hydride (Re–H). Such Re^{δ+} species can activate CO₂ molecularly, especially after κ¹-HCOO* formation. Notably, the observed κ¹-HCOO* is rarely reported over metal-supported catalysts since its formation is likely not possible over the extended metal surface (e.g. Re⁰), yet they can be identified over the metal active center of molecular complexes (e.g. Ru and Ir complexes).^{70,71} Further hydrogenation of κ¹-HCOO* to CH₃OH requires H supplied from Re⁰ species, thus requiring two types of sites for efficient

hydrogenation of $\kappa^1\text{-HCOO}^*$. The simplified mechanism is shown in **Figure 5.13**.

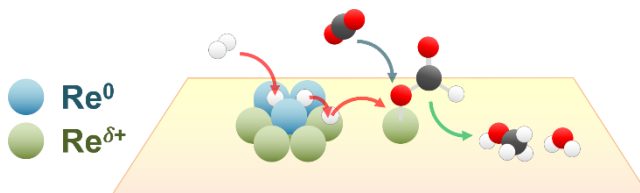


Figure 5.13 The simplified mechanism involving Re^0 and $\text{Re}^{\delta+}$ species.

The mechanistic propositions above are congruent with the structure-relationship reported previously.¹⁶ In the previous work, the wt% of Re/TiO_2 was studied at 0.2, 1, 5, 10, and 20 wt %. The highest CH_3OH selectivity was obtained from the 1 wt% Re/TiO_2 , which contained the subnanometer size of the Re species. The CH_4 selectivity gradually increases with the loading of at 5-20 wt%, which should be related to the increased fraction of Re^0 species that can over-hydrogenate CO^* to CH_4 . However, isolated single Re species more dominantly present for 0.2 wt% Re sample favor CO formation via formate decomposition, since single atom $\text{Re}^{\delta+}$ species alone lack the ability to activate H_2 when formate is coordinating to the Re center, and further hydrogenate $\kappa^1\text{-HCOO}^*$ to CH_3OH . Therefore, it can be concluded that the Re/TiO_2 requires both Re^0 and $\text{Re}^{\delta+}$ species for efficient methanol formation. Insufficient H supply from Re^0 species can lead to formate decomposition to CO, while the excess leads to over-hydrogenation to CH_4 . $\text{Re}^{\delta+}$ species can activate CO_2 and stabilize $\kappa^1\text{-HCOO}^*$ for faster hydrogenation to CH_3OH .

5.3 Conclusion

In summary, Re/TiO_2 was superior to $\text{Cu}/\text{ZnO}/\text{Al}_2\text{O}_3$ for CO_2 -to- CH_3OH at low temperatures thanks to the distinct reaction pathway, activated by the unique interactions between Re and TiO_2 , and less formation of HCOOCH_3 over Lewis acid sites on Al_2O_3 . During operation using 3 wt% Re, Re clusters become more dispersed, increasing the number of cationic Re single atoms and forming rhenium tricarbonyl complexes. On the other hand, metallic Re species remain a major fraction and act as an H_2 activator for H-spillover to the cationic Re sites. The formation of Re-H is the first step in CO_2 activation to monodentate formate over the cationic Re species before its further hydrogenation to CH_3OH or spillover onto TiO_2 support, becoming less reactive bidentate formate (spectator). Formed CH_3OH tends to adsorb

strongly over the hydroxyl sites on TiO₂, forming methoxy species (spectator). Surface bicarbonates are observed as an intermediate for carbonyl species, which is further hydrogenated into methyl species, leading to CH₄ formation. These mechanistic insights explain the unique reactivity of Re/TiO₂ with two kinds of sites, being able to form active formate and further hydrogenation at low temperatures and, can help polish the concept to design more selective low-temperature methanol synthesis catalysts.

5.4 Experimental

Experimental procedures, commercial chemicals, catalyst preparation procedures, instrument specifications, and characterization techniques are covered in greater detail in the Supporting Information.

5.5 References

- 1 A. Goepfert, M. Czaun, J.-P. Jones, G. K. Surya Prakash, and G. A. Olah, *Chem. Soc. Rev.*, 2014, 43, 7995–8048.
- 2 G. A. Olah, A. Goepfert and G. K. S. Prakash, *Beyond Oil and Gas: The Methanol Economy*, Wiley, 2009, vol. 44.
- 3 G. A. Olah, *Angew. Chem., Int. Ed.*, 2013, 52, 104–107.
- 4 A. Álvarez, A. Bansode, A. Urakawa, A. v. Bavykina, T. A. Wezendonk, M. Makkee, J. Gascon and F. Kapteijn, *Chem. Rev.*, 2017, 117, 9804–9838.
- 5 J. G. van Bennekom, J. G. M. Winkelman, R. H. Venderbosch, S. D. G. B. Nieland and H. J. Heeres, *Ind. Eng. Chem. Res.*, 2012, 51, 12233–12243.
- 6 J. G. van Bennekom, R. H. Venderbosch, J. G. M. Winkelman, E. Wilbers, D. Assink, K. P. J. Lemmens and H. J. Heeres, *Chem. Eng. Sci.*, 2013, 87, 204–208.
- 7 A. Bansode and A. Urakawa, *J. Catal.*, 2014, 309, 66–70.
- 8 R. Gaikwad, H. Reymond, N. Phongprueksathat, P. Rudolf von Rohr and A. Urakawa, *Catal. Sci. Technol.*, 2020, 10, 2763–2768.
- 9 Y. Yang, C. A. Mims, D. H. Mei, C. H. F. Peden, and C. T. Campbell, *J. Catal.*, 2013, 298, 10–17.
- 10 E. L. Kunkes, F. Studt, F. Abild-Pedersen, R. Schlögl and M. Behrens, *J. Catal.*, 2015, 328, 43–48.
- 11 A. Karelovic, G. Galdames, J. C. Medina, C. Yévenes, Y. Barra and R. Jiménez, *J. Catal.*, 2019, 369, 415–426.
- 12 E. Lam, J. J. Corral-Pérez, K. Larmier, G. Noh, P. Wolf, A. Comas-Vives, A. Urakawa and C. Copéret, *Angew. Chem., Int. Ed.*, 2019, 58, 13989–13996.
- 13 T. Iizuka, M. Kojima and K. Tanabe, *J. Chem. Soc. Chem. Commun.*, 1983, 638–639.
- 14 Z. Xu, Z. Qian, K. Tanabe, H. Hattori, *Bull., Chem. Soc. Jpn.*, 1991, 64, 1664–1668.
- 15 C. Shen, K. Sun, R. Zou, Q. Wu, D. Mei and C. J. Liu, *ACS Catal.*, 2022, 12, 12658–12669.
- 16 K. W. Ting, T. Toyao, S. M. A. H. Siddiki and K. Shimizu, *ACS Catal.*, 2019, 9, 3685–3693.

- 17 M. L. Gothe, F. J. Pérez-Sanz, A. H. Braga, L. R. Borges, T. F. Abreu, R. C. Bazito, R. V. Gonçalves, L. M. Rossi and P. Vidinha, *J. CO₂ Util.*, 2020, 40, 101195.
- 18 K. W. Ting, Z. Maeno, S. M. A. Hakim Siddiki, K. I. Shimizu and T. Toyao, *Chem. Lett.*, 2021, 50, 158–161.
- 19 S. R. Bare, S. D. Kelly, F. D. Vila, E. Boldingh, E. Karapetrova, J. Kas, G. E. Mickelson, F. S. Modica, N. Yang and J. J. Rehr, *J. Phys. Chem. C*, 2011, 115, 5740–5755.
- 20 S. Avramescu, C. D. Ene, M. Ciobanu, J. Schnee, F. Devred, C. Bucur, E. Vasile, L. Colaciello, R. Richards, E. M. Gaigneaux, et al., *Catal. Sci. Technol.*, 2022, 12, 167–180
- 21 G. Noh, S. R. Docherty, E. Lam, X. Huang, D. Mance, J. L. Alfke and C. Copéret, *J. Phys. Chem. C*, 2019, 123, 31082–31093.
- 22 G. Noh, E. Lam, D. T. Bregante, J. Meyet, P. Šot, D. W. Flaherty and C. Copéret, *Angew. Chem., Int. Ed.*, 2021, 60, 9650–9659.
- 23 A. Urakawa, T. Bürgi and A. Baiker, *Chem. Eng. Sci.*, 2008, 63, 4902–4909.
- 24 P. Müller and I. Hermans, *Ind. Eng. Chem. Res.*, 2017, 56, 1123–1136.
- 25 P. D. Srinivasan, B. S. Patil, H. Zhu and J. J. Bravo-Suárez, *React. Chem. Eng.*, 2019, 4, 862–883.
- 26 J. J. Corral-Pérez, C. Copéret and A. Urakawa, *J. Catal.*, 2019, 380, 153–160.
- 27 J. J. Corral-Pérez, A. Bansode, C. S. Praveen, A. Kokalj, H. Reymond, A. Comas-Vives, J. VandeVondele, C. Copéret, P. R. von Rohr and A. Urakawa, *J. Am. Chem. Soc.*, 2018, 140, 13884–13891.
- 28 E. Lam, J. J. Corral-Pérez, K. Larmier, G. Noh, P. Wolf, A. Comas-Vives, A. Urakawa and C. Copéret, *Angew. Chem., Int. Ed.*, 2019, 58, 13989–13996.
- 29 M. T. Greiner, T. C. R. Rocha, B. Johnson, A. Klyushin, A. Knop-Gericke and R. Schlögl, *Z. Phys. Chem.*, 2014, 228, 521–541.
- 30 K. W. Ting, S. Mine, A. Ait El Fakir, P. Du, L. Li, S. M. A. H. Siddiki, T. Toyao, K.-I. Shimizu, *Phys. Chem. Chem. Phys.*, 2022, 24, 28621–28631.
- 31 J. Chen, J. Kawai, K. Ozawa, R. Toyoshima, K. Tomishige and H. Kondoh, *J. Phys. Chem. C*, 2022, 126, 11544–11552.
- 32 T. Toyao, K. W. Ting, S. M. A. H. Siddiki, A. S. Touchy, W. Onodera, Z. Maeno, H. Ariga-Miwa, Y. Kanda, K. Asakura and K. K.-I. Shimizu, *Catal. Sci. Technol.*, 2019, 9, 5413–5424.
- 33 M. A. Vuurman, D. J. St. A. Oskam and I. E. Wachs, *J. Mol. Catal.*, 1992, 76, 263–285
- 34 B. Liu, Q. H. L. Wen and X. Zhao, *Thin Solid Films*, 2009, 517, 6569–6575.
- 35 X. Jiang, Y. Zhang, J. Jiang, Y. Rong, Y. Wang, Y. Wu and C. Pan, *J. Phys. Chem. C*, 2012, 116, 22619–22624.
- 36 X. Secordel, E. Berrier, M. Capron, S. Cristol, J. F. Paul, M. Fournier and E. Payen, *Catal. Today*, 2010, 155, 177–183.
- 37 S. Mine, K. W. Ting, L. Li, Y. Hinuma, Z. Maeno, S. M. A. H. Siddiki, T. Toyao and K. I. Shimizu *J. Phys. Chem. C*, 2022, 126, 4472–4482.
- 38 C.-C. Chuang, W.-C. Wu, M.-C. Huang, I.-C. Huang and J.-L. Lin, *J. Catal.*, 1999, 185, 423–434
- 39 A. C. Lukaski and D. S. Muggli, *J. Catal.*, 2004, 223, 250–261.
- 40 G. Y. Popova, T. v. Andrushkevich, Y. A. Chesalov and E. S. Stoyanov, *Kinet. Catal.*, 2000, 41, 805–811.
- 41 J. Raskó, T. Kecskés and J. Kiss, *J. Catal.*, 2004, 224, 261–268.
- 42 J. J. Corral-Pérez, A. Billings, D. Stoian and A. Urakawa, *ChemCatChem*, 2019, cctc.201901179.
- 43 K. Zhao, L. Wang, E. Moiola, M. Calizzi and A. Züttel, *J. Phys. Chem. C*, 2019, 123, 8785–8792.
- 44 F. Solymosi and T. Bánsági, *J. Phys. Chem.*, 1992, 96, 1349–1355.

- 45 L. F. Bobadilla, J. L. Santos, S. Ivanova, J. A. Odriozola and A. Urakawa, *ACS Catal.*, 2018, 8, 7455–7467.
- 46 H. Y. T. Chen, S. Tosoni and G. Pacchioni, *ACS Catal.*, 2015, 5, 5486–5495.
- 47 L. C. Grabow and M. Mavrikakis, *ACS Catal.*, 2011, 1, 365–384.
- 48 A. de Juan, J. Jaumot and R. Tauler, *Anal. Methods*, 2014, 6, 4964–4976.
- 49 J. Jaumot, A. de Juan and R. Tauler, *Chemom. Intell. Lab. Syst.*, 2015, 140, 1–12.
- 50 F. Solymosi and T. Bánsági, *J. Phys. Chem.*, 1992, 96, 1349–1355.
- 51 X. Wang, H. Shi and J. Szanyi, *Nat. Commun.*, 2017, 8, 1–6.
- 52 A. Urakawa, T. Bürgi and A. Baiker, *Chem. Eng. Sci.*, 2008, 63, 4902–4909.
- 53 E. D. Goodman, A. C. Johnston-Peck, E. M. Dietze, C. J. Wrasman, A. S. Hoffman, F. Abild-Pedersen, S. R. Bare, P. N. Plessow and M. Cargnello, *Nat. Catal.*, 2019, 2, 748–755.
- 54 N. C. Nelson, L. Chen, D. Meira, L. Kovarik and J. Szanyi, *Angew. Chem., Int. Ed.*, 2020, 59, 17657–17663.
- 55 J. C. Parker and R. W. Siegel, *Appl Phys Lett*, 1990, 57, 943–945.
- 56 G. Liu, H. G. Yang, X. Wang, L. Cheng, H. Lu, L. Wang, G. Q. Lu and H. M. Cheng, *J. Phys. Chem. C*, 2009, 113, 21784–21788.
- 57 A. Beck, M. Zabilskiy, M. A. Newton, O. Safonova, M. G. Willinger and J. A. van Bokhoven, *Nat. Catal.*, 2021, 4, 488–497.
- 58 F. Solymosi and T. S. Zakar, *J. Mol. Catal. A. Chem.*, 2005, 235, 260–266.
- 59 L. Mino, G. Spoto, and A. M. Ferrari, *J. Phys. Chem. C*, 2014, 118, 25016–25026.
- 60 M. L. Gothe, K. L. C. Silva, A. L. Figueredo, J. L. Fiorio, J. Rozendo, B. Manduca, V. Simizu, R. S. Freire, M. A. S. Garcia and P. Vidinha, *Eur. J. Inorg. Chem.*, 2021, 4043–4065.
- 61 B. B. Wayland and B. A. Woods, *J. Chem. Soc., Chem. Commun.*, 1981, 700–701
- 62 R. F. Einrem, E. T. Jonsson, S. J. Teat, N. S. Settineri, A. B. Alemayehu and A. Ghosh, *RSC Adv.*, 2021, 11, 34086–34094.
- 63 C. S. Vasam, S. Modem, S. Kankala, S. Kanne, G. Budige and R. Vadde, *Cent. Eur. J. Chem.*, 2010, 8, 77–86.
- 64 M. A. Henderson, *J. Phys. Chem. B*, 1997, 101, 221–229.
- 65 F. P. a Johnson, M. W. George, F. Hartl and J. J. Turner, *Organometallics*, 1996, 15, 3374–3387.
- 66 Y. Kou, Y. Nabetani, D. Masui, T. Shimada, S. Takagi, H. Tachibana and H. Inoue, *J. Am. Chem. Soc.*, 2014, 136, 6021–6030.
- 67 Y. Kou, Y. Nabetani, R. Nakazato, N. v. Pratheesh, T. Sato, S. Nozawa, S. ichi Adachi, H. Tachibana, and H. Inoue, *J. Catal.*, 2022, 405, 508–519.
- 68 I. R. Beattie and P. J. Jones, *Inorg. Chem.*, 1979, 18, 2318–2319.
- 69 G. Li, J. Meeprasert, J. Wang, C. Li and E. A. Pidko, *ChemCatChem*, 2022, 14, e202101646.
- 70 A. Urakawa, F. Jutz, G. Laurenczy and A. Baiker, *Chem. Eur. J.*, 2007, 13, 3886–3899.
- 71 A. Urakawa, M. Iannuzzi, J. Hutter, and A. Baiker, *Chem. Eur. J.*, 2007, 13, 6828–6840.

Supporting information

Chapter 5

Supplementary experimental

Materials and catalyst preparation

The obtained reagents were used as received. TiO_2 (ST-01) was purchased from Ishihara Sangyo Co., Ltd. Its BET (Brunauer-Emmett-Teller) specific surface area is $188 \text{ m}^2/\text{g}^{-1}$. Re_2O_7 and ReO_2 were purchased from Strem Chemicals Inc. and HydruS Chemical Inc., respectively. NH_4ReO_4 and metallic Re were purchased from Sigma Aldrich. The commercial methanol synthesis catalyst ($\text{Cu}/\text{ZnO}/\text{Al}_2\text{O}_3$) was purchased from Alfa Aesar (Product ID: 45776).

Precursors for Re/TiO_2 were prepared by mixing the support material with the metal sources, that is, an aqueous solution of NH_4ReO_4 . For the preparation of Re/TiO_2 , typically 0.072 g of NH_4ReO_4 was added to a glass vessel (500 mL) containing 100 mL of deionized water ($[\text{Re}] = 0.0027 \text{ M}$). After sonication (1 min) to completely dissolve the NH_4ReO_4 , TiO_2 (4.95 g) was added to the solution. The mixed solution was then stirred at 200 rpm for 30 min at room temperature. Subsequently, the solvent of the mixture was evaporated at $T = 50^\circ\text{C}$, followed by drying in the air ($T = 110^\circ\text{C}$; $t = 12 \text{ h}$). The thus obtained material was calcined ($T = 500^\circ\text{C}$, $t = 3 \text{ h}$, in the air).

Catalyst characterization procedure

Scanning electron microscope (SEM) images were obtained by Hitachi HD-2000. High-angle annular dark-field imaging (HAADF) was performed using a JEM-ARM200F scanning transmission electron microscope (STEM). Samples were prepared by dropping an ethanol solution containing the catalyst on carbon-supported Cu grids.

Catalytic activity testing procedure at high pressure

The catalytic tests were carried out in a high-pressure setup as reported elsewhere.¹ In a typical test, 500 mg catalyst was packed between quartz wool inside a 1/4 inch fixed-bed continuous flow reactor (ID 2.79 mm). The catalyst was reduced *in situ* at 450 °C with 90% H₂/Ar (25 NmL min⁻¹) for 1 h under atmospheric pressure. After cooling down to 30 °C, the H₂/CO₂/Ar mixture with vol% of 69%/23%/8% was fed into the reactor and pressurized to 360 bar (the reactant pressure is 331 bar). The total flow rate of the gas mixture is kept at 16.7 NmL min⁻¹ to achieve a gas-hourly space velocity of 2000 h⁻¹ equivalent. The products were analyzed by an online gas chromatograph (Bruker, GC-450) equipped with a flame ionization detector for methanol, methyl formate, diethyl ether, and other hydrocarbons, and a thermal conductivity detector for permanent gases e.g. CO₂, H₂, Ar, CO, CH₄.

Transient experimental setup and procedures of *operando* XAS, Raman, and DRIFTS

The flow of gases (H₂, CO₂, and He) is controlled by 6 mass flow controllers (Bronkhorst). Switching between two reactant gas streams is done by a 4-way valve. The pressure of the two gas streams (to the cell and vent) is controlled by back pressure regulators (Bronkhorst). The outlet gas stream is analyzed by a Pfeiffer OmniStar GSD 300C mass spectrometer.

Before the measurements, the sample is reduced *in situ* at 500 °C in the H₂ stream (20 NmL min⁻¹ H₂) for 1 h and subsequently cooled to a reaction temperature of 150 °C in the He stream. The cell is pressurized to 10-20 bar and immediately exposed to the reactant mixture (H₂/CO₂ = 3/1 molar ratio, total flow 20 NmL min⁻¹) at the same pressure by the switching valve. The transient experiment utilizes a periodic perturbation of a system by external parameters (stimulation) to influence the concentration of active species.² This experiment is performed in the above-mentioned setup by using a switching valve to change the stream of reactant gases to introduce the periodic concentration perturbation.

Operando XAS

Operando XAS measurements were carried out using a fixed-bed capillary reactor (ID: 2 mm) at 150 °C, 10 bar, and H₂/CO₂ = 3/1 coupled with the detection of the formed products by the mass spectrometer. XAS measurements were performed over Re (3 wt%)/TiO₂ at Re L₃-edge (10.54 keV) will be performed.

Operando Raman

Raman measurements were performed using a BWTEK dispersive i-Raman portable spectrometer equipped with a 785 nm excitation laser and a TE-cooled linear array detector. The reaction was carried out in a fixed-bed capillary reactor (ID: 2 mm) with identical procedures to *operando* XAS.

Operando DRIFTS and SSITKA

The catalyst powder (10-15 mg) is located in a cylindrical cavity (3 mm in diameter and 3 mm vertical length) of a custom-made high-pressure reaction cell (tested up to 40 bar). The cell is mounted in a Harrick Praying Mantis diffuse reflection (DRIFTS) accessory. The spectra were collected using a Thermo Scientific Nicolet 6700 FT-IR spectrometer equipped with a liquid-nitrogen-cooled MCT detector at 4 cm⁻¹ resolution. The spectra were acquired continuously every 10 seconds in a time-resolved manner to monitor the reaction, stabilization process of the catalysts as well as evolution of surface species. No baseline correction was applied to the time-resolved spectra due to the baseline movement.

Multivariate spectral analysis

Multivariate spectral analysis is performed by the Multivariate Curve Resolution-Alternating Least Squares (MCR-ALS) algorithm, as described elsewhere.³ MCR is a chemometric method used for better data processing and deconvolution of complex spectra down to individual components based on kinetic resolution. It can deliver the pure response profiles (e.g. spectra, pH profiles, time profiles, elution profiles) of the chemical species of an unresolved mixture when no previous information is available about the nature and composition of these mixtures.

AP-XPS

Ambient pressure X-ray photoelectron spectroscopy (AP-XPS) measurements were performed at beamline 13B of Photon Factory (PF) at the High Energy Accelerator Research Organization (KEK). A powder of Re/TiO₂ with Re loading of 3 wt%, pre-reduced under H₂ at 500 °C for 30 min, was coated on a Si substrate by using deionized water as a dispersant with a drop-and-dry method. The temperature of the samples was measured by using a thermocouple directly attached to the sample holder in the analysis chamber.

The gases were introduced into the chamber by using variable leak valves. The samples were pretreated by exposure to H₂ (0.1 Torr) at 450 °C for 30 min followed by cooling to 150 °C under the H₂ atmosphere. Gases were then introduced into the analysis chamber and all the XPS spectra were collected at 150 °C. Re 4f measurements were performed with a photon energy of 630 eV. Binding energy was calibrated using the Ti 2p_{3/2} peak of Ti⁴⁺ species (TiO₂; 485.5 eV). XPS spectra were analyzed with the convolution of Gaussian and Lorentzian with a Shirley background in the range of 34-46.5 eV. An asymmetric Doniach–Sunjic peak shape was used to fit the peaks for metallic rhenium.

Table S5.1 Assignment of surface species

Wavenumber (cm ⁻¹)			Vibrational mode	Band assignment	Ref.
CO ₂ +H ₂ Feed	CO ₂ +D ₂ Feed	¹³ CO ₂ +H ₂ Feed			
3716	2704	3716	$\nu(\text{O-H})$	Hydroxy (OH*) on TiO ₂	4
2950		2941	$\nu_{\text{as}}(\text{C-O}) + \delta(\text{C-H})$	Formate (HCOO*) on TiO ₂	5-7
2927		2918	$\nu_{\text{as}}(\text{C-H})$	Methoxy (CH ₃ O*) on TiO ₂	5,8,9
2869	2121	2860	$\nu(\text{C-H})$	Formate (HCOO*) on TiO ₂	5-7
2829	2065	2821	$\nu_{\text{s}}(\text{C-H})$	Methoxy (CH ₃ O*) on TiO ₂	5,8,9
1960	1335	1960	$\nu(\text{Re-H})$	Rhenium hydride (Re-H)	10-14
1656			$\nu_{\text{as}}(\text{C-O})$	Monodentate bicarbonates (HCO ₃ *) on TiO ₂	15
1618			$\nu_{\text{as}}(\text{C-O})$	Bidentate bicarbonates (b-HCO ₃ *) on TiO ₂	15
1583			$\nu_{\text{as}}(\text{C-O})$	Monodentate carbonate (m-CO ₃ *) on TiO ₂	15
1560	1560	1527	$\nu_{\text{as}}(\text{C-O})$	Formate (HCOO*) on TiO ₂	5-7
1503			$\nu_{\text{as}}(\text{C-O})$	Bidentate bicarbonates (b-HCO ₃ *) on TiO ₂	15
1429			$\nu_{\text{as}}(\text{C-O})$	Monodentate bicarbonates (HCO ₃ *) on TiO ₂	15
1369			$\nu_{\text{as}}(\text{C-O})$	Monodentate carbonate (CO ₃ *) on TiO ₂	15
1357	1357	1334	$\nu_{\text{s}}(\text{C-O})$	Formate (HCOO*) on TiO ₂	5-7
1334			$\nu_{\text{s}}(\text{C-O})$	Adsorbed carbon dioxide (CO ₂ *)	15
1223			$\nu_{\text{b}}(\text{C-O-H})$	Bidentate bicarbonates (HCO ₃ *) on TiO ₂	15

Table S5.2 Mass-to-charge ratio mass spectrometer

Gases	m/z
H ₂	2
He	4
CH ₄	15
¹³ CH ₄	17
CH ₃ D	17
H ₂ O	18
CH ₂ D ₂	18
CHD ₃	19
CD ₄	20
CO	28
¹³ CO	29
CH ₃ OH	31
¹³ CH ₃ OH	33
CH ₃ OD	33
CD ₃ OH	35
CD ₃ OD	36
CO ₂	44
¹³ CO ₂	45

Supplementary results

In situ characterization of the catalyst during CO₂ hydrogenation

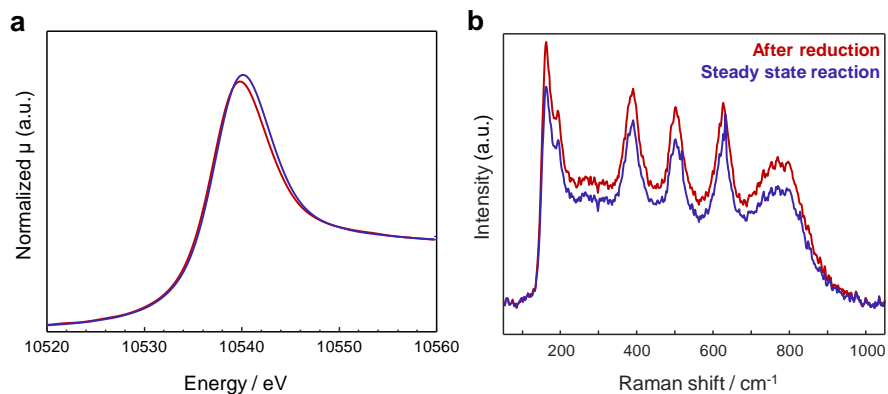


Figure S5.1 *In situ* characterization of 3 wt% Re/TiO₂ catalyst after reduction and during steady state reaction with H₂+CO₂: **a** *operando* Re L₃-edge XANES spectra and **b** *operando* Raman spectra. Reaction conditions: ca. 10 mg catalyst, H₂/CO₂ = 3, T = 150 °C, P = 10 bar, F_{total} = 10 NmL min⁻¹.

DRIFTS: CO₂ hydrogenation (using D₂) over Re/TiO₂

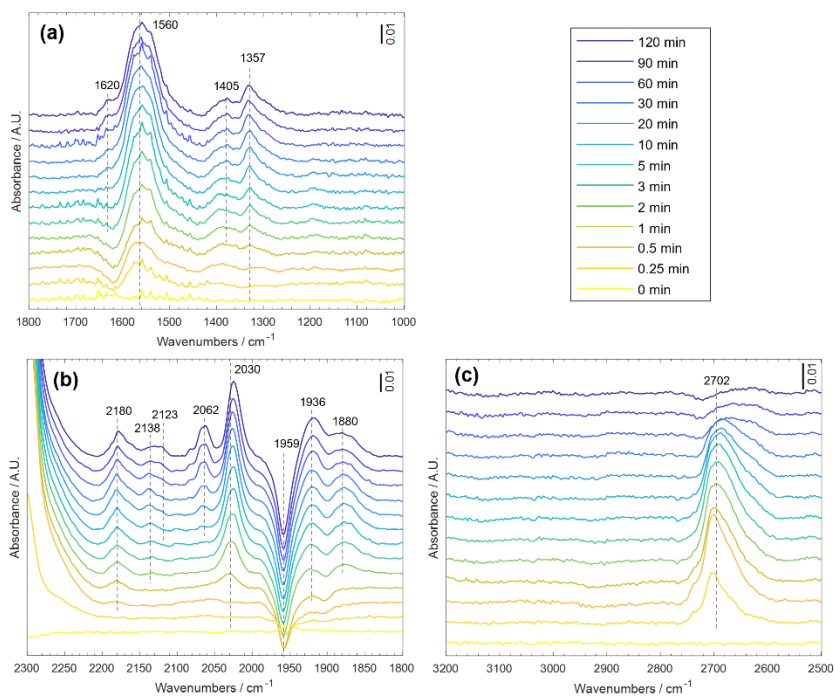


Figure S5.2 Temporal evolution of surface species obtained from *in situ* DRIFTS during reaction with D₂+CO₂ over 3 wt% Re/TiO₂. Reaction conditions: 10 mg catalyst, H₂/CO = 3, T = 150 °C, P = 10 bar, F_{total} = 10 NmL min⁻¹.

DRIFTS: $^{13}\text{CO}_2$ hydrogenation over Re/TiO_2

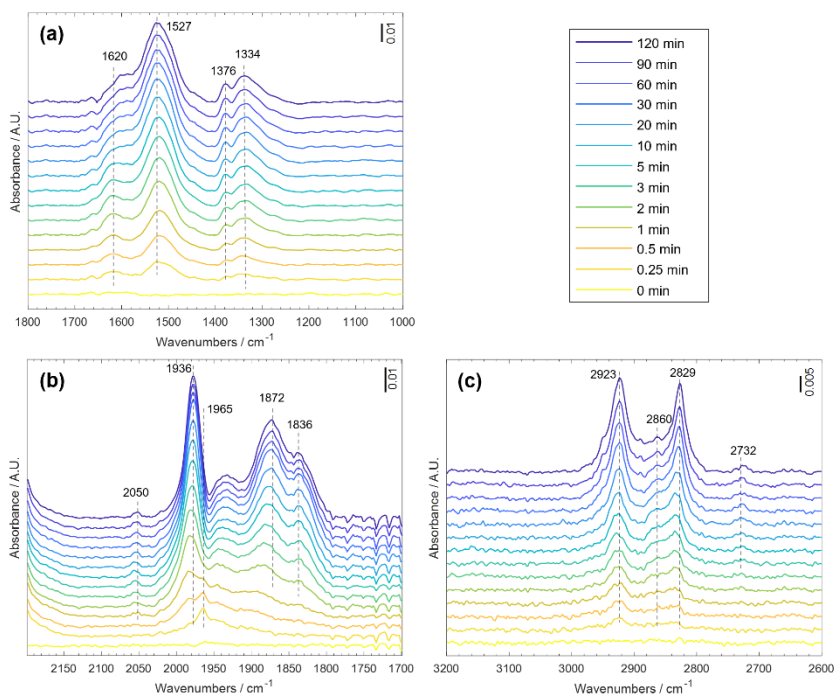


Figure S5.3 Temporal evolution of surface species obtained from *in situ* DRIFTS during reaction with $\text{H}_2 + ^{13}\text{CO}_2$ over 3 wt% Re/TiO_2 . Reaction conditions: 10 mg catalyst, $\text{H}_2/\text{CO}_2 = 3$, $T = 150^\circ\text{C}$, $P = 10$ bar, $F_{\text{total}} = 10 \text{ NmL min}^{-1}$.

DRIFTS: CO₂ hydrogenation over TiO₂

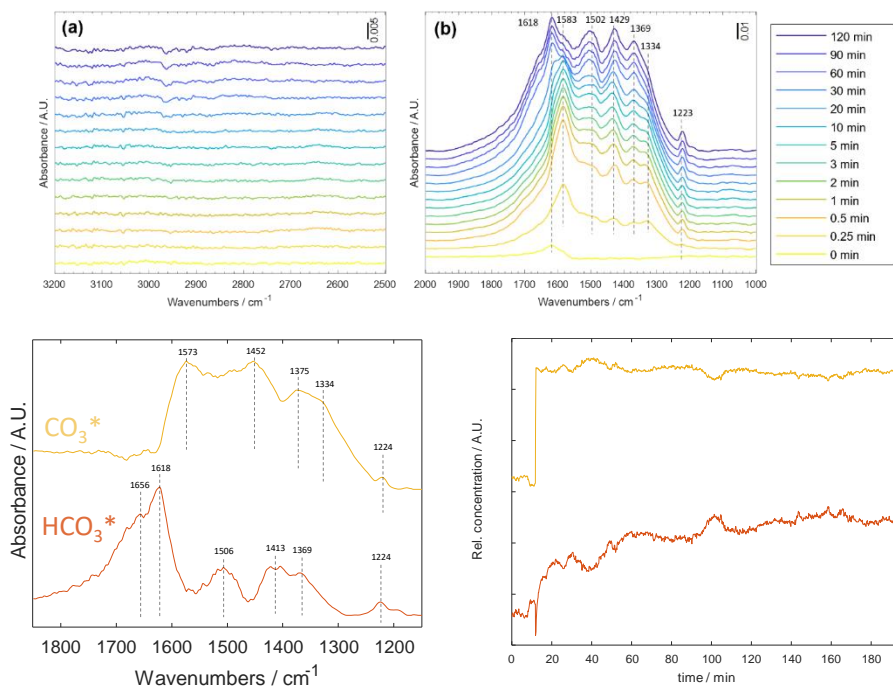


Figure S5.4 Temporal evolution of surface species obtained from *in situ* DRIFTS during reaction with H₂+CO₂ over TiO₂ (top), components spectra obtained by MCR applied on the time-resolved DRIFT spectra (bottom-left), and concentration profiles of the spectra of the corresponding components obtained by MCR (bottom-right). Reaction conditions: 10 mg catalyst, H₂/CO₂ = 3, T = 150 °C, P = 10 bar, F_{total} = 10 NmL min⁻¹.

DRIFTS: CH₃OH adsorption over Re/TiO₂ and titration of CH₃O* adlayer with D₂

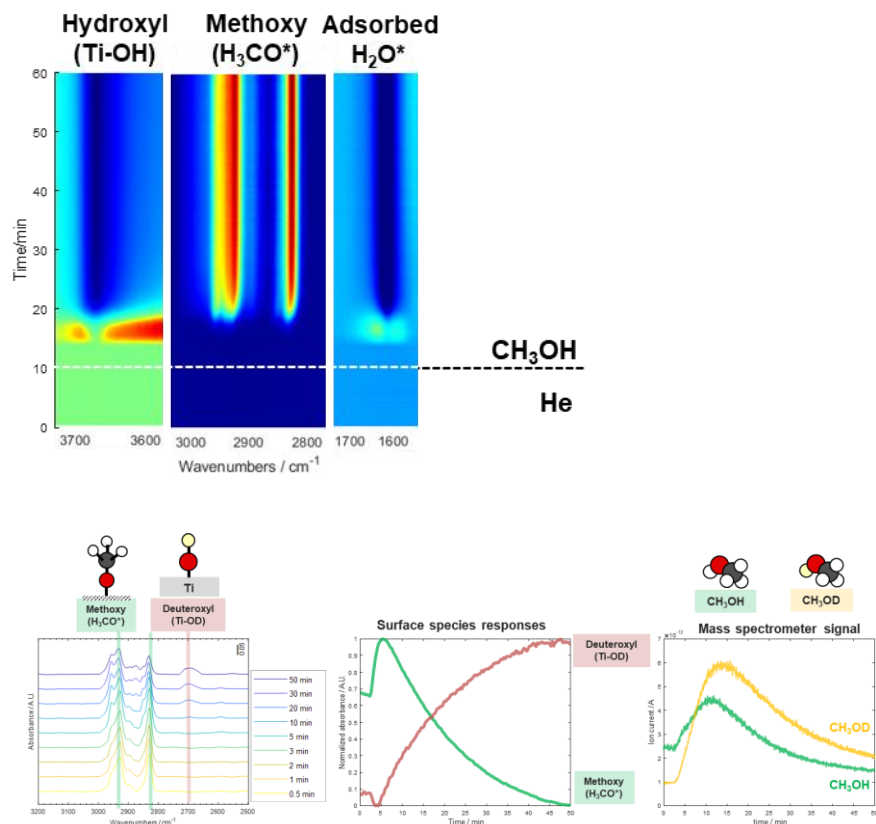


Figure S5.5 Time-resolved CH₃OH adsorption over Re/TiO₂ (upper) and the reaction of CH₃O* adlayer with D₂ after flushing with He (bottom). Reduction condition: 300 °C under 10 NmL min⁻¹ of H₂ for 1 h. (pre-reduced at 500 °C with H₂ and passivated with 1%O₂/N₂). Reaction conditions: ca. 10 mg catalyst, 2000 ppm CH₃OH in N₂, T = 150 °C, P = 5 bar, F_{total} = 20 NmL min⁻¹.

DRIFTS: CH₃OH adsorption over TiO₂ and titration of CH₃O* adlayer with D₂

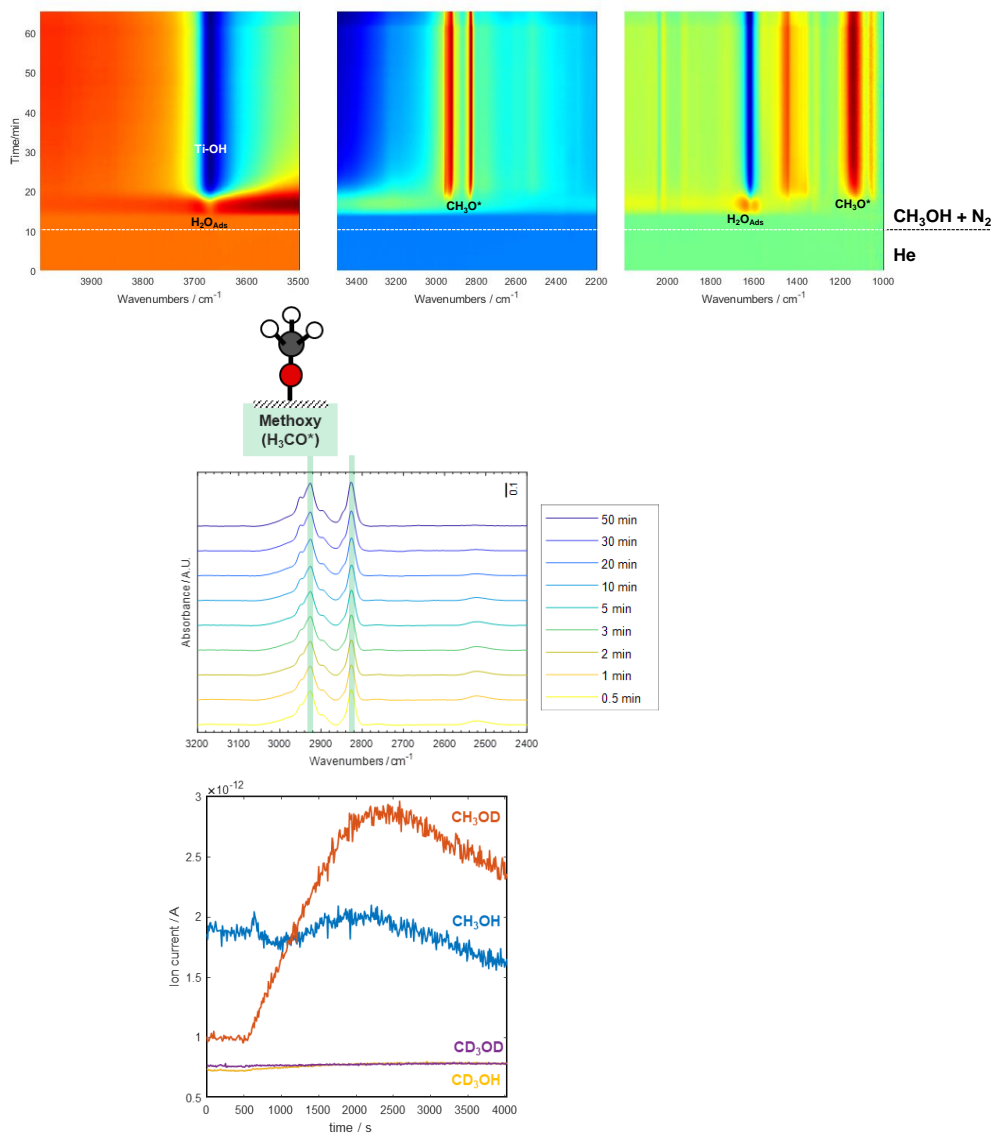


Figure S5.6 Time-resolved CH₃OH adsorption over TiO₂ (upper) and the reaction of CH₃O* adlayer with D₂ after flushing with He (bottom). Reduction condition: 300 °C under 10 NmL min⁻¹ of H₂ for 1 h. Reaction conditions: ca. 10 mg catalyst, 2000 ppm CH₃OH in N₂, T = 150 °C, P = 5 bar, F_{total} = 20 NmL min⁻¹.

DRIFTS: CO hydrogenation over Re/TiO₂

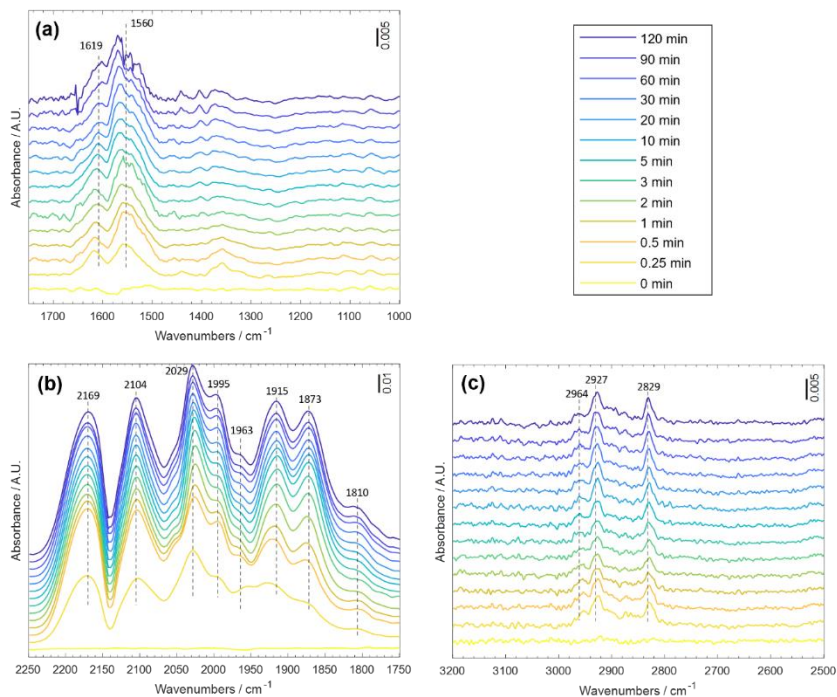


Figure S5.7 Temporal evolution of surface species obtained from *in situ* DRIFTS during reaction with H₂+CO over 3 wt% Re/TiO₂. Reduction condition: 300 °C under 10 NmL min⁻¹ of H₂ for 1 h. (Pre-reduced at 500 °C with H₂ and passivated with 1%O₂/N₂). Reaction conditions: 10 mg catalyst, H₂/CO = 3, T = 150 °C, P = 10 bar, F_{total} = 10 NmL min⁻¹.

DRIFTS-SSITKA: $\text{H}_2 + \text{CO}_2 \rightarrow \text{D}_2 + \text{CO}_2$

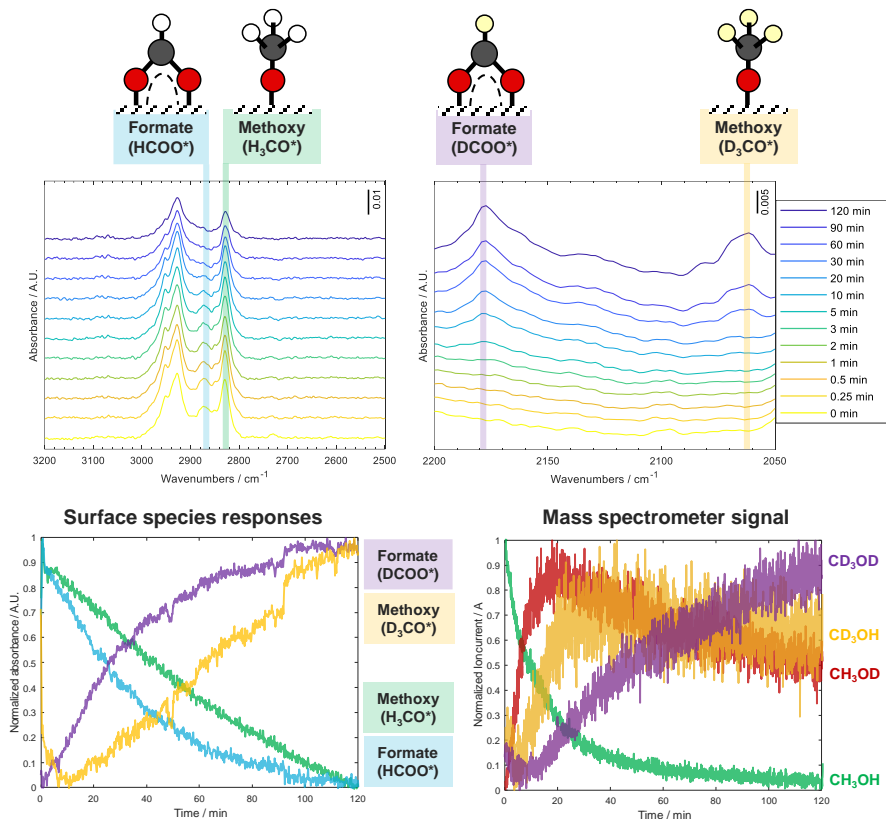


Figure S5.8 Transient responses of surface species and gas products during the steady-state isotopic switching from $\text{CO}_2 + \text{H}_2$ to $\text{CO}_2 + \text{D}_2$. Time-resolved DRIFT spectra of a DCOO^* and CD_3O^* , and b HCOO^* and CH_3O^* (top). Concentration profiles of the spectra of the corresponding components obtained by MCR (bottom-left). Corresponding normalized ion current signal of isotope-labeled products (bottom-right). Reaction conditions: 10 mg catalyst, $\text{H}_2(\text{or } \text{D}_2)/\text{CO}_2 = 3$, $T = 150^\circ\text{C}$, $P = 10\text{ bar}$, $F_{\text{total}} = 10\text{ NmL min}^{-1}$.

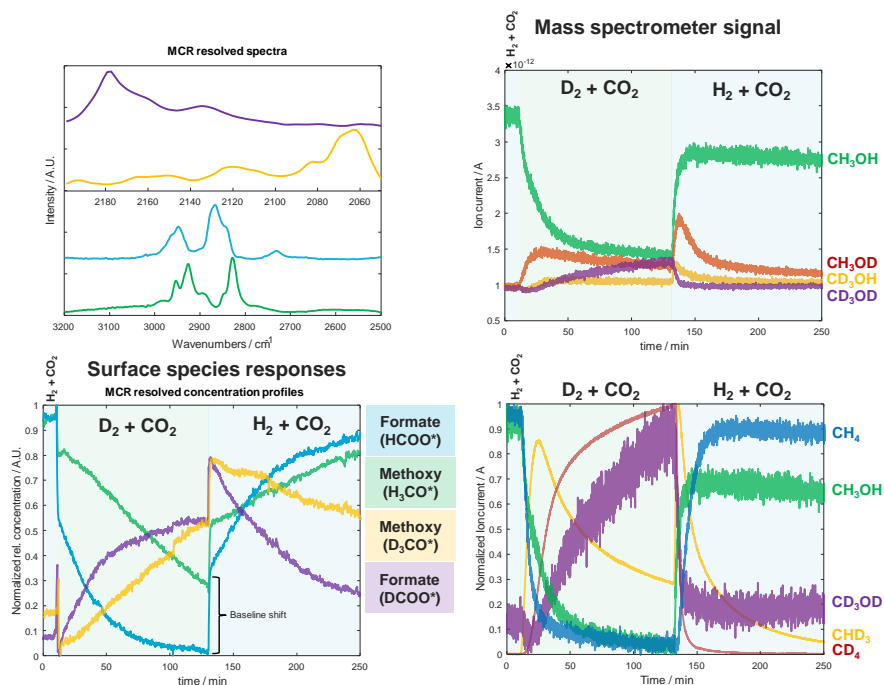


Figure S5.9 Transient responses of surface species and gas products during the steady-state isotopic switching from $\text{CO}_2 + \text{H}_2$ to $\text{CO}_2 + \text{D}_2$ to $\text{CO}_2 + \text{H}_2$. Components spectra obtained by MCR applied on the time-resolved DRIFT spectra (top-left). Concentration profiles of the spectra of the corresponding components obtained by MCR (bottom-left). Corresponding normalized ion current signal of isotope-labeled products (right). Reaction conditions: 10 mg catalyst, $\text{H}_2(\text{or } \text{D}_2)/\text{CO}_2 = 3$, $T = 150^\circ\text{C}$, $P = 10\text{ bar}$, $F_{\text{total}} = 10\text{ N mL min}^{-1}$.

Raman: Transient H_2+CO_2 vs $\text{He}+\text{CO}_2$

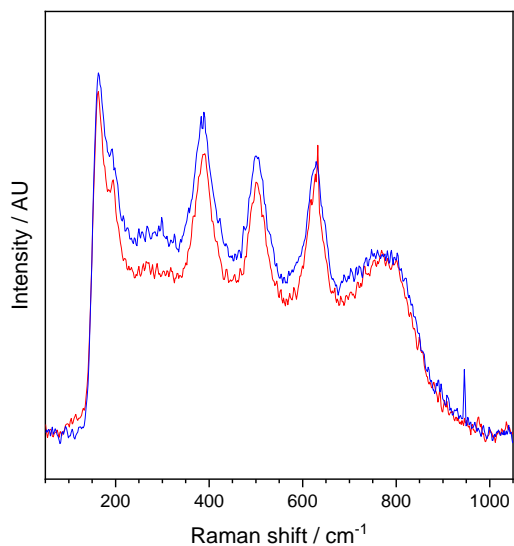


Figure S5.10 *In situ* characterization of 3 wt% Re/TiO_2 catalyst during transient H_2+CO_2 vs $\text{He}+\text{CO}_2$ experiment before (blue) and after (red) quasi-steady state. Reaction conditions: ca. 10 mg catalyst, $\text{H}_2/\text{CO}_2 = 3$, $T = 150\text{ }^\circ\text{C}$, $P = 10\text{ bar}$, $F_{\text{total}} = 10\text{ NmL min}^{-1}$.

DRIFTS: Transient H_2+CO_2 vs $\text{He}+\text{CO}_2$

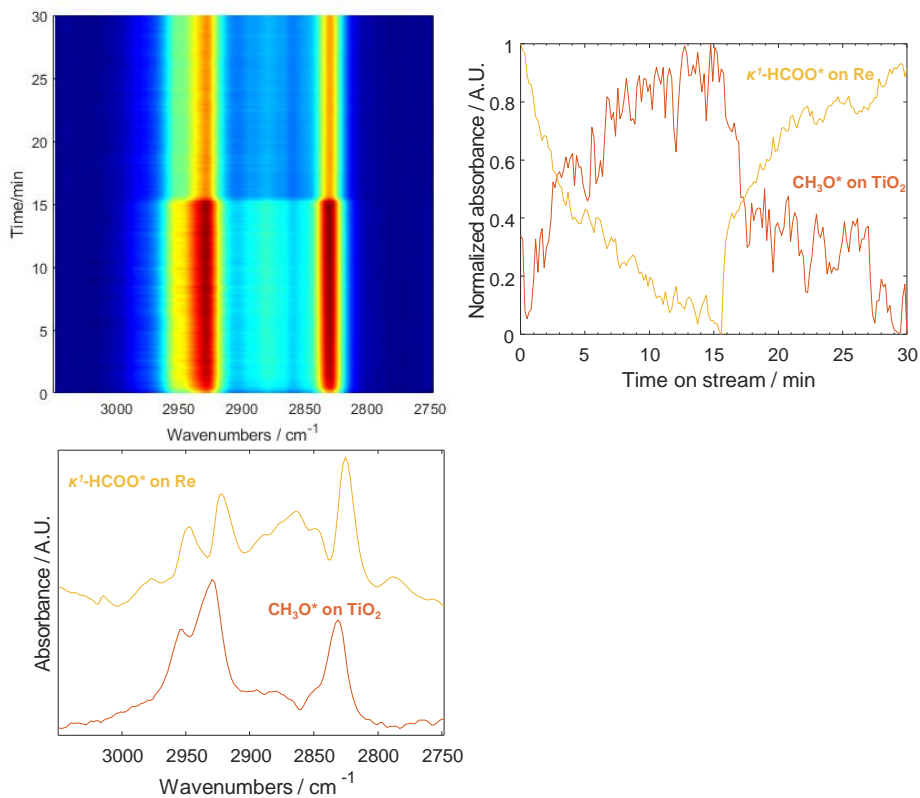


Figure S5.11 Transient DRIFTS study on CO_2 hydrogenation over 3 wt % Re/TiO_2 catalyst, time-resolved DRIFT spectra upon transient concentration perturbation using H_2+CO_2 (0-15 mins) and H_2+He (15-30 min). Reaction conditions: 10 mg catalyst, $\text{H}_2/\text{He} = \text{He}/\text{CO}_2 = 3$, $T = 150^\circ\text{C}$, $P = 10\text{ bar}$, $F_{\text{total}} = 10\text{ NmL min}^{-1}$.

DRIFTS: Transient H_2+He vs $\text{He}+\text{CO}_2$

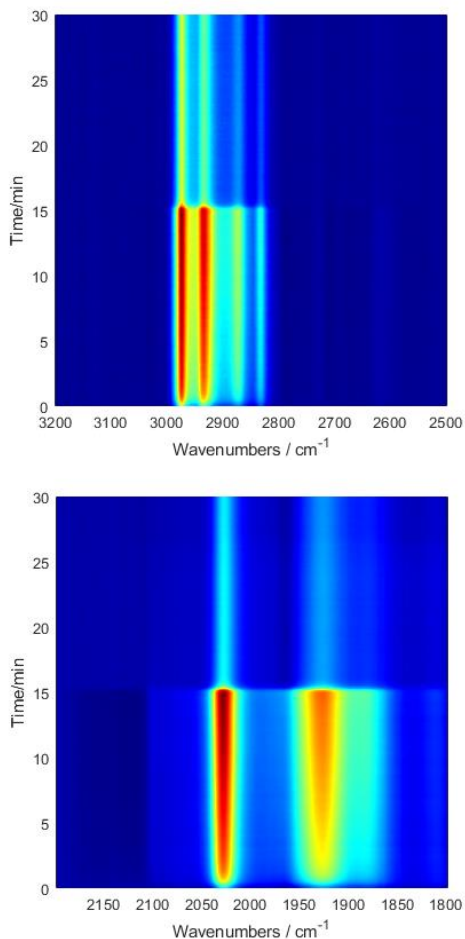


Figure S5.12 Transient DRIFTS study on CO_2 hydrogenation over 3 wt % Re/TiO_2 catalyst, time-resolved DRIFT spectra upon transient concentration perturbation using $\text{He}+\text{CO}_2$ (0-15 mins) and H_2+He (15-30 min). Components spectra obtained by MCR applied on the time-resolved DRIFT spectra (bottom-left). Concentration profiles of the spectra of the corresponding components obtained by MCR (top-right). Reaction conditions

References

- 1** A. Bansode and A. Urakawa, *J. Catal.*, 2014, 309, 66–70.
- 2** A. Urakawa, T. Bürgi and A. Baiker, *Chem. Eng. Sci.*, 2008, 63, 4902–4909.
- 3** J. Jaumot, A. de Juan and R. Tauler, *Chemom. Intell. Lab. Syst.*, 2015, 140, 1–12.
- 4** Y. P. Jackson, *J. Chem. Soc., Faraday Trans. 1*, 1972, 68, 896–906
- 5** K. W. Ting, T. Toyao, S. M. A. H. Siddiki and K. Shimizu, *ACS Catal.*, 2019, 9, 3685–3693.
- 6** Y. Wang, B. Wen, A. Dahal, G. A. Kimmel, R. Rousseau, A. Selloni, N. G. Petrik and Z. Dohnálek, *J. Phys. Chem. C*, 2020, 124, 20228–20239.
- 7** H. Uetsuka, M. A. Henderson, A. Sasahara, and H. Onishi, *J. Phys. Chem. B*, 2004, 108, 13706–13710.
- 8** C. Y. Wang, H. Groenzin and M. J. Shultz, *J. Am. Chem. Soc.*, 2005, 127, 9736–9744.
- 9** D. Yang, Y. Li, X. Liu, Y. Cao, Y. Gao, Y. R. Shen, and W. T. Liu, *Proc. Natl. Acad. Sci. USA*, 2018, 115, E3888–E3894.
- 10** S. Bolaño, J. Bravo, S. García-Fontán and J. Castro, *J. Organomet. Chem.*, 2003, 667, 103–111.
- 11** N. Li, Y. Xie, R. B. King and H. F. Schaefer, *Eur. J. Inorg. Chem.*, 2011, 4626–4636.
- 12** R. H. Morris, *Inorg. Chem.*, 2018, 57, 13809–13821.
- 13** H. G. Cho and L. Andrews, *Organometallics*, 2007, 26, 4098–4101.
- 14** S. Feracin, T. Bürgi, V. I. Bakhmutov, I. Eremenko, H. Berke, V. I. Bakhmutov, E. v. Vorontsov and A. B. Vimenits, *Organometallics*, 1994, 13, 4194–4202.
- 15** L. Mino, G. Spoto, and A. M. Ferrari, *J. Phys. Chem. C*, 2014, 118, 25016–25026.

A synergistic interplay between Ag and Re supported on TiO₂

promotes methanol selectivity
in low temperature CO₂ hydrogenation



Abstract

The major challenge of low-temperature CO₂ hydrogenation to methanol is overcoming the sluggish kinetics, thus leading to the exploration of highly active and selective catalysts below 200 °C. Various M/TiO₂ (M = Cu, Rh, Pd, Ag, Re, Pt, or Au) were tested at 150-200 °C and 60 bar, and Re/TiO₂ remained the most promising. The main commonality between Re/TiO₂ and the conventional Cu/ZnO/Al₂O₃ is high methyl formate selectivity at low temperatures (125 °C), which reflects the ability to stabilize formate species against its decomposition to CO. High methyl formate selectivity at increasing temperatures (175 °C) over Ag/TiO₂ demonstrated the excellent formate stabilization of metallic Ag. The addition of a small amount of Ag to Re/TiO₂ improved the methanol selectivity significantly by suppressing methane formation. STEM-EDS showed that Re clusters migrated and distributed around the Ag nanoparticles over Re-Ag/TiO₂ after the reaction. *Ex situ* XAS reveals no alloy formation between Re-Ag after reduction. After CO₂ hydrogenation, Ag remained metallic while Re was oxidized creating cationic Re species. *Operando* DRIFTS studies confirm that the reaction mechanism over Re-Ag/TiO₂ is identical to that of Re/TiO₂ but Ag addition helps boost forming surface formate species while suppressing carbonyl species which is the intermediate for methane formation. Metallic Re species act as H₂ activators, leading to H-spillover and importantly to hydrogenation of active formate intermediate present over cationic Re species. The role of metallic Ag is ascribed to complementarily activate CO₂ to formate and supply it to cationic Re species via spillover, driving forward the hydrogenation of the formate to methanol. Re-Ag/TiO₂ showed high stability in CO₂-to-methanol and improved catalytic performance over time on stream up to 40 h.



This chapter is based on the following publication:

Phongprueksathat, N., Wirner L.C., Phadke S.M., Safonova O.V. &
Urakawa, A
In preparation

6.1 Introduction

Carbon dioxide (CO₂) utilization is one of the emerging strategies to minimize the effects of climate change for future generations.¹ From the possible compounds that can be synthesized from CO₂, methanol is an attractive choice due to its importance as a bulk chemical and the potential to achieve a carbon-neutral economy, independent of fossil fuels.² Currently, conventional Cu/ZnO/Al₂O₃ catalysts for methanol synthesis from syngas are employed for commercial-scale CO₂ (together with CO) hydrogenation to methanol, under conditions of 200-300 °C and 10-100 bar.³ However, it is thermodynamically not possible to achieve both very high CO₂ conversion and methanol selectivity under such conditions without effluent stream recycling. Lower temperatures are more favorable according to Le Chatelier's principle to achieve almost full CO₂ conversion and CH₃OH selectivity.⁴ Moreover, less energy consumption and less deactivation by sintering are expected at lower temperatures.

In practice, the catalytic activity of Cu-based catalysts is not optimal below 200 °C.^{5,6} Even at thermodynamically favorable conditions ($P = 331$ bar and $H_2/CO_2 = 10$), Cu/ZnO/Al₂O₃ also suffers high CO selectivity below the optimal temperature of 260 °C,^{7,8} and requires, for example, the promotion by amine or alcohol additives for high CH₃OH selectivity (TON up to 7.6 at up to 170 °C).⁹⁻¹¹ Cu-based catalysts are also less selective to CH₃OH at low temperatures than noble metal catalysts (e.g. Pd, Pt, Au, Ag) since the latter are superior in activating hydrogen and CO₂ under milder conditions.¹²

Most state-of-the-art low temperature CO₂-to-methanol catalysts take advantages of bifunctionality originating from metal-metal, metal-support, metal-N, and metal-OH interactions, or tandem catalysts (involving the cooperation of catalysts and additives).¹³ Cu/Mo₂C and Pd/Mo₂C were found active for the CH₃OH production via direct CO₂ hydrogenation with a small amount of CO and CH₄ formation since Mo₂C served as both a support and a co-catalyst possessing distinct sites for CH₃OH after Cu and Pd deposition (0.7 h⁻¹ TOF, $S_{CH_3OH} = 79\%$, $H_2/CO_2 = 3$, 135 °C, and 40 bar).¹⁴ Recently, MoS₂ was shown to be active in CO₂ dissociation at in-plane sulfur vacancies enabling selective CO₂ hydrogenation at low temperature ($X_{CO_2} = 12.5\%$, $S_{CH_3OH} = 94.3\%$, $H_2/CO_2 = 3$, 180 °C, and 50 bar).^{15,20} Pt₄Co(nanowires) with abundant steps/edges on Pt-rich surfaces were found active and stable for CO₂ hydrogenation (1773 h⁻¹ TOF, $H_2/CO_2 = 3$, 150 °C, and 31 bar).¹⁶ Au nanoclusters supported on ZrO₂ show higher activity in methanol formation than other M/ZrO₂ (M = Co, Ni, Ru, Pd, and Pt) due to small Au size and appropriate electron transfer from ZrO₂ support compared to CeO₂, TiO₂, and ZnO (20 h⁻¹ TOF, $S_{CH_3OH} = 73\%$, $H_2/CO_2 = 3$, 180 °C, and 40 bar).¹⁷ Pt/TiO₂ could

be selective for CH₃OH formation in the presence of reduced MoO_x (Pt/MoO_x/TiO₂, 3588 TON, S_{CH₃OH} = 92%, H₂/CO₂ = 5, 150 °C, and 60 bar), since the redox of Mo species takes place and catalyzes CO₂ hydrogenation via the oxygen-vacancy-driven mechanism.¹⁸ Pt/UiO-67 (Pt nanoparticles encapsulated in Zr-containing MOF) showed higher activity than Pt/Al₂O₃ and Pt/SiO₂ (36 h⁻¹TOF, S_{CH₃OH} = 40%, H₂/CO₂ = 6, 170 °C, and 1 atm).^{19,20} The proximity between Pt and Zr metal played a crucial role in the stabilization of intermediates.¹⁵ Re/TiO₂ showed the most promising activity (44 TON, S_{CH₃OH} = 82%, H₂/CO₂ = 5, 150 °C, and 60 bar) among various metal catalysts (e.g. Pt, Pd, Rh, Ir, Ru, Ni, Co, Ag, and Cu) and supports (e.g. ZrO₂, SiO₂, Al₂O₃, CeO₂, etc.), and the subnanometer size Re with average oxidation states between Re⁰ and Re⁴⁺ served as active sites for methanol formation.²¹ The bi-functionality of Re supported on TiO₂ was elucidated in **Chapter 5**.

Multiple transition metal catalysts supported on metal oxides reported previously for low-temperature methanol synthesis (<200 °C) were studied under batch conditions where Re was found particularly promising when supported on TiO₂.^{18,21} In this study, the focus is given to evaluate promising transition metals for CO₂ hydrogenation under a continuous operation using a fixed-bed reactor and TiO₂ as the support material. For the most promising catalyst, additional promotion by a coinage metal (Cu, Ag, or Au) is evaluated due to its known function to activate CO₂ to produce reactive formates, which could further facilitate methanol formation.

6.2 Results and Discussion

6.2.1 Insights from the catalytic performance of M(3)/TiO₂ catalysts (M = Cu, Rh, Pd, Ag, Re, Pt, and Au)

The catalytic activity of M(3)/TiO₂ (M = Cu, Rh, Pd, Ag, Re, Pt, or Au) and the commercial Cu/ZnO/Al₂O₃ at 150 °C and 60 bar is summarized in **Table 6.1**. The Cu/ZnO/Al₂O₃ showed very low CO₂ conversion (<1%) at a low temperature, despite the highest CH₃OH selectivity among the studied catalysts. The effects of temperature over M/TiO₂ and Cu/ZnO/Al₂O₃ are shown in **Figure S6.1**. Although CO₂ conversion increases with temperature, the effects of the metal on CH₃OH selectivity vary among catalysts. Over most catalysts except for Ag/TiO₂ and Pt/TiO₂, the CH₃OH selectivity declined above 150 °C and exhibited a trade-off between CO₂ conversion and CH₃OH selectivity at the reaction pressure of 60 bar. The formation rates for each product over M/TiO₂ are also summarized in **Figure 6.1**.

The commonalities between Re/TiO₂ and Cu/ZnO/Al₂O₃ are high selectivities towards CH₃OH and methyl formate (HCOOCH₃) at 150 °C,

although CH_4 selectivity increases with temperature over the former. HCOOCH_3 formation becomes significant at low temperatures, which is not usually observed under the higher temperature of the industrial methanol synthesis conditions due to its tendency to decompose to CH_3OH and CO .²² On the other hand, the HCOOCH_3 formation reflects the ability to stabilize formate species (HCOO^*) in the presence of adsorbed methanol,^{23–25} which can occur over Lewis acidic sites of Al_2O_3 ²² as well as cationic $\text{Re}^{\delta+}$ species and TiO_2 (Chapter 5). As shown in Figure 6.2, both $\text{Cu}/\text{ZnO}/\text{Al}_2\text{O}_3$ and Re/TiO_2 show high activity for HCOOCH_3 formation, especially at 125 °C. The decline in HCOOCH_3 at higher temperatures was hypothesized due to HCOOCH_3 decomposition and/or HCOO^* decomposition. Based on the insights from Chapters 4 & 5, high CO selectivity at higher temperatures originates from the inability to stabilize HCOO^* and/or hydrogenate HCOO^* .

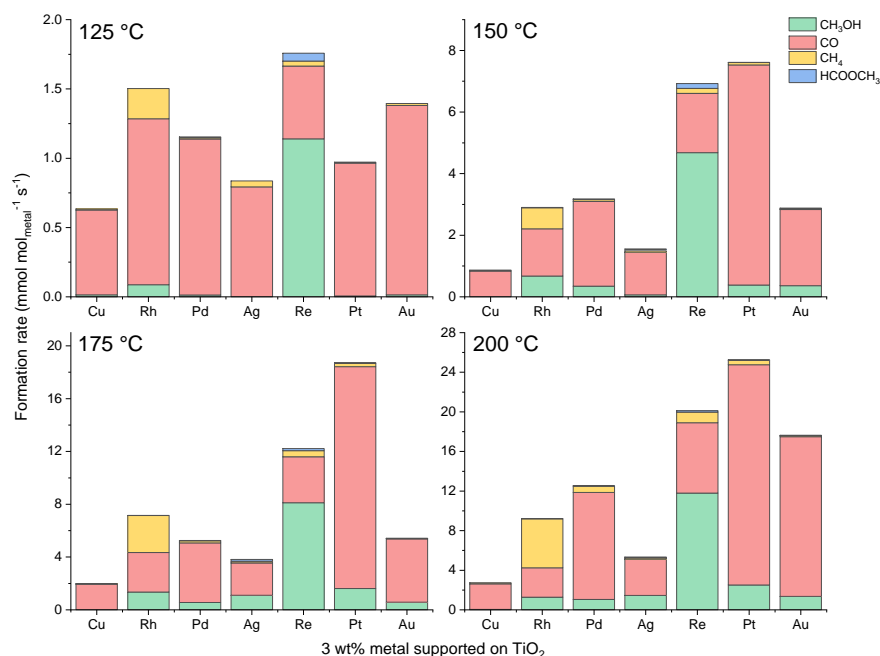


Figure 6.1 Formation rates of products during CO₂ hydrogenation over M(3)/TiO₂ (M = Cu, Rh, Pd, Ag, Re, Pt or Au). Reaction conditions: T = 125–200 °C, P = 60 bar, H₂/CO₂ = 3, SV = 3505 NmL g_{cat}⁻¹ h⁻¹, TOS = 4 h.

Notably, Ag/TiO_2 exhibited unique CH_3OH and HCOOCH_3 selectivity trends among all catalysts, giving the maximum selectivity at 175 °C (Figure 6.2 and S1).

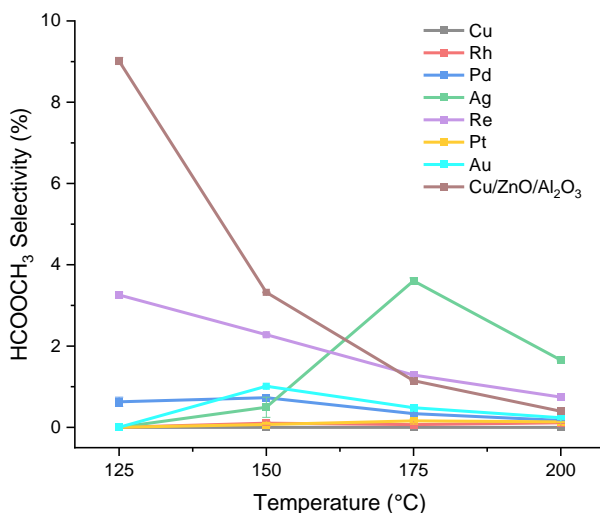


Figure 6.2 Effects of temperatures on HCOOCH₃ selectivity during CO₂ hydrogenation over M(3)/TiO₂ (M = Cu, Rh, Pd, Ag, Re, Pt, or Au) and Cu/ZnO/Al₂O₃ catalysts. Reaction conditions: T = 125–200 °C, P = 60 bar, H₂/CO₂ = 3, SV = 3505 NmL g_{cat}⁻¹ h⁻¹, TOS = 4 h.

From the mechanistic insights disclosed in **Chapter 5**, Re/TiO₂ exhibited high performance due to the combination of Re⁰ species as an excellent hydrogen activator, and Re^{δ+} species as a monodentate HCOO* stabilizer. However, the limitation of Re/TiO₂ to control and enhance CH₃OH selectivity is the balance between Re^{δ+} and Re⁰ species, which is determined by cluster sizes and the size distribution. The high dispersion of Re clusters is also influenced by the reducibility of the supports (e.g. CeO₂, TiO₂, and ZrO₂).²⁶ The Lewis acidity plays important role in driving reaction toward CH₃OH, e.g. Re/ZrO₂ favors CH₃OH formation, while Re/SiO₂ favors CH₄ formation.²⁷ The role of Zr⁴⁺ sites as Lewis acidic sites in promoting CH₃OH selectivity is related to the HCOO* and CH₃O* intermediates at the Zr⁴⁺ sites,²⁸ which was expected to occur via formate spillover as described in **Chapter 4**.

Several combinations of Re with other transition metals have been investigated for a library of reactions, ranging from the hydrogenation of carboxylic acids and amides to the production of biomass-derived chemicals.^{29–32} The addition of Re to Pt/TiO₂ decreased the particle size of Pt, while Pt assisted the reduction of ReO_x via H spillover.²⁹ Similar effects were observed over Pd-Re/SiO₂, where Pd aided in partial reduction of Re₂O₇ to active Re⁴⁺ state.³⁰ The Re addition on Ag, can promote ethylene epoxidation by weakening the Ag-O bond and reducing the electron density of adsorbed O*.³¹ ReO_x with Re⁴⁺ to Re⁷⁺ states also dispersed around the Ag particles causing electrons to shift toward the Re atom and facilitating the formation

of weakly adsorbed O*.³² Despite not being directly related, less affinity toward O of metal suppresses CO formation via CO₂ dissociation.³³

In the previous work, coinage metals (e.g. Cu, Ag, or Au) were shown to act as CO₂ activators to form bidentate formate (κ^2 -HCOO),²³ followed by further spillover to Lewis acidic support.²⁴ Addition of those metals to Re/TiO₂ is expected to complement the roles of Re ^{δ^+} sites in activating CO₂, stabilizing κ^1 -HCOO* for further hydrogenation to CH₃OH, and/or supplying κ^2 -HCOO* to Re ^{δ^+} sites via spillover. The promotional effects of Re-M/TiO₂ (M = Cu, Ag, or Au) will be discussed in the next section.

Table 6.1 Catalytic activity of M(3)/TiO₂ (M = Cu, Rh, Pd, Ag, Re, Pt, or Au) during CO₂ hydrogenation and Cu/ZnO/Al₂O₃. Pretreatment: reduction under H₂ (27.4 NmL min⁻¹, T = 500 °C, 90 min). Reaction conditions: T = 150 °C, P = 60 bar, H₂/CO₂ = 3, 500 mg catalyst, SV = 3505 NmL g_{cat}⁻¹ h⁻¹, TOS = 4 h.

Catalysts	CO ₂ conversion (%)	Selectivity (%)				
		CH ₃ OH	CO	CH ₄	HCOOCH ₃	CH ₃ OCH ₃
Re/TiO ₂	3.6	67.5	27.8	2.4	2.3	0.0
Cu/TiO ₂	1.3	0.0	96.6	3.4	0.0	0.0
Rh/TiO ₂	2.7	23.4	52.7	23.8	0.1	0.0
Pd/TiO ₂	2.9	10.9	86.5	1.8	0.7	0.0
Ag/TiO ₂	1.4	3.9	90	3.1	0.5	2.5
Pt/TiO ₂	3.8	5.0	93.9	1.0	0.1	0.0
Au/TiO ₂	1.4	12.2	86.3	0.5	1.0	0.0
^a Cu/ZnO/Al ₂ O ₃	0.6	86.5	10.1	0.1	3.3	0.0

^a reduction temperature of 300 °C was used.

6.2.2 Promotional effects of Cu, Ag, and Au on Re/TiO₂

H₂-temperature programmed reduction (TPR) (**Figure S6.2**) shows the influence of Cu, Ag, and Au addition on the reduction temperature of Re/TiO₂ indicating higher or lower reducibility of Re(3)-M(1)/TiO₂ (M = Cu, Ag, or Au). Obviously, these coinage metals facilitate the reduction of bulk Re_xO_y (the first major peak), likely by enhanced H₂ activation and H-spillover on TiO₂.^{29,34} However, the broad shoulders at ca. 350 °C from all promoted catalysts suggests the presence of some residual isolated ReO_x species attached to the TiO₂ surface that was less influenced by H-spillover. These ReO_x species interacted strongly with TiO₂ and cannot be reduced completely at 500 °C, which resulted in multi-oxidation states of Re.²¹ This indicated that the Re ^{δ^+} species remain over Re-M/TiO₂ after the addition of Cu, Ag, or Au.

The influences of the reaction temperature on the catalytic activity of Re-M/TiO₂ are shown in **Figure 6.3**. Most prominently, the addition of Ag over Re/TiO₂ increased the CH₃OH selectivity across the temperature range studied (up to 7% at 150 °C) but did not improve CO₂ conversion. The

enhanced CH₃OH selectivity originated from the suppression of CO and CH₄ formation. On the other hand, the promotional effects of Cu and Au on CH₃OH selectivity were more prominent at 125 °C, but they became negligible at 150-200 °C. The CO₂ conversion was improved by the addition of Cu and Au. Notably, all Cu, Ag, and Au promoters did not alter the HCOOCH₃ selectivity (**Figure S6.3**), indicating the HCOOCH₃ formation is governed by factors other than the coinage metal, for example, the nature of support.²⁴

The catalytic activity of Re-M/TiO₂ at the optimal temperature for CH₃OH selectivity is summarized in **Table 6.2**. The CH₃OH selectivity decreases in the order of Ag > Au > Cu, which is congruent to a more facile formation of stable κ^2 -HCOO* over Ag (111), i.e., lower activation barriers to form bidentate formate as predicted by DFT calculations in the following order of the activation energy Ag (0.61 eV) < Cu (0.71 eV) < Au (0.97 eV).²³ Since the activation energy is the interplay between weak HCOO* adsorption and strong H* adsorption, the lowest value over Ag is attributed to weak H* binding and sufficiently strong HCOO* binding to Ag. On the contrary, the higher values are attributed to too weak HCOO* binding over Au, and too strong H binding over Cu.

Based on the information and observation above, the highest CH₃OH selectivity at 125 °C over Re-Au/TiO₂ could be originated from more HCOO* species on Au that more strongly adsorb and/or are less likely to decompose at relatively lower temperatures. On the other hand, Re-Cu/TiO₂ promoted CH₄ selectivity via produced CO*, since dissociation of CO₂³³ and decomposition of strongly bound HCOO* to CO* can occur over Cu (**Chapter 4**) and also CO* is an intermediate for CH₄ (**Chapter 5**). The suppression of CH₄ selectivity over Re-Ag/TiO₂ is directly related to CO*/HCOO* ratio on the surface (*vide infra*). In summary, higher CH₃OH selectivity over a catalyst originated from a lower CO₂ activation barrier promoted by coinage metals.

Figure 6.4 shows the stability tests of Re(3)/TiO₂ (**Figure 6.4a**) and Re(3)-Ag(1)/TiO₂ (**Figure 6.4b**) at 150 °C and 60 bar for 40 h, demonstrating gradually improving catalytic performance over the time on stream. The CO₂ conversion over both catalysts noticeably increased, while CH₃OH selectivity increased slightly against CO selectivity. The improved CH₃OH selectivity may be originated from the redispersion of Re into smaller clusters or single atoms due to electronic interactions between Re and TiO₂,²⁶ as shown in **Chapter 5**. The addition of Ag did not seem to hinder this process, and its agglomeration did not affect the catalyst stability within 40 h of the reaction. The nature of the active site over Re-Ag/TiO₂ will be discussed in the next section.

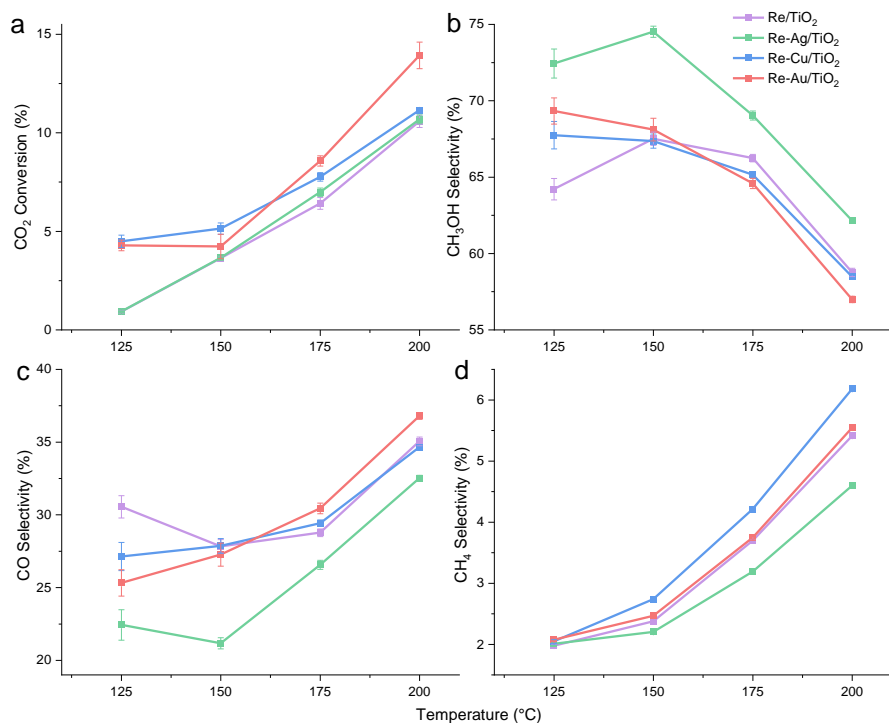


Figure 6.3 Effects of temperatures on CO₂ conversion and product selectivities of **b** CH₃OH **c** CO and **d** CH₄ during CO₂ hydrogenation over Re(3)-M(1)/TiO₂ (M = Cu, Ag, or Au). Reaction conditions: T = 125-200 °C, P = 60 bar, H₂/CO₂ = 3, SV = 3505 NmL g_{cat}⁻¹ h⁻¹, TOS = 4 h.

Table 6.2 Catalytic activity of Re(3)-M(1)/TiO₂ (M = Cu, Ag, and Au) during CO₂ hydrogenation at optimal conditions. Pretreatment: reduction under H₂ (27.4 NmL min⁻¹, T = 500 °C, 90 min). Reaction conditions: T = 150 °C, P = 60 bar, H₂/CO₂ = 3, 500 mg catalyst, SV = 3505 NmL g_{cat}⁻¹ h⁻¹, TOS = 4 h.

Catalyst	Temperature (°C)	CO ₂ conversion (%)	Selectivity (%)			
			CH ₃ OH	CO	CH ₄	HCOOCH ₃
Re/TiO ₂	150	3.6	67.5	28.0	2.4	2.3
Re-Cu/TiO ₂	150	5.1	67.0	28.0	2.7	2.0
Re-Ag/TiO ₂	150	3.6	74.5	21.2	2.2	2.1
Re-Au/TiO ₂	125	4.3	69.3	25.3	2.1	3.3

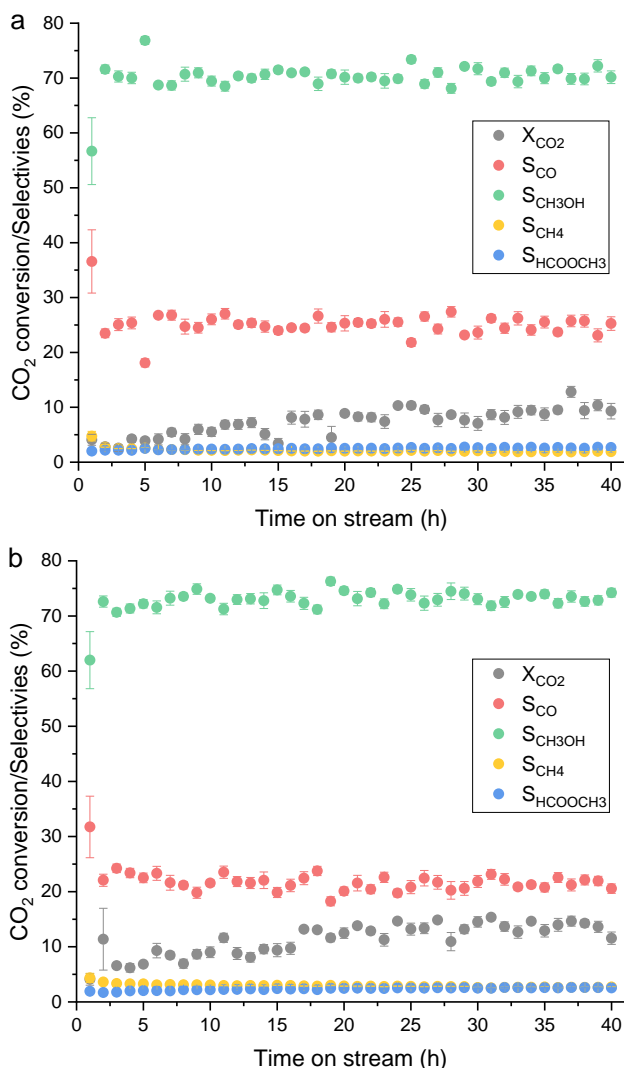


Figure 6.4: Catalytic stability during CO₂ hydrogenation of **a** Re(3)/TiO₂ and **b** Re(3)-Ag(1)/TiO₂. Reaction conditions: T = 150 °C, P = 60 bar, H₂/CO₂ = 3, SV = 3505 NmL g_{cat}⁻¹ h⁻¹.

6.2.3 The unique interplay between Re and Ag on Re-Ag/TiO₂

The promotional effects of Ag on Re were so far investigated by adding 1wt% Ag to Re(3)/TiO₂. The effects of Re/Ag ratios were studied further by varying the Re and Ag amounts, Re(x)-Ag(4-x)/TiO₂ (x = 1, 2, or 3). The effects of temperature on CO₂ conversion and product selectivities over

Re-Ag/TiO₂ were similar to those over Re-Cu/TiO₂ and Re-Au/TiO₂, giving the optimal temperature for CH₃OH selectivity at 150 °C (**Figure S6.4**). At the optimal temperature, the influences of Re and Ag on catalytic activity (**Figure 6.5**, and **Table 6.3**) showed that a small amount of Ag addition (Re(3)-Ag(1)/TiO₂) improves the CH₃OH selectivity of Re/TiO₂ by suppressing CO and CH₄ formation. The improved reducibility was also observed (**Figure S6.5** and **Table S6.1**). On the other hand, a smaller amount of Re, i.e., Re(1)-Ag(3)/TiO₂, can significantly improve the CO₂ conversion as well as CH₃OH and HCOOCH₃ selectivities of Ag/TiO₂.

Notably, the highest HCOOCH₃ selectivity over Re(1)-Ag(3)/TiO₂ confirmed the role of Ag in CO₂ activation to HCOO*, the role of active Re^{δ+} sites in HCOO* stabilization, and the roles of Re⁰ in H₂ dissociation and spillover to Re^{δ+} sites for CH₃OH formation. Subsequently, the abundance of HCOO* over Ag led to HCOOCH₃ formation via reaction with CH₃OH, as well as, less tendency of HCOO* decomposition to CO. Increasing Re/Ag ratio not only resulted in lower CO selectivity due to HCOO* hydrogenation (than decomposition) but also higher CH₄ selectivity due to excessive hydrogenation of CO*. The optimal CH₃OH selectivity was obtained from Re(3)-Ag(1)/TiO₂, which originated from the balance between HCOO* supplied by Ag and adsorbed H via H₂ dissociation over Re⁰.

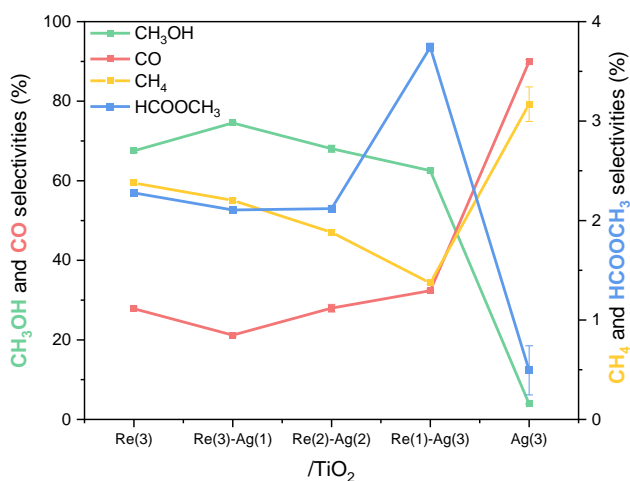


Figure 6.5 Effects of Re/Ag ratios of Re-Ag/TiO₂ on the selectivity of CH₃OH, CO, and CH₄. Reaction conditions: T = 125–200 °C, P = 60 bar, H₂/CO₂ = 3, SV = 3505 N mL g_{cat}⁻¹ h⁻¹, TOS = 4 h.

Table 6.3 Catalytic activity of Re(x)-Ag(4-x)/TiO₂ (x = 1, 2, and 3) during CO₂ hydrogenation. Pretreatment: reduction under H₂ (27.4 NmL min⁻¹, T = 500 °C, 90 min). Reaction conditions: T = 150 °C, P = 60 bar, H₂/CO₂ = 3, 500 mg catalyst, SV = 3505 NmL g_{cat}⁻¹ h⁻¹, TOS = 4 h.

Re/Ag ratio	CO ₂ conversion (%)	Selectivity (%)				
		CH ₃ OH	CO	CH ₄	HCOOCH ₃	CH ₃ OCH ₃
3:0	3.6	67.5	28.0	2.4	2.3	0.0
3:1	3.7	74.5	21.0	2.2	2.1	0.0
2:2	4.0	68.0	28.0	1.8	2.1	0.0
1:3	4.8	63.0	32.0	1.4	3.7	0.0
0:3	1.4	3.9	90.0	3.1	0.5	2.5

The structure of Re(3)-Ag(1)/TiO₂ was further investigated using scanning transmission electron microscopy (STEM). After calcination, Re_xO_y and Ag_xO particles on Re(3)-Ag(1)/TiO₂ become highly and homogeneously dispersed, as shown in **Figures 6.6** and **S6.6**. Average particle sizes of Re and Ag were found to be ca. 0.8 and 1 nm, respectively. As shown by HR-TEM Ag in Ag(3)/TiO₂ tends to agglomerate to larger particles (**Figure S6.7a**) in contrast to atomic dispersion and ultimately sub-nanometer size clusters of Re in Re(3)/TiO₂ (**Figure S6.7b**). Notably, a small amount of Re also aided Ag in improving its dispersion over Re(1)-Ag(3)/TiO₂, keeping the particle sizes smaller than Ag(3)/TiO₂, 0.8 nm and 1.2 nm respectively (**Figure S6.8**).

After the reaction, Re clusters migrated and distributed around the Ag nanoparticles as shown by STEM-EDS (**Figure 6.7**). The particle size of Ag on spent Re(3)-Ag(1)/TiO₂ increased to ca. 5 nm. In the previous work, the effects of Ag particle size were not evidenced for the formation of HCOOCH₃ and CO when methanol was cofed with CO₂ and H₂ to enhance HCOOCH₃ formation.²⁴ Under such a condition, support, and metal-type effects were more pronounced than the particle size, because methanol adsorption, found to be the rate-limiting step of HCOOCH₃ formation, is mainly determined by the nature of the support material. However, in CO₂ hydrogenation the balance between CO* and HCOO* populations on metal (e.g. Pd) is influenced by particle size (wt% loading) and eventually affected CH₄ and CO selectivity.³⁵ As reported in **Chapter 5**, the size of Re does play role in altering selectivity. Hence, the particle size changes and the unique assembly of Re and Ag during the reaction are likely important to understand the reactivity and product selectivity.

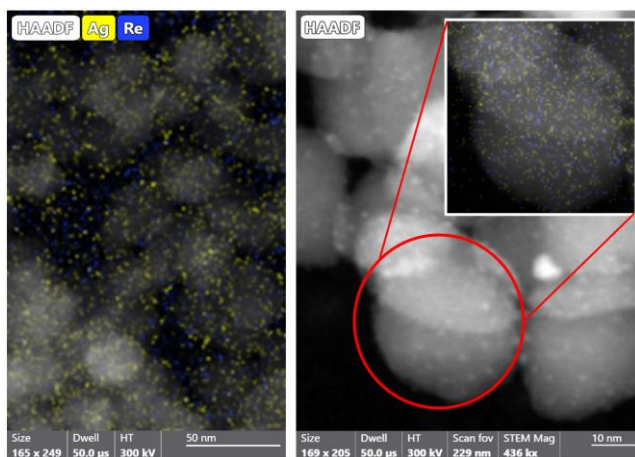


Figure 6.6 Representative high-angle annular dark-field scanning transmission electron microscopy (HAADF-STEM) images and energy dispersive spectroscopy (EDS) analysis of calcined Re(3)-Ag(1)/TiO₂.

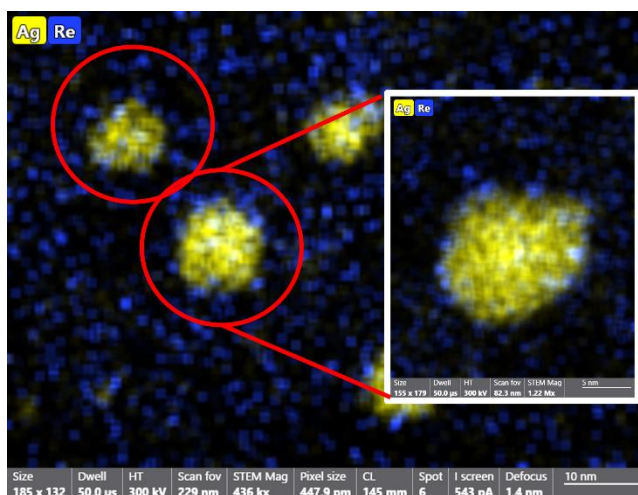


Figure 6.7 Representative high-angle annular dark-field scanning transmission electron microscopy (HAADF-STEM) images and energy dispersive spectroscopy (EDS) analysis of spent Re(3)-Ag(1)/TiO₂.

The Ag K-edge XANES spectra of calcined Ag(3)/TiO₂ and Re(3)-Ag(1)/TiO₂ (**Figure S6.9**) showed lower edge energy than Ag foil suggesting the presence of Ag₂O.³⁶ A higher white-line intensity of Re(3)-Ag(1)/TiO₂ was attributed to smaller particle size as shown by HR-TEM. After reduction, the white line energy of all samples matched with the reference Ag foil (**Figure 6.8**), suggesting the reduction of Ag₂O to Ag⁰. The

unchanged white line position also suggests the unoxidized Ag^0 after reacting with CO_2 due to the weak O binding on Ag.

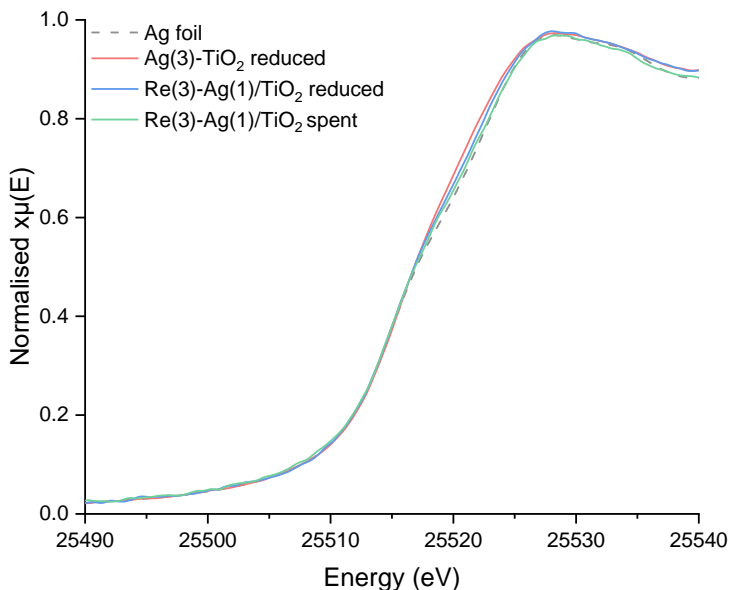


Figure 6.8 Ag K-edge XANES spectra of Ag foil reference, reduced Ag(3)/TiO₂, reduced and spent Re(3)-Ag(1)/TiO₂. The XAS spectra were taken at room temperature without exposure to air after the reduction treatment by sealing the samples under N₂.

The Re L₃-edge XANES spectra (**Figure S6.10**) showed the shift in absorption edge energy indicating the reduction of Re₂O₇ species toward metallic Re⁰ over both Re(3)/TiO₂ and Re(3)-Ag(1)/TiO₂.³⁷ As described in **Chapter 5**, Re after reduction contains multi-oxidation states of Re⁰, Re²⁺, and Re⁴⁺. Both the calcined and reduced samples of Re(3)-Ag(1)/TiO₂ had higher absorption energy than Re(3)/TiO₂. The addition of Ag does not change the oxidation state of Re but the spent Re(3)-Ag(1)/TiO₂ displayed higher absorption edge energy by 1.2 eV compared to the reduced sample (**Figure 6.9**), which indicated the oxidation of Re⁰ after reacting with CO₂. This finding is consistent with the results from AP-XPS in **Chapter 5**.

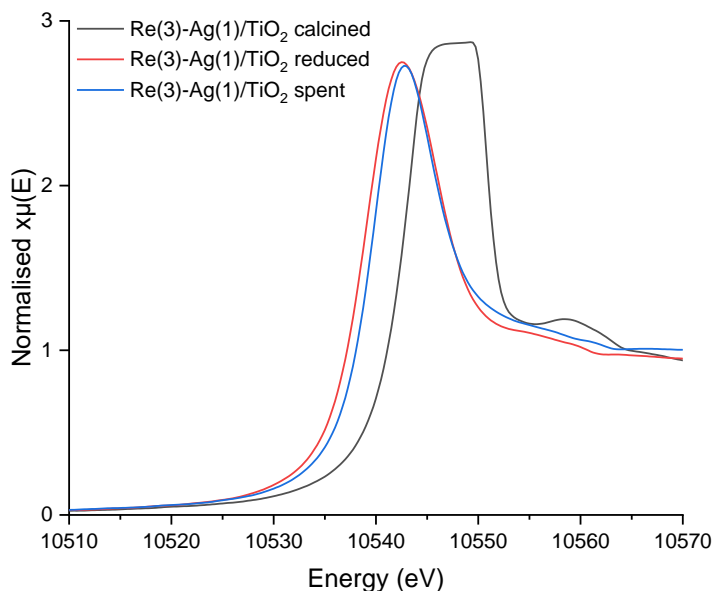


Figure 6.9 Re L_3 -edge XANES spectra of calcined, reduced, and spent Re(3)-Ag(1)/TiO₂. The XAS spectra were taken at room temperature without exposure to air after the reduction treatment by sealing the samples under N₂.

The low signal-to-noise of the Re L_3 -edge spectra in the EXAFS region limits the quantitative analysis (**Figure S6.11a**). Visual comparisons between the R-space plots displayed a diminished intensity of a peak after reduction treatment at an average radial distance of 1.3 Å representing a Re-O (**Figure S6.11b**). As shown in **Figure 6.10** the EXAFS analysis from the Ag K-edge of Ag(3)/TiO₂ and Re(3)-Ag(1)/TiO₂ showed no Re-Ag interaction indicating the absence of alloy formation. However, the increase in the average coordination number of the spent Re(3)-Ag(1)/TiO₂ (**Table 6.4**) suggested larger particle sizes of Ag⁰, as confirmed by STEM. The time-resolved *operando* XAS would be a powerful technique to observe the changes of Ag and Re during the time on stream. In this study, the time-resolved *operando* DRIFTS was used to observe the surface species over Ag, Re, and TiO₂ and provide insight into the reaction mechanism.

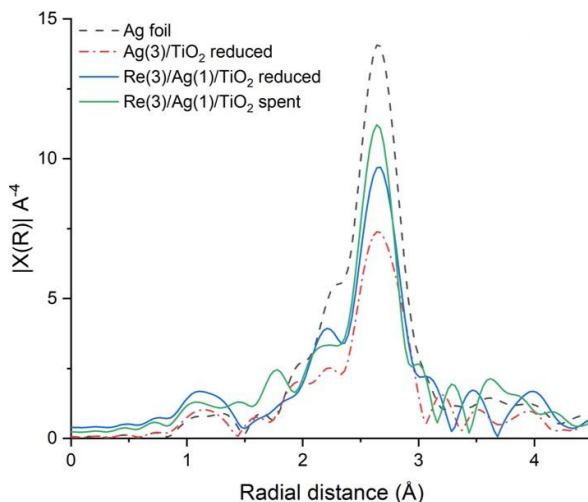


Figure 6.10 Fourier-transformed Ag K-edge EXAFS of Ag foil, reduced Re(3)-Ag(1)/TiO₂, reduced and spent Re(3)-Ag(1)/TiO₂. The XAS spectra were taken at room temperature without exposure to air after the reduction treatment by sealing the samples under N₂.

Table 6.4 Model parameters obtained from fitting of Ag K-edge EXAFS spectra. The amplitude reduction factor (S_0^2) was set to 0.973. N = average coordination number, σ^2 = average variation in path length, ΔE^0 = adjustment used for fitting, R = average distance between atoms.

Sample	Scatter	N	R (Å)	E ₀ (eV)	σ^2 (Å ²)
Ag foil (reference)	Ag-Ag	10.76 ± 0.60	2.86	3.80	0.01
Ag(3)/TiO ₂ reduced	Ag-Ag	7.18 ± 0.54	2.85	2.90	0.01
Re(3)-Ag(1)/TiO ₂ reduced	Ag-Ag	8.13 ± 0.83	2.85	4.20	0.01
Re(3)-Ag(1)/TiO ₂ spent	Ag-Ag	9.27 ± 0.54	2.85	4.20	0.01

6.2.4 Mechanistic insight over Re-Ag/TiO₂

Operando DRIFTS provided insights into surface species over TiO₂, Re(3)/TiO₂, Ag(3)/TiO₂, and Re(3)-Ag(1)/TiO₂ during CO₂ hydrogenation at 125-200 °C and 20 bar. Over TiO₂ (**Figure S6.12** and **S6.13**), bicarbonate (HCO₃^{*}, 1223, 1429, and 1503 cm⁻¹), bidentate carbonate (κ^2 -CO₃^{*}, 1369 and 1583 cm⁻¹), weakly adsorbed carbon dioxide (CO₂^{*}, 1334 cm⁻¹) and water (H₂O^{*}, 1610 cm⁻¹) were the only surface species from CO₂ activation/interaction. Undetectable bidentate formate (κ^2 -HCOO^{*}) over TiO₂ suggested the role of supported metals for C–H formation.

As shown in (**Figure S6.14**), on the other hand, the κ^2 -HCOO^{*} on TiO₂ (1370, 1570, 2870, and 2950 cm⁻¹) was the major intermediate across temperature ranges over Ag/TiO₂. The methoxy on TiO₂ (CH₃O^{*} (TiO₂), 2830

and 2930 cm^{-1}) originated from CH_3OH adsorption on hydroxyl group (OH^*) and appeared above 175 $^\circ\text{C}$. This is congruent with catalytic testing results when Ag/TiO_2 becomes active for CH_3OH and HCOOCH_3 formation at that temperature. Notably, no carbonyls (CO^*) were detected due to its weak binding to Ag and more favorable desorption of CO^* to CO .³⁸

The temporal evolution of surface species over Ag/TiO_2 (**Figure S6.15**) showed a broad peak at 1395 cm^{-1} at the initial state of reaction (0.1-0.5 min), which is attributed to HCOO^* on Ag.²⁴ The HCOO^* (Ag) subsequently disappeared with the appearance of $\kappa^2\text{-HCOO}^*$ (TiO_2) at 1370 cm^{-1} , which supports the formate spillover to TiO_2 support, as described in **Chapter 5**.

Over Re/TiO_2 (**Figure S6.17**) a similar $\kappa^2\text{-HCOO}^*$ (TiO_2) was observed while CH_3O^* (TiO_2) was formed at lower temperatures (125 $^\circ\text{C}$). The less pronounced $\kappa^2\text{-HCOO}$ (TiO_2) intensity compared with CH_3O^* (TiO_2) is consistent with the HCOO^* hydrogenation activity of Re. The CO^* species on Re at 2030, 1910, and 1875 cm^{-1} were also identified as rhenium tricarbonyl complexes ($\text{Re}(\text{CO})_3$).³⁹ As shown in **Figure S6.17**, the consumption of rhenium hydride (Re-H , 1960 cm^{-1}),⁴⁰ and the subsequent formation of monodentate formate on Re ($\kappa^1\text{-HCOO}$, 1420 and 1590 cm^{-1}) at the initial state of reaction (0.1-0.3 mins) confirmed the initial CO_2 activation over $\text{Re}^{\delta+}$ via hydride transfer in **Chapter 5**. The appearance of $\kappa^2\text{-HCOO}^*$ (TiO_2) after $\kappa^1\text{-HCOO}$ (Re) also suggested a similar formate spillover as on Ag/TiO_2 .

In general, the surface species over $\text{Re-Ag}/\text{TiO}_2$ (**Figure S6.18**) were similar to those over Re/TiO_2 and Ag/TiO_2 , and CO_2 conversion seemed to follow the same reaction pathways i.e. CO_2 activation over both Ag and $\text{Re}^{\delta+}$ to formate and subsequent spillover to TiO_2 support (**Figure 6.11**). The formation of $\text{Re}(\text{CO})_3$ occurred after formate spillover (0.5 min) and after consumption of Re-H , which supports CO^* formation over Re via carboxylate (**Chapter 5**).

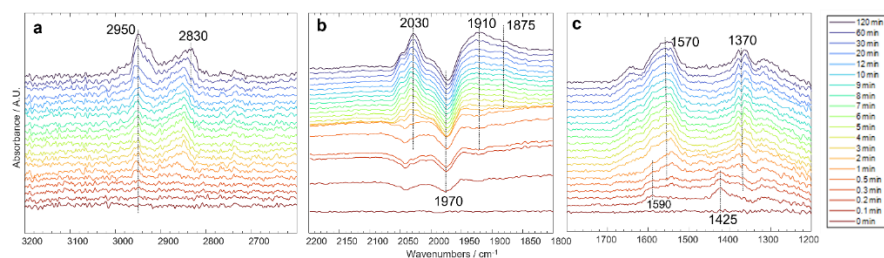


Figure 6.11 Temporal evolution of surface species obtained from operando DRIFTS during reaction CO_2 hydrogenation over $\text{Re(3)-Ag(1)}/\text{TiO}_2$. Reaction conditions: 10 mg catalyst, $\text{H}_2/\text{CO}_2 = 3$, $T = 125\text{ }^\circ\text{C}$, $P = 10$ bar, $F_{\text{total}} = 10\text{ NmL min}^{-1}$.

Lastly, the role of Ag on surface species concentration over Re-Ag/TiO₂ was studied by evaluating the ratio between the relative intensity of CO* and HCOO* (**Figure 6.12**). The reduction in the CO*/HCOO* ratio, which represented the ratio of Re(CO)₃/κ²-HCOO*(TiO₂), could be originated from either the increase in HCOO* surface concentration supplied by Ag or the decrease CO* concentration over Re. Hydrogenation of CO* formed via formate decomposition is the rate-determining step for CH₄ formation over Pd/Al₂O₃, and the balance between HCOO* and CO* hydrogenation kinetics can govern the selectivities of CH₄ and CO.³⁵ From **Chapter 5**, CH₄ formation occurs from the hydrogenation of CO* on Re. On the other hand, Ag made CO* desorption more favorable than undergoing CO* hydrogenation to CH₄. Ag can stabilize more HCOO* for hydrogenation by Re.

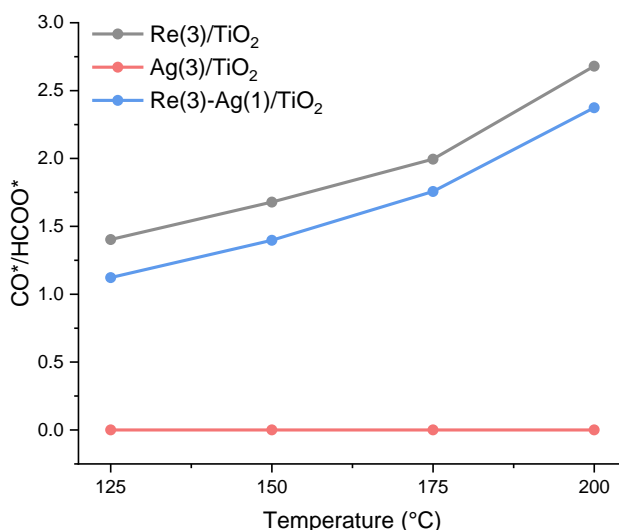


Figure 6.12 Effect of Ag addition of CO*/HCOO* ratio calculated from absorbance during *operando* DRIFTS over Ag(3)/TiO₂, Re(3)/TiO₂ and Re(3)-Ag(1)/TiO₂. Reaction conditions: 10 mg catalyst, H₂/CO₂ = 3, T = 125–200 °C, P = 10 bar, F_{total} = 10 NmL min⁻¹, TOS = 4 h.

6.3 Conclusion

CH₃OH selectivity over 3 wt% Re/TiO₂ can be improved by adding a small amount of Ag (1 wt%). During the reaction, Re clusters relocated to the vicinity of Ag nanoparticles. Despite the absence of alloy formation between Re-Ag, parts of Re⁰ were transformed into Re^{δ+} species, expectedly by redispersion, while Ag⁰ remained in its original state. The role of Ag was attributed to more facile activation of CO₂ to HCOO* in the form of bidentate

formate, in contrast to the monodentate formate over $\text{Re}^{\delta+}$. This formate form on Ag likely facilitates its spillover toward the TiO_2 support. Enhanced formates formed over Ag^0 improved CH_3OH selectivity of Re-Ag/TiO_2 possibly via HCOO^* spillover to $\text{Re}^{\delta+}$ for further hydrogenation, while Re^0 plays a role as an H_2 activator similar to the original Re/TiO_2 .

Moreover, unfavorable CO^* adsorption over Ag suppressed CO hydrogenation to CH_4 , ultimately increasing CH_3OH selectivity. The improved catalytic performance over time on stream up to 40 h also suggested great stability of Re-Ag/TiO_2 . This work has important implications for other bifunctional systems where the balance between different catalytic functions determines the rates and product distribution.

6.4 Experimental

6.4.1 Catalyst materials and preparation

All chemical precursors used to synthesize the catalysts were acquired from commercial suppliers. TiO_2 (ST-01 anatase) was supplied by Ishihara Sangyo Ltd. For the synthesis of various transition metals on TiO_2 ($\text{TM}(3)/\text{TiO}_2$ where $\text{TM} = \text{Cu, Rh, Pd, Ag, Re, Pt, Au}$), respective metal precursors were mixed with TiO_2 , following the wetness impregnation method. These precursors were NH_4ReO_4 , $\text{Au}(\text{CH}_3\text{COO})$, $4\text{NH}_3\text{Pt}(\text{NO}_3)_2$, nitrates of Cu and Ag, and chlorides of Rh and Pd. For the preparation of $\text{Re}(3)/\text{TiO}_2$, 0.090 g of NH_4ReO_4 powder was dissolved in 40 mL of water. After sonication (1 min) to ensure thorough dissolution, 2.0 g of TiO_2 was added to the solution. The resulting mixture was allowed to mix for 30 minutes at 250 rpm at room temperature, followed by evaporation of water at 50 °C for 12 h. Subsequently, the resulting powder was dried further for 10 h at 100 °C and finally calcined in the air ($T = 500\text{ °C}$, $t = 3\text{ h}$, heating rate = 10 °C min^{-1}). All other $\text{TM}(3)/\text{TiO}_2$ catalysts were synthesized with the method described above.

Equal precursors were used to synthesize $\text{Re}(3)\text{-M}(1)/\text{TiO}_2$ ($\text{M} = \text{Cu, Ag, Au}$). Furthermore, a similar procedure as described above was followed with the addition of the respective precursor together with NH_4ReO_4 .

6.4.2 Catalyst Characterization

X-ray diffraction (XRD) measurements were performed using a Bruker D8 Advance-ECO with a Bragg-Brentano X-ray diffractometer. For transmission electron microscopy (TEM) imaging, a JEM3200-FSC (JEOL) microscope was utilized, operated at 300 kV. Temperature programmed

reduction (TPR) was performed in an in-house setup. For STEM-EDS mapping analysis, an FEI cubed Cs corrected Titan was used. *Ex situ* Ag K-edge and Re L₃-edge X-ray absorption spectra were measured at the superXAS beamline at SLS (Villigen, Switzerland). DRIFTS experiments were carried out in an in-house high-pressure reaction cell equipped with a ZnSe window mounted on a Praying Mantis (Harrick). A ThermoScientific Nicolet 6700 FT-IR spectrometer equipped with an MCT (Mercury Cadmium Telluride) detector was used to obtain the IR spectra. The detector was constantly cooled with liquid N₂. Gases (H₂, CO₂, and He) were controlled via mass flow controllers (Bronkhorst). All samples were reduced at 300 °C under H₂ (19.1 mL min⁻¹) and subsequently reacted with CO₂ and H₂ at 20 bar (T = 125, 150, 175, 200 °C, H₂/CO₂ = 3, 19.0 mL min⁻¹).

6.4.3 Catalytic testing

Hydrogenation at lower pressure was performed using a commercial PID Microreactivity Efficient reactor. 500 mg of catalyst was added to a quartz reactor (ID = 4 mm) and was reduced under H₂ (27.4 mL min⁻¹) at T = 500 °C (300 °C in the case of Cu/ZnO/Al₂O₃). After cooling to 25 °C under N₂, the reaction took place at 125, 150, 175, and 200 °C at 60 bar (23.5 vol% CO₂, 70.5 vol% H₂, 6 vol% N₂). Outlet gases were analyzed using a gas chromatograph (Interscience) equipped with a flame ionization detector (FID) and two thermal conductivity detectors (TCD). Stability tests were performed similarly to that described above, with the difference of maintaining 150 °C for 40 h.

6.5 References

- 1 A. Goeppert, M. Czaun, J.-P. Jones, G. K. Surya Prakash, and G. A. Olah, *Chem. Soc. Rev.*, 2014, 43, 7995–8048.
- 2 G. A. Olah, A. Goeppert and G. K. S. Prakash, *Beyond Oil and Gas: The Methanol Economy*, Wiley, 2009, vol. 44.
- 3 G. A. Olah, *Angew. Chem., Int. Ed.*, 2013, 52, 104–107.
- 4 A. Álvarez, A. Bansode, A. Urakawa, A. V. Bavykina, T. A. Wezendonk, M. Makkee, J. Gascon and F. Kapteijn, *Chem. Rev.*, 2017, 117, 9804–9838.
- 5 P. S. Murthy, W. Liang, Y. Jiang and J. Huang, *Energy Fuels*, 2021, 35, 8558–8584.
- 6 J. Niu, H. Liu, Y. Jin, B. Fan, W. Qi and J. Ran, *Int. J. Hydrogen. Energy.*, 2022, 47, 9183–9200.
- 7 A. Bansode and A. Urakawa, *J. Catal.*, 2014, 309, 66–70.
- 8 R. Gaikwad, A. Bansode and A. Urakawa, *J. Catal.*, 2016, 343, 127–132.
- 9 J. Zeng, K. Fujimoto and N. Tsubaki, *Energy Fuels*, 2002, 16, 83–86.
- 10 R. Yang, X. Yu, Y. Zhang, W. Li and N. Tsubaki, *Fuel*, 2008, 87, 443–450.
- 11 J. Kothandaraman, R. A. Dagle, V. L. Dagle, S. D. Davidson, E. D. Walter, S. D. Burton, D. W. Hoyt and D. J. Heldebrant, *Catal. Sci. Technol.*, 2018, 8, 5098–5103.
- 12 F. Sha, Z. Han, S. Tang, J. Wang and C. Li, *ChemSusChem*, 2020, 13, 6160–6181.
- 13 S. T. Bai, G. de Smet, Y. Liao, R. Sun, C. Zhou, M. Beller, B. U. W. Maes and B. F. Sels, *Chem. Soc. Rev.*, 2021, 50, 4259–4298.
- 14 Y. Chen, S. Choi and L. T. Thompson, *J. Catal.*, 2016, 343, 147–156.
- 15 J. Hu, L. Yu, J. Deng, Y. Wang, K. Cheng, C. Ma, Q. Zhang, W. Wen, S. Yu, Y. Pan, J. Yang, H. Ma, F. Qi, Y. Wang, Y. Zheng, M. Chen, R. Huang, S. Zhang, Z. Zhao, J. Mao, X. Meng, Q. Ji, G. Hou, X. Han, X. Bao, Y. Wang and D. Deng, *Nat. Catal.*, 2021, 4, 242–250.
- 16 S. Bai, Q. Shao, Y. Feng, L. Bu, and X. Huang, *Small*, 2017, 13, 1–6.
- 17 C. Wu, P. Zhang, Z. Zhang, L. Zhang, G. Yang and B. Han, *ChemCatChem*, 2017, 9, 3691–3696.
- 18 T. Toyao, S. Kayamori, Z. Maeno, S. M. A. H. Siddiki and K. I. Shimizu, *ACS Catal.*, 2019, 9, 8187–8196.
- 19 U. Olsbye, A. Nova, E. S. Gutterød, S. H. Pulumati, G. Kaur, A. Lazzarini, B. G. Solemsli, A. E. Gunnæs, C. Ahoba-Sam, M. E. Kalyva, J. A. Sannes, S. Svelle and E. Skúlason, *J. Am. Chem. Soc.*, 2020, 142, 17105–17118.
- 20 E. S. Gutterød, A. Lazzarini, T. Fjermestad, G. Kaur, M. Manzoli, S. Bordiga, S. Svelle, K. P. Lillerud, E. Skúlason, S. Øien-Ødegaard, A. Nova and U. Olsbye, *J. Am. Chem. Soc.*, 2020, 142, 999–1009.
- 21 K. W. Ting, T. Toyao, S. M. A. H. Siddiki and K. Shimizu, *ACS Catal.*, 2019, 9, 3685–3693.
- 22 E. Lam, J. J. Corral-Pérez, K. Larmier, G. Noh, P. Wolf, A. Comas-Vives, A. Urakawa and C. Copéret, *Angew. Chem., Int. Ed.*, 2019, 58, 13989–13996.
- 23 J. J. Corral-Pérez, A. Bansode, C. S. Praveen, A. Kokalj, H. Reymond, A. Comas-Vives, J. VandeVondele, C. Copéret, P. R. von Rohr and A. Urakawa, *J. Am. Chem. Soc.*, 2018, 140, 13884–13891.
- 24 J. J. Corral-Pérez, C. Copéret and A. Urakawa, *J. Catal.*, 2019, 380, 153–160.
- 25 J. J. Corral-Pérez, A. Billings, D. Stoian and A. Urakawa, *ChemCatChem*, 2019, cctc.201901179.
- 26 S. Mine, K. W. Ting, L. Li, Y. Hinuma, Z. Maeno, S. M. A. H. Siddiki, T. Toyao and K. I. Shimizu, *J. Phys. Chem. C*, 2022, 126, 4472–4482.
- 27 T. Iizuka, M. Kojima and K. Tanabe, *J. Chem. Soc. Chem. Commun.*, 1983, 638–639.

- 28** E. Lam, K. Larmier, P. Wolf, S. Tada, O. v. Safonova and C. Copéret, *J. Am. Chem. Soc.*, 2018, 140, 10530–10535.
- 29** J. Pritchard, A. Ciftci, M. W. G. M. T. Verhoeven, E. J. M. Hensen and E. A. Pidko, *Catal. Today*, 2017, 279, 10–18.
- 30** J. D. Kammert, J. Xie, I. J. Godfrey, R. R. Unocic, E. Stavitski, K. Attenkofer, G. Sankar and R. J. Davis, *ACS Sustain. Chem. Eng.*, 2018, 6, 12353–12366.
- 31** Y. Jun, D. Jingfa, Y. Xiaohong and Z. Shi, *Appl. Catal. A: Gen.*, 1992, 92, 73–80.
- 32** D. Ren, G. Cheng, J. Li, J. Li, W. Dai, X. X. Sun and D. Cheng, *Catal. Letters.*, 2017, 147, 2920–2928.
- 33** L. Dietz, S. Piccinin and M. Maestri, *J. Phys. Chem. C*, 2015, 119, 4959–4966.
- 34** A. Ciftci, D. A. J. M. Ligthart, A. O. Sen, A. J. F. van Hoof, H. Friedrich and E. J. M. Hensen, *J. Catal.*, 2014, 311, 88–101.
- 35** X. Wang, H. Shi and J. Szanyi, *Nat. Commun.*, 2017, 8, 1–6.
- 36** K. ichi Shimizu, J. Shibata, H. Yoshida, A. Satsuma and T. Hattori, *Appl. Catal. B*, 2001, 30, 151–162.
- 37** S. R. Bare, S. D. Kelly, F. D. Vila, E. Boldingh, E. Karapetrova, J. Kas, G. E. Mickelson, F. S. Modica, N. Yang and J. J. Rehr, *J. Phys. Chem. C*, 2011, 115, 5740–5755.
- 38** S. Choi, B. I. Sang, J. Hong, K. J. Yoon, J. W. Son, J. H. Lee, B. K. Kim and H. Kim, *Sci. Rep.*, 2017, 7, 1–10.
- 39** F. Solymosi and T. Bánsági, *J. Phys. Chem. C*, 1992, 96, 1349–1355.
- 40** N. Li, Y. Xie, R. B. King and H. F. Schaefer, *J. Phys. Chem. A*, 2010, 114, 11670–11680.

Supporting information

Chapter 6

1. Exploring the transition metals for low temperature

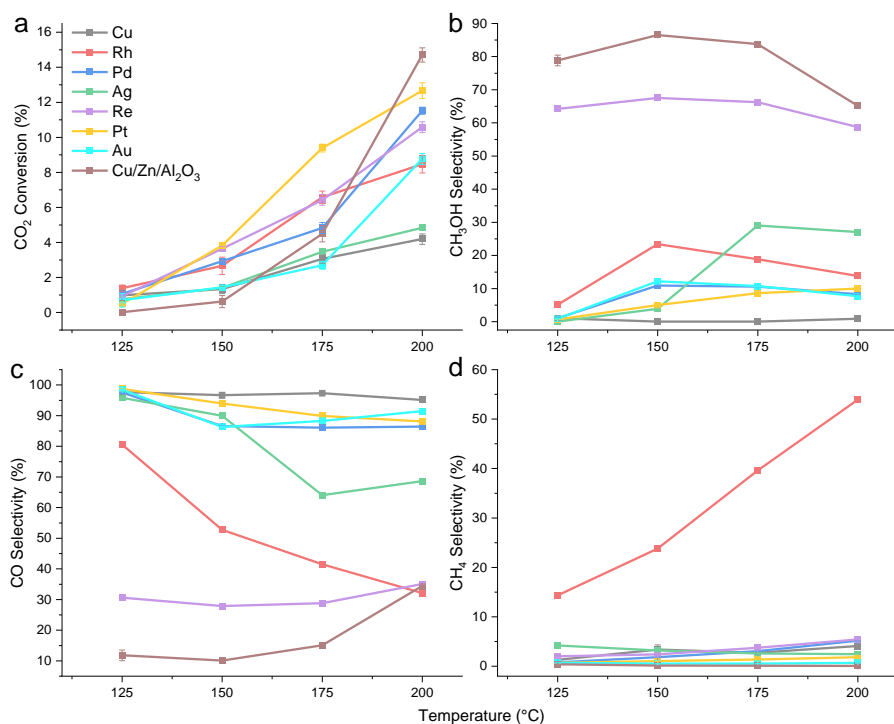


Figure S6.1 Effects of temperatures on **a** CO₂ conversion and product selectivities of **b** CH₃OH **c** CO and **d** CH₄ during CO₂ hydrogenation over M(3)/TiO₂ (M = Cu, Rh, Pd, Ag, Re, Pt or Au). Reaction conditions: T = 125-200 °C, P = 60 bar, H₂/CO₂ = 3, SV = 3505 NmL g_{cat}⁻¹ h⁻¹, TOS = 4 h.

2. Promotional effects of Cu, Ag, and Au on Re/TiO₂

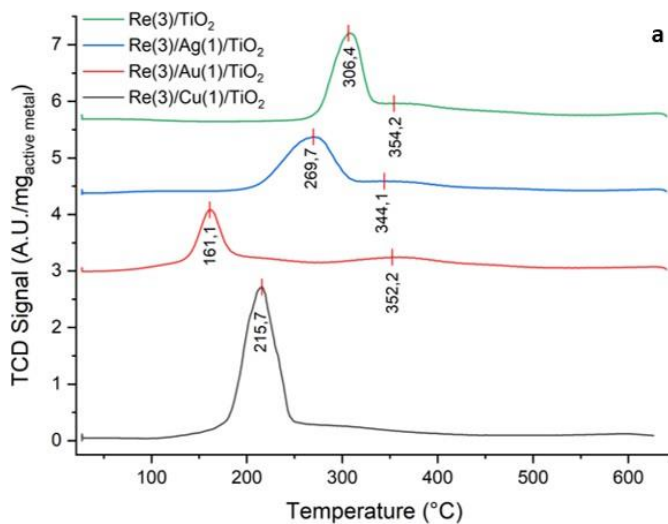


Figure S6.2 H₂-TPR profiles of Re(3)/TiO₂, Ag(1)/TiO₂, Re(3)-Au(1)/TiO₂ and Re(3)-Cu(1)/TiO₂. Reduction conditions: 5% H₂/N₂, F = 20 mL min⁻¹, T = 50-650 °C and heating rate = 2 °C min⁻¹.

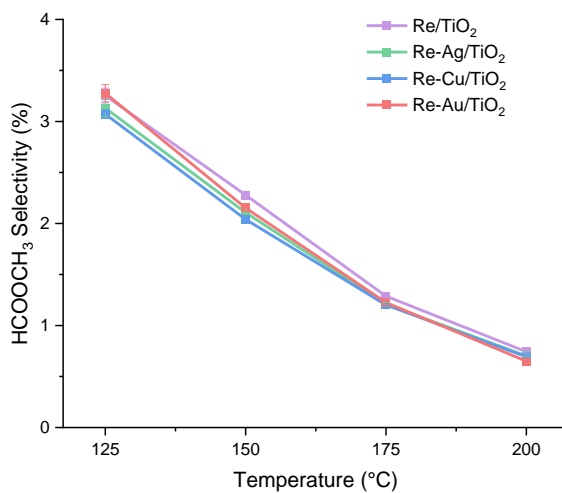


Figure S6.3 Effects of temperatures on HCOOCH₃ selectivity during CO₂ hydrogenation over Re(3)-M(1)/TiO₂ (M = Cu, Ag, and Au). Reaction conditions: T = 125-200 °C, P = 60 bar, H₂/CO₂ = 3, SV = 3505 NmL g_{cat}⁻¹ h⁻¹, TOS = 4 h.

3. The unique interplay between Re and Ag on Re-Ag/TiO₂

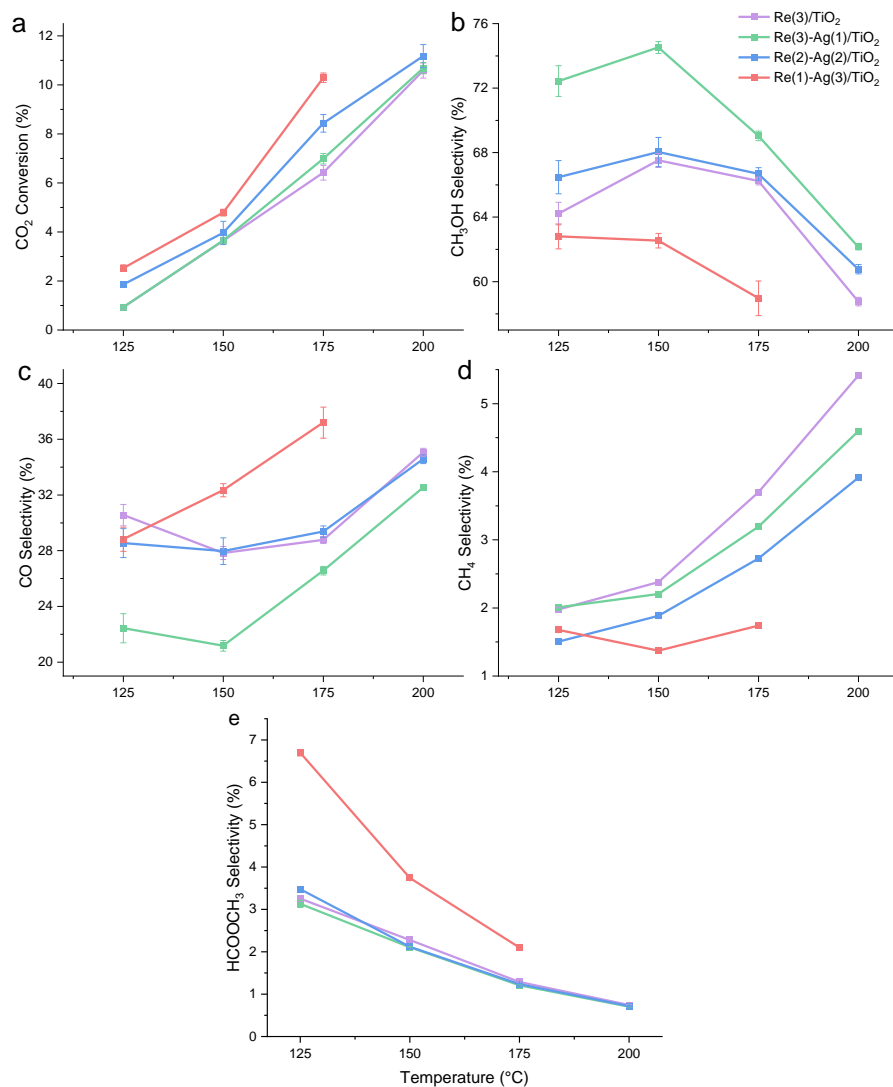


Figure S6.4 Effects of temperatures on **a** CO₂ conversion and products selectivities of **b** CH₃OH **c** CO and **d** CH₄ **e** HCOOCH₃ during CO₂ hydrogenation over Re(x)-Ag(4-x)/TiO₂ (x = 1, 2, and 3). Reaction conditions: T = 125–200 °C, P = 60 bar, H₂/CO₂ = 3, SV = 3505 NmL g_{cat}⁻¹ h⁻¹, TOS = 4 h.

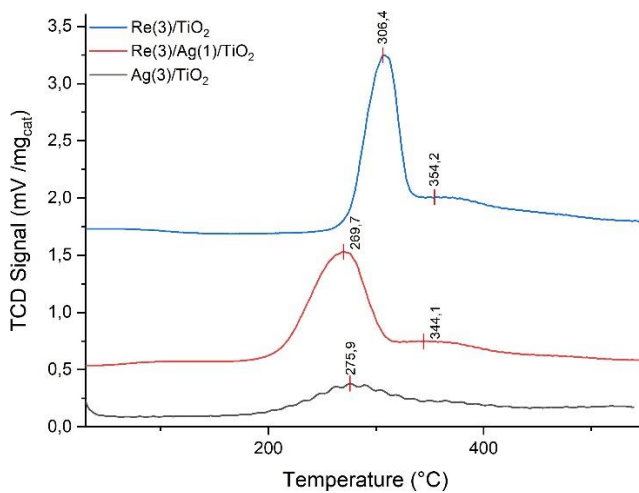


Figure S6.5 H₂-TPR profiles of Re(3)/TiO₂, Re(3)-Ag(1)/TiO₂ and Ag(3)/TiO₂. Reduction conditions: 5% H₂/N₂, F = 20 NmL min⁻¹, T = 50-650 °C and heating rate = 2 °C min⁻¹.

Table S6.1 Data obtained from TPR analysis, including peak reduction temperature, normalized area of the peak reduction concerning Re(3)/TiO₂, and its full width at half maximum (FWHM)

Catalyst	Temperature of highest H ₂ uptake (°C)	Normalized peak area with Re(3)/TiO ₂	FWHM (a.u.)
Re(3)/TiO ₂	306.9	1.0	35.4
Re(3)-Ag (1)/TiO ₂	269.7	1.0	60.4
Ag(3)/TiO ₂	275.9	0.4	83.6

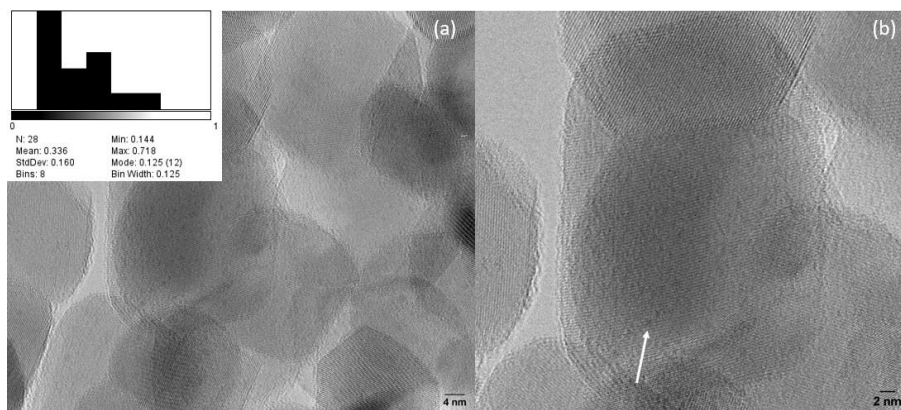


Figure S6.6 Representative HR-TEM images of calcined Re(3)-Ag(1)/TiO₂.

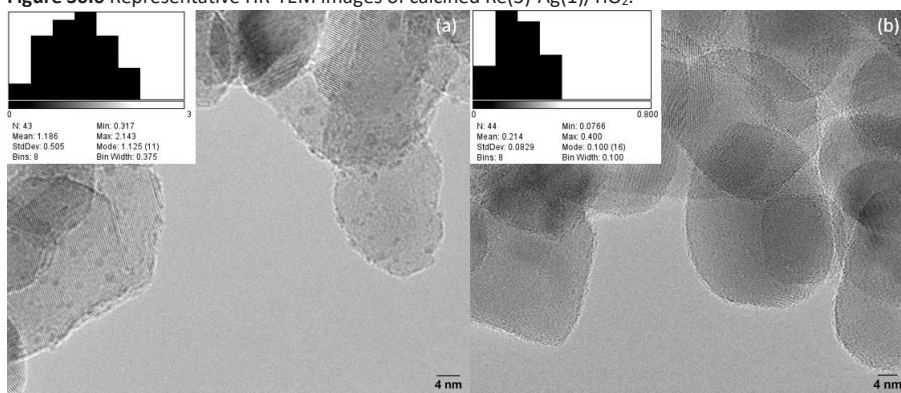


Figure S6.7 Representative HR-TEM images of calcined **a** Ag(3)/TiO₂ and **b** Re(3)/TiO₂.

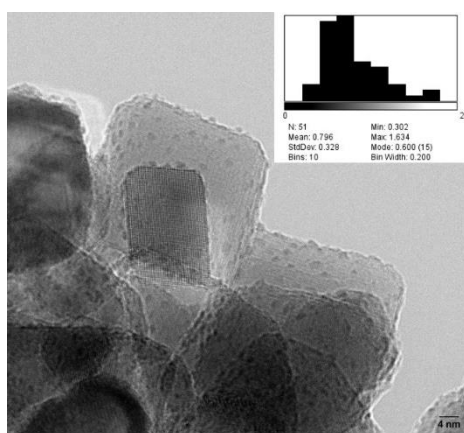


Figure S6.8 Representative HR-TEM images of calcined Re(1)-Ag(3)/TiO₂.

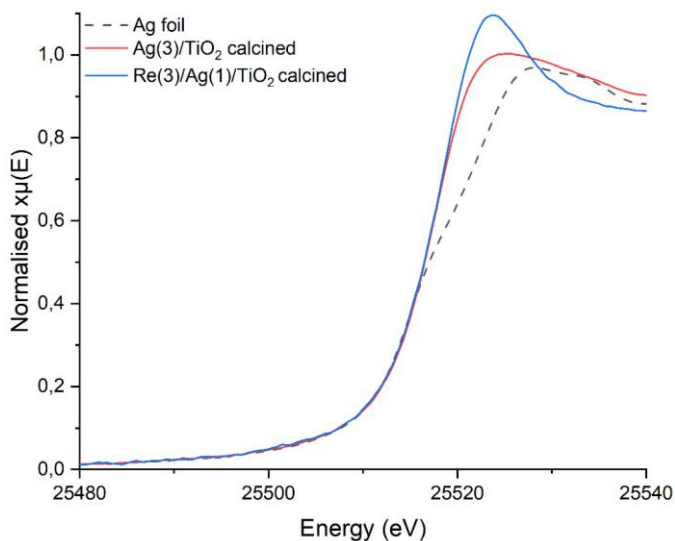


Figure S6.9 Ag K-edge XANES spectra of calcined Ag(3)/TiO₂ and Re(3)-Ag(1)/TiO₂. The XAS spectra were taken at room temperature without exposure to air after the reduction treatment by sealing the samples under N₂.

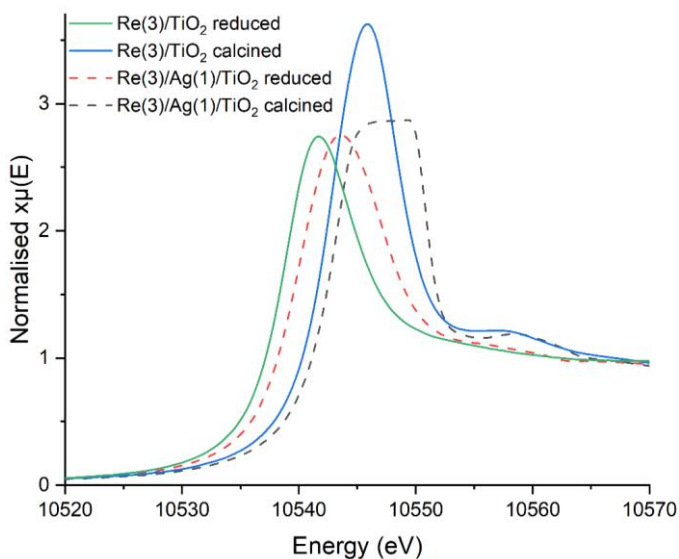


Figure S6.10: Re L₃-edge XANES spectra of calcined and reduced Re(3)/TiO₂ and Re(3)-Ag(1)/TiO₂. The XAS spectra were taken at room temperature without exposure to air after the reduction treatment by sealing the samples under N₂.

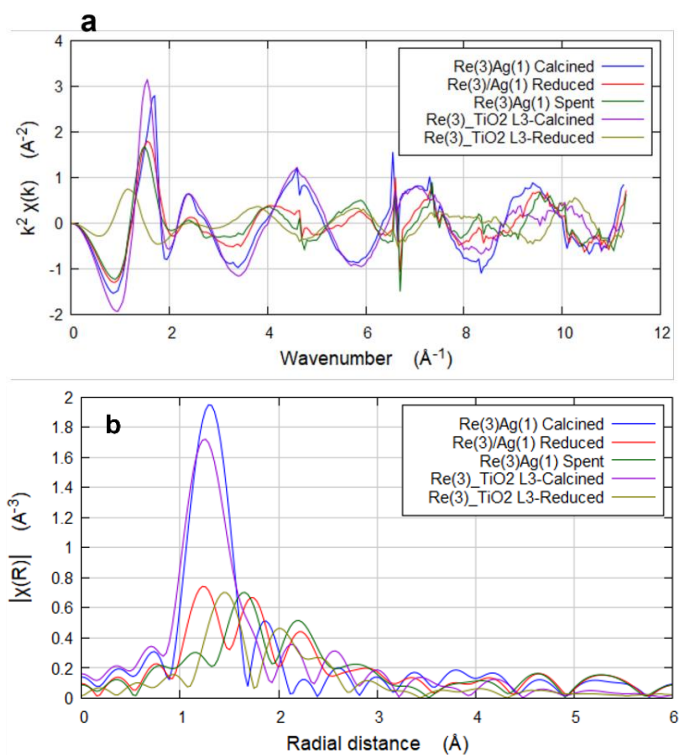


Figure S6.11 Re L₃-edge EXAFS of calcined and reduced Re(3)TiO₂, and calcined, reduced and spent Re(3)-Ag(1)/TiO₂. The XAS spectra were taken at room temperature without exposure to air after the reduction treatment by sealing the samples under N₂.

4. Mechanistic insight Re-Ag/TiO₂

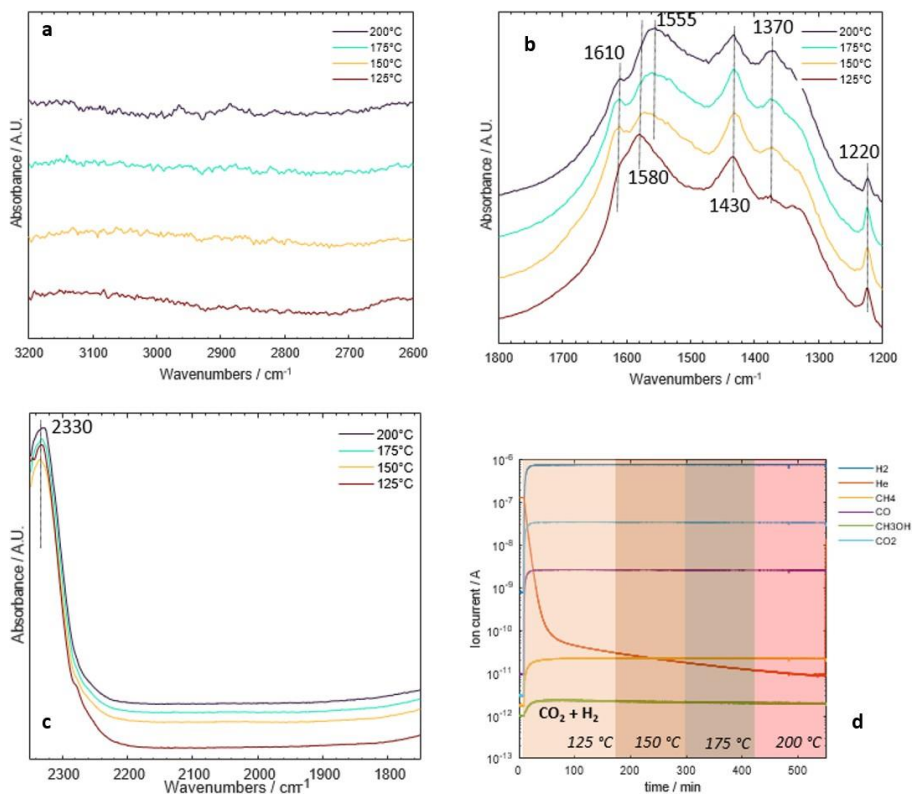


Figure S6.12 a-c Effects of temperatures on surface species obtained from operando DRIFTS during CO₂ hydrogenation over TiO₂. **d** Corresponding normalized ion current signal of products obtained from the mass spectrometer. Reaction conditions: 10 mg catalyst, H₂/CO₂ = 3, T = 125-200 °C, P = 10 bar, F_{total} = 10 NmL min⁻¹.

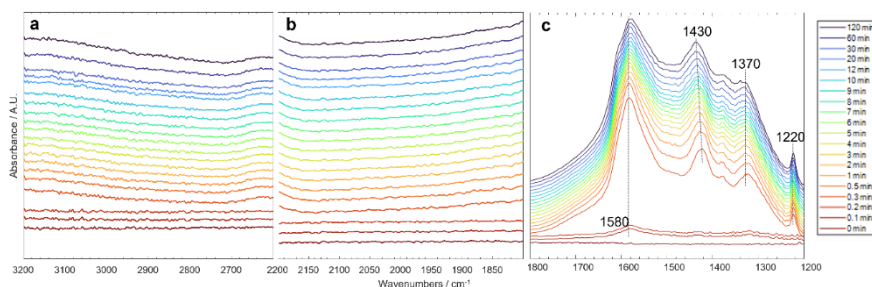


Figure S6.13 Temporal evolution of surface species obtained from operando DRIFTS during reaction CO₂ hydrogenation over TiO₂. Reaction conditions: 10 mg catalyst, H₂/CO₂ = 3, T = 125 °C, P = 10 bar, F_{total} = 10 NmL min⁻¹.

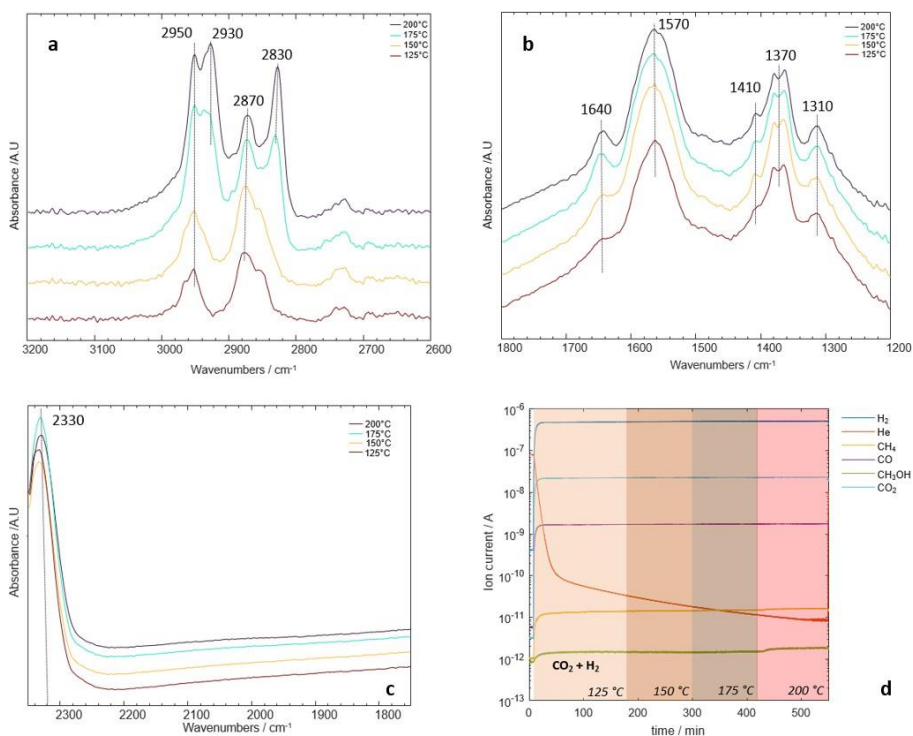


Figure S6.14 a-c Effects of temperatures on surface species obtained from operando DRIFTS during CO₂ hydrogenation over Ag(3)/TiO₂. **d** Corresponding normalized ion current signal of products obtained from the mass spectrometer. Reaction conditions: 10 mg catalyst, H₂/CO₂ = 3, T = 125-200 °C, P = 10 bar, F_{total} = 10 NmL min⁻¹.

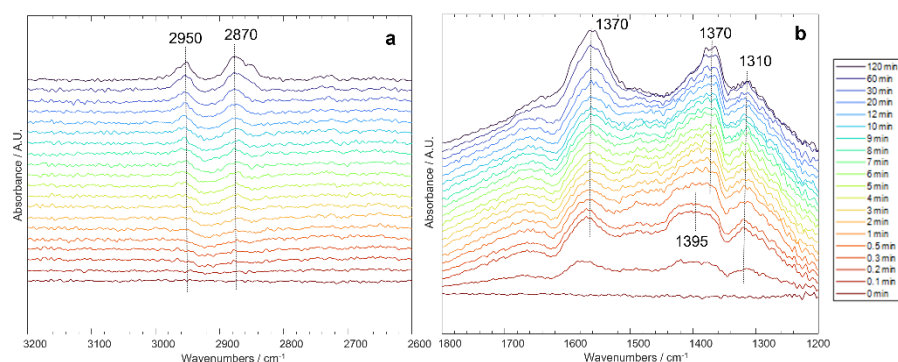


Figure S6.15 a-b Temporal evolution of surface species obtained from operando DRIFTS during reaction CO₂ hydrogenation over Ag(3)/TiO₂. Reaction conditions: 10 mg catalyst, H₂/CO₂ = 3, T = 125 °C, P = 10 bar, F_{total} = 10 NmL min⁻¹.

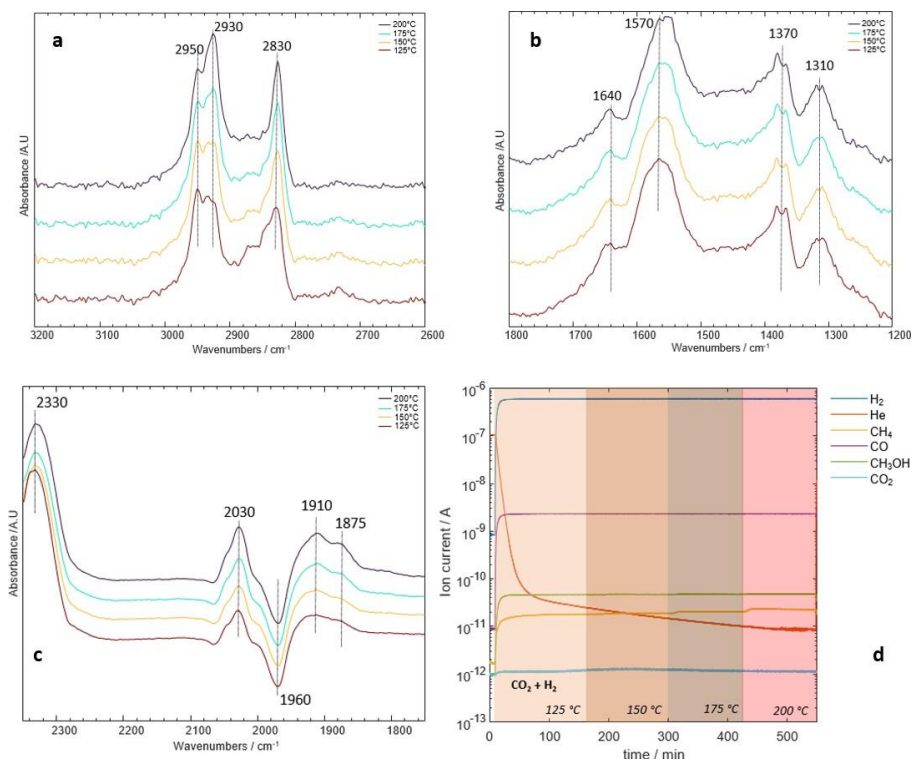


Figure S6.16 a-c Effects of temperatures on surface species obtained from operando DRIFTS during CO₂ hydrogenation over Re(3)/TiO₂. **d** Corresponding normalized ion current signal of products obtained from the mass spectrometer. Reaction conditions: 10 mg catalyst, H₂/CO₂ = 3, T = 125-200 °C, P = 10 bar, F_{total} = 10 NmL min⁻¹.

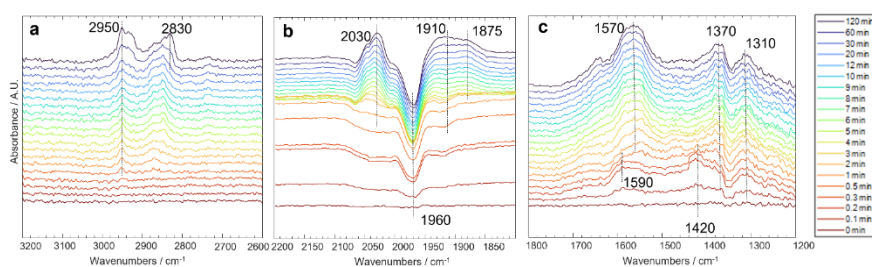


Figure S6.17 Temporal evolution of surface species obtained from operando DRIFTS during reaction CO₂ hydrogenation over Re(3)/TiO₂. Reaction conditions: 10 mg catalyst, H₂/CO₂ = 3, T = 125 °C, P = 10 bar, F_{total} = 10 NmL min⁻¹.

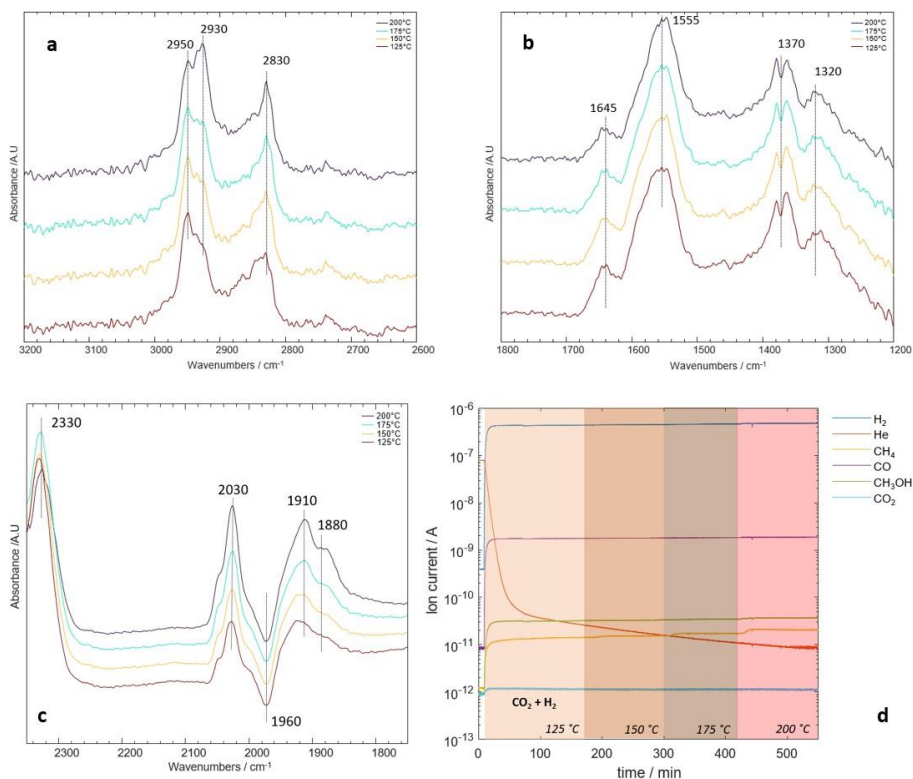


Figure S6.18 a-c Effects of temperatures on surface species obtained from operando DRIFTS during CO₂ hydrogenation over Re(3)-Ag(1)/TiO₂. **d** Corresponding normalized ion current signal of products obtained from the mass spectrometer. Reaction conditions: 10 mg catalyst, H₂/CO₂ = 3, T = 125-200 °C, P = 10 bar, F_{total} = 10 NmL min⁻¹.

Outlook



Soon, the technologies for recycling CO₂ into chemicals or fuels will become more crucial in alleviating environmental problems caused by global warming. As a well-established and relatively matured technology, CO₂ hydrogenation into methanol will play an important role in closing the carbon cycle and utilizing CO₂ sustainably. In such processes, the Cu-based catalysts will remain extensively employed due to high performance and cost-effectiveness. However, the limitation of theoretical methanol yield by thermodynamics at current industrial conditions (>220 °C) will be the rationale behind low-temperature CO₂ hydrogenation. This chapter provides the outlooks for the two important parts of the dissertation focusing on Cu-based catalysts (**Part I**) and rhenium-based catalysts for low temperature (**Part II**).

The next steps for Cu-based catalysts

The long-lasting three challenges for CO₂ hydrogenation to methanol over Cu-based and any other catalysts are (1) catalytic activity, (2) selectivity, and (3) stability. The ideal catalyst should achieve reasonable CO₂ conversion and maximum CH₃OH selectivity under industrially relevant conditions with the ability to maintain its catalytic activity for a longer period. Comprehending the fundamentals of reaction conditions, the nature of active sites and reaction mechanisms that determine the catalytic performance is always useful in the design and synthesis of novel catalysts.

The greener synthesis route in **Chapter 2** produced less wastewater during the co-precipitation process. However, catalysts prepared via co-precipitation methods always require high Cu content to achieve the optimal activity (e.g. up to 68 wt% for Cu/ZnO/Al₂O₃). The catalyst did not utilize most Cu atoms suggested by the Cu particle. The catalyst synthesis process should use less metal by enhancing the Cu dispersion and maximizing interaction between Cu and ZnO with suitable catalyst preparations (e.g. with a surfactant or reducing agent). The Cu-ZnO synergy is also determined by Cu-Zn alloying during activation and ZnO dealloying during the reaction. Yielding an active and long-lasting catalyst still requires optimization of the start-up process. Moreover, high-pressure conditions promote the formation of a more stable phase ZnCO₃, which might be beneficial against water and sintering.

The space-resolved methodologies used in **Chapter 3** helped study the effects of temperature and pressure under *operando* conditions on dominant reaction pathways. However, detecting the reactants/products *in situ* without disturbing reaction and/or creating spaces between catalyst beds remains the challenge since they affect the axial concentration, temperature,

and pressure profiles. High-pressure spatial samplings of reactants/products from within the catalyst bed using capillary sampling and simultaneously measuring temperature using a thermocouple probe is a novel approach to obtaining the actual concentration and temperature profiles, which are necessary for kinetic modeling. Moreover, *in situ/operando* characterization of catalyst structures using the existing space-resolved methodologies described in this dissertation could study the dynamic changes during activation and reaction.

The promotional effects of supports are usually defined by catalyst properties, e.g. improved dispersion, redox ability, oxygen mobility, and acidity. In **Chapter 4**, the effects of promoters on methanol selectivity were unveiled by mechanistic studies using *operando* transient DRIFTS combined with isotopic transient kinetic analysis (ITKA). Even though the reaction mechanisms are still under debate, comprehending the roles of promoters on active intermediates, which can be common between methanol and CO formation, can help suppress excessive CO formation and achieve higher methanol selectivity. These insights will be more powerful when combined with simultaneous *operando* characterization of catalyst structure to obtain activity–structure relationship. A holistic understanding of the functions of catalyst structures on surface intermediates will allow the synthesizing of suitable catalysts that destabilize the undesired surface species or redirect the reaction pathway toward the desired products. This will require a design of a reactor (cell) that is suitable for reaction engineering (e.g., kinetic studies) and *operando* characterizations (e.g., by X-ray absorption spectroscopy (XAS) and DRIFTS) under identical mass transfer regimes or flow patterns.

Rational design of catalysts for low temperatures

Exploring high-performance catalysts for low-temperature CO₂ hydrogenation to methanol is a contemporary research subject and remains a challenging task. Although high pressure is still required for desirable catalytic performance, low pressure will significantly reduce the energy demand. In such conditions, noble metals are required to overcome the inferior activity of Cu-based catalysts despite the high price and limited resources. Improved metal utilization can be assisted by support, e.g. through a strong metal-support interaction.

The optimal bifunctional properties of metal-support combinations are crucial for high methanol selectivity. In **Chapter 5**, the bifunctionality of Re was enhanced by TiO₂ yielding both sub-nanoclusters and single atoms of Re. This did not only improve the metal utilization but also provide multiple oxidation states of Re, which are the origins of high methanol selectivity. As

mentioned in **Chapter 4**, the holistic understanding of the functions of Re species and their interactions with surface intermediates allowed the rational modification of Re/TiO₂ with a small amount of Ag to destabilize the undesired surface species (carbonyl) and redirect selectivity toward desired methanol, as described in **Chapter 6**. A deeper understanding of the interplay between Re and Ag and the dynamic nature of the Re-Ag/TiO₂ catalyst remains unexplored by *operando* transient techniques used in previous chapters. Future insights will help modify the preparation technique to maximize the synergistic interplay between Re and Ag. For example, the precise control of Re cluster sizes and the way they are depositing over Ag. Lastly, DFT simulation and micro-kinetic modeling will become more important to fully grasp the whole reaction pathways of Re/TiO₂ and relevant intermediates, especially the experimentally undetectable fast-forming intermediates after formate hydrogenation steps.

Appendices



*“You should never sacrifice
what you could be for what you are.”*

— Jordan B. Peterson

from 12 Rules for Life: An Antidote to Chaos

Acknowledgments

Pursuing PhD demands sacrifices. It could be in the form of time, money, personal relationships, physical or mental health, etc. In my case, a PhD demands the sacrifice of my former self. Earning the Dr. title might be the major motivation to pursue PhD for some people since their self-worth relies on titles and external validations that come with it. Such a fake accomplishment constructed from a fragile ego and self-discontentment is not worth pursuing. Earning the Dr. title at the end of PhD is meaningless if there were not a chance to find purpose, manifest a better version of myself, and prevail over hardships. All the struggles during PhD are analogous to 'falling into the abyss' or 'valley of despair' (Dunning-Kruger effect). One could also say, "If you gaze into the abyss long enough, you will see the light, not the darkness". It was true. Eventually, I saw a way to climb up on my own. However, since I also gazed long enough into an abyss, I cannot deny that the abyss also gazed back into parts of me.

In the past years of pursuing PhD, countless interactions with various people have inspired, influenced, and motivated me to achieve the outcomes in this dissertation. With whom I have interacted profoundly, I am glad that we knew each other. The chances for two people to meet, have positive interactions, and develop relationships beyond acquaintances are very slim. Therefore, I would like to use this section maximally to convey the following messages to all of you.

First and foremost, **Atsushi** – my promoter, supervisor, mentor, leadership role model, etc. I am sincerely appreciative of all the opportunities you granted me. I had chances to discover purposes, work on challenging subjects, find the meanings in research and life, and leave legacies in the Urakawa group. It was a privilege to have almost unlimited autonomy and be connected to your powerful collaborators. Thanks for all the support during both the toughest time (hospital, moving, and burning out) and the most enjoyable times (countless).

Evgeny – thanks for accepting to be my co-promoter and later becoming the committee member of all my master's students. All the questions, comments, and feedback you gave to all my students are valuable for this dissertation.

Atul – from my interviewer for PhD position to the most important colleague. Your actions are the main chance that got me here in the Urakawa group. Thanks for being a well-respected predecessor who always guides the

younglings when necessary. I learned plenty from you since Day 1 and have grown considerably just by working with you on our setups, and the legacies of this group. Also, I knew whom I can rely on when it comes to all sorts of electronics.

Thank all the collaborators who contributed considerably to my PhD research. We could gain a much deeper understanding and insights because of your unlimited support. Copéret group (ETH Zurich) – **Prof. Christophe, Dr. Gina and Scott**, Müller group (ETH Zurich) – **Prof. Christoph, Dr. Hui Dr. Alexey and Dr. Olga** (Paul Scherrer Institute) – thanks for the amazing collaborations through the Sinergia projects. Working with the world's top scientists always put me out of my comfort zone and propelled me to improve. Their contributions led to the work shown in **Chapter 4. Dr. Takashi Dr. Shinya**, and **Kah Wei** from Shimizu group (Hokkaido University) – thanks for your trusting me in carrying on your projects. It was tough but made me grow significantly. Our beamtimes at SLS are eye-opening, paradigm shift, and enjoyable experiences. Their contributions led to the work shown in **Chapter 5**.

I would like to sincerely thank the committee members, **Prof. Hensens, Prof. van Bokhoven, Prof. de Jong**, and **Dr. Abdala** for scrutinizing the dissertation, providing valuable feedback, and examining me in the thesis defense ceremony.

I would like to thank all the book editors, **Prof. Himeda, Dr. Wey Yang, Prof. Ng**, and **Dr. Sit**, for welcoming me to the book publishing world and having my own two chapters (**Chapter 1**). I had fun writing them and helped me learn substantially through extensive literature reviews.

Thank all PhD candidate fellows at TU Delft and ICIQ who shared the same purpose, pain, and pleasure. Thank **Lingjun** (and her husband **Jean**) for being a good friend since the first day in ICIQ and always being there for me when I needed help the most (both personal and professional matters). We always shred our suffering (joking) in the afternoon break at ICIQ and the way you peeled all kinds of fruit with a Swiss knife is unforgettable. You are one of the few people who were able to drag me out of the home to enjoy more life (e.g., a hotpot party and several day trips). Your help on the infrared camera and MATLAB script also led to the work shown in **Chapter 3. Sorin** – my devil's advocate. Thanks for being a reliable friend since my time at ICIQ. You are a few people whom I will ask for a second opinion when it comes to the serious stuff. I guess we shared so many traits, and that why is Atsushi chose us both. **Donato** – my No.1 complainer who annoyingly pushed me forward in a unique way. Our conversation is bantering, so I did not know whether it was serious or not. Thanks for taking a lead and organizing so many enjoyable events with authentic Italian food. You are my

main role model in enjoying life. Thank **Min** for being a good friend, paronymph, gym mate, wing girl, party buddy, etc. It was hard to find a pal who walk alongside me on a self-improvement journey and supported me to get out of my comfort zone (e.g., surviving Yoga, Pilates, and Zumba classes full of women). Since we are the same age (my metabolic age and your actual age), we still like to crash a party together. **Ahmad** – my success of PhD project, who can also teach me about other aspects of life apart from research. Your presence can lessen the intense atmosphere in the room (with your perfume?). It is nice to see you grow and be transformed into a scientist. You **Rohit** – my predecessor. thanks for the warm welcome and your help in setting up my life in Tarragona. You are always there when I needed the most, even at the lowest point of my life (operation in hospital). Your time during the end of PhD for the knowledge transfer is appreciated. Our shared work is also shown in **Chapter 3**. **Jordi** –my PhD interviewer who help me adapt to Tarragona. Thanks for encouraging me to have more balance in life and dragging me out to enjoy the nightlife in Tarragona. **Martha** – thanks for many good comments and suggestions during the first year of PhD. I found them very practical and efficient. **Juanjo** – stop calling me Dr. Peanuts!!! (with Spider-Man theme song). Thanks for teaching me many things in my first year and even third year (about DRIFTS). **Silvia** – it was nice to learn a bit about Spanish popular songs, thanks.

Thanks to all the veterans (Post-Doc) for mental support. You all are one of the smartest guys I have ever known. Thank **Disha** for being a good friend, paronymph, and encyclopedia. Since we have been in similar situations, we tended to share the same value in life, and it was fun discussing about science for self-improvement and daily life with you. More importantly, your sincere and honest feedback helped me better as a scientist and as a person. **Thomas** – my fellow gaming friend. We rarely discussed catalysis, but we talked passionately about the META (Most Efficient Tactic Available) of our game (which I quit!). It was nice to have someone whom I can act childish with. Thanks for pulling me out of my turtle shell to enjoy the nightlife in Delft. **Jose** – thanks for being a mature and good brother (in law) and always calming down when I was too aggressive and overbearing. You taught me how to approach conflict like a gentleman. You inspired me to hit the gym to have your abs, as well as, to have a good family. **Dimitry** – thanks for a warm welcome and support during our time in building 67. I enjoyed our lunchtime and our discussion about politics and Dutch courses. **Pratik** – an amazing storyteller. I learned so many things from your funny stories and unpleasant experiences. Many stories seem a bit too unfortunate to be true but give valuable less if listen to meticulously. Thanks a lot for always cheering me up during hard times and supporting my extreme

opinions. **Afreen** – a very talkative person with a unique lifestyle (with OCD). It was fun teasing and bantering with you. Thanks for always being around and helping me on many occasions. **Benjamin** – the funniest German I ever met! since our sense of humor is understandable only by a science geek. Thanks for bringing both knowledge and positivity to our group in my last few months finalizing my thesis. Bantering with you is always fun.

Next, I want to thank Master students who grow together with me as a researcher and contributed so much to my dissertation. **Adarsh** – a versatile student. Thanks for always being supportive of my journey. I knew your research was tough because everything kept breaking but I am glad you have survived. **Meet** – thanks for your support and keep pushing me forward in the time I lost my motivation working on **Chapter 5**. I believed you are the most enthusiastic and motivated guy I ever worked with, and few people cheer me up to publish in Nature as you did. I believed we shared so many fond memories and meaningful conversations. **Sumant** – a younger version of myself who used to share the same personality. We never missed any chance to crash a party. “Part of the journey is the end” also came to me not only to you. Our path diverges but hopes we will be always in contact. **Ása** – a gym girl. After COVID-19, most students have social anxiety but thanks to your Donut Friday (a mandatory social event) you have initiated that made the population in building 67 become social creatures again! Sincerely, thanks for being highly independent even though I did not have a chance to give you my best supervision. **Luca** – a good kohai, friend and mentor (in other areas of life), and professional pianist. Thanks for making the last year of PhD even more enjoyable and meaningful by initiating sports events. You also inspired me to resurrect my drumming and start learning piano. Your contributions in **Chapter 6** are massive and I look forward to your future achievement. **Ralph** – I have taught him like my own students. Most of our discussions are nonsense but thanks for your moral support and seemingly sarcastic feedback. **Damian** – a highly ambitious, motivated, conscientious, competitive, irritating disagreeable brother (and a competitive rival in soccer). You sometimes want someone like this in your life to keep you motivated, challenged, and out of complacency. You brought so much fun into my last year of PhD and our group. If you represent vices, I will represent virtues. If you were ‘Yin’, I would be ‘Yang’. We need each other bro! **Cees, Moaz, Binder, Pablo, and Daphne** – donut, and pizza Friday fellows in building 67. It was tough after COVID-19 and WFH but thanks for trying your best to enjoy socialization. **Jesse** – the most independent, motivated, and smart BEP student I ever met. Thanks for always responding to my selfish requests. Looking forward to seeing your bright future. **Manoj** – my potential BEP student whom I rejected! Thanks for helping translate the summary. I

will accept and support you in whatever you have chosen to become. **Jim** – also thanks for the help with the translation. You are a great event organizer. Good jobs at Christmas dinner during COVID-19 time and international dinner. **Carlos** – thanks for bringing positivity to the last corner of PhD. I will always consider you a relationship expert.

Thanks to all the technicians and supporting staffs who made my research run smoothly as silk. **Harrie** – area supervisor, my No. 1 in building 67 and Dutch cultures. Thanks for babysitting me from the first step at TU Delft and always being my best assistant. In my research approaches, what I considered safe could look like a high risk for you, but thanks for trusting me and being willing to compromise. **Bart, Liliana, and Willy** – the persons behind the successes of all my MEP students. My MEP students definitely met you more than me and madly bothered you all the time for training and troubleshooting. Thanks for being patient and willing to help them. **Erwin and Alex** – the genies of the gas team. Thanks for always fulfilling all my wishes for gas cylinders and pressure regulators. **Frédéric** – the IP protector. Thanks for working so hard on the patent application related to the co-precipitation method (**Chapter 2**) and trying to keep it survive. **José Luis, and Xavier** – the magicians of the mechanical and glass-blowing workshop at ICIQ. Thanks for indulging me by crafting everything I have imagined. **Georgiana and Marta** – scientific staff at ICIQ. Thanks for your support in the first year of PhD.

There was a constant influx of visiting researchers coming to our group. **Satoshi, Takuya, Shunsaku, and Asami** – I always connect well with Japanese, especially when I am abroad. Thanks for helping me in the transition period (1st year of PhD), when I had limited capacity to connect with people. You all are always nice and kind, but your conscientiousness also motivated me to work harder. **Reina** – Thanks for all the Japanese snacks your mom sent you. I enjoyed talking to you about Japan since I went there several times. Your reaction when I am speaking Japanese is amazing! **Giulia** – I knew you liked Thailand so much. Hope you got a chance to go there again. Having a chance to teach you also help me gain a deeper understanding of my project. **Ishani** – Thanks for keeping me sociable when there were far fewer people in building 67 during COVID-19. Since we used to live in Tarragona, we connected really well. **Michela** – I enjoyed teasing you the most. You are a kind and sincere person but are also on the opposite end of the spectrum. Thanks anyway for your crazy suggestions. **Louise** – a uniquely bright person who is mature for her age. Since we shared many similar traits and values, our deep conversations are always enjoyable. I have never thought that I could be vulnerable and learn so many valuable lessons from our interactions, which will change the course of my life. Thanks for

everything! **Sarah-Alexandra** – a unique passionate chemist who shared a nerdy sense of humor, a goal for Angewandte Chemie, and a love for synchrotrons. Thanks for allowing me to be your personal psychiatrist, psychologist, neuroscientist, etc to help with your sleep and stress (my second dream job, not beamline scientist!). I saw the development and wholeheartedly believe that what other people considered your intrinsic is alterable. **Khurram** – thanks for always being around and helping me on many occasions. **Tomone** – the funniest Japanese I met so far! Thanks for bringing humor and joy to the last few months of PhD.

I would like to thank the secretaries of the group for their administrative support. **Aurora** – amazing supporter of the Urakawa group at ICIQ. Thanks for taking good care of me all the time in Tarragona, especially during the hospital operation. **Els** – thanks for helping me settle down and continue working in Delft as smoothly as silk.

Thank the Thai student community in Delft that kept me in touch with Thainess. **Krissada** – a Thai student met via Airbnb by chance. Thanks for introducing me to the Thai community and being a good bro. **Siwarak** – the event organizer. Thanks for always holding parties and asking me to join. **Jittima** – theoretical chemist of ISE (whom I rarely met on campus). Thanks for answering some stupid questions regarding **Chapter 4** and making me find the conclusion. Your Thai cooking skills are also legendary! Thanks, **Sirasak**, **Saowanit**, **Laddaporn**, **Tasama**, **Gunntranutt**, **Krit**, **Polpat**, **Warakan**, **Poomisub**, and other Thais who were there to share the fun.

Vissanu – my former MEP supervisor, former boss, mentor, and father figure. Thanks for being my role model since I graduated with the MSc and motivated me to pursue a PhD. I would not have come this far without your mentoring, guiding, and inspiring during my time at MUT. Hope we can travel together again in the future.

Lastly, I thank my family, **Sritham**, and **Peangpen** – my parents, and **Napat** – my younger brother, for your constant moral support and a meaningful conversation via video calls during the time abroad away from home. I am grateful for my parent who placed special care on my education since I was young and supported my passion for science. All the books and encyclopedias in the house were the evidence. I especially thank my dad who always drove me to cram schools, I would never come this far without your dedication. The environment at home where I can only concentrate on studying without worrying about anything else was also bliss, and I have never realized that it was an unfair advantage that helped put me here.

List of publications

Journal articles

Within the scope of the thesis

† Gaikwad, R., Reymond, H., **Phongprueksathat, N.**, Rudolf von Rohr, P., & Urakawa, A. (2020). From CO or CO₂?: space-resolved insights into high-pressure CO₂ hydrogenation to methanol over Cu/ZnO/Al₂O₃. *Catalysis Science & Technology*, 10(9), 2763–2768.

† *The three first authors contributed equally to this work.*

Phongprueksathat, N., Bansode, A., Toyao, T., & Urakawa, A. (2021). Greener and facile synthesis of Cu/ZnO catalysts for CO₂ hydrogenation to methanol by urea hydrolysis of acetates. *RSC Advances*, 11(24), 14323–14333.

Outside the scope of the thesis

Phongprueksathat, N., Thanasujaree, T., Meeyoo, V., & Rirksomboon, T. (2022). Spatially resolved investigation into the coke formation and chemical states of nickel during autothermal reforming of acetic acid over Ni/CeO₂–ZrO₂ catalysts. *Reaction Chemistry & Engineering*.

Docherty, S. R., **Phongprueksathat, N.**, Lam, E., Noh, G., Safonova, O. V., Urakawa, A., & Copéret, C. (2021). Silica-Supported PdGa Nanoparticles: Metal Synergy for Highly Active and Selective CO₂-to-CH₃OH Hydrogenation. *JACS Au*, 1(4), 450–458.

Meeyoo, V., Panchan, N., **Phongprueksathat, N.**, Traitangwong, A., Guo, X., Li, C., & Rirksomboon, T. (2019). Low Temperature Methanation of CO₂ on High Ni Content Ni-Ce-ZrO₈ Catalysts Prepared via One-Pot Hydrothermal Synthesis. *Catalysts*, 10(1), 32.

Phongprueksathat, N., Meeyoo, V., & Rirksomboon, T. (2019). Steam reforming of acetic acid for hydrogen production: Catalytic performances of Ni and Co supported on Ce_{0.75}Zr_{0.25}O₂ catalysts. *International Journal of Hydrogen Energy*, 44(18), 9359–9367.

Book chapters

Phongprueksathat, N., & Urakawa, A. (2021a). Enhancing Sustainability Through Heterogeneous Catalytic Conversions at High Pressure. In *Heterogeneous Catalysts* (pp. 633–648). Wiley.

Phongprueksathat, N., & Urakawa, A. (2021b). Heterogeneously Catalyzed CO₂ Hydrogenation to Alcohols. In *CO₂ Hydrogenation Catalysis* (pp. 207–236). Weinheim, Germany: WILEY-VCH GmbH.

Patents

Urakawa, A. & **Phongprueksathat, N.**, (2021). Co-precipitation method and catalyst thereof, *European Patent Office*, EP3769837.

Oral contributions

Phongprueksathat, N., Ting, K.W., Toyao, T., & Urakawa, A. “Mechanistic insights into low-temperature CO₂ hydrogenation to methanol over Re/TiO₂ catalyst using Operando DRIFTS-SSITKA” TOCAT9 24-29, July 2022 in Fukuoka Japan.

Poster contributions

Phongprueksathat, N., & Urakawa, A. “A greener preparation route of Cu/ZnO catalyst for hydrogenation of carbon dioxide to methanol.” EuropaCat 2019, 18-23 August 2019 in Aachen, Germany

Curriculum Vitae

Nat Phongprueksathat was born on the 25th of August 1988 in Surat Thani, Thailand. He completed his secondary school education in 2007 at the Suratthani school. During high school, he obtained a bronze medal from Thailand Chemistry Olympiad (TChO). He started his BEng studies in Petrochemical and Polymeric Materials at Silpakorn University that same year and finalized it in early 2011 with *magna cum laude*. He did his internship at an oil refinery of Bangchak Corporation in Bangkok. In the same year, he continued his international MSc study in Petrochemical Technology at the Petroleum and Petrochemical College (PPC) of Chulalongkorn University. His master's thesis on heterogeneously catalyzed steam reforming was supervised by prof. dr. ir. Vissanu Meeyoo and prof. dr. ir. Thirasak Rirksomboon. From 2013 to 2017, he worked as a lecturer in the Department of Chemical Engineering at the Mahanakorn University of Technology. He carried out several industrial research projects with PTT Global Chemical and the National Research Council of Thailand (NRCT) in the group of prof. dr. ir. Vissanu Meeyoo. Since October 2017, he had been pursuing his PhD study in the group of prof. dr. Atsushi Urakawa at the Institute of Chemical Research of Catalonia (ICIQ) in Tarragona, Spain, before relocation to the Catalysis Engineering section of the Chemical Engineering Department at the Delft University of Technology. The most important works during his PhD are described in this dissertation.

